UNIVERSITY OF TRENTO

Doctoral School in Civil, Environmental and Mechanical Engineering

Curriculum 1. Civil and Environmental Engineering

Marina Amadori

On the physical drivers of transport processes in Lake Garda:

A combined analytical, numerical and observational investigation

2020 - Doctoral thesis

UNIVERSITY OF TRENTO - Italy
Department of Civil, Environmental and Mechanical Engineering

Doctoral School in Civil, Environmental and Mechanical Engineering
Topic 1. Civil and Environmental Engineering - XXXII cycle 2016/2019

Doctoral Thesis - January 2020

Marina Amadori

On the physical drivers of transport processes in Lake Garda:

A combined analytical, numerical and observational investigation

Supervisor
Marco Toffolon, University of Trento

Credits of the cover image .....

University of Trento
Doctoral School in Civil, Environmental and Mechanical Engineering
http://web.unitn.it/en/dricam
Via Mesiano 77, I-38123 Trento
Tel. +39 0461 282670 / 2611 - *dicamphd@unitn.it*

Abstract

This doctoral thesis provides the first comprehensive study on the physical processes controlling hydrodynamics and transport in Lake Garda. The investigation is carried out in parallel on three different levels: data collection and analysis, three-dimensional numerical modeling and theoretical study.

On the first level, data are collected by building up a network of research institutes and local administrations in the lake area. New data are acquired through traditional field campaigns (CTD, thermistor chains, satellite imagery), while a citizen-science approach, based on local knowledge harvesting, is successfully tested to gather qualitative data on surface circulation.

On the second level, a three-dimensional modeling chain is set up, by coupling one-way a mesoscale atmospheric model to a hydrodynamic model. Both models are validated on multiple temporal and spatial scales, allowing to identify the main interactions between the weather forcing and the hydrodynamic response of the lake. Circulations in Lake Garda are found to be very sensitive to the thermal stratification, to the spatial distribution of the wind forcing and to the Earth's rotation. Surface cyclonic gyre patterns develop in the lake as a residual outcome of alternating wind forcing of local breezes and differential acceleration induced by Earth's rotation, whereas unidirectional currents flow under a nearly uniform and constant wind. Both model and observations evidences show that, under weak thermal stratification, Ekman transport activates a secondary circulations in the northern part of the lake, driving surface water to the deep layers and possibly preconditioning the lake for subsequent buoyancy-driven deep mixing events.

On the third level, the relevance of the Coriolis term in the equations of motion for relatively narrow closed basins is analytically addressed. The classical Ekman problem is solved by including the presence of lateral boundaries and a new analytical solution is formulated. The validity of the new solution is proved by numerical tests of idealized domains of different size, geographical location and turbulent regime, and on Lake Garda as a real test case. The meaningful length scales are discussed, and the significance of Rossby radious as a reference horizontal scale is disproved for steady-state circulations driven by wind and planetary rotation.

Acknowledgements

This research was supported by the Department of Civil, Environmental and Mechanical Engineering of University of Trento, on a proposal by my supervisor prof. Marco Toffolon. He is the first person I need to acknowledge here for his trust, constructive comments and guidance. Thank you Marco for believing in me, for your patience, for all the things you taught me. When I look back at the years we have been working together, I feel I could not have asked for a better supervisor.

I would like to express my gratitude to prof. Dino Zardi and Dr. Lorenzo Giovannini, from our Department, for sharing with us the ambition of the first physical study on Lake Garda and for all the work done together. Accordingly, I thank all the researchers and institutions of Cluster Garda who picked up our initial idea and shared knowledge, data, ideas and time with us. I truly hope this was just the first step for successful and fruitful opportunities of joint research.

Part of the results presented in this dissertation were obtained within the project "Lake Garda Mixindg Dynamics" lead by prof. Henk A. Dijkstra from the Institute of Marine and Atmospheric Research of the University of Utrecht, in collaboration with Dr. Sebastiano Piccolroaz. I express my deepest appreciation to prof. Dijkstra for his generous encouragement and inspiring suggestions, and to Dr. Piccolroaz for his meticulous comments and for our adventurous field trips in Lake Garda. I also want to thank the people from IMAU for their warm hospitality during my visiting periods in the Netherlands, Michael Kliphuis for his help with Cartesius supercomputer anytime I needed, Hans van Haren (NIOZ) for insightful discussions, Menno Genseberger (Deltares) for his initial work on the Delft3D model of Lake Garda, and to all master students who partially contributed to this doctoral research.

Special thanks to my colleagues and PhD students I spent most of my time with, and in particular to my dear fellow Serena Petrini, for sharing the effort with me, once again.

Thanks to my friends, to my family, to all those who have always been there for me.

Contents

Chapter 1

Introduction

1.1 Aim and motivation

Over the last decades, large perialpine European lakes have experienced a progressive deterioration due to increasing anthropogenic pressures [Salmaso et al., 2018], despite a growing awareness on the role they play as climate regulators, water reserve and biodiversity hot-spots. Due to their shape, size and depth, they store important water volumes, with often long renewal times, oligomictic mixing regimes and delicate ecological equilibria. These factors make them extremely vulnerable to pollution and climate change, especially when they are located in densely populated and industrialized areas, as many of the large subalpine Italian lakes are.

This doctoral research takes Lake Garda, the largest sub-alpine Italian lake, as case study. The reasons for the choice of this case study are twofold: first, Lake Garda represents an uncharted territory for new scientific explorations, and secondly, it is a complex and challenging case study where innovative approaches can be exploited for public engagement.

On the first point, Lake Garda hydrodynamics are still largely unexplored, despite the high relevance at local and international level of the lake. As it will be reviewed further on, research literature on Lake Garda mostly focused on eutrophication and water quality studies, and often overlooked the hydrodynamics underlying transport processes in the lake. Hence, the first aim of this research is taking a first step in filling such a gap in the knowledge of the physical processes in Lake Garda.

On the second point, Lake Garda is an extraordinary example of environmental and political complexity. Its unique shape makes it an interesting case study for limnological investigations, as it combines two completely different morphologies. One is a deep and narrow northern trunk, regularly shaped and nestled in a steep alpine orography, and the other is a shallower

and wider southern region, characterized by a more heterogeneous bathymetry and surrounded by a hilly landscape. Such a complexity of under and above water topography is associated to a variegated atmospheric and lake circulation, whose mutual interactions have never been explored in this lake. From a political point of view, Lake Garda is at the mercy of multiple and diverse interests, as it is intensely used as a touristic attraction (the lake is visited by more than 24 million tourists every year [1]) but also as resource for agricultural and municipal water supply. Moreover, the political administration of the lake is fragmented among two separate regions (Lombardia, Veneto) and one province (Autonomous Province of Trento), each having different policies on the portion of the lake within their own jurisdiction. The existence of many stakeholders makes any lake-wise intervention difficult to manage, and complicates also the research activity, from its early stages, (e.g. raising funds, planning monitoring activity, requesting formal authorizations and data) until the very last steps (e.g. publication of results, acknowledgments).

Aiming at a systematic approach, the investigation is carried out in parallel on three different levels: analytical, numerical and observational. While each one of these levels has its own dignity, we believe that a systematic approach has to be built on the integration of experimental and analytical work, in order to achieve a complete understanding of the investigated processes.

1.2 Physical limnology in large and deep perialpine European lakes

The perialpine European region is punctuated by several large lakes that fit in the definition of 'large and deep lakes'. Since the XX century, many of these lakes have been subject of an increasing number of limnological studies ranging from pure physical investigations to bio-ecological monitoring of their ecosystem functioning.

In this section, we are far from the purpose to provide an exhaustive review of the existing literature on these lakes, for which we refer to the valuable work already available by Ambrosetti and Barbanti [1992]; Salmaso and Mosello [2010]; Salmaso et al. [2018]. Our aim is instead

[1] According to 2017 statistical survey, see *https://www.ilsole24ore.com/art/vacanze-lago-garda-guida-classifica-italia-AEoST0CC*

to recall the key characteristics of these lakes by referring to those studies that focused on their physical dynamics and addressed research questions of the kind we will pose. Towards this aim, amongst all the potential case studies located in temperate perialpine regions, we select the following: Lake Como, Iseo, Maggiore (Italy), Lugano (Italy, Switzerland), Lake Geneva (Switzerland, France), Lake Constance (Germany, Switzerland, Austria), Lake Zurich (Switzerland). Fig. 1.1 shows the lakes above in their geographical context, including Lake Garda, while Tab. 1.1 collects their main physical characteristics.

	Altitude [m a.g.l.]	Length [km]	Width [km]	Maximum depth [m]	Surface area [km^2]	Water volume [km^3]	Residence time [years]
Garda	65	52	3-18	346	368	49	27
Iseo	186	25	4.1	251	62	7.57	4.1
Como	198	45.7	0.65 - 4.4	410	146	22.5	4.5
Maggiore	193	64.37	5	370	213	37.5	4.1
Lugano	271	35	3	288	28	4.69	12.4
Geneva	372	73	14	310	580.03	89	11.4
Constance	396	63	14	253	536	55	4.3
Zurich	406	40	3	136	88	3.9	1.2

Table 1.1: Physical characteristics of the selected large and deep perialpine lakes.

Figure 1.1: Geographical location of the deep and large perialpine lakes Como, Iseo, Maggiore, Lugano, Geneva, Constance, Zurich (Switzerland)

As the definition itself outlines, all mentioned lakes share common morphological characteristics, which influence their hydrological and dynamic behaviour and their interaction with the surrounding environment. These lakes are often defined as 'large', 'elongated' and 'narrow'

due to their large surface extension with a predominant horizontal dimension (length) of at least one order of magnitude bigger than the other (width). They are deep lakes, with a sharp bathymetry often replicating, below the water, a steep delimiting orography along the shores. The combination of a significant surface extension and depths makes these lakes reservoirs of high water volume, with often long residence time if their catchment area is limited (as in the case of Lake Garda, Lugano, Geneva).

The thermal regime of these lakes is typically characterized by long periods of stable stratification (with deep temperatures usually above 4°C), when the exchanges between surface and deeper layers are inhibited by strong density gradients. These lakes are classified as warm monomictic lakes [Hutchinson, 1957], as they do not freeze and overturn completely during early spring. Most of them reach the complete homogenization of the water column at the end of harsh winters only, thus meeting more appropriately the definition of oligomictic (Lake Garda, Maggiore and Como [Ambrosetti and Barbanti, 1999], Geneva [Schwefel et al., 2016]). Several authors addressed to the warming climate the principal cause of the intensification of thermal stratification and the reduction of the seasonal spring vertical mixing process [Salmaso, 2005], leading in some cases to meromixis (Lake Iseo [Garibaldi et al., 1999] and Lugano [Barbieri and Mosello, 1992]). The thermal structure and its sensitivity to climate change have been recently investigated by means of modeling works, e.g. in Lake Zurich[Peeters et al., 2002], Geneva [Perroud et al., 2009], Constance [Wahl and Peeters, 2014], Iseo [Valerio et al., 2015a], and Maggiore [Fenocchi et al., 2018], among others.

Most of the studies investigating the response of these lakes to the climate change, or more in general to the atmospheric forcing, observed similar regional climatology. In fact, due to their common location inside of an alpine topography, they are typically subject to wind channeled between their steep shores and uniformly distributed over the lake surface. These winds are normally thermal breezes blowing from one direction in the morning, and from the opposite in the afternoon, each one having its local name (e.g. 'Le Vent' and 'the Bise' in Lake Geneva [Lemmin and D'Adamo, 1997]; The 'Vet' and the 'Ora' in Lake Iseo [Valerio et al., 2017], 'Peler', 'Balin' and 'Ora' in Lake Garda Giovannini et al. [2017]) and following more the dynamics of mountain-valley rather than lake-land breezes. However, it is not uncommon for these lakes to be subject to long-lasting storm winds at a synoptic scale, e.g. Föhn winds. After such winds,

[Lemmin and D'Adamo, 1997] observed in Lake Geneva direct circulations of the kind described by Strub and Powell [1986], Appt et al. [2004] upwelling phenomena in Lake Constance, and Vilhena et al. [2013] non linear internal waves in Lake Iseo.

Currents and transport patterns in these lakes are specifically dependent on the wind distribution, on the local topography and on the thermal conditions. Investigations on this topic have been carried on with the help of current measurements and numerical modeling (Lake Geneva [Bauer and Graf, 1979; Bohle, 1991; Razmi et al., 2013], Lake Constance [Hollan, 1978; Boehrer et al.]), with a focus ranging from the formation of gyres (Lake Geneva [Razmi et al., 2017], Lake Constance [Hollan, 2013]), to the interaction with riverine inflow and sediment transport (Lake Lugano [Cesare et al., 2006], Lake Geneva [Razmi et al., 2014], Lake Maggiore [Laborde et al., 2010; Fenocchi et al., 2017], Lake Iseo [Pilotti et al., 2014, 2018]).

However, literature on these lakes has mostly focused on their behaviour as oscillators [Hutter et al., 2011b]. Due to their sensitivity to the external forcing for the establishment, development and eventually breaking of vertical density gradients, they are subject to an intense oscillating activity. We cite here a selected sample of relevant studies on perialpine deep and large lakes, either focusing on seiches (Lake Geneva Lemmin et al. [2005], Constance Hamblin and Hollan [1978], Zurich Horn et al. [1986]) or topographic and gravity waves (Lake Geneva Bohle-Carbonell [1986], Bouffard and Lemmin [2013], Constance Appt et al. [2004]; Wang et al. [2000], Zurich Lemmin [1987], Lugano Hutter et al. [1983], Iseo Valerio et al. [2012], Como Guyennon et al. [2014]).

We have seen that the common physical features and dynamical behaviour of the perialpine lakes allowed 'hot-spots of specialized research' [Salmaso et al., 2018] to flourish in specific case studies. While more lakes fall into the category of interest of this doctoral research (e.g. Lucerne, Neuchâtel, Thun, Walenstadt in Switzerland, Ammersee in Germany, Annecy and Bourget in France), but they are subject of eco-biologically oriented research, rather than physical limnology.

The above is particularly relevant for the case of Lake Garda. Drawing inspiration from the studies on similar lakes, this doctoral thesis aims to provide an essential starting point for a novel and comprehensive limnological investigation on Lake Garda.

1.3 Previous studies on Lake Garda

Lake Garda has been the object of scientific research since the 18th century, with studies concerning its genesis and morphology [Marsili, 1930]. In the early XX century, Defant [1908] and Vercelli [1909] provided pioneering contributions to the knowledge of surface seiches as a response of the lake to meteorological forcing. After those early contributions, which gave rise to a historical controversy on the period of the binodal seiche [Vercelli, 1910; Caloi, 1948], most of the following studies focused on the ecology and biology of the lake.

Over the last decades Lake Garda has been a deeply investigated case study for the seasonality and distribution of relevant phytoplankton species in large subalpine lakes [Salmaso, 1996, 2000, 2002]. In this research field, a key role was recognized to vertical mixing on the nutrients availability [Salmaso et al., 2003], and to climatic fluctuations on the interannual trophic variability [Salmaso, 2005; Salmaso et al., 2014].Salmaso and Mosello [2010] and Salmaso et al. [2017] identified existing ecological shifts in Lake Garda (as well as in several other alpine lakes). They suggested that the increasingly rare deep mixing processes, traditionally associated to negative buoyancy during harsh winters, can be the sign of a transition of Lake Garda from oligomixis [Ambrosetti and Barbanti, 1992] to meromixis due to climate change. While these studies analyzed the role of the physical processes on the ecological shifts, they focused on their consequences rather than their drivers. Hence, the contribution of such investigations, while being significant under an ecological perspective, from a physical point of view is limited to a qualitative description of the lake thermal patterns in the context of climate change.

Remote sensing activities have been conducted since the 90s [Zilioli et al., 1994] using data gathered from multi-spectral Landsat and Sentinel-2 sensors [e.g. Bresciani et al., 2018], ocean color radiometers as MERIS and MODIS [e.g. Bresciani et al., 2011b], and imaging spectrometry from both satellite [Giardino et al., 2007] and airborne platforms [Bresciani et al., 2012]. Lake Garda was extensively adopted as a remarkable case study for water quality monitoring, mainly in terms of chlorophyll-a and lake surface temperature [Bresciani et al., 2011a; Lenstra et al., 2014; Di Nicolantonio et al., 2015; Pareeth et al., 2016], shallow water mapping [Giardino et al., 2014], and algorithm developing and testing [e.g. Guanter et al., 2010; Odermatt et al., 2010].

The effects of a changing climate on lake ecosystem and temperature dynamics have been recently analyzed in the framework of the European Lakes Under Environmental Stressors project (EULAKES), implemented through the Central Europe Programme and co-financed by the European Regional Development Fund (http://www.eulakes.eu/). Within the framework of this EU project, several results on Lake Garda response to climate change were achieved. Bresciani et al. [2011a] performed a correlation analysis between lake surface temperature and Chlorophyll-a concentration based on MODIS and MERIS data,and found a low correlation between growth of phytoplankton and thermal stratification. Piccolroaz et al. [2013] projected the future response of lake surface temperature to a warming air temperature during the next century. Bolpagni et al. [2013] conducted a large sampling campaign for a total of 865 sampling points to assess the distribution and diversity of charophytes, and found that the lake is an important reserve for many rare and threatened charophytes at a national and European level. Salmaso and Cerasino [2012] studied the cascading effects on the limnological characteristics of the lake originating from the year-to-year oscillations in the winter East Atlantic teleconnection index, and [Salmaso et al., 2014] documented the deterioration of the quality and the aesthetic appearance of Lake Garda water. Specific paleo-limnological investigations on deep sediment cores were also carried on by the same research group, with interesting outcomes on the lake ecological history from the Middle Age [Milan et al., 2015] and on the effect of long term nutrient and climate variability [Milan et al., 2017].

The meteorological processes of the Garda region have often been the focus of studies, with special interest on the development of peculiar wind circulations. This phenomenom is caused by the thermal contrast between the lake and the surrounding orography. [Laiti et al., 2013b, 2014; Giovannini et al., 2015b]. Moreover, a wind atlas for Trentino, including the area of Lake Garda, was recently produced, based on 10-year long meteorological simulations (2004-2013) with the Weather Research and Forecasting (WRF) model [Skamarock et al., 2008a] by Giovannini et al. [2014a].

An attempt to improve the hydrodynamic description of Lake Garda was proposed by Casulli and Pecenik [1994], who simulated water circulation with a three-dimensional model under constant and uniform wind forcing. Their model, which was numerically stable and had a sufficiently refined grid resolution both along the horizontal and vertical dimension, was the first

model specifically designed for Lake Garda and was intended to be integrated with biological and ecological modules. However, such implementation was never made, and only few practical hydrodynamic applications followed. Mari et al. [2009] employed the simulated hydrodynamic fields to evaluate larval transport of an idealized aquatic sedentary population. Lovato and Pecenik [2012] applied the model to investigate the short-term dispersion of a degradable organic pollutant under uniformly distributed and alternating wind forcing. The link with ecology was attempted by the same authors to study mixed layer and phytoplankton dynamics through a combined 1-D turbulence-eutrophication model Pecenik and Lovato [2011].

Recently, a renewed interest toward hydrodynamic investigations was found in Lenstra et al. [2014], who provided high-resolution profiles of temperature and fluorescence in the southern part of the lake. The study aimed at gaining a first insight into the turbulence-related quantities (i.e., eddy diffusivity, dissipation of turbulent kinetic energy and of thermal variance) of Lake Garda in early spring. In the same year, the dutch company Deltares run pilot tests of the Delft3D model on the lake [Donners et al., 2014], although these tests were not followed by a deeper analysis from the same authors.

The modeling part of this research activity stems from the preliminary implementation of the Delft3D model by Deltares. As the latest physical investigations on Lake Garda, we report here our contributions Amadori et al. [2018] and Piccolroaz et al. [2019], whose contents are part of this doctoral thesis.

1.4 Thesis outline

Based on the above introductory remarks, the following list highlights and summarizes the main contributions of this thesis and its outline:

1. *Construction of a comprehensive dataset*

   Lake Garda is ruled by three separate administrations. Each one monitors the lake with its own protocols, in its own points and often without coordination with the others. Moreover, the lake has been, and still is, subject of studies carried out from different research groups, each one acquiring data on its own field of investigation. Hence, the overall dataset was

composed by dis-homogeneous, sparse and fragmentary data. In Chapter 2, all the existing data on Lake Garda physical quantities, and those acquired in 2017-2018 [Toffolon et al., 2017], are described, collected and processed.

2. *Setup of a three-dimensional model*

   The calibration and validation of a hydrodynamic model is a fundamental prerequisite when studying physical processes in any lake. In Chapter 3, setup, calibration and validation of the three-dimensional model for Lake Garda is presented. Moreover, role and limits of the model parameterizations are discussed, together with the issues related to the choice of the appropriate indexes for the assessment of the model performance at each time scale.

3. *Description of typical basin scale circulation*

   We provide a first description of typical seasonal circulation of Lake Garda at a basin scale. In Chapter 4, a preliminary modeling exercise allows to infer the role of wind variability and Earth rotation in the development of lake circulation during the stratified (i.e. summer, early winter) and unstratified (i.e. early spring) thermal conditions. Once the general understanding of the lake basin scale response to external drivers is achieved, we perform a citizen science experiment, where the knowledge held by the lake community on lake surface currents is satisfactorily tested trough our validated numerical.

4. *Understanding of deep mixing dynamics*

   The comprehension of the thermal patterns in Lake Garda and the physical processes affecting its mixing regime is one of the main aims of this research activity. Based on our previous findings on the lake circulation under long lasting storms winds, Chapter 5 combines the most recent field campaign, conducted in 2017, and *ad hoc* numerical simulations. This allows to investigate the contribution of wind-driven deep mixing and inertia-driven secondary flows to the occurrence of deep mixing events in the northern basin of Lake Garda.

5. *Ekman transport in narrow elongated lakes*

   The secondary flows driven by Earth rotation, of the kind discussed above, have never been previously observed in lakes of the shape and size of Lake Garda. In Chapter 6 we provide

a brief review of the-state-of-the-art on the effect of Earth rotation on wind-driven steady circulation in lakes. We also discuss the dynamics of horizontal and vertical transport by means of a simple analytical solution, which is an extension of the well-known Ekman solution to the case of an elongated lake. The analytical solution we derive is compared with numercal results from idealized domains and is then applied to our case study.

As stated in the very beginning of this doctoral research, the case study plays a central role on the investigation we carried on. Lake Garda has been investigated for decades by an heterogeneous scientific community, therefore we could benefit from several interdisciplinary approaches and different, inspiring, viewpoints. Lake Garda is also a strategic resource for multiple stakeholders. In this regard, we tried not to lock our results into an ivory tower, but to actively involve citizens, lake users and political representatives, at several stages of our research activity. Although there will not be a specific chapter on this, such a collaborative and engaging spirit marked all the work contained in this manuscript. We hope that the last contribution of this doctoral thesis is to have raised awareness on the urgent research questions that still need to be addressed on Lake Garda physical dynamics.

Chapter 2

Lake Garda dataset

Contents

The contents of this chapter have been partially derived from:

Amadori, M., Morini, G., Piccolroaz, S., and Toffolon, M. Involving citizens in hydrodynamic research: A combined local knowledge - numerical experiment on Lake Garda, Italy. *Science of The Total Environment*, 722:137720, 2020b. doi: 10.1016/j.scitotenv.2020.137720

Amadori, M., Giovannini, L., Toffolon, M., Piccolroaz, S., Zardi, D., Bresciani, M., Giardino, C., Luciani, G., Kliphuis, M., van Haren, H., and Dijkstra, H. A. Multi-scale validation of a 3D atmosphere-lake model based on standard monitoring data. *Under review for Environmental Modeling & Software*, 2020a

2.1 Lake Garda case study

Lake Garda is one of the most important subalpine lakes in Europe and the largest in Italy by surface area and volume. It is located in the northern part of Italy (Fig. 2.1) at 45°40′ N mean latitude and 10°40′ E mean longitude, and the average free surface level is at 65 m above sea level.

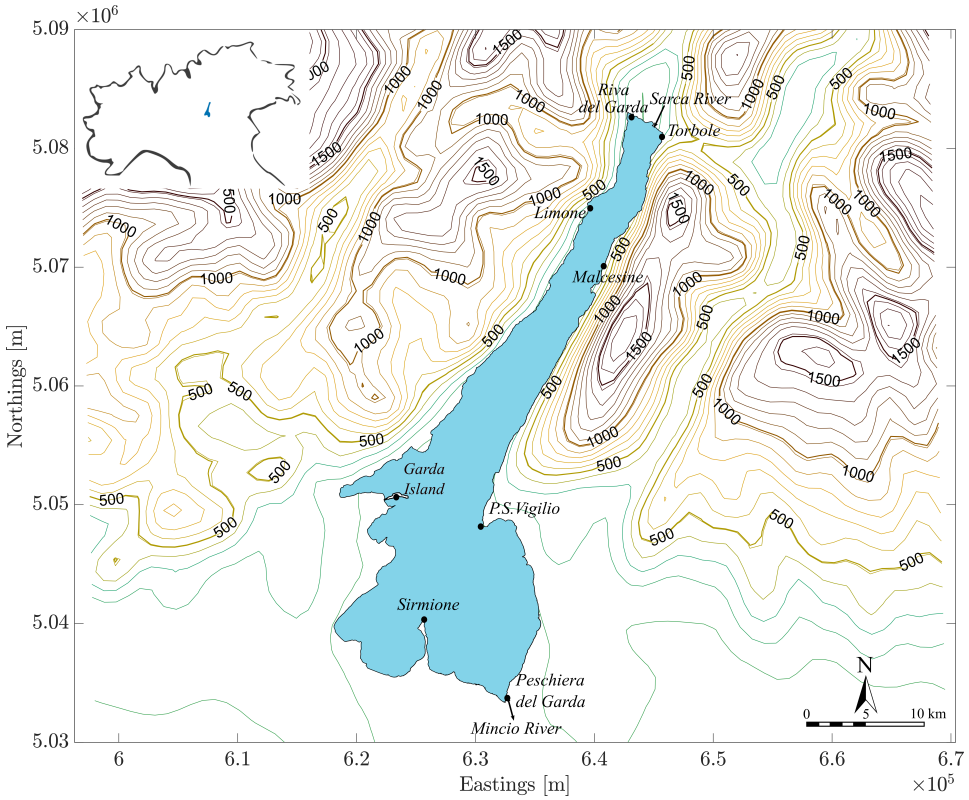

Figure 2.1: Location of Lake Garda in northern Italy, orography of the surrounding area, inflow, outflow and relevant locations.

The basin surface area is 367 km^2, with a maximum length of 52 km from the north-west (Riva del Garda) to the south-east (Peschiera del Garda), and a maximum width of 18 km in the southern part of the lake, for a total perimeter of 162 km. Due to substantial morphological differences, the lake is traditionally divided into two sub-basins. The northern basin is called 'high lake' by locals, is elongated, narrow (about 3 km wide), and deep (maximum depth $\sim$ 350 m). In this basin, steep shores plunge almost vertically into the lake as a canyon between the complex mountain range of Garda Prealps (which reaches up to 2000 m a.s.l.). The southern basin is round-shaped, wide (mean width of 15 km) and shallow (maximum depth 80 m), is

surrounded by low moraine hills and plain areas, and is called 'low lake'. A submerged ridge runs eastward from the peninsula of Sirmione to Punta San Vigilio and divides the lake into the two sub-basins. At the beginning of this doctoral research, the only available bathymetric survey was the one performed in 1966 by the Italian Military Geographic Institute (IGM). Such bathymetry was composed by single points and isobaths at irregular spatial resolution ($\sim$ 100-500 m). For its utilization it was digitalized by hand and successively rasterized with a nominal resolution of 100 m. In Fig. 2.2 the original bathymetry (a) and its digitalized version (b) is displayed.

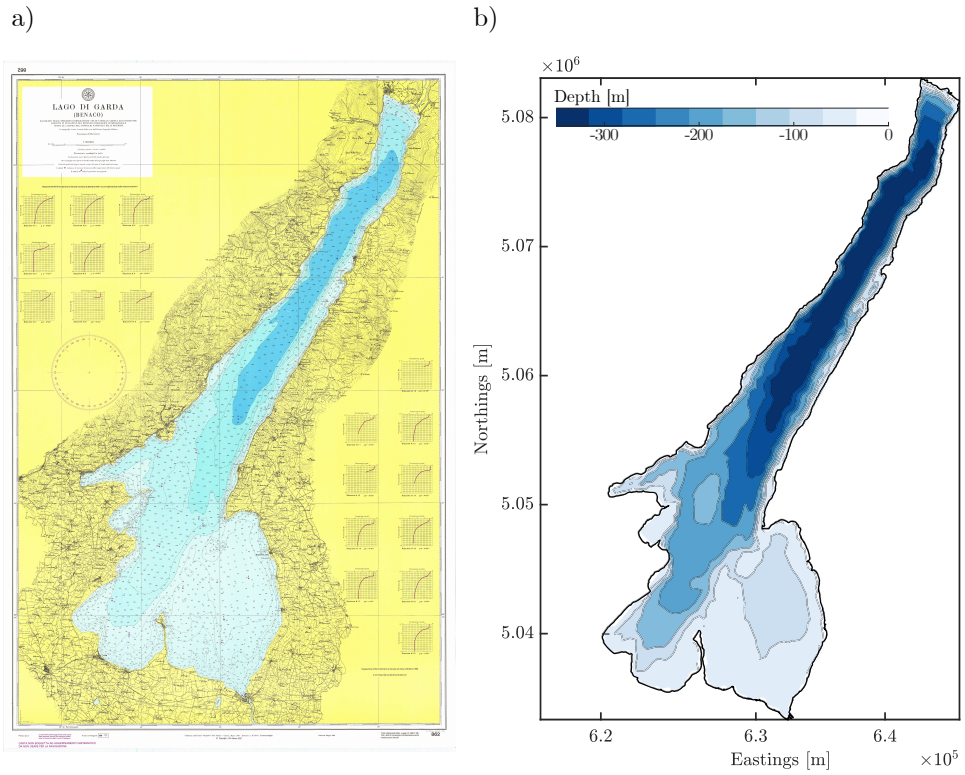

Figure 2.2: Bathymetry of Lake Garda from the latest IGM relief in 1966. a) original hard copy; b) digitalized version.

In the end of 2019, a new high resolution (5 m) bathymetry was made available for the northern part of the lake by the Italian Navy Hydrographic Institute (IIM) thanks to a new relief started with a dual-head multibeam echosounder [1].

Lake Garda has only one main inflow, the Sarca river to the north, and one outflow, the

[1]The relief started in 2017 within the framework of the project ACCURATE, *Accurate Climate Change Unified Risk Assessment* for Territory and Environment in sub-alpine lakes, in collaboration with Università Cattolica in Brescia, and will end in 2020 with the final survey of the southern part of the lake. The preliminary data were shared by virtue of the active cooperation declared in the Carta di Verona.

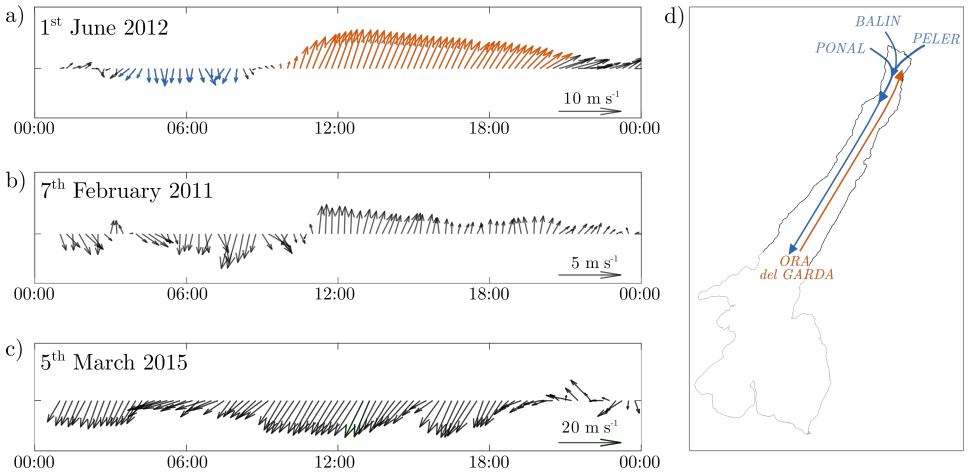

Figure 2.3: Typical breezes in the northern part of Lake Garda in a) summertime (06/01/2012); b) wintertime (02/07/2011); c) during a Föhn episode in early spring (04/05/2015); d) spatial development of main northerly (blue arrows) and southerly (orange arrows) thermal breezes.

Mincio river from the south. During extreme flood events, an artificial tunnel named 'Adige-Garda gallery' occasionally discharges part of the Adige river waters to lake Garda to prevent the flooding of the downstream city of Verona. Its outlet is located near Torbole, very close to the mouth of the Sarca river. Many small islands rise in Lake Garda: the two largest are the Trimelone island, in the high lake, and the Garda island, in the low lake.

The typical winds in Lake Garda are mainly thermal breezes driven by the topography of the surrounding region [Giovannini et al., 2017]. The regular alternation of persistent breezes characterizes the high lake: in fact, the Prealps shield easterly and westerly winds, so that winds are channeled by the steep lateral mountains and blow along the lake longitudinal axis.

During the warm season (Fig. 2.3a) and in general on sunny days (Fig. 2.3b), daily-periodic thermally-driven atmospheric circulations develop over the northern basin of Lake Garda: northerly breezes blow from north-east and north-west at night and until late morning, when they are replaced by southerly lake breezes blowing until sunset [Defant, 1909; Laiti et al., 2013a,b, 2014; Giovannini et al., 2015a]. Northerly breezes rise when the temperature over the lake is higher than the temperature in the northern valleys (i.e., in the morning and during the night, e.g. 'Peler', 'Balin' and 'Ponal' breezes), while southerly winds blow when the opposite condition occurs (i.e., late in the morning and in the afternoon, 'Ora del Garda' breeze). All these breezes reach the center of the northern trunk and blow intensely in alignment with the

main axis of the lake (Fig. 2.3d). During winter, winds are usually weaker than in the warm season (Fig. 2.3b), with the exception of some cases of strong synoptic northerly winds, mainly related to Föhn episodes (Fig. 2.3c) from the north, with duration of a few days and almost uniform spatial distribution on the lake surface. In the low lake, where winds blow freely in any direction, several local breezes develop, with lower intensity and duration, each one with a proper name given by the locals.

The mixing regime of Lake Garda is classified as oligomictic with prolonged periods of incomplete mixing interspersed with occasional complete overturns that involve the entire water column Ambrosetti and Barbanti [1999]; Salmaso [2005]. This can be verified in Fig. 2.4, where surface, interior and bottom water temperature from 90s until 2018 at the surface are plotted from measurements in one deep point (APPA point, see next section for the description of data and Fig. 2.5 for the location of the point).

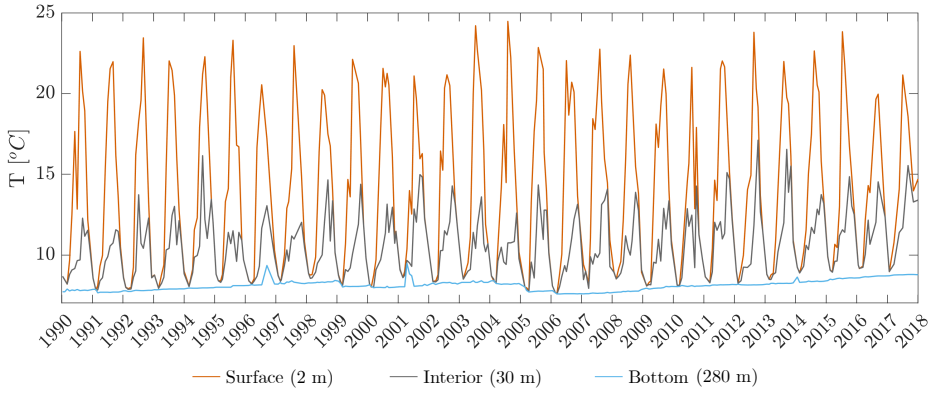

Figure 2.4: Trends of temperature at surface (2 m), interior (30 m) and bottom (280 m) from observations APPA point.

Throughout the year, temperature is always and everywhere above that of maximum density, hence thermobaric effects [McDougall, 1987] do not affect the mixing regime of the lake. Moreover, salinity is low and its vertical gradients are small, thus playing secondary effects on the stability of the water column. Complete (i.e., down to the bottom) buoyancy-driven convective deep mixing events were typically observed following particularly harsh winters causing surface cooling [Salmaso, 2005]. The occurrence of complete overturns can be clearly observed in Fig. 2.4 where the three curves of surface, interior and deep temperature intersect in 1991, 1999, 2000, 2005 and 2006. Since then, water temperature underwent a progressive increase along the whole water column. From 2007 to present, the lake experienced the longest period of meromixis ever

recorded since 1990 according to Salmaso et al. [2017], who ascribed such a shift in the mixing dynamics to climate change.

2.2 Existing data collection

In the last three decades the lake has been monitored by several institutions. The data described here will be used in all following chapters, especially in Chapter 3 for the full 3D atmosphere-lake model validation.

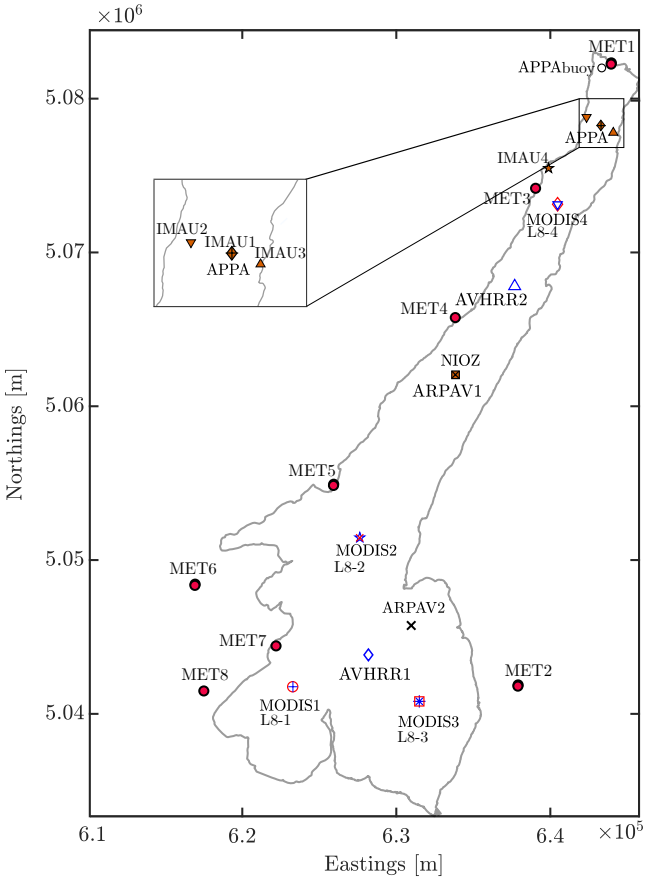

Figure 2.5: Map of Lake Garda monitoring stations with a zoom on IMAU stations along a cross section having APPA point as mid-point. Note: APPA-IMAU1 and MODIS-L8 points overlap.

Fig. 2.5 shows the location of *in-situ* observations and weather stations. In this work, a dataset of water temperature data was built by merging: i) historical long-term *in situ* data of the water column at different locations, ii) multi-site high-resolution profiles measured between 2017 and 2018 during a dedicated monitoring program, and iii) remote sensing maps acquired

Table 2.1: Summary of all *in-situ* and and remotely sensed data used in this study.

In situ water temperature data

Time availability	Institution	ID	East	North	Frequency	Type of data	Depth	n
1990-2018	EPA Province of Trento	APPA	643286	5078237	monthly	profiles	0- 70 m	151
2008-2018		APPA buoy	643308	5082367	hourly	time series	10 m	78848
2000-2018	EPA Veneto Region	ARPAV1	634031	5062154	monthly	profiles	0-330 m	137
2000-2018		ARPAV2	630893	5045631		profiles	0 - 70 m	148
2017-2018	IMAU-UniTrento	IMAU1	643430	5078401	monthly	profiles	2- 100 m	20
		IMAU2	642544	5078596				18
		IMAU3	644214	5077921				18
		IMAU4	640555	5075483				14
2017-2018	NIOZ	NIOZ	635637	5063948	5 seconds	profiles	187 - 337 m	5906

Satellite products

Time availability	Satellite	Sensor	ID	East	North	Frequency	Sp. resolution	Acquisition time	n
1989-2013	NOAA	AVHRR	AVHRR1	628235	5044098	daily	1 km	see Riffler et al.	5117
			AVHRR1	637973	5067770				5117
2004-2010	Aqua	MODIS	MODIS1	623394	5042025	daily	1 km	12:45 UTC	1302
			MODIS2	626743	5051353				1300
			MODIS3	631143	5040947				1302
			MODIS4	640711	5072895				1079
2013-2018	Landsat-8	TIRS	L8-1	623394	5042025	bi-weekly	100 m	09:50 UTC	25
			L8-2	626743	5051353				29
			L8-3	631143	5040947				57
			L8-4	640711	5072895				53
			L8 full maps	1440 pixels					18

Meteorological data

Time availability	Institution	ID	East	North	Frequency	Altitude	Wind meas.	n
2004-2018	Edmund Mach Foundation	MET1	643975	5082174	hourly	63 m asl*	5 m agl**	354415
2004-2018	EPA Veneto Region	MET2	637944	5041943	hourly	142 m asl	10 m agl	376358
2012-2018	EPA Lombardia Region	MET3	639088	5074143	hourly	74 m asl	16 m agl	162889
2013-2018		MET4	633895	5065781		420 m asl	10 m agl	127213
2012-2018		MET5	626016	5054923		67 m asl	21 m agl	161487
2013-2018		MET6	617051	5048460		284 m asl	10 m agl	129299
2017-2018		MET7	622300	5044545		66 m asl	6 m agl	18510
2016-2018		MET8	617629	5041631		182 m asl	10 m agl	46563

*m above sea level

**m above ground level

by different satellites. The dataset covers the period from 1990 to present and amalgamates data acquired with different techniques, within different projects, and by different institutions. At the same time, meteorological data from several weather stations were used to validate the atmospheric model. In Table 2.1 all the data used in this study are summarized, while the locations of the observation points are displayed in Figure 2.5. In particular, Table 2.1 provides details on the monitoring activities on the lake, including the time availability of the data, the data provider, the geographic location of the stations, the sampling frequency, relevant metadata, and the number of available measurements. In the following paragraphs, each dataset is described in detail.

The detailed description of each dataset is provided in the following subsections.

2.2.1 Meteorological data

Several weather stations are located all around Lake Garda, providing regular measurements of the main atmospheric variables. Ground weather stations are operated by various agencies, as shown in Table 2.1. In particular, the northernmost station (MET1) is operated by the Edmund Mach Foundation (FEM), the station on the east coast (MET2) belongs to the Enviromental Protection Agency of the Veneto Region (ARPAV), while the other ones (MET3 to MET8) to the Enviromental Protection Agency of the Lombardia Region (ARPAL). The meteorological variables used in this study are air temperature, relative humidity, air pressure, shortwave solar radiation and wind speed and direction. The incoming longwave solar radiation is not available as a measured quantity at any weather station. For a more detailed description of all the terms contributing to the heat budget of the lake, and depending on the meteorological data, we refer to Chapter 3. In fact, these terms were computed in the modeling phase of this study. The wind speed and direction at these weather stations are measured at different heights above ground, as specified in Table 2.1. Air temperature and relative humidity are measured at 2 m above ground in all weather stations.

2.2.2 EPAs routine in-situ measurements

The current database of *in situ* observations provided by the Environmental Protection Agencies (EPAs) of the Autonomous Province of Trento (APPA) and of the Veneto Region (ARPAV) represents the most complete time series of water temperature available for Lake Garda. Vertical profiles of the temperature are collected on a monthly/bi-monthly basis. Temperature profiles are measured through a shipborne Conductivity Temperature Depth (CTD) profiler. The APPA data are available from 1990 up to the present. Measurements are taken in the 'APPA' monitoring point, located about 4 km from the northern edge of the lake (Figure 2.5). In addition, APPA is in charge of continuous (hourly record) temperature measurements at 10 m below water surface through a buoy located close to the north-western edge of the lake. These data were also used in the present study and are hereafter referred to as 'APPA buoy'. ARPAV profiles are taken in several locations, but the longest series (2000 to present) are available at two points, namely Brenzone (the deepest point of the lake), indicated in the map as 'ARPAV1',

and Bardolino, in the shallow and wide sub-basin, indicated as 'ARPAV2'.

2.2.3 Remote sensing imagery

Lake surface water temperature (LSWT) data were collected from different satellite sensors. The longest time series was taken from the dataset produced by Riffler et al. for European Alpine lakes (1989–2013). This dataset is based on the images from AVHRR (Advanced Very High Resolution Radiometer) onboard various NOAA satellite platforms. Within this database[1], LSWT is available on a daily basis as an average over a 3x3 pixel array (pixel resolution: 1 km) at two specific locations in the lake (we refer to Table 2.1 for the exact coordinates).

In addition, six-year long multi-temporal records from MODIS products (MYD11A, derived from MODIS sensors onboard Aqua) were used in four stations in Lake Garda. The MODIS sensor from the Aqua satellite acquires surface temperature at 9:45 UTC. Both AVHRR and MODIS sensors have a nominal resolution of 1 km. We combined the daily information from those sensors with the spatially more resolved Landsat-8 satellite imagery. Landsat-8 images provide fine scale mapping of lake surface temperature at 100-m spatial resolution (TIRS sensor onboard), with a biweekly revisit time.

Landsat-8 products from 2013 to 2018 were obtained by transforming TIRS radiances at satellite level in water temperature at-the-surface level (i.e., skin temperature). For a similar use of these maps we refer to Barsi et al. [2005] and to Prats et al. [2018], who used Landsat to estimate lake skin surface temperature for more than 400 French water bodies. The full Landsat-8 maps were used for model validation when all pixels covering the lake surface were available (18 dates in 5 years). In addition, LSWT values in correspondence of the same 1 km^2 target areas of the MODIS Aqua products were extracted from the Landsat-8 maps, allowing for comparing model output and data from different sensors locally.

[1]Data can be downloaded from https://doi.pangaea.de/10.1594/PANGAEA.830988 and https://doi.pangaea.de/10.1594/PANGAEA.830987 for upper/lower Lake Garda respectively

2.3 Field campaigns and data acquisition in 2017-2018

Prior to 2017, the only experience on hydrodynamics measurements (e.g., velocity field, turbulent quantities) in Lake Garda dates to the experiment of Lenstra et al. [2014]. During 2017-2018 new data on turbulence related quantities and velocity where achieved thanks to the collaboration between University of Trento, University of Utrecht and NIOZ.

2.3.1 IMAU - UNITN field campaign

High-resolution profiles of temperature were collected from 2017 to 2018 during a joint field campaign of the Institute for Marine and Atmospheric Research Utrecht (IMAU, Utrecht University) and of the University of Trento [Toffolon et al., 2017; Piccolroaz et al., 2019]. Data were acquired using a turbulence microprofiler (MicroCTD, distributed by Rockland Scientific International, Canada) operated at depths down to 100 m at four stations (see Figure 2.5). IMAU1 point coincides with the APPA monitoring station. IMAU2 and IMAU3 are located on opposite sides with respect to IMAU1, respectively close to the western and eastern shores. Together, these three stations define a cross-section perpendicular to the lake main axis, which is oriented in a northeast-southwest direction. The fourth station, IMAU4, is located further south, near Limone.

A total of 652 profiles were taken in the period from 8 March 2017 to 11 June 2018. Sampling was always conducted between mid morning and early afternoon, at least on a monthly basis. The upper $\sim$ 2 m of each profile were removed in the post-processing step due to non-homogeneous profiling speed of the instrument.

2.3.2 NIOZ deep mooring

Concurrent with the IMAU-UniTrento field campaign, temperature data were measured by a taut-wire submerged mooring station comprising a single point current meter and a thermistor chain. The mooring was deployed by NIOZ (Royal Netherlands Institute for Sea Research) a few km north of the ARPAV1 monitoring point (see Figure 2.5). The local depth at the point where the instrument was installed is 344 m, with a bottom slope of about 3.6^o (1 km scale).

Temperature data were measured between 187 and 337 m below the water surface by 100 self-contained high-resolution temperature sensors ('NIOZ4') deployed at 1.5 m vertical intervals, at a sampling rate of 0.5 Hz. Data were corrected for the electronic drift, and are available with a precision as small as 0.5 mK and a noise level of less than 0.1 mK [Van Haren, 2018].

The mooring was operational from 24 May 2017 (10 UTC) and was recovered on 31 May 2018 (09 UTC). In this study, temperature data until 26 March 2018 (23 UTC) were used, since after that day 50% of the temperature sensors failed due to insufficient batteries and interpolation was not performed. Here we used a reduced set of hourly sampled data.

Chapter 3

Three-dimensional model setup and validation

Contents

This chapter is based on:

Amadori, M., Giovannini, L., Toffolon, M., Piccolroaz, S., Zardi, D., Bresciani, M., Giardino, C., Luciani, G., Kliphuis, M., van Haren, H., and Dijkstra, H. A. Multi-scale validation of a 3D atmosphere-lake model based on standard monitoring data. *Under review for Environmental Modeling & Software*, 2020a

3.1 Introduction

When modeling thermo-hydrodynamics in lakes, two main factors guide the choice of the appropriate numerical model and of the calibration/validation procedure. One is the process to be investigated, and the other is the available data. Once the proper model has been chosen and the data gathered, the model is set up, calibrated and validated. It is usually assumed that, when the model reproduces reasonably the observed data, it can be accepted as reliable and it is used to address specific research questions. However, an exact and complete model verification can never be fully achieved, and such limitation can be significant if the available measurements are restricted to water temperature data, ignoring the velocity field. In principle, a given vertical profile of temperature can be compatible with different velocity fields, and indeed one-dimensional (1D) models have been successfully used. If a three-dimensional (3D) model is used, water temperature observations should be supplemented with velocity measurements at several locations and with sufficient temporal resolution. This is to guarantee that both temperature and flow fields are consistently reproduced, i.e., transport dynamics are properly solved. In most practical cases, however, advanced monitoring systems providing such a comprehensive dataset for a full model validation are simply not available. Thus, the only viable option is to use the largest number of (incomplete) data from standard monitoring schemes (often not specifically designed for modeling applications), and to carefully define the modeling goals, so that the information provided by observations is sufficient to justify that the model is ''fit for purpose' for the specific scientific question.

The typical modeling approach is to address research questions related to phenomena at a specific time scale. In this regard, lake modeling applications can be divided into three categories: (i) long-term simulations and climate change projections; (ii) seasonal to daily lake-wide circulation and transport; (iii) short-term, non-stationary processes, such as internal waves involving multiple scales from hours to several days.

In case (i), large-scale temperature variations and long-term trends of water temperature (warming trends, most frequently) are investigated. Due to the relevant computational costs of such long-term simulations, this research topic is commonly addressed by using 1D models

forced by climate change scenarios [e.g. Fang and Stefan, 2009; Perroud and Goyette, 2010; Kirillin, 2010; Piccolroaz and Toffolon, 2013a, 2018; Butcher et al., 2015; Valerio et al., 2015a; Schwefel et al., 2016; Schlabing et al., 2014, among others]. Instead, 3D model simulations in this field are still rare [Beletsky et al., 2006; Yamashiki et al., 2010; Wahl and Peeters, 2014; Xue et al., 2017], and are normally validated on a monthly basis. When moving down from interannual to seasonal, or even daily time scales (as in case (ii) above), the range of the relevant physical processes widens. This is the scale of, e.g., wind-driven circulation and up/downwelling, surface gyres and riverine intrusions, which in turn interact with the spatial heterogeneity of the atmospheric forcing and topography. In this context, the literature offers several examples of three-dimensional short-term modeling studies on lake circulation and heat transport [e.g. Razmi et al., 2013; Bouffard et al., 2018; Piccolroaz et al., 2019]. In such heterogeneity of potential investigations, also the methodologies for model validation are diverse. In general, multi-site validation is generally performed, but the time resolution ranges from monthly to hourly, or even sub-hourly, time series [Pilotti et al., 2013a; Råman Vinnå et al., 2017]. When approaching the daily and shorter time scales (case (iii) above), the internal waves dynamics are investigated, as they affect the basin-scale circulation and produce sub-daily temperature fluctuations. For such investigations, high-resolution observations are crucial. Most of the studies [e.g. Hodges et al., 2000; Pan et al., 2002; Rueda and Schladow, 2003; Laval et al., 2003; Pilotti et al., 2013a; Soulignac et al., 2017; Valerio et al., 2017; Dissanayake et al., 2019] validated the models with hourly or sub-hourly temperature data sampled by moored thermistors. Frequently, the model performance in these applications is evaluated with sophisticated tools such as signal decomposition through basis functions analyses (e.g., Fourier series and wavelet functions).

Most of the studies mentioned above aimed at investigating targeted processes, for which the model was calibrated and validated. Few of them benefited from comprehensive datasets, including water velocity measurements, but most of them relied on water temperature data only. In this contribution, we face the challenge of validating a 3D lake model at all the time scales discussed above, by relying only on water temperature observations. The motivating idea is that coherent lake dynamics can be satisfactorily reproduced by distilling information from water temperature data at different spatial and temporal scales.

The choice of a multi-scale evaluation also allows to fully understand the model's capabilities

and make the best use of it. In this regard, a deep understanding of the weaknesses and the strengths of a lake model also requires an analysis of the atmospheric conditions used to force it. In fact, weather forcing plays a leading role in the development of water temperature dynamics, as it directly regulates air-lake heat fluxes, and indirectly controls lake mixing and circulation. Either being applied as uniform or spatially resolved (e.g. by interpolating observations or modeling/forecasting), these quantities severely affect lake dynamics [e.g. Strub and Powell, 1986; Lemmin and D'Adamo, 1997; Laval et al., 2005; Amadori et al., 2018; Piccolroaz et al., 2019], such that two-way atmosphere-lake coupling procedures have been tested [e.g. Song et al., 2004; Leon et al., 2007; Xue et al., 2017].

Here, we critically discuss the steps of setup, calibration and validation of a one-way coupled atmospheric (WRF) and hydrodynamic (Delft3D-Flow) model for Lake Garda. The aim of our investigation is twofold: on the one hand, we aim at demonstrating that a full validation of a 3D model can be performed on water temperature at multiple spatial and temporal scales. On the other hand, we show how the performance of the externally modeled atmospheric forcing affects the results of the hydrodynamic model, again at multiple scales.

3.2 Methods

For the construction of the three-dimensional model, all the data collected and presented in Chapter 2 were used. To facilitate reading, the localization of the observation points is reported here (Fig. 3.1) together with the bathymetric map of Lake Garda. For the detailed description of the data, we will refer to the table 2.1 throughout the text.

3.2.1 Model setup

3.2.1.1 Atmospheric Model

The atmospheric simulations used in this work were run with the WRF model [Skamarock et al., 2008b], which was successfully used in previous studies to reproduce thermally-driven winds in the Alpine valleys surrounding Lake Garda [Giovannini et al., 2014c]. Part of the simulations (period 2004-2013) are derived from the Trentino Wind Atlas [Giovannini et al., 2014a].

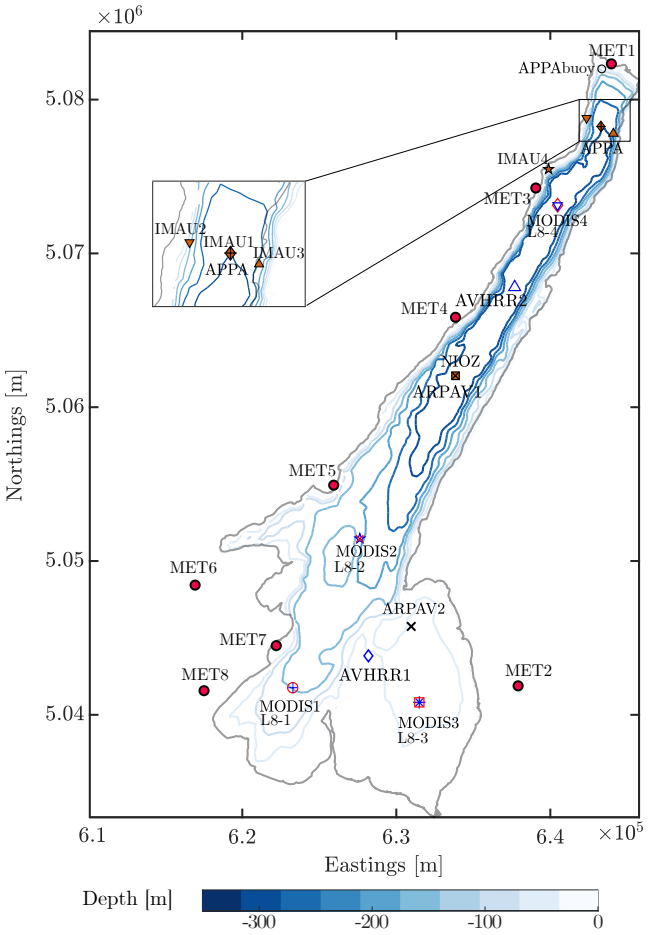

Figure 3.1: Map of Lake Garda monitoring stations, bathymetry, and zoom on IMAU stations along a cross-section having the APPA point as mid-point. Note: APPA-IMAU1 and ARPAV1-NIOZ points overlap.

The remaining part (period 2014-2018) was performed *ad hoc*, adopting the same modeling setup as for the above Atlas. The computational domain is composed of four nested domains with increasing horizontal resolution of 54, 18, 6 and 2 km respectively, each having 28 vertical levels. In the present work, we validated the model only on the inner domain, covering the area of interest. Initial and boundary conditions were supplied by the 6-hourly National Center for Environmental Prediction (NCEP) Final Operational Global Analysis data on 1-degree grids. The simulations were initialized at 00:00 UTC of the last day of each month and finish at the end of the following month; the first day, which is mostly affected by the initialization, was not considered for the validation analysis. The model output was written every hour.

As for the physical settings, the Noah scheme [Chen and Dudhia, 2001] was used as land surface model, while the Yonsei State University scheme [Hong et al., 2006] was adopted as

Model settings			
Simulation time step	30 s	Wall boundary conditions	*free slip*
Grid size	64 x 224 x 100	Heat fluxes model	*Ocean*
Horizontal grid resolution	$100 - 400$ m	Turbulence model	$k - \varepsilon$
Vertical grid resolution	$1 - 25$ m	Secchi depth	*monthly measured values*
Wind drag coefficient Cd [1]	4.40×10^{-3}	Bottom roughness (Chézy)	60 $m^{1/2}$ s^{-1}
	1.00×10^{-3}		
	2.00×10^{-3}		
Calibration parameters	Value	Range of variation	
Stanton number	6.50×10^{-4}	$1.77 \times 10^{-4} - 2.00 \times 10^{-3}$	
Dalton number	1.30×10^{-3}	$3.95 \times 10^{-4} - 2.30 \times 10^{-3}$	
Free convection coefficient	1.00×10^{-1}	$5.00 \times 10^{-2} - 5.00 \times 10^{-1}$	
Horizontal eddy viscosity [m^2/s]	2.00×10^{-2}	1.00×10^{-3}–2.00	
Horizontal eddy diffusivity [m^2/s]	2.00×10^{-2}	1.00×10^{-3}–2.00	
Background vertical eddy viscosity [m^2/s]	1.00×10^{-6}	$1.00 \times 10^{-6} - 1.00 \times 10^{-3}$	
Background vertical eddy diffusivity [m^2/s]	1.00×10^{-6}	$1.00 \times 10^{-6} - 1.00 \times 10^{-3}$	

[1] Breakpoints for the piecewise linear function of wind speed (1 - 5 - 10 m/s) at 10 m above lake surface

Table 3.1: Delft3D model setup and calibration parameters.

planetary boundary layer parameterization. The long-wave radiation was parameterized with the Rapid Radiative Transfer Model [Mlawer et al., 1997], while the Dudhia scheme [Dudhia, 1989] was used for the short-wave radiation, including the effects associated with slope inclination and topographic shading. The microphysics scheme adopted is the WRF single-moment 3-class simple ice scheme [Hong et al., 2004]; the Kain-Fritsch cumulus scheme [Kain and Fritsch, 1993] was used in the three outer domains, while no cumulus parameterization was adopted in the inner domain. In the two inner domains we adopted the correction for wind speed over complex terrain proposed by Jiménez and Dudhia [2012], which considers the effects of unresolved topographic features. The original resolution of the Digital Elevation Model adopted in the inner domain is 30" ($\sim$ 0.9 km).

3.2.1.2 Hydrodynamic Model

Lake thermo-hydrodynamics are simulated using the open-source modeling suite Delft3D [Lesser et al., 2004] from 2004 to 2018. Tab. 3.1 summarizes the main model settings.

The domain is discretized by a non-uniform, locally-orthogonal curvilinear grid staggered in space with 64×224 cells× 100 vertical layers. The horizontal resolution is of $\sim$200 m, while the thickness of the vertical layers increase from 1 m at the surface to 25 m at the bottom. The simulation time step is set to 30 s to meet the requirements of the model stability. Initial conditions for Delft3D are set as water at rest, horizontal water level, and horizontally uniform

vertical temperature profile according to the profile measured by ARPAV in the ARPAV1 point in December 2003. Monthly Secchi depth is given as a monthly mean value according to the measurement in ARPAV1 point. Free slip conditions are imposed at the lateral boundaries of the domain. Vertical eddy diffusivity and viscosity are computed by Delft3D through a k-ε turbulence model, while the values of the horizontal viscosity and diffusivity are fixed and used as calibration parameters together with the background vertical values. Wind drag coefficients are defined as a piecewise linear function of wind velocity (at 10 m above ground level). The breakpoints values are chosen coherently with Wüest and Lorke [2003] after testing also other relations (e.g. Wahl and Peeters, 2014) in the calibration phase. The *'Ocean'* heat fluxes model is used, in the version originally formulated for the North Sea based on Gill [1982] and then extended to large lakes. The boundary conditions (i.e. atmospheric forcing) are provided by the WRF model for the whole simulation time. The weather variables required by the model are air temperature, relative humidity, incoming shortwave solar radiation and cloudiness, wind velocity and air pressure. These variables are provided as space and time varying on the lake surface. The model parametrizes the total heat flux through the free surface by computing each term of the heat balance equation, excluding the net incident solar radiation (short wave, Q_{sn}), which is provided by the atmospheric model directly in order to take into account of the shadowing effect of the mountains. The heat budget terms computed by the model from the meteorological variables are the net incident atmospheric radiation (long wave, Q_{an}), the long wave back radiation (Q_{br}), the evaporative heat flux (Q_{ev}) and the convective heat flux (Q_{co}). In the latter two terms, the effect of wind in forcing heat fluxes of latent or sensible heat (respectively) is also taken into account.

Simulation outputs are saved every day at 10:00 UTC in the whole computational domain. At some observation points, corresponding to the monitoring locations, numerical outputs are saved every hour. The choice of the calibration parameters is discussed in the dedicated section 3.2.2.

Mean Absolute Error $MAE = \frac{1}{N}\sum_{i=1}^{N}\lvert M_i - O_i\rvert$	Mean error $ME = \frac{1}{N}\sum_{i=1}^{N}(M_i - O_i)$
Root Mean Square Deviation $RMSD = \sqrt{\frac{1}{N}\sum_{i=1}^{N}(M_i - O_i)^2}$	Normalized centred Root Mean Square Deviation $NRMSD = \frac{\sqrt{\sum_{i=1}^{N}\left[(M_i - \bar{M}) - (O_i - \bar{O})\right]^2}}{\sqrt{\sum_{i=1}^{N}(O_i - \bar{O})^2}}$
Standard Deviation $SD_O = \sqrt{\frac{1}{N}\sum_{i=1}^{N}(O_i - \bar{O})^2}$ $SD_M = \sqrt{\frac{1}{N}\sum_{i=1}^{N}(M_i - \bar{M})^2}$	Normalized Standard Deviation $NSD = \frac{\sqrt{\sum_{i=1}^{N}(M_i - \bar{M})^2}}{\sqrt{\sum_{i=1}^{N}(O_i - \bar{O})^2}}$
Correlation $CORR_{MO} = \frac{\sum_{i=1}^{N}(M_i - \bar{M})(O_i - \bar{O})}{\sqrt{\sum_{i=1}^{N}(M_i - \bar{M})^2}\sqrt{\sum_{i=1}^{N}(O_i - \bar{O})^2}}$	Nash Satcliffe Efficiency (or R^2) $NSE = 1 - \frac{\sum_{i=1}^{N}(M_i - O_i)^2}{\sum_{i=1}^{N}(O_i - \bar{O})^2}$

Table 3.2: Statistical indices for the assessment of the model performance.

3.2.1.3 Assessment of the performance of the models

The performance of both atmospheric and hydrodynamic models was assessed by evaluating the metrics summarized in Table 3.2. We selected those metrics that have been most extensively used in environmental modeling applications [see e.g., Hipsey et al., 2020].

Mean Absolute Error (MAE), Mean Error (ME, i.e., bias), Root Mean Square Deviation ($RMSD$), Standard Deviation (SD) and Correlation ($CORR$) were computed comparing modeled M_i and observed values O_i, where $i = 1, ..., N$ indicates time index and N the total number of observations. In the mentioned table, the bar symbol $\overline{M}(\overline{O})$ refers to the average over time of modeled (observed) quantities. An exception was made when comparing the water temperature from the hydrodynamic model and from Landsat-8 satellite maps: here i denotes a number of pixels, N the total number of pixels (as discussed later), $\overline{M}(\overline{O})$ the spatial mean over the lake surface.

In order to account for the site-specific variability on the evaluation of the performance metrics, the Standard Deviation of the observed data (SD_O) was used as normalization factor

for computing the Normalized Centered Root Mean Square Deviation $NRMSD$ [according to Taylor, 2001], and the Normalized Standard Deviation of model results NSD. In addition, the Nash-Sutcliffe efficiency (NSE) was computed to test the robustness of the hydrodynamic model results only.

For both models, data from stations (point measurements) were compared with model's output (gridded fields). Such a comparison is unavoidably affected by the different meaning of point-wise vs spatially distributed data. In fact, local observations may not be representative for a large surrounding area, and the computational grid of the model output may be too coarse to capture the local conditions observed at the monitoring stations. In this regard, errors may be introduced also by the discretization of the computational domain, either along the horizontal or vertical direction. An example of this effect can be found in both models: in the atmospheric model, when areas with steep slopes are smoothed and underrepresented or when specific microclimatic conditions at the transition between land and water are not appropriately captured; in the hydrodynamic model, when the vertical variation along the water column is not properly reproduced because of too thick layers. To overcome these issues, the metrics listed in Table 3.2 were computed by adopting some specific corrections, which will be presented in the following two subsections.

3.2.1.4 Meteorological Model

The validation of the atmospheric model results focused on wind speed at 10 m above ground level and on air temperature and relative humidity at 2 m above ground level. In fact, these variables mainly affect the results of the hydrodynamic model. For a fair evaluation of the atmospheric model performance, corrections were made on the variables as described below.

1. Air temperature

   In some stations, especially those located on the north-western side of the lake, a significant mismatch exists between the real and the computational orography. In these areas, the elevation of each model grid cell can be significantly higher than the elevation of the corresponding weather station. For this reason, the temperature simulated by the model was corrected considering the altitude difference between the model grid cell and the

actual height of the weather station. We assumed a constant lapse rate and used the mean standard tropospheric value $\Gamma = -dT/dz = 6.5\,\mathrm{K\ km^{-1}}$.

2. Relative humidity.

   In the same stations listed above, relative humidity was corrected according to the corrected air temperature, without changes in the water content simulated by the model.

3. Wind speed.

   For consistency between measurements and model results, wind observations were extrapolated to the standard height of 10 m above ground level by assuming a logarithmic profile with a neutrally stratified atmosphere. We used a roughness length of 0.001 m for MET1 and MET7, as these stations are located on a dock, and of 0.01 m for MET3 and MET5, located over grass [Oke, 1987].

3.2.1.5 Hydrodynamic model

When testing the performance of the hydrodynamic model, the structural inhomogeneity of observation data is an issue to be addressed. Since data were available in several formats (e.g., vertical profiles, pixels of different resolution from remote sensing maps), the variables M and O considered in the performance indices of Table 3.2 had to be computed according to the data format, for the comparison to be consistent. Below, we specify how we handled each source of data, using X to indicate the generic variable, either observed (O) or modeled (M), obtained by spatially averaging the single realization x.

1. Vertical profiles of temperature (APPA, ARPAV, IMAU, NIOZ).

   Observed and modeled values were averaged within layers of pre-defined thickness. The mean $X_{i,j}$ value per each layer j at the i-th time step was computed as follows:

$$X_{i,j} = \frac{1}{K_j} \sum_{n=1}^{K_j} x_{i,n}\,, \tag{3.1}$$

   where $x_{i,n}$, $n = 1, ..., K_j$ are the values within the j-th layer, at time i.

2. Satellite time series at single pixels (AVHRR, MODIS, LANDSAT8).

Observations are referred to a pre-defined area A generally larger than the single computational grid cells. Hence modeled values were computed by evaluating a horizontal average among the computational cells laying within A:

$$X_i = \frac{1}{N} \sum_{n=1}^{N} x_{i,n} \,, \tag{3.2}$$

where $x_{i,n}$, $n = 1, ..., N$ are the values within A and i is the time step.

3. Satellite maps (LANDSAT-8 maps).

   The number of pixels where observations are available depends on the sensor resolution (100 m), the cloudiness conditions and the acquisition time. Satellite and model LSWT were upscaled to a regular grid of 500 m resolution, which is comparable with the largest hydrodynamic grid cell. On these maps, the synthetic indices in Table 3.2 indicate space instead of time: hence the index i identifies a particular pixel, such that $i = 1...N$, with N the total number of up-scaled pixels where LSWT from satellites is available at each acquisition time.

   Although a bias might exist between the temperature retrieved from satellite imagery (skin) and the in-situ water temperature (bulk) [e.g., Prats et al., 2018], in this study the skin-to-bulk correction was not applied. Such bias can reach up to few Celsius degrees, it is larger in daylight hours and is strictly dependent on the meteorological conditions [Wilson et al., 2013]. Therefore, in order to overcome the skin-to-bulk issue, a centred (i.e., unbiased [1]) anomaly $\Delta_c T$ was computed for comparing model results with Landsat LWST full maps. We determined this index in each i-th pixel of the maps as follows:

$$\Delta_c T_i = (M_i - \overline{M}) - (O_i - \overline{O}) \,, \tag{3.3}$$

   where $\overline{M}$ ($\overline{O}$) is the spatial mean of modeled (observed) temperature over the lake surface in one single scene, and M_i (O_i) is the single pixel of the scene. The computation of this index allows to filter out the inherent difference between remotely sensed skin temperature and the modeled lake surface temperature, assuming that this is associated to the respective biases.

[1] We refer to Taylor [2001] for the use of the term 'centered' in the sense of 'unbiased'.

When moving down from monthly to daily and sub-daily scales, the range of variation of temperature greatly reduces. In our dataset, temperature data at a scale shorter than one month are only available from the APPA buoy (see Table 2.1 for the temporal resolution and Figure 3.1 for the location of the point) and from the NIOZ thermistor chain. To analyze the performance of the model in these two points, we used the wavelet time–frequency analysis, which was already applied to process non-stationary temperature signals in other lakes [e.g. Antenucci et al., 2000; Boegman et al., 2005; Guyennon et al., 2014; Woolway et al., 2014]. We performed this analysis on the time series of water temperature and wind. Both signals were decomposed by using the Morlet continuous wavelet [Grossmann and Morlet, 1984], in order to derive the variation in time of the power spectrum of dominant frequencies (WPS, Wavelet Power Spectrum). By integrating in time the WPS, the Global Wavelet Spectrum (GWS) was also computed, which allows for a consistent estimation of the most energetic levels within the power spectrum of the time series.

3.2.2 Model calibration

The hydrodynamic model was calibrated comparing the simulated vertical profiles of temperature in the APPA point with the corresponding measured temperature profiles in the biennium 2004-2005. The calibration period was chosen in order to correctly reproduce one year of meromixis (2004) and one year when a complete overturn occurred (2005).

The Delft3D model allows tuning a limited number of parameters, some related to the heat flux model (Stanton, Dalton and free convection coefficients), some to the turbulence model (background eddy viscosity and diffusivity, both horizontal and vertical) and to the boundary conditions at the surface and at the bottom (wind and bottom drag coefficients). In this work, we calibrated the Stanton, Dalton and free convection coefficients, and the background vertical turbulent terms.

Table 3.1 lists the calibrated parameters, the chosen values and the range of values we tested, while in Table 3.3 the statistics from the calibration run are displayed in terms of the indices presented in Table 3.2. The indices of performance were computed on the temperature profiles in the APPA point considering 4 layers: 0-2 m (surface), 2-20 m (epilimnion), 20-100 m

ID	Depth	MAE [°C]	ME [°C]	RMSD [°C]	NRMSD [-]	NSD [-]	CORR [-]	NSE [-]
APPA	0-2 m	1.08	-0.40	1.49	0.26	1.03	0.97	0.93
	2-20 m	0.98	-0.25	1.32	0.29	1.08	0.96	0.91
	20 -100 m	0.33	-0.02	0.39	0.41	1.21	0.95	0.83
	100 - 270 m	0.21	-0.21	0.23	0.33	0.91	0.95	0.21

Table 3.3: Performance metrics of the hydrodynamic model in the calibration phase (APPA point, 2004-2005 run).

(metalimnion), 100-270 m (hypolimnion). The performance of the model is satisfactory at all depths: the maximum MAE is obtained at the surface and in the epilimnion (1.08 °C and 0.98 °C respectively), corresponding to a RMSD of 1.49 °C and 1.32 °C. This error is below 30% of the standard deviation of temperature in both surface and epilimnion (NRMSD of 0.26 and 0.29). In these layers NSD, CORR and NSE indices are very close to 1, showing that the model is very well correlated with observations, even in case of extreme temperature values. However, smaller MAE (0.33 °C) and RMSD (0.39 °C) in the interior layer are associated with a normalized error of the order of 40%, as the standard deviation of temperature in the metalimnion is smaller than in the surface layer. Nevertheless, the good performance of the model is demonstrated by the other indices, which are still very close to 1. In the bottom layer, the order of magnitude of MAE and RMSD is the same as ME. CORR and NSD are close to 1 (0.95 and 0.91, respectively), but NSE is below the "good" threshold value (0.5 according to Moriasi et al., 2007), suggesting that the error is small but systematic, and larger than the very limited variability of observations. As a general trend, the model bias (ME) is negative in all layers, indicating that the modeled temperatures are on average slightly colder (less than 0.5 °C along the whole water column) than the observed ones.

3.3 Results

In this section, the validation of the models on the whole dataset is presented. We perform a long-term simulation on the period 2004-2018 and compare the numerical results with observations in all the monitoring points described in Fig. 3.1. We recall here that the calibration is performed using only one dataset (APPA) and for the limited period 2004-2006. The overall

performance of the meteorological and atmospheric models is presented at first, as the fundamental step ensuring the consistency of the subsequent analyses. Then, the validation of the hydrodynamic model is provided at all the temporal and spatial scales according to the different datasets.

3.3.1 Overall validation of the two models on the available dataset

3.3.1.1 Meteorological model

Table 3.4 summarizes the performance metrics from the validation of the WRF model in terms of wind speed, air temperature and relative humidity at hourly time resolution.

The model tends to overestimate wind speed at all weather stations except MET2, with ME of the order of $\sim$ 1 m s^{-1}. A similar overestimation of the wind speed, in particular in low wind speed conditions, was also found in other studies using WRF (e.g., Horvath et al., 2012). The modeled air temperature leads to negative ME at most weather stations, with the largest values at MET3 (-1.39 °C) and MET4 (-1.79 °C), while the highest MAE and RMSD are found at MET1 (2.50 °C and 3.42 °C) and MET5 (2.67 °C and 3.22 °C). NSD values are close to 1 at all stations, showing that the model is able to capture the actual temperature variability. Finally, the relative humidity predicted by the model is generally lower than the observed value, with negative ME up to -10.64% (MET8), with the exception of MET2 (0.02%). Air humidity is underestimated at those stations located in mixed water-soil cells, where the model hardly captures the microclimatic conditions. In fact, the stations close to the shores are affected by the higher humidity coming from the lake.

As a general pattern, the largest errors were found at the stations located along the north-western shores of the lake (MET1, MET3, MET4 and MET5), this being related to the poor representation of the steep topography characterizing this area, due to the 2 km resolution of the model grid.

Figure 3.2 shows the ME of WRF for wind speed and temperature at MET1 and MET2, evaluated on a monthly basis. MET1 (Figure 3.2a) shows a clear positive correlation between temperature and wind speed MEs. In fact, overestimation (underestimation) of air temperature

Wind speed					
ID	MAE [ms^{-1}]	ME [ms^{-1}]	RMSD [ms^{-1}]	NRMSD [-]	NSD [-]
MET1	1.78	0.19	2.49	0.14	0.77
MET2	1.49	-0.24	2.05	0.13	0.93
MET3	1.89	1.16	2.5	0.21	1.32
MET4	1.84	1.49	2.46	0.23	1.92
MET5	1.96	1.09	2.91	0.21	1.82
MET6	1.33	0.96	1.84	0.22	1.9
MET7	1.64	0.03	2.21	0.15	1.17
MET8	1.42	1.03	1.97	0.27	1.86
Temperature					
ID	MAE [°C]	ME [°C]	RMSD [°C]	NRMSD [-]	NSD [-]
MET1	2.52	-1.27	3.23	0.08	0.96
MET2	2.19	-1.11	2.95	0.06	1.01
MET3	2.5	-1.39	3.1	0.08	0.95
MET4	2.67	-1.79	3.22	0.07	0.9
MET5	2.33	-0.68	2.91	0.07	0.92
MET6	1.97	-0.81	2.5	0.06	0.98
MET7	2	-0.68	2.5	0.08	1.45
MET8	1.9	0.03	2.41	0.05	0.98
Relative Humidity					
ID	MAE [%]	ME [%]	RMSD [%]	NRMSD [-]	NSD [-]
MET1	15.01	-8.37	19.17	0.19	0.8
MET2	13.05	0.02	17.06	0.19	0.91
MET3	13.3	-7.14	17.02	0.18	0.82
MET4	15.3	-5.88	19.44	0.21	0.71
MET5	13.34	-5.44	17.16	0.19	0.82
MET6	14.82	-8.8	19.36	0.21	0.86
MET7	13.79	-8.84	17.84	0.22	1.18
MET8	15.51	-10.64	20.15	0.23	0.79

Table 3.4: Performance metrics of the WRF model.

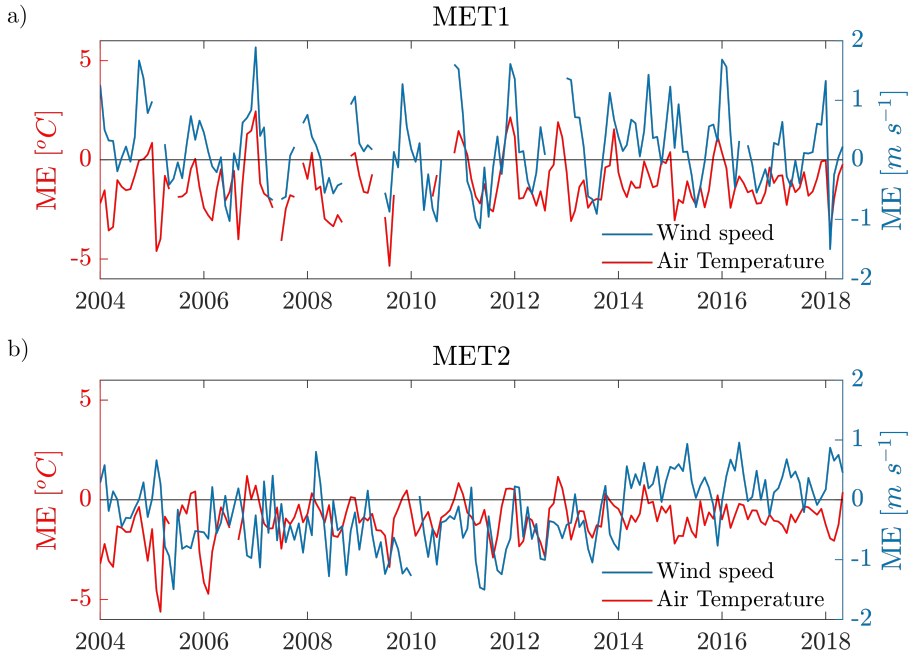

Figure 3.2: Trends of wind speed and air temperature mean error at a) MET1 and b) MET2.

leads to larger (smaller) land-lake thermal contrasts, and, as a consequence, to stronger (weaker) lake breezes, especially during spring and summer. Moreover, errors present a seasonality, with positive MEs in winter and negative in summer. Also at MET2 (Figure 3.2b), air temperature tends to be overestimated during wintertime, but no evident correlation with wind speed errors is found. In fact, MET2 is located some kilometers away from the lake shore and thus it is less affected (than MET1) by lake breezes.

3.3.1.2 Hydrodynamic model

The hydrodynamic model was validated by testing the modeled water temperature against the whole dataset (i.e., at all observation points and for the whole simulated period). The performance metrics are those summarized in Table 3.2. Results are provided in Table 3.5 for each dataset, and are summarized in Figure 3.3.

For data available along the water column (temperature profiles), the modeled and observed values were averaged following Equation (3.1) in four depth intervals (0-2 m, 2-20 m, 20-100 , 100-330 m), where the performance metrics were computed. We included in the surface layer

ID	Depth	MAE [° C]	ME [° C]	RMSD [° C]	NRMSD	NSD	CORR	NSE
APPA	0-2 m	1.44	0.65	2.17	0.42	1.20	0.94	0.81
	2-20 m	1.21	0.48	1.70	0.39	1.18	0.95	0.84
	20 -100 m	0.53	-0.28	0.70	0.54	1.04	0.86	0.65
	100 - 270 m	0.25	-0.21	0.32	0.63	1.27	0.87	0.29
APPA buoy	10 m	1.94	1.47	2.85	0.55	1.25	0.90	0.58
ARPAV1	0-2 m	1.12	-0.22	1.94	0.38	1.13	0.94	0.85
	2-20 m	1.03	0.25	1.49	0.32	1.14	0.96	0.89
	20 -100 m	0.43	-0.26	0.54	0.44	1.00	0.90	0.75
	100 - 330 m	0.22	-0.20	0.30	0.49	1.14	0.90	0.55
ARPAV2	0-2 m	1.04	-0.57	1.73	0.30	1.09	0.96	0.90
	2-20 m	1.04	0.34	1.57	0.31	1.14	0.96	0.90
	20 -70 m	0.52	-0.19	0.74	0.51	1.03	0.87	0.72
IMAU1	2-20 m	0.76	0.52	1.40	0.35	1.30	0.99	0.86
	20 -100 m	0.34	0.05	0.45	0.35	1.16	0.96	0.88
IMAU2	2-20 m	0.72	0.47	1.37	0.34	1.29	0.99	0.87
	20 -100 m	0.32	0.05	0.41	0.31	1.23	0.98	0.90
IMAU3	2-20 m	0.84	0.45	1.52	0.38	1.31	0.98	0.84
	20 -100 m	0.35	-0.05	0.45	0.35	1.11	0.95	0.88
IMAU4	2-20 m	0.68	0.49	1.44	0.36	1.30	0.98	0.85
	20 -100 m	0.36	-0.10	0.47	0.33	1.05	0.95	0.88
NIOZ	100-330m	0.04	-0.04	0.04	1.37	2.24	0.92	-8.18
AVHRR1	surface	1.18	-0.23	1.59	0.25	1.07	0.97	0.93
AVHRR2	surface	1.13	0.18	1.52	0.27	1.09	0.97	0.93
MODIS1	surface	1.54	0.14	2.01	0.32	1.09	0.96	0.90
MODIS2	surface	1.65	-0.02	2.17	0.35	1.05	0.94	0.88
MODIS3	surface	1.64	-0.19	2.16	0.34	1.05	0.95	0.88
MODIS4	surface	2.51	-0.34	3.14	0.46	0.88	0.89	0.78
L8-1	surface	1.45	-0.09	1.70	0.32	1.12	0.96	0.90
L8-2	surface	1.37	-0.07	1.86	0.33	1.08	0.95	0.89
L8-3	surface	1.98	0.47	2.57	0.45	1.12	0.92	0.79
L8-4	surface	1.88	1.32	2.53	0.46	1.25	0.94	0.71

Table 3.5: Performance of the hydrodynamic model in the validation phase (all points, 2004-2018 run).

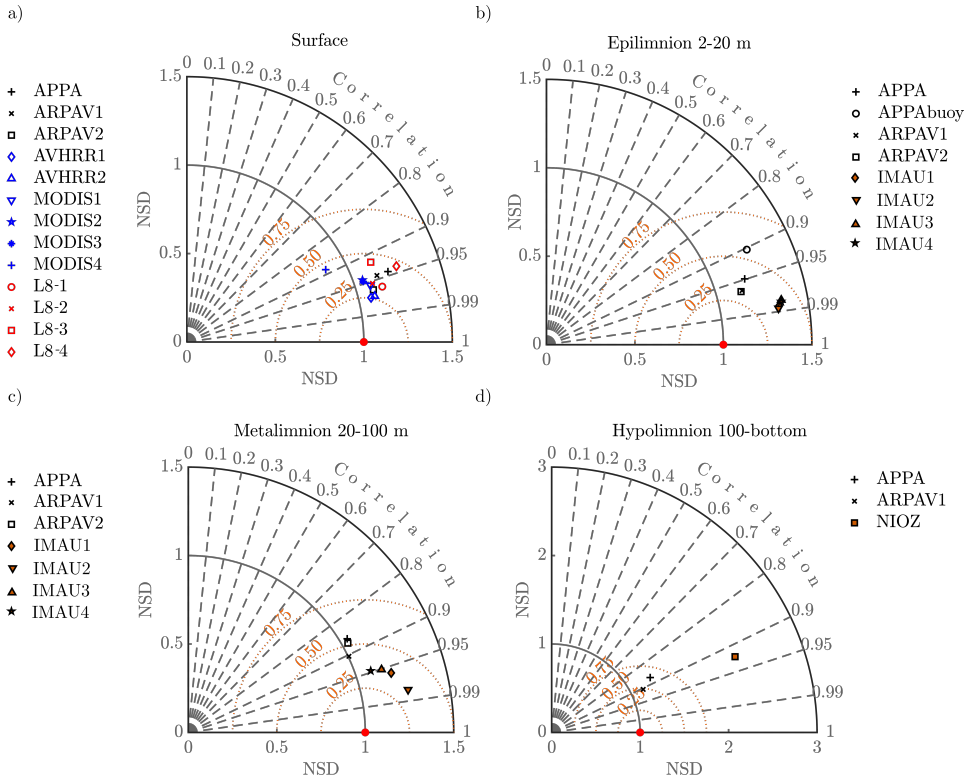

Figure 3.3: Taylor diagrams comparing the Delft3D model performance against all data available in different layers: a) surface, b) epilimnion, c) metalimnion; d) hypolimnion. RMSD and SD are normalized as defined in Tab. 3.2. The numerical values of the points are provided in Tab. 3.5.

(i.e., 0-2 m, Figure 3.3a) also the comparison with the time series of satellite data: in this case the indices were derived according to Equation (3.2) .

In Figure 3.3, the four Taylor diagrams [Taylor, 2001] display the NSD and the NRMSD of the simulations versus the measurements for each layer. Differently from the standard use of Taylor diagrams, we use the numerical outputs as the reference (red dot), and compare them with the measurements in the different locations (different markers). Since each observation point has its SD, the normalization of the statistical indices is necessary for the comparison. In the four diagrams, all the points are in the bottom right part of the plot and close to the reference point. This indicates that the model is well correlated with all datasets and captures the temperature variability in each location along the water column.

In the surface layer (Figure 3.3a), the NRSMD is between 0.25 and 0.5 almost everywhere, with the lowest values in AVHRR points. Among all remote sensed time series, AVHRR1 and AVHRR2 show the best agreement with model results, with MAE less than 1.2 °C, while MAE

is 2.5 °C in MODIS, and between 1.3 and 2 °C in Landsat-8 control points (see also Table 3.5 for the numerical values of the performance metrics). The worst performances are found in MODIS-4, L8-4 and APPA *in situ* point. All these points are located at the center of the northern narrow trunk of the lake and are very close each other, but interestingly the NSD is larger than 1 in APPA (1.20) and L8-4 (1.25), but smaller than 1 in MODIS4 (0.88). Similarly, the ME in this point switches from positive in APPA (0.65), APPA buoy (1.47) and L8-4 (1.32), to negative in MODIS4 (-0.34).

In the epilimnion (Figure 3.3b), all IMAU points show larger NSD in comparison with APPA point (IMAU $\sim$ 1.30, APPA $\sim$ 1.18). On the other hand, unsatisfactory performances are registered in the APPA buoy point (providing data at 10 m below water surface). In this location, the largest ME and RMSD are achieved (1.47 °C and 2.85 °C), but the correlation is extremely high (0.90). Both in surface and epilimnion layers the NSE is above 0.8 everywhere except for APPA buoy points, where it is still >0.5.

In the metalimnion (Figure 3.3c), the model errors reduce in absolute terms, but the normalized performance indices increase due to the smaller variation range of temperature observations: in this layer, the largest NRMSD is in the APPA point (0.54). Correlation is everywhere larger than 0.90 with the exception of APPA (0.86). The NSE reduces due to the limited variance of data, but the values are still acceptable and the minimum value is again in the APPA point (0.65, see Table 3.5).

In the hypolimnion (Figure 3.3d), the comparison is limited to a small number of observation points. The smallest RMSD in this layer (0.04 °C) in the NIOZ point is linked to the largest NRMSD (1.37) and NSD (2.24). In APPA and ARPAV1 points, the normalized indices present better values (NRSD = 0.63, 0.49, NSD = 1.27, 1.14, respectively), but the RMSD is larger (0.32, 0.30, respectively). In general, the normalized indices (NRSD, NSD) provide worse results for deeper layers and shorter time series, due to the smaller standard deviation of the observations, which is the normalization factor. In fact, the EPAs datasets span a longer period, and the bottom temperature varied up to 1 °C in the 14 simulated years, while the NIOZ dataset contains measurements for just one year (2017-2018), during which the maximum temperature variation was about $\sim$0.3 °C. Hence, even if the RMSD is 10 times smaller in the NIOZ point

(0.04 °C against 0.30 °C in APPA and ARPAV1), the normalized values and the Taylor diagram (Figure 3.3d) suggest that the model performance is poor in that point (NRMSD = 1.37 against 0.63 and 0.49 in APPA and ARPAV1 points, respectively). On the other hand, the correlation (CORR) is very good in all datasets. The same applies also to NSE, which is positive in APPA and ARPAV1 (being even larger than 0.5 in the latter point), with the exception of the NIOZ point, where the negative NSE is again due to the small range of variability of the time series. In all deep points, however, the RMSD is on the same order of magnitude as the ME, and the error can be attributed to a negative bias of the model near the bottom. In this regard, ME is generally negative everywhere in the surface and in the bottom, except for the surface layer in the northern sub-basin (APPA, APPA buoy, AVHRR2, L8-4, IMAU points). At the same time, the metalimnetic layer shows a positive bias in all points.

3.3.2 Interannual variability

In this section, we analyze the long-term variation of the temperature dynamics, showing also how it may be affected by specific events, as in the case of complete overturns that produce a long-lasting legacy on deep water temperature.

To this end, we focus on the observed and modeled temperature trends during the simulated 14 years in two observation points: ARPAV1 and ARPAV2 (see Figure 3.1). This helps evaluating the model performance in reproducing the interannual variability of the lake's thermal regime.

As a first comparison, we plot the interannual trend of the thermocline depth as observed in ARPAV1 deep point and and modeled by Delft3D (Fig. 3.4). Here we define thermocline as the depth where the vertical gradient of temperature $\frac{\Delta T}{\Delta z}$ occurs. Model outputs (continuous lines) are provided at hourly resolution, and a moving average of one day span is also computed in order to smooth the sub-daily variations. Observed data (dots) are instead available at a monthly basis, each value being however representative of the lake conditions at the sampling time. The figure shows that the mean daily variation of modeled thermocline depth reasonably reproduces the observed trend throughout the 14 simulated years, with a correct description of the summer stratification and of the deep mixing events of 2005 and 2006, when the thermocline

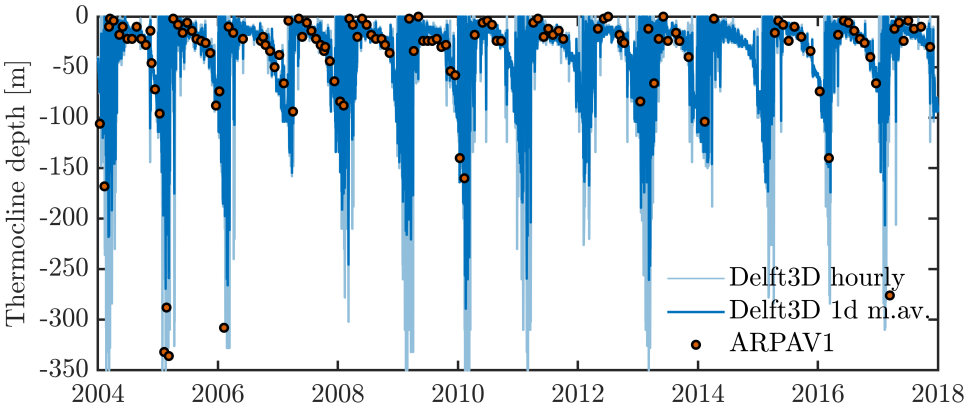

Figure 3.4: Depth of the thermocline from observations in ARPAV1 point (orange dots) and from model results (continuous lines) with hourly resolution (light blue) and resulting from a 1-day moving average (dark blue).

nearly reached the bottom of the lake. Interestingly, the model seems to greatly overestimate the thermocline depth in the early spring from 2009 to 2011 and in 2013. The reason of such error are more easily explained by looking at the temperature and at the model error directly. With this aim, in Figure 3.5 and 3.6, the modeled daily temperatures in ARPAV1 and ARPAV2 points are compared with the temperature measured monthly by the EPA of Veneto Region. The morphological characteristics of the lake are very different in these two points 3.1: ARPAV1 is located in the deepest point of the northern trunk (maximum depth 344 m), while ARPAV2 is located in the southern wider basin, where the bottom depth is 69 m. Thus, the comparison between modeled and measured temperature in these two points allows for testing the different performance of the model in the upper (ARPAV1) and the lower parts of the lake (ARPAV2).

In Figure 3.5a, the temperature in ARPAV1 at three depth levels is plotted. Both model and measured values are obtained as the mean value over the upper 10 m (hereafter referred as "surface"), the deepest 10 m ("bottom"), and in a 10 m-thick layer around the depth of 30 m ("interior"), according to Equation (3.1). The figure shows that the model captures the interannual trend of temperature and the thermal gradients between surface and deeper layers. Despite bottom temperature does not change significantly during single years, an overall heating of 1° C is reproduced from 2004 to 2018 by the model. The model correctly predicts the occurrence of deep mixing events in 2005 and 2006 (the last events Lake Garda experienced according to Salmaso et al. [2017]), and the partial mixing in 2017 that Piccolroaz et al. [2019] attributed to wind-driven deep mixing.

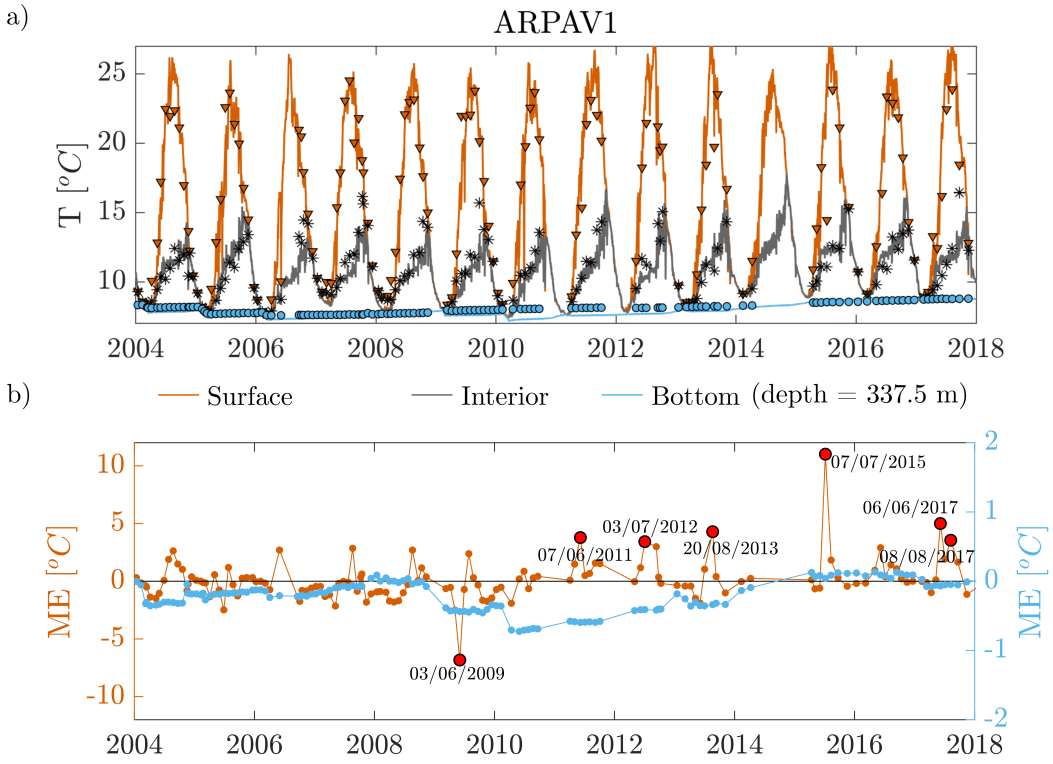

Figure 3.5: a) Trends of temperature at surface (mean over the first 10 m), interior (mean between 25 and 35 m depth) and bottom (mean over the deepest 10 m) from model results (continuous lines) and observations (markers) at ARPAV1 (a) point. b) Trends of mean error at the surface (orange dotted line) and at the bottom (light blue dotted line)at the same point. Red dots indicate those days when surface $|ME|$ >3 °C.

The temporal evolution of the mean model error is plotted in Figure 3.5b: to ease the reading of the plot, different scales have been used for surface (left, orange) and bottom (right, light blue) errors. The model error, both at the surface and at the bottom, does not increase in time, thus it does not propagates throughout the simulation. The largest surface errors occur during late summer-autumn, and are often connected with the large negative error at the bottom. The latter is maximum between 2009 and 2013, when the model prediction is colder than observations. As it was clear from Figure 3.4, this is due to the erroneous simulation of deep mixing events in 2009 and 2010, which did not occur in reality and cause a drop in the bottom temperature. In Figure 3.6, the same plots are provided for ARPAV2 point. Maximum summer temperatures at ARPAV2 point are generally higher than at ARPAV1 (Figure 3.5a). The model error at ARPAV2 point (Figure 3.6b) is smaller at the surface if compared with those in ARPAV1 point (Figure 3.5b), and larger in the bottom. The latter is due to the fact that the maximum depth here is 69 m (instead of 344 m) and have the order of magnitude of MAE shown for the metalimnion layer in Table 3.5. For this same reason, the bottom temperature at the shallower ARPAV2 point shows larger variability with respect to ARPAV1 point. The complete homogenization of the whole water column is well predicted by the model every year.

In both Figure 3.5b and 3.6b, red dots indicate those days when significant inaccuracies affect the surface model temperature ($|ME| > 3°$ C). A significant error is found on April 2005 in ARPAV2 point, where modeled surface (bottom) temperature is 10° C (1° C) colder than the measured temperature. Such error is due to the combination of a large underestimation of air temperature and overestimation of wind speed in that region of the lake (see Figure 3.2b) during the previous months. In fact, the atmospheric model commits a mean error on air temperature of 4.56° C in February and 5.61° C in March 2004, which drives the fictitious cooling of the water column detected in April. A negative error is found in ARPAV1 as well, but the absolute value is much smaller than in ARPAV2 ($< 2.5°$ C at the surface, $< 0.5°$ C at the bottom), due to the larger local depth.

Analogously, the other days characterized by large water temperature errors coincide with periods when the wind forcing is significantly over/underestimated by the atmospheric model. In Figure 3.7 the comparison between the modeled and observed wind speed at hourly scale is provided for some of these days. In all cases reported it can be seen that the meteorological model

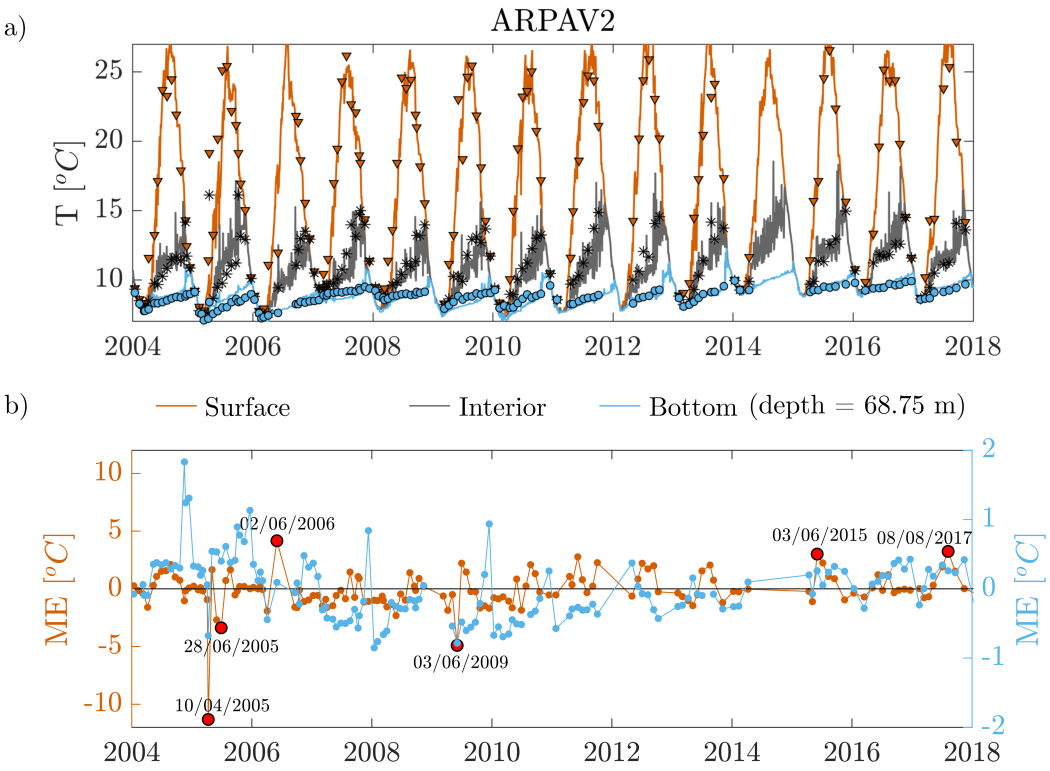

Figure 3.6: a) Trends of temperature at surface (mean over the first 10 m), interior (mean between 25 and 35 m depth) and bottom (mean over the deepest 10 m) from model results (continuous lines) and observations (markers) at ARPAV2 (a) point. b) Trends of mean error at the surface (orange dotted line) and at the bottom (light blue dotted line)at the same point. Red dots indicate those days when surface $|ME|$ >3 °C. Yellow dots highlight those dates for which a more detailed analysis of the atmospheric forcing is provided in Figure 3.7.

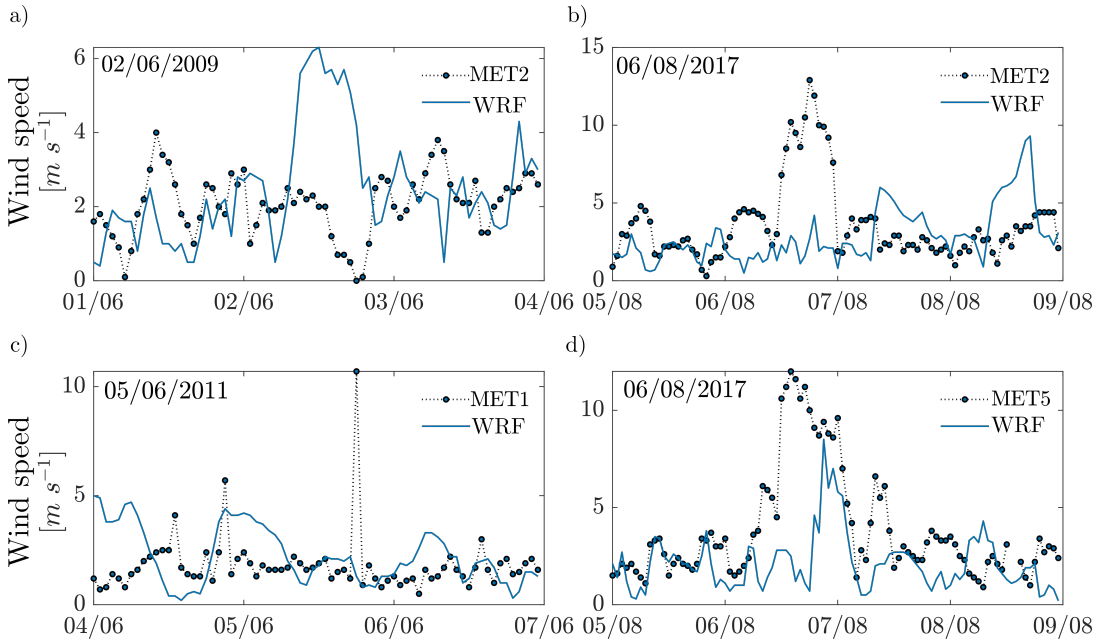

Figure 3.7: Time series of observed and simulated wind speed at a) MET2 on 2 June 2009, b) MET2 and MET5 on 6 August 2017, c) MET1 on 5 June 2011.

reproduces reasonably the observed values, except for a limited time slot. More in detail, the WRF model significantly overestimates wind speed at MET2 in the central hours of 02/06/2009 (Fig 3.7a), which causes the excessive cooling modeled in both ARPAV points on 03/06/2009. On the contrary, an increase of wind speed is not reproduced at MET2 and MET5 in the evening of 06/08/2017 (Figure 3.7b,d respectively), leading to the underestimation of wind-driven cooling on 08/08/2017. A similar explanation holds for the positive mean error detected in ARPAV1 on 07/06/2011: observations at MET1 on 05/06/2011 show a sudden increase of wind speed at 18:00 UTC+1, probably due to a local thunderstorm, which is not captured by the atmospheric model (Figure 3.7c).

Analogously, the other days characterized by large errors coincide with periods when the wind forcing is significantly over/underestimated by the atmospheric model. In Figure 3.7, the comparison between the modeled and observed wind speed at hourly scale is provided for some of these days. In all cases reported, it can be seen that the atmospheric model provides a good representation of the observed values, except for a limited time slot. More in detail, the WRF model significantly overestimates wind speed at MET2 in the central hours of 02/06/2009 (Fig 3.7a), which causes the excessive cooling modeled in both ARPAV points on 03/06/2009. On the contrary, an increase of wind speed is not reproduced at MET2 and MET5 in the evening

of 06/08/2017 (Figure 3.7b and d, respectively), leading to the underestimation of wind-driven cooling on 08/08/2017. A similar explanation holds for the positive mean error detected in ARPAV1 on 07/06/2011: observations at MET1 on 05/06/2011 show a sudden increase of wind speed at 18:00 UTC+1, probably due to a local thunderstorm, which is not captured by the atmospheric model (Figure 3.7c).

3.3.3 Seasonal cycle

In this section, focusing on shorter time scales we characterize the seasonal variability of water temperature in the lake in a simple and effective way that contains most of the relevant information. In Figure 3.8, the temperature variation along the water column is shown at the deepest point ARPAV1 for each month of the year from the model and the observations. The modeled profiles are obtained by computing the statistics on the whole validation period from the simulation output. The distribution of simulated temperature is indicated with boxplots (excluding outliers for the sake of clarity). Single temperature profiles from observations are plotted as grey dots.

The figure shows four characteristic periods for Lake Garda stratification dynamics in its deepest part. From February to March, the lake is nearly unstratified, with temperatures ranging in an interval of less than 1 °C throughout the water column. April, May and June are characterized by the developing stratification, and temperature experiences a great variability (surface temperature is comprised in a range of 10 °C in June). The largest surface-bottom difference is reached in the summer months, from July to September, when it ranges between 10 and 20 °C, and surface layers experience a similar range of variability (15 °C). From October to January, the autumn-early winter destratification typically occurs, and the range of surface variability decreases from 5 °C (October) to 2 °C (January).

The model correctly reproduces the range of variation of the temperature in each month and along the whole water column. Exceptions are found in summer months (June, July and August), when few episodes of very cold temperatures are not captured by the model. These observations lie beyond the normal range of variability, and correspond to extremely strong wind days not properly reproduced by the atmospheric model (see Figure 3.7), with subsequent errors

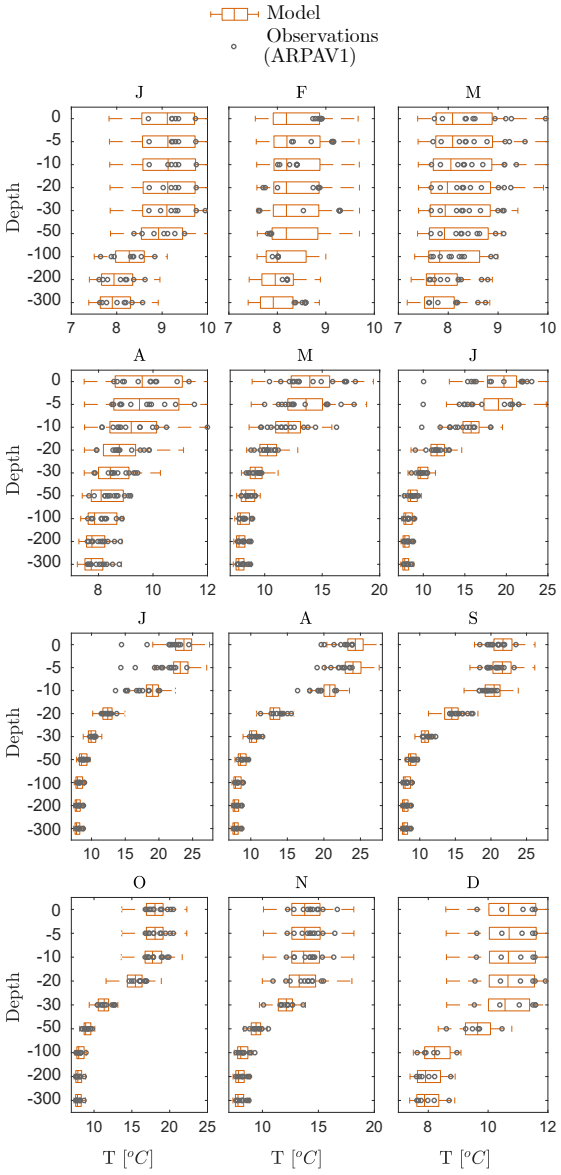

Figure 3.8: Comparison between monthly averaged temperature profiles over 2004-2018 among model results (orange box plots) and observations (gray dots) in the reference point ARPAV1. The boxes depict the median, the 25th and 75th percentiles of the monthly variation of temperature according to the model results. The whiskers extend to the minimum and maximum data points not considering outliers, which are not plotted. Observations are plotted as single scattered profiles.

in the hydrodynamic results (see Figure 3.5b and 3.6b for the details on the dates).

3.3.4 From monthly to sub-daily dynamics

In this section, we refer to the data at hourly scale available for the APPA buoy (surface) and the NIOZ thermistor chain (deep water), and compare observed and modeled temperature in the epilimnion and hypolimnion, using a wavelet time-frequency analysis. Contextually, we also analyze observed and modeled wind speed at the nearest weather stations, using the same approach. Figure 3.9 presents the results for the near surface dynamics from 2013 to 2018. The figure compares the wavelet power spectra (WPS) of measured (a) and modeled (b) wind velocity at MET1 station, and the epilimnetic water temperature at 10 m depth at APPA buoy station (d,e). Additionally, the global wavelet spectrum (GWS) for both variables (wind, c, and temperature, f) displays the time-averaged relevant energetic levels from observed and modeled time frequencies.

The figure shows that the WPS of the model results is fully coherent with that of the data, for both the wind and the water temperature signals. More energetic areas (orange to yellow) correspond to the summertime period, while less energetic (blue to purple) periods are found in wintertime. The wind signal (Figure 3.9a,b) shows that much more energy is associated to semi-diurnal and diurnal breezes in summer (as described by Giovannini et al., 2017). On the contrary, the signal is less intense during wintertime, when synoptic events are responsible for the energy peaks at longer time scales (some days to one week). At a global scale, the main energetic levels are at 12 and 24 hours (Figure 3.9c).

The epilimnetic temperature spectrum (Figure 3.9d,e) resembles the wind signal at the semi-diurnal to diurnal periodicity. The large power in summer depicts the heterogeneity of the internal wave field, which involves multiple scales (from hours to months) and causes a richer spectrum at a global scale (GWS, Figure 3.9f).

In Figure 3.10, the dynamics of the last simulated year (2017-2018) are presented at the NIOZ point. The figure compares the WPS of measured (a) and modeled (b) wind velocity at MET5 station, and hypolimnetic water temperature at 187 m depth at NIOZ station (d,e). Also in this case, the GWS of wind (c) and deep water temperature (f) summarize the main

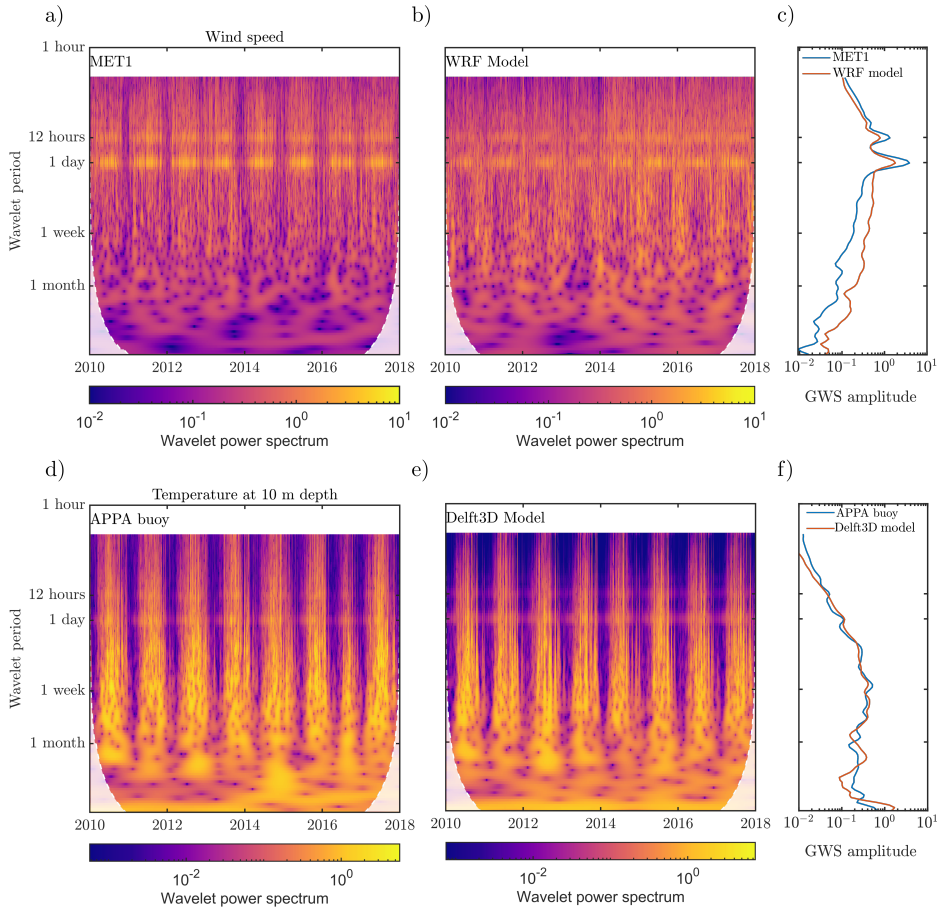

Figure 3.9: Wavelet analysis of (top plots) wind velocity and (bottom plots) epilimnetic temperature. Left plots: wavelet power spectrum (WPS) of a) wind observations at MET1 weather station; b) wind modeled by WRF at the corresponding model cell; d) water temperature measured by Appa buoy thermistor at at 10 m depth; e) water temperature modeled by Delft3D at APPA buoy point at 10 m depth. Right plots: global wavelet spectrum (GWS) computed from the previous WPS on (c) wind and (f) epilimnetic water temperature signal.

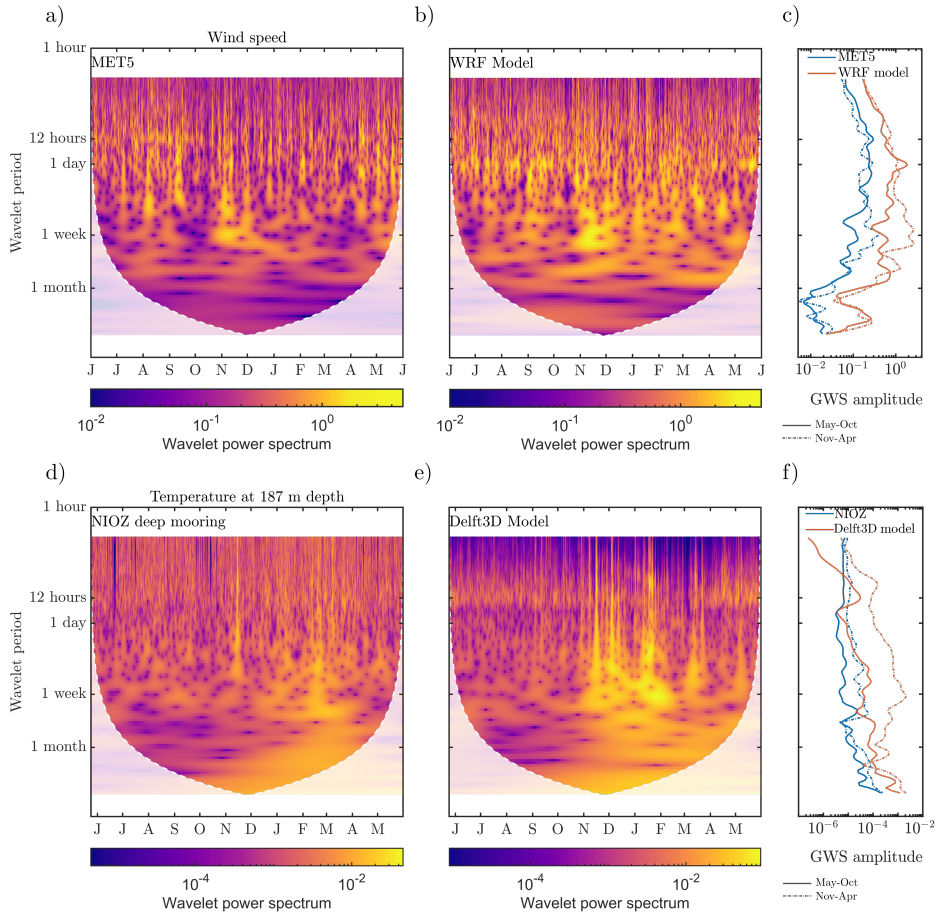

Figure 3.10: Wavelet analysis of (top plots) wind velocity and (bottom plots) hypolimnetic temperature. Left plots: wavelet power spectrum (WPS) of a) wind observations at MET5 weather station; b) wind modeled by WRF at the corresponding model cell; d) water temperature measured by NIOZ thermistor at 187 m depth; e) water temperature modeled by Delft3D at NIOZ point at 187 m depth. Right plots: global wavelet spectrum (GWS) computed from the previous WPS on (c) wind and (f) hypolimnetic water temperature signal.

energetic levels. In order to better identify the seasonal alternation, the GWS for both variables are distinguished between spring to autumn integrated spectrum (stratified period, from May to October, continuous lines) and winter spectrum (nearly unstratified period from November to April, dashed lines). Measured (a) and modeled (b) wind velocity display dominant energetic levels at semi-diurnal and diurnal frequencies (mainly in the stratified period, see subplot c) and few intense events of daily to weekly periodicity (e.g., November 2017 and March-April 2018). The wavelet analysis confirms that the atmospheric model missed the intense wind event occurred in August 2017 (as already seen in Sect. 3.3.2, Figure 3.7b,d).

The signature of semi-diurnal, daily and synoptic winds can be found in the observed (d) and modeled (e) deep temperature signal as well. The hydrodynamic model reproduces predominant semi-diurnal periodicity during the stratified period (see the GWS in subplot e), while during winter periodicities around 5-6 days is more energetic. These results are consistent with the observations of Van Haren et al. [2020]. The global power spectra (Figure 3.10c,f) highlight that both atmospheric and hydrodynamic model overestimate the energy of wind and deep water temperature signal at all energetic levels, especially at the longer scales in winter.

3.3.5 Spatial gradients

In the previous sections, the hydrodynamic model performance in different regions of the lake was presented (sections 3.3.1.2 and 3.3.2). While it was acceptable in most of the in-situ locations (see Table 3.5), difficulties arose when comparing the model performance (i.e., the numerical values of the metrics) in different parts of the lake. In fact, the comparison of statistical indexes is hindered by the different sampling frequencies and lengths of the time series. In order to overcome this issue, in this section we compare the modeled surface water temperature with remote sensing LSWT data from Landsat-8 full maps (see Table 2.1 for the technical details of the sensor and the time availability of data). The consistency of such a comparison is ensured by the fact that each pixel of the satellite LSWT maps is associated to the same time and to the same sampling method.

Figure 3.11 shows the absolute value of the centered (unbiased, hence removing the spatial mean) anomaly $\Delta_c T$ between modeled and observed LSWT (see Equation (3.3), Sect. 3.2.1.3).

In the top left corner of each subplot, we report the RMSD and ME computed for the single maps according to Table 3.2, without removing the spatial mean, thus providing the order of magnitude of the error over the whole lake surface. In most of the investigated dates, the RMSD is very similar to the ME. This suggests that most of the error is due to the bias between skin (retrieved from satellite imagery) and bulk (simulated by the hydrodynamic model) temperature, which can reach up to few Celsius degrees according to the meteorological conditions, especially during daytime [Wilson et al., 2013; Baracchini et al., 2020a].

For this reason, the advantage of introducing the unbiased anomaly $\Delta_c T$ index is easily understood. Indeed, by getting rid of the biases of both model and satellite data, the spatial distribution of the difference between the two can be visualized in an efficient way.

In most maps, $|\Delta_c T|$ <1 °C is generally found over the whole lake surface (e.g., Figure 3.11a). Differently, the largest $\Delta_c T$ (up to 3 °C) is found in those days when also significant differences between ME and RMSD occur (panels c-d, g, j). The largest differences between model results and satellite data are localized in the northern trunk and during the summer-early autumn period (panels b-d, g, j, m), and often along the eastern shore (panels b-d, g, k, m, o, r). In the southern basin, larger errors can occur again along the eastern shore (panels a-d,f-g, j, m, q), while patterns with smaller errors are frequent in the middle of the sub-basin (panels a, k, m, q).

A similar comparison, but taking into account the sign of the unbiased anomaly, is provided in Figure 3.12. By comparing the areas of large anomalies from the previous figure with the sign of the anomalies in the present figure, a clear pattern is visible. In the northern trunk, large anomalies are caused by warmer modeled temperatures (panels b-d, f-h, j-n). In the southern basin, the anomalies along the eastern shore are due to colder model temperatures (panels a-d, f-g, j, m, q). In the middle of the sub-basin, the sign of the anomaly oscillates between negative (panels a, k-m) and positive (panels b-c, f, q-r).

These anomalies can be related to transport processes that are not well captured by the model and for which the timing can be crucial. In fact, the two areas showing the largest mismatch patches were found to be affected by specific current patterns in previous studies. Gyre circulations were observed in the middle of both southern and northern basins by Amadori

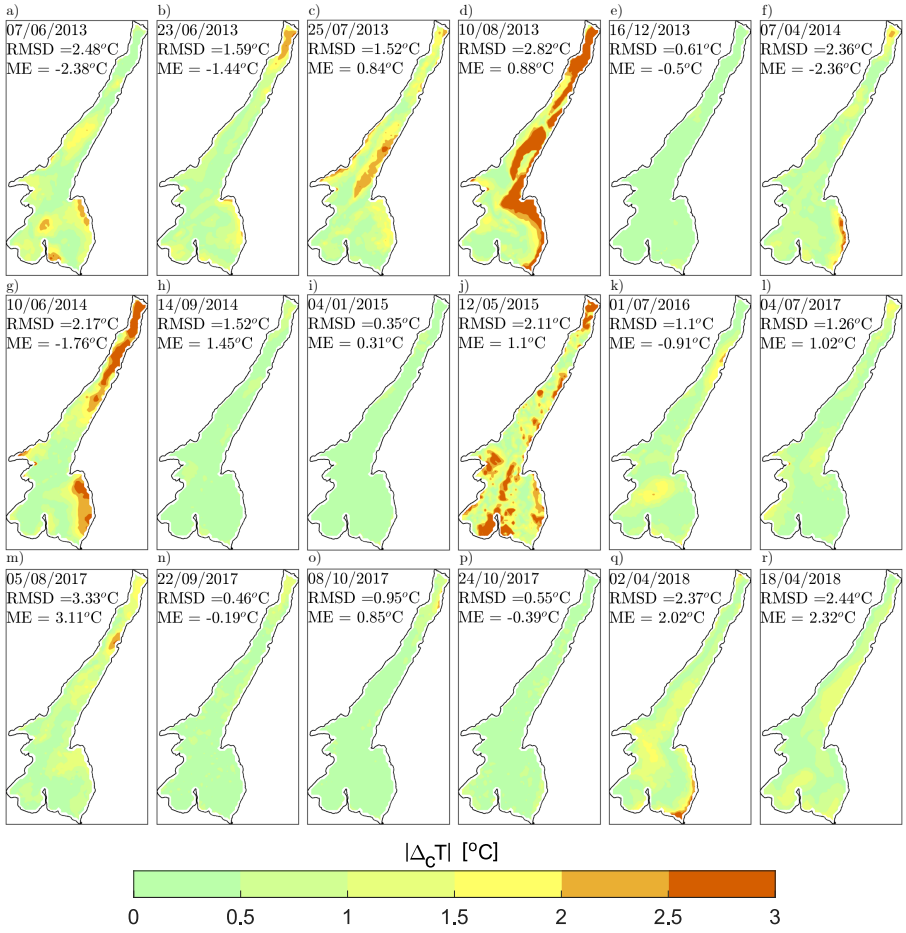

Figure 3.11: Absolute unbiased temperature anomaly between modeled and Landsat-8 LSWT computed as in Eq. (3.3) from all available complete satellite maps. Each subplot reports the date, the RMSD and the ME (bias). The two indices are computed as in Table 3.2, with i indicating each pixel and N the total number of pixels.

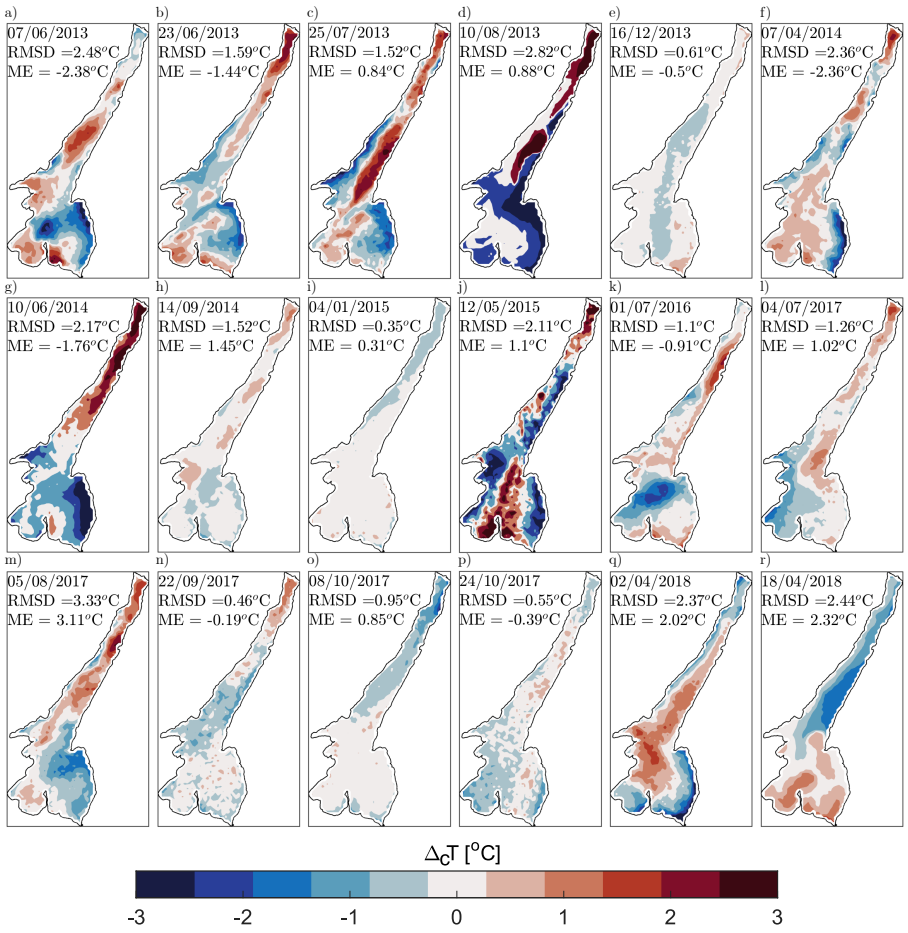

Figure 3.12: The same plot as in Fig. 3.11, but keeping the sign of the unbiased temperature anomaly.

et al. [2018, 2020b]. Moreover, in the northern trunk, Piccolroaz et al. [2019] observed and modeled up/downwelling along the shores due to intense and long lasting wind events. The latter processes could actually be responsible of the mismatch between Landsat images (colder) and modeled (warmer) surface temperature along the eastern shore, especially in late morning (Landsat acquisition time is 9:50 UTC). In fact, the model might have missed a cold upwelling caused by a local wind named 'Peler', which regularly rises late at night and blows persistently from northeast until late morning. In this regard, the absence of current measurements or satellite maps at a different times did not allow us to examine this bias in detail.

3.4 Discussion

The main goal of this work was to present the validation of a 3D hydrodynamic model over different time and spatial scales of water temperature variability, and to infer how the atmospheric model affects the lake model performance. As mentioned in Sect. 3.2.1.2, not all parameters could be effectively tuned, as we calibrated the model on temperature data solely. For these parameters, either the default value was adopted (Chézy coefficient, horizontal turbulence terms) or we referred to formulations existing in the literature (wind drag coefficient).

The performance of the numerical simulations were evaluated with typical statistical metrics (Sect. 3.3.1), whose values are consistent with previous results available in the literature, both for the model we used, Delft3D [e.g., Wahl and Peeters, 2014; Soulignac et al., 2017; Dissanayake et al., 2019], and for similar models [e.g., Hodges et al., 2000; Rueda and Schladow, 2003; Valerio et al., 2017]. Differently from the mentioned experiences, however, we evaluated not only the hydrodynamic model, but also the atmospheric model used to assign the surface boundary conditions. Additionally, both models were tested on different spatial and temporal scales.

The analysis of the interannual variability (Sect. 3.3.2) highlighted that the hydrodynamic model correctly predicts the differences in the thermal regime of the two sub-basins of Lake Garda, i.e., oligomixis in the northern part, and monomixis in the southern part. However, the model reproduced two false complete overturns in the deepest part of the lake. This was also found by previous experiences in large and deep Alpine lakes and was attributed to excessive bottom mixing, either in 1D [e.g. Schwefel et al., 2016] or 3D models [e.g. Råman Vinnå et al.,

2017]. For the case of deep Lake Garda, as in many other oligomictic lakes [Imboden et al., 1987], it has been demonstrated that deep mixing is traditionally buoyancy-driven [Salmaso et al., 2017], but that intense and long-lasting wind events can occasionally cause the complete or partial entrainment of the water column, causing deep ventilation [Piccolroaz et al., 2019]. Hence, a significant role is played by the atmospheric forcing (both air temperature and wind), which has to be captured properly in order not to miss deep mixing events or reproduce false positives. In our case, the interannual trend of the WRF performance at the northern station MET1 (Figure 3.2a) showed a positive ME on wind and air temperature during wintertime. However, in some years an overestimation of wind speed of 1 or 2 m^{-1} coincided with underestimated air temperatures (e.g., February 2009 and 2010, see Figure 3.2), leading to complete overturns in the nearly unstratified period (late winter to early spring, see Figures 3.5a). This issue could be overcome through data assimilation [Chen et al., 2019; Baracchini et al., 2020b] or restart procedures [Bouffard et al., 2018], forcing mixing to be well reproduced. In this work, where none of these techniques were applied and a single long run simulated, the results achieved in the deep water region are still acceptable, as such errors occurred only in two out of 14 simulated years.

In Sect. 3.3.3, we showed that the lake model satisfactorily captured the seasonal variations of water temperature along the vertical column. From this analysis, exceptional cooling events were easily identified. During such exceptional events, the hydrodynamic model provided the largest errors, especially in the northern region and on those days when the wind forcing was wrongly predicted by the atmospheric model. In this part of the lake, the resolution of the atmospheric model was not completely adequate to capture local-scale circulations in such a complex topography, since the grid size is 2 km over an average width of 4 km in the northern trunk. Hence, the under-representation of these topographic areas causes the inaccuracies of modeled wind, which is very sensitive to orography [see e.g., Carvalho et al., 2012; Mughal et al., 2017, for WRF applications]. In this regard, it is well known that in very complex terrain sub-kilometer resolution should be adopted to well reproduce local-scale circulations [Giovannini et al., 2014a; Le Roux et al., 2018; Schmidli et al., 2018]. This resolution was not feasible for the present application, due to the high computational costs involved to simulate 14 years. Relevant inaccuracies occasionally occurred also in the southern part of the lake. Here, the atmospheric

model struggled in reproducing local-scale phenomena (e.g., the thunderstorm of 6th August 2017, see Figure 3.7) and occasionally caused large errors in the simulation of wind speed and/or air temperature over localized areas near the shore. However, it is likely that errors are lower over the lake's surface, where the spatial heterogeneity of the meteorological fields is expected to be less significant. Unfortunately, no long-term meteorological measurements are available over the water. In this regard, in the recent application on Lake Garda reported by Piccolroaz et al. [2019], the authors warned that wind speed above the lake was not well described by the measurements from the nearest ground stations. They found that the wind speed above the lake was on average 1.6 times stronger than land measurements at MET3. Otherwise, WRF results were representative of the lake forcing conditions in the investigated periods. It is not redundant to stress that the spatial variability of the wind forcing is crucial for an appropriate representation of the basin-scale circulation and transport patterns, as already demonstrated for Lake Garda by Amadori et al. [2018], and by e.g., Strub and Powell [1986], Lemmin and D'Adamo [1997] and Laval et al. [2005] for other lakes.

Going down to the shorter time scales (Sect. 3.3.4), the wavelet analysis of the higher time resolution data at MET1, MET5, APPA buoy and NIOZ points gave satisfactory results for both models. The analysis showed that both models capture the relevant time scales associated to wind velocity and temperature fluctuations (both at the surface and at the bottom). In the series of epilimnetic water temperature, the predominant semi-diurnal and diurnal periodicity was perfectly reproduced by both atmospheric and hydrodynamic models. In the deep NIOZ point and the corresponding weather station MET5, the two models reproduced the main energetic levels, in good agreement with the observations by Van Haren et al. [2020]. However, both models overestimated the energy associated to each time scale. It is reasonable that the excessive energy predicted by WRF in MET5 was transferred to the hydrodynamic model. However, the error of the latter can also be magnified by the k-ε model implemented in Delft3D, which does not take into account wave breaking. Hence, the turbulence model might miss the dissipation associated with this process, eventually overestimating the energy of internal waves.

From Sect. 3.3.2 to Sect. 3.3.4, several time scales were considered, but also the spatial distribution of data. We saw that not only the length of the series, but also the geographic location of the point affected the model performance. In this regard, the case of the northern trunk of

the lake is emblematic, as the worst performances were found in this area. We already stressed that the resolution of the atmospheric model is too large to capture the sharp topographical variations of that region. However, its complexity also makes not only modeling, but also *in situ* measurements and remote sensing difficult to interpret. In fact, in this area residual effects from the adjacent land might affect the retrieval of LSWT from satellites in AVHRR, MODIS and Landsat-8 control points. In this regard, Pareeth et al. [2016] also observed that mountains have a shadowing effect on the remotely sensed LSWT in this part of the lake, which is likely to affect also *in situ* measurements depending on the time of the day when they are sampled.

The comparison of LSWT maps retrieved from satellite and those computed by the model (Sect. 3.3.5) provided useful insights on the model's performance over the whole lake surface. In fact, both remote sensing maps and *in situ* data provided the general picture that the model tends to overestimate LSWT in the northern part of the lake and to underestimate it in the south-eastern basin. If the issues related with the atmospheric model uncertainty are put aside for a moment, it is useful to consider that the two sub-basins are extremely different: the northern one is deep and narrow, with steep shores going sharply down to the bottom, while the south-eastern one is wide and shallow with a more uniform bathymetry. The way the lake exchanges heat through its surface is significantly different between the two sub-basins, with different thermal (thus mixing) regimes due to the lake heterogeneity. Hence, the adopted parameterization can produce opposite effects: not enough heat loss in the deep part (model too warm at the surface) and too much in the shallow part (model too cold). While currently available hydrodynamic models allow for various types of turbulence parameterization, from assigned eddy coefficients to more or less complex turbulence models (e.g., k-ε as in our case, or more recent approaches like LES, as proposed by Santo et al., 2017), one single parameterization of the heat fluxes across the lake surface is normally adopted for the whole domain. Our conclusion is that a more sophisticated parameterization of mixing on both sides (atmosphere and water) should be developed for applications on multi-basin lakes, in the same way as time-varying parameters are now obtained through data assimilation. This issue offers a lead for further research efforts in the future. Finally, the spatial distribution of anomalies of LSWT obtained from remote sensing compared to that from numerical modeling could also be exploited to infer whether the hydrodynamic model is able to capture the surface transport dynamics in the lake. In

such analysis, we noted some discrepancies between the two, but it is not easy to attribute them to malfunctioning of the model of misinterpretation of satellite data. Here, the timing for the comparison is essential: for instance, upwelling phenomena can be episodic and rapidly disappearing and just a few hours of difference matter. If more maps at a higher time resolution were available, the transport patterns could be reconstructed [Steissberg et al., 2005] providing a precious way to validate also the flow field, at least at the lake surface. In this regard, the availability of additional remotely sensed measurements will represent a key factor to improve this kind of analyses.

3.5 Conclusions

In this chapter, we presented a multiple-scale validation of a 3D lake model (Delft3D) forced by an atmospheric model (WRF). We compared the results of a single long-term (14 years) simulation with a number of different datasets of measurements from ground weather stations, buoys, thermistor chains and satellite imagery. While it is obvious that testing the numerical model against measured data is the necessary step for any reliable application, in this work we critically analyzed the model's performances at multiple scales with diverse types of available data.

Our focus was on the validation of the water temperature field, as water flow measurements are not always available in standard monitoring schemes. While a full validation of a 3D model would require to consider also other variables (e.g., water level, flow velocity, and turbulent quantities) here we coped with the typical scarcity of this type of data and extracted all possible information from water temperature data (typically available from routine lakes' monitoring) at different spatial and temporal scales. Even though some parameters were not calibrated, and the hydrodynamic quantities not verified directly, the 3D field of water temperature was satisfactorily reproduced at all investigated spatial and temporal scales. In fact, the model correctly reproduced the interannual variability of temperature along the water column, the main seasonal trends, the daily and subdaily internal variation and the main spatial patterns.

The approach we adopted allowed us to highlight how different scales interact, eventually affecting the results. On the one hand, we were able to interpret the hydrodynamic model

flaws on single days by observing the performances of the atmospheric model in the preceding months/years (e.g., in 2004 and 2005). On the other hand, we highlighted how single events can affect the model's performance for many years afterwards (e.g., the error at the bottom from 2009 to 2013 caused by the wrong prediction of deep mixing event in 2009). In those cases where inaccuracies occurred, the multi-purpose approach also allowed for tracing back to the source of the error, either being the atmospheric model (interannual to daily scale), the numerical resolution (in the northern trunk region), or the flow field uncertainty (largest patches of mismatch between satellite and model maps). In this regard, our results suggest that better performances could be achieved by improving the resolution of the atmospheric model, ideally assimilating meteorological data from stations located within the lake, and sampling current measurements for interpreting transport dynamics. Our suggestion is to adopt such approach when a model is intended to be applied at an operational level, as it helps identifying the model strengths and weaknesses, and leads the way for further improvements.

Acknowledgments

We thank the EPAs of the Autonomous Province of Trento (APPA), Veneto (ARPAV) and Lombardia Regions (ARPAL), and Edmund Mach Foundation (FEM), for kindly providing many of the data used in this study. We are also grateful to Circolo Vela Arco for logistic support during the IMAU-UniTrento field campaign, and to the firefigthers nautical rescue team of Trento (Corpo Permanente dei Vigili del Fuoco Trento) and M. van Haren for their assistance in the deployment and recovery of the NIOZ mooring. We also acknowledge Menno Genseberger (Deltares) for his initial work on the Delft3D model of Lake Garda. The Delft3D simulations were carried out on the Cartesius supercomputer at SURFsara (www.surfsara.nl). Part of this work was supported by Utrecht University and by the EU Horizon 2020 programme through the EOMORES project [grant number 730066].

Chapter 4

Basin scale circulation

Contents

This chapter is based on:

Amadori, M., Piccolroaz, S., Giovannini, L., Zardi, D., and Toffolon, M. Wind variability and Earth's rotation as drivers of transport in a deep, elongated subalpine lake: The case of Lake Garda. *Journal of Limnology*, 77(3), 2018. doi: 10.4081/jlimnol.2018.1814

Amadori, M., Morini, G., Piccolroaz, S., and Toffolon, M. Involving citizens in hydrodynamic research: A combined local knowledge - numerical experiment on Lake Garda, Italy. *Science of The Total Environment*, 722:137720, 2020b. doi: 10.1016/j.scitotenv.2020.137720

4.1 Role of wind variability and Earth rotation in basin scale circulation of Lake Garda

Water motions in lakes are predominantly driven by the action of wind forcing on the water surface. In particular the wind action produces two main effects: triggering both surface and internal waves, as well as driving lake circulation. While the latter process was a common subject in early pioneering contributions [e.g., see the reviews in Heaps, 1984; Hutter et al., 2011a], in the last decades the scientific literature has mostly focused on the motions produced by internal waves in stratified conditions [e.g., Hodges et al., 2000; Umlauf and Lemmin, 2005].

From a modeling point of view, the interaction between atmosphere and lake dynamics has been addressed by increasingly numerous investigations [e.g., Crosman and Horel, 2010], thanks to the advances in computational power [e.g., Notaro et al., 2013; Huziy and Sushama, 2017; Zhong et al., 2016]. Numerical models including different features and complexity have been developed to simulate lake physical processes under different meteorological constraints, ranging from simple, decoupled one-dimensional lake models [e.g., Goudsmit et al., 2002; Perroud et al., 2009; Piccolroaz and Toffolon, 2013a], to more complex, two-way coupled three-dimensional models [e.g., Song et al., 2004; Leon et al., 2007; Xue et al., 2017], with a wide range of intermediate examples [e.g., Schwab et al., 1989; Hostetler et al., 1993; Goyette and Perroud, 2012; Schimmelpfenning et al., 2012].

In principle, a two-way coupling approach is needed to achieve a detailed description of lake-atmosphere interaction. However, lacustrine dynamics under atmospheric forcing are routinely described by one-way coupled models [e.g., Kelley et al., 1993; Pan et al., 2002; Valerio et al., 2017], or stand-alone uncoupled hydrodynamic models, driven by realistic meteorological conditions through spatial interpolation of observations [e.g., Laval et al., 2003]. Oversimplified atmospheric forcing, such as horizontally uniform and/or stationary wind fields, can instead produce large inaccuracies [Strub and Powell, 1986], resulting in modeled lake circulations poorly representative of real conditions.

However, wind is not the only factor controlling lake hydrodynamics. Stratification conditions and the effect of Earth rotation chiefly concur to affect residual circulation (here defined

as the time-averaged velocity field), turbulence (described by increasingly complex approaches, e.g., Large Eddy Simulations [Santo et al., 2017]), mixing dynamics (e.g., deep mixing processes, upwelling/downwelling regions), and the fate of nutrients, pollutants and particulate matter. A deep understanding of how these main drivers interact is a key step for any comprehensive description of the physical behavior of a lake and for supporting optimal lake management. This may be often challenged by the increasing complexity of two factors: the shape and the bathymetry of the lake, whereby deep and narrow regions react differently than wide and shallow ones, and the surrounding orography, which controls the spatial and temporal variations of the wind field [Rueda et al., 2005]. In this respect, Lake Garda is an extraordinary example of both aspects and represents a relevant, yet almost entirely unexplored, case study.

In this section we take a first step towards the understanding of the flow field in Lake Garda under realistic wind and thermal stratification conditions. Numerical experiments were performed by means of the three-dimensional hydrodynamic model Delft3D to quantify the transport processes resulting from wind field and thermal conditions typical of the summer and winter seasons. At the time of this experiment, no hydrodynamic measurements were available in Lake Garda, thus effectively precluding proper calibration and validation of the simulated flow field. However, our intent in this investigation was not to set up a predictive tool for Lake Garda, but to achieve a first-order description of the possible hydrodynamic behavior of the lake under typical seasonal conditions. To this aim, model experiments were designed as single-day simulations where stratification conditions are specified on the basis of measured temperature profiles, while wind fields are obtained from atmospheric model (WRF) runs specifically set up for the study region [Giovannini et al., 2014b].

The underlying question how circulation and transport processes in elongated and deep perialpine lakes are affected by thermal stratification, the temporal and spatial variability of the wind forcing, and Earth rotation.

4.1.1 Methods

We report in Fig. 4.1 the map of Lake Garda with the key locations for the description of the basin scale circulation.

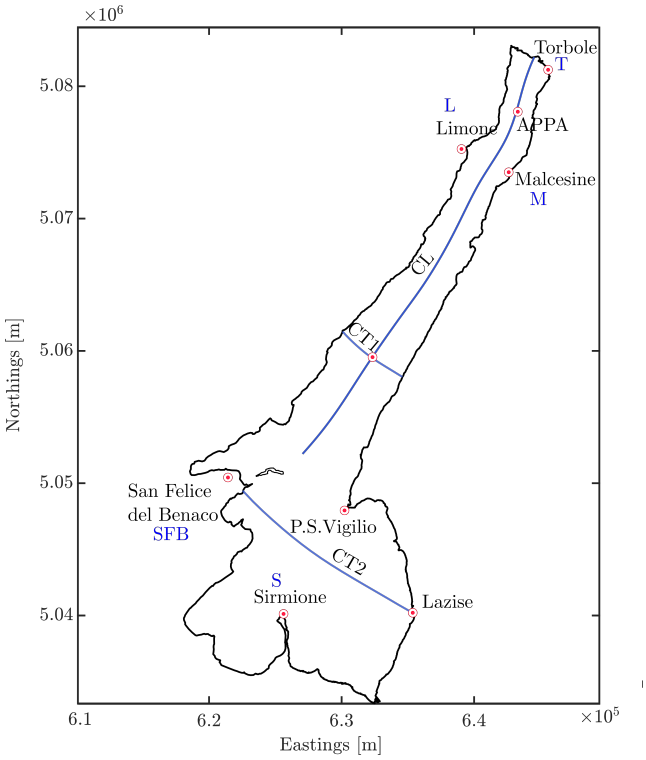

Figure 4.1: Map of Lake Garda with the relevant locations for investigating basin scale circulation and seasonal transport patterns. Blue lines depict the longitudinal (CL) and crosswise (CT1, CT2) sections where transport will be evaluated.

4.1.1.1 Model setup

We arranged a modeling chain composed by WRF [Skamarock et al., 2008a] and Delft3-Flow [Lesser et al., 2004], similarly to that described in Chapter 3. For this work, *ad hoc* simulations were run with both models in order to reproduce the specific wind days considered representative of typical seasonal patterns.

Atmospheric Model The WRF simulations performed for the present work covered 48 hours each. The first 24 hours are spin-up time, and were not taken into account for the analysis. The horizontal domain covered an area that includes Lake Garda and was composed of three two-way nested domains with 94x90, 112x97 and 73x106 cells, and grid spacing of 9, 3 and 1 km, respectively. For the vertical resolution, 30 levels were used. The initial and boundary conditions were supplied by the 6-hourly National Centers for Environmental Prediction (NCEP) Final Operational Global Analysis data on 1-degree grids. Relevant variables for forcing the hydrodynamic model from the last domain (1 km spatial resolution) were saved every 15 minutes

starting from the midnight (00:00 UTC+0) of the simulation day. Three different one-day

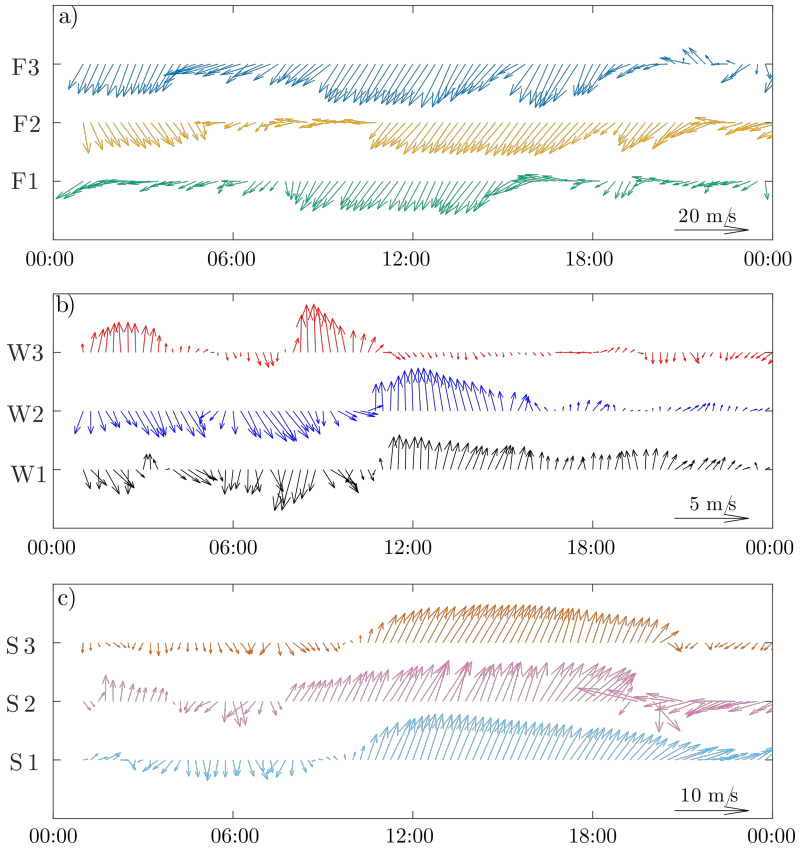

Figure 4.2: Simulated diurnal wind cycles at 10 m above ground level for winter Föhn days (a), winter breeze days (b) and summer (c) breeze days in the APPA monitoring point. Time given in UTC+1 (local time zone).

periods were simulated in summer and six in winter, for a total of nine different scenarios. The use of more than one scenario per season was preferred to get more robust results and a better description of the differences between the two seasons. In particular, six wintertime scenarios were chosen to study two different wind patterns occurring in Lake Garda in this season. Three of them (F1, F2 and F3) are representative of synoptic Föhn winds blowing from north-east. In the others (W1, W2 and W3) weak breezes develop. In Fig. 4.3 the spatial distribution (a) of the Föhn wind is shown for F3. Analogously, three summertime scenarios (S1, S2, and S3) were selected on the basis of the development of the typical thermally-driven 'Peler' and 'Ora del Garda' breezes over the lake. Their spatial pattern (b and c) is presented in Fig. 4.3 for the case of S3. All wind diurnal cycles of wind are shown in Fig. 4.2, while Tab. 4.1 reports the dates selected for the wind conditions and the respective mean wind speeds.

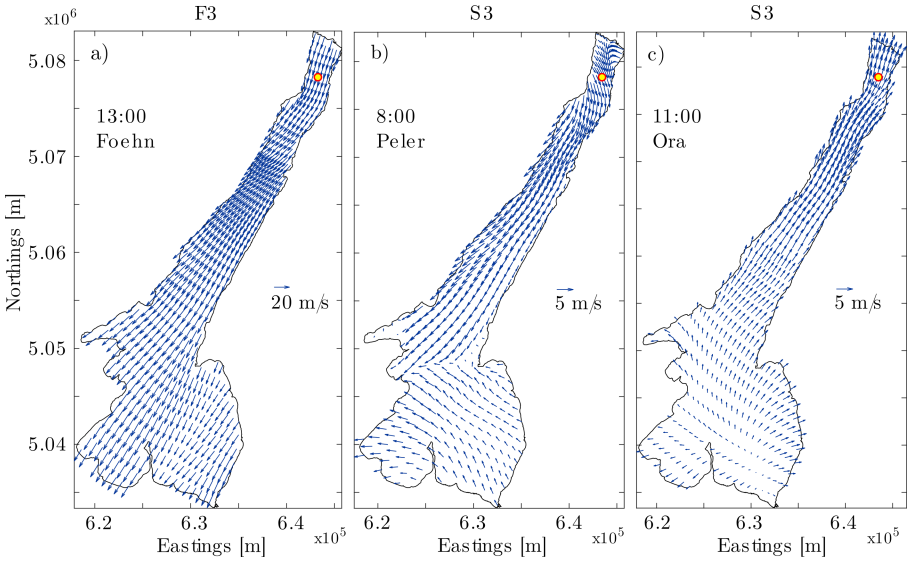

Figure 4.3: Simulated wind field for (a) Föhn wind in F3 winter scenario, (b) 'Peler' and (c) 'Ora del Garda' breezes in S3 summer scenario. Time is given in UTC+1 (local time zone).

Simulation ID	Wind day from WRF	Mean wind speed [m s^{-1}]	Initial condition temperature for Delft3D
F1	17 January 2013	14.3	22 January 2013
F2	12 March 2013	15.8	13 March 2013
F3	5 March 2015	15.3	18 February 2015
W1	7 February 2011	1.8	14 March 2011
W2	2 March 2012	1.7	13 February 2012
W3	27 January 2016	1.7	19 January 2016
S1	16 June 2012	2.8	5 June 2012
S2	29 July 2012	3.9	16 July 2012
S3	19 August 2012	2.6	21 August 2012

Table 4.1: Simulations characteristics for each scenario.

Hydrodynamic Model Consistent with the atmospheric simulations, nine hydrodynamic runs were performed, one for each one-day period for which the wind field was available. The main parameter settings of the hydrodynamic model runs are reported in Tab. 4.2. Simulation time was set at UTC+00 in accordance with atmospheric simulations.

A staggered orthogonal curvilinear grid of 64 x 224 cells was adopted with a non-uniform mesh, and cell size varying from 100 m in the northern narrow part to 400 m in the southern wider part. Vertical discretization was based on horizontal layers (Z-model), for a total number of 61 layers with increasing thickness from the top layer (1 m) to the bottom layer (50 m). Three representative cross-sections were considered in the analysis (Fig. 4.1): the longitudinal cross-section (CL) along the narrow and elongated trunk region; two transverse cross sections, one at the center of the northern elongated trunk (CT1) and one in the southern basin from

Model settings					
Simulation time step	1 min			Simulation time	4 days
Grid size	64 x 224 x 61			Wall boundary conditions	*free slip*
Horizontal grid resolution	$100 - 400$ m			Heat fluxes model	*ocean*
Vertical grid resolution	$1 - 50$ m			Turbulence model	$k - \varepsilon$
Wind drag coefficient Cd [1]	4.4×10^{-3}	1×10^{-3}	2×10^{-3}	Bottom roughness (Chézy)	60 $m^{1/2}$ s^{-1}
Horizontal eddy viscosity	2×10^{-2} m^2/s			Background vertical eddy viscosity	10^{-6} m^2/s
Horizontal eddy diffusivity	2×10^{-2} m^2/s			Background vertical eddy diffusivity	10^{-6} m^2/s

[1] Breakpoints for piecewise linear function of wind speed (1 - 5 - 10 m/s) at 10 m above lake surface

Table 4.2: Delft3D-FLOW parameters.

Lazise to San Felice del Benaco (CT2).

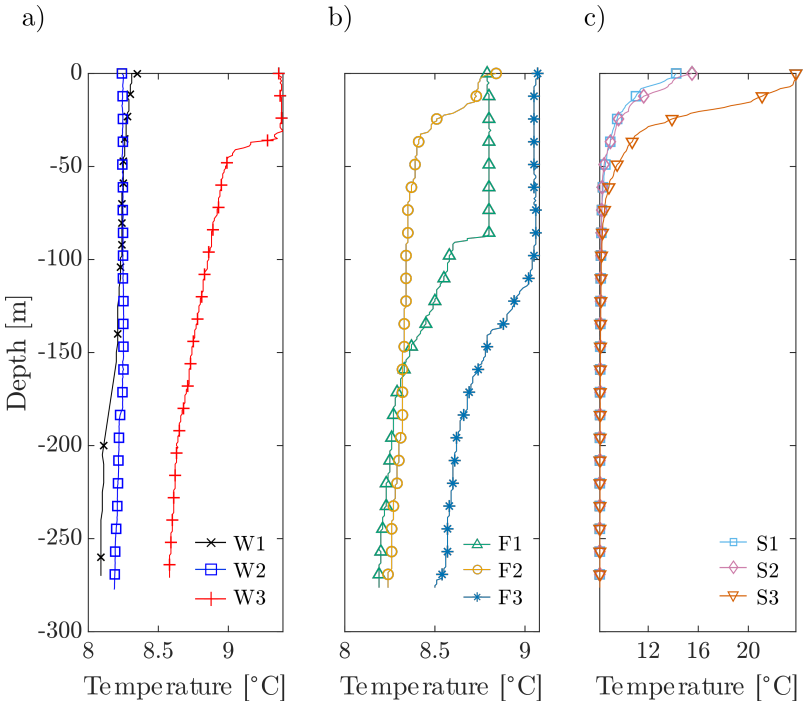

Figure 4.4: Temperature profiles used in winter (a,b) and summer (c) numerical simulations (measured at APPA monitoring point, see Fig. 4.1).

We refer to Chapter 3 for the description of the other parameters reported in Tab.-4.2. WRF simulations provided space and time varying fields of wind speed (10 m above ground level) and surface atmospheric pressure. Initial conditions were set as water at rest and perfectly horizontal water level; an initial temperature profile was applied uniformly over the whole lake according to temperature profiles measured at the APPA monitoring point (see Fig. 4.4). Temperature profiles are sampled monthly on dates not coinciding with the reference wind dates. Hence, as initial condition of our model we adopted the closest temperature profile to the wind day. The discrepancy between these two dates (see Tab. 4.1) is not critical here, since simulations are

meant to associate typical wind pattern to corresponding plausible stratification conditions in different seasons. The contribution of inflows and outflows was neglected because of the long water renewal time in Lake Garda, estimated by IRSA [1974] in 27 years. Similarly, all additional parameters that were not crucial in the analysis of seasonal scenarios were discarded. For this reason, the exchange of heat through the lake surface is not computed, and we modeled the lake as an adiabatic system, with wind stress as the only driver. This simplification eases the interpretation of the results. In fact, we focused on the direct effects of wind, vertical density gradients and Earth rotation, while filtering out the additional complexity of surface heat fluxes parametrization.

Hydrodynamic simulations were run for a four-day cycle replicating the same daily atmospheric forcing. The results discussed in the following sections are obtained from the third day of simulation: in fact, in order to have consistent and representative time-averaged results (i.e., residual circulation), two days have been considered as necessary (and sufficient) for the establishment of periodic conditions on surface currents. The estimate is mainly based on direct observation of the periodic patterns reproduced by the numerical results after the second day (not showed here). Choosing a longer spin-up time would have drawbacks: since thermal fluxes are neglected and the same daily wind pattern is repeated for consecutive days, preliminary simulations showed that destratification appears to be relevant after the fourth simulation day, since wind mixing is not balanced by the heat source at the surface during the day. Accordingly, we needed to find a compromise between the reduced influence of the initial conditions and the deterioration of the thermal stratification due to vertical diffusion and wind mixing turbulence. The third simulation day was used as representative of fully developed flow conditions.

Particle tracking model Trajectories of individual particles released in the computational domain were traced through the particle-tracking module available within the Delft3D suite (Delft3D-Part). The model processes flow data from the hydrodynamic model to compute transport and mixing in the mid-field. The effects of dispersion were neglected, so that advection is the only driver of Lagrangian particles. Non-buoyant particles (i.e., having the same density as the ambient water) were released at 318 locations uniformly distributed in the surface layer of the computational domain. In each location 100 particles were instantaneously released within

a radius of 10 m.

Five additional release points were placed in geographically significant positions: Torbole (T), Malcesine (M), Limone (L), San Felice del Benaco (SFB), and Sirmione (S) (Fig. 4.1). Particles were instantaneously released at the beginning of the third simulation day (00:00) of the hydrodynamic model (i.e., at the end of the 2-day spin-up period). In Lagrangian simulations the time step was 15 minutes (i.e., the time interval of flow data storage) and the total simulation time was two days (i.e., the third and the fourth days of the simulations). In such a way, regime conditions are achieved and thermal stratification is substantially preserved. Lagrangian trajectories were obtained neglecting diffusive processes in the particle tracking simulations. Such a simplification was necessary as additional calibration parameters would be needed to adequately compute the dispersion parameters in Delft3D-Part, and calibration was not yet possible at that stage.

Additional simulations were performed with different release times (06:00, 12:00, 18:00, and 24:00 of the third day of the hydrodynamic simulation) to test the sensitivity of the Lagrangian patterns to the instantaneous flow field. In the discussion section we will show that the trajectories walked after two days of simulation were substantially insensitive from the release time. In the following sections, the results of particle tracking simulations are presented and analyzed in terms of surface trajectories, horizontal traveled distance, and depth reached by the particles.

Evaluation of residual transport The analysis of simulation results is carried out referring to both the Eulerian flow field and the Lagrangian trajectories, with a specific focus on the residual circulation, defined here as the time-averaged velocity field resulting from the third day of each hydrodynamic simulation. We analyzed the factors affecting the outcoming circulation and transport patterns,like bathymetry, wind intensity and direction and Earth rotation.

The most important transport mechanisms in lakes are produced by wind drag and by momentum transfer from the surface water to the underlying water mass. Vertical momentum transfer occurs by means of the turbulent vertical exchanges described through the concept of eddy viscosity. In the simplest ideally-shaped lakes, this direct action simply moves water downwind, possibly with a return flow at the bottom [Heaps, 1984], whereas more complex dynamics arise for real lakes especially when stratification is present. Nevertheless, in large

and deep water bodies, water circulation can be significantly affected by the Coriolis force. The transport is associated with a spiral flow for which the standard theory [e.g., Hutter et al., 2011b] provides an estimate of the reference depth (thickness of the Ekman layer),

$$D_E = \sqrt{\frac{2\nu_{z0}}{f}}\,, \tag{4.1}$$

where ν_z is the vertical eddy viscosity, $f = 2\Omega \sin\phi$ is the Coriolis frequency, with $\Omega = 7.2921 \times 10^{-5}$ rad s^{-1} the angular speed of Earth rotation. The subscript 0 refers to the constant values used to derive the analytical solution. In an infinitely deep water body, the vertically integrated transport q_E (per unit length, hence in m^3 s^{-1} m^{-1}) occurs in the lateral (i.e. cross-wind) direction, and can be estimated as

$$q_E = \frac{\tau}{\rho_0 f}\,, \tag{4.2}$$

where τ is the wind stress module and ρ_0 the water density. Corrections to q_E over finite depths can also be obtained analytically [Hutter et al., 2011a].

It is often claimed that the effect of Coriolis force can be neglected in lakes narrower than the Rossby radius

$$R = \frac{U}{f}\,, \tag{4.3}$$

where U is a reference value of water velocity at the surface. Indeed, R is the radius of theoretically circular trajectories associated with inertial currents, whose period is $T_i = 2\pi/f$.

$$T_i = \frac{2\pi}{f}\,. \tag{4.4}$$

However, Earth rotation can also significantly modify the large-scale circulation in narrow lakes where inertial currents cannot develop.

In an elongated narrow lake where the wind field is forced by the adjacent topography to blow along the lake main axis, the Coriolis force may induce a secondary lake circulation orthogonal to the wind direction, generating onshore downwelling and upwelling. Toffolon [2013] derived an analytical relationship to estimate the secondary circulation in lakes shallower than D_E under simplified conditions (rectangular domain, steady state, constant viscosity). In this case, the

lateral transport per unit length can be quantified as:

$$q_T = \alpha \frac{\tau\, H^4}{\rho_0\, \nu_{z0}^2} f\,, \tag{4.5}$$

where H is the depth of the equivalent rectangular domain, and the dimensionless coefficient α depends on turbulence anisotropy and bottom friction.

Although in principle none of the above analytical expressions for the lateral transport is strictly valid for the general case of enclosed basins, both eq.s (4.2) and (4.5) are linearly dependent on the wind shear stress, which can be empirically related to wind speed as $\boldsymbol{\tau} = \rho_a\, C_d |\boldsymbol{U_w}| \boldsymbol{U_w}$, where $\boldsymbol{U_w}$ is the wind speed vector, ρ_a the air density, and C_d the drag coefficient. Hence, as a first approximation, we can reasonably assume that the theoretical lateral transport per unit length can be expressed as

$$q_{th} \propto V_w^2\,, \tag{4.6}$$

where V_w is the longitudinal component of the wind speed $\boldsymbol{U_w}$. An analogous scaling with the square of the wind speed was also successfully used to quantify coastal downwelling due to inshore Ekman transport in the larger and deeper Lake Baikal by Piccolroaz and Toffolon [2013a, 2018]. Further attempts towards the definition of an improved relation for the lateral transport are beyond the scope of the present analysis.

The analytical dependence suggested by eq. (4.6) is here tested. We define as 'lateral' dimension the local coordinate x corresponding to the crosswise direction (y being the along-wind direction). Then the mean lateral transport per unit length $q_x = Q_x/L$ is computed numerically. L is the length of the examined longitudinal cross-section CL, and

$$Q_x = \int_0^L \int_0^{z_x} \bar{u}_x \, dz \, dy \tag{4.7}$$

is the total transport flowing through it (expressed as $\mathrm{m}^3\ \mathrm{s}^{-1}$). We compute $\bar{u}_x$ as the average in time of the velocity component in x direction crossing CL. In eq. (4.7), $\bar{u}_x$ is the lateral velocity (orthogonal to the main axis of the lake) varying with depth z. The vertical integral (4.7) is calculated from the surface to the inversion depth z_x, which represents the center of the

secondary circulation, i.e., the depth where $\bar{u}_x$ changes sign.

4.1.2 Results

As a first analysis, the hydrodynamic response of the lake was simulated considering typical winter episodes of intense synoptic wind blowing approximately uniform and constant. Simulations were run for three periods in winter when stratification was weak (Fig. 4.4c) and in presence of Föhn wind blowing from the north-east (Fig. 4.3a,b).

As a second analysis, the effect of weak winter breezes on lake circulations was investigated. Lake stratification was still weak and similar to the previous simulations (Fig. 4.4b), while in this case more gentle winds blew over the lake,. Such breezes have high space and time variability in both intensity and direction.

4.1.2.1 Föhn wind scenarios

Simulations were run for three periods in winter when the Föhn wind blew from the north-east (Fig. 4.2a, Fig. 4.3a) and stratification was weak (Fig. 4.4b). Residual surface currents (Fig. 4.5a-c), are directed from the north-east to the south-west along the lake longitudinal axis, as surface water is driven downwind by the wind shear stress. The flow field is almost uniform in the northern, elongated, narrow part of the basin, where water is channeled between the steep shores towards the southern, wider part. Flow deviates to the right relative to the wind direction due to the effect of Earth rotation, and no gyre circulation develops in the surface layer. Particle tracks (Fig. 4.5d-f) confirm the flow field described by the residual circulation. During the two-day Lagrangian simulation, particles released in the northern part of the basin travel a $5 - 20$ km distance range, with a clear deviation to the right relative to the wind direction.

The strong wind ($|\boldsymbol{U_w}| \sim 15$ m s^{-1}), persistently blowing over the lake, induces velocities sometimes larger than ~ 30 cm s^{-1} at the lake surface. This is a rather large value in lakes, but it is consistent with typical observations of the wind factor $U/|\boldsymbol{U_w}|$ of 1.5-3% [Henderson-Sellers, 1988; Monismith and MacIntyre, 2010]. A large-scale vertical circulation is induced in the longitudinal cross section CL (Fig. 4.6a), with water moving towards the south at the surface, and towards the north in the deeper layers, in accordance with the classical description [e.g.,

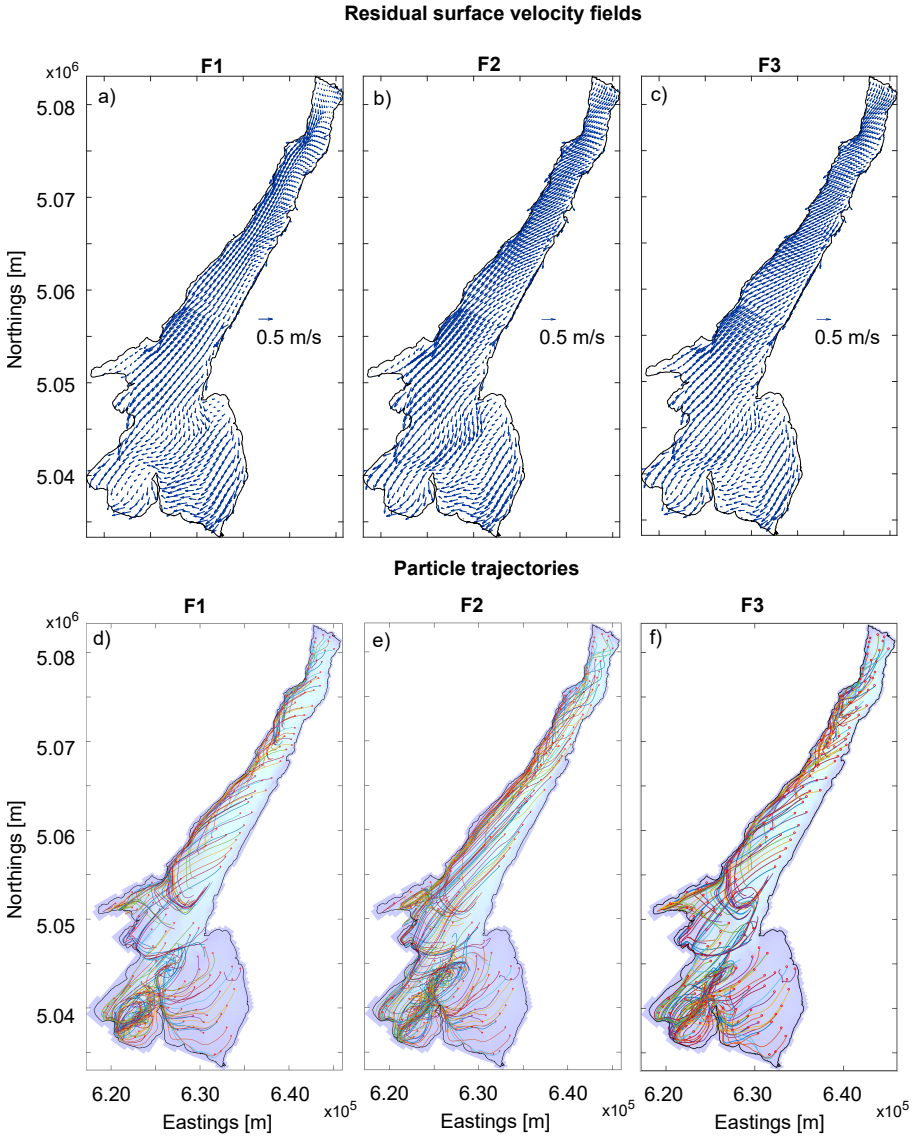

Figure 4.5: Horizontal transport in all winter Föhn wind simulations. Top plots: residual surface currents from simulations F1 (a), F2 (b), F3 (c), obtained by an average over day 3. Bottom plots: particles trajectories after two-days Lagrangian tracking in simulations F1 (d), F2 (e), F3 (f). Particles positions are computed through an average over 100 particles in some release points and plotted at 15 minutes intervals from the release time (00:00 of hydrodynamic simulation day 3) to the end of Lagrangian simulation (24:00 of hydrodynamic simulation day 4). Note: to ease the comprehension of the figure, 60% of the total number of trajectories is plotted after a random sampling.

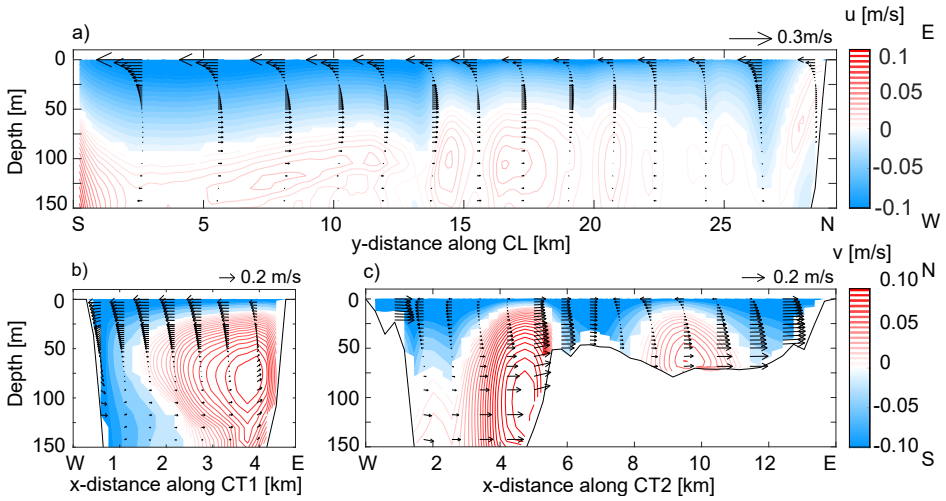

Figure 4.6: Residual cross-section circulation from winter simulation F3, obtained by a time average over day 3: (a) longitudinal section CL, (b) northern transverse section CT1 and (c) southern transverse section CT2. The contour plot shows the magnitude of the orthogonal component of the velocity; contour lines are plotted for positive velocities, filled contour plot is for negative velocities. Arrows indicate the circulation in the section. To ease the comprehension of the figure, not all grid cells are drawn in quiver plot.

Lemmin and D'Adamo, 1997; Wang et al., 2000]. An almost closed secondary circulation moves the surface water westward, producing downwelling close to the western shore, a return bottom water flow eastward, and upwelling rising on the eastern shore. An example of this secondary circulation is provided in Fig. 4.6b for the northern transverse cross section CT1, located in the central part of the narrow and elongated sub-basin.

The behavior in the southern sub-basin is more complex because of strong inhomogeneities both in the shape and in the bathymetry of the lake. Two secondary circulations develop in CT2 (Fig. 4.6c), where two distinct sub-sections are separated by the submerged ridge from the peninsula of Sirmione to Punta San Vigilio. A return flow occurs only in the deeper regions, whereas over the ridge the whole water column is set in motion with a uniform velocity profile.

The vertical circulations shown in Fig. 4.6 for simulation F3 can be easily verified also in simulations F1 and F2.

4.1.2.2 Winter breezes scenarios

The effect of winter breezes on lake circulation was investigated under weak thermal stratification (Fig. 4.4a). In this case, winds are more gentle and characterized by high variability, space

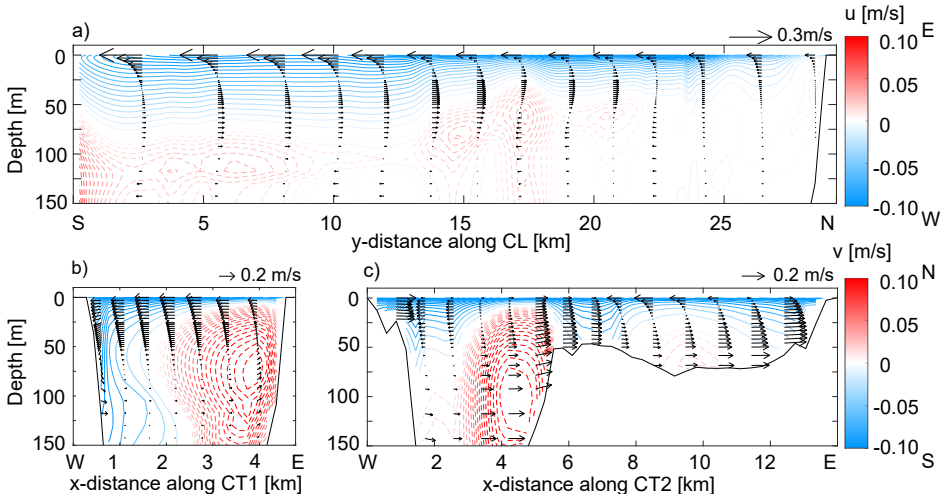

Figure 4.7: Residual cross-section circulation from winter simulation F1, obtained by a time average over day 3: (a) longitudinal section CL, (b) northern transverse section CT1 and (c) southern transverse section CT2.

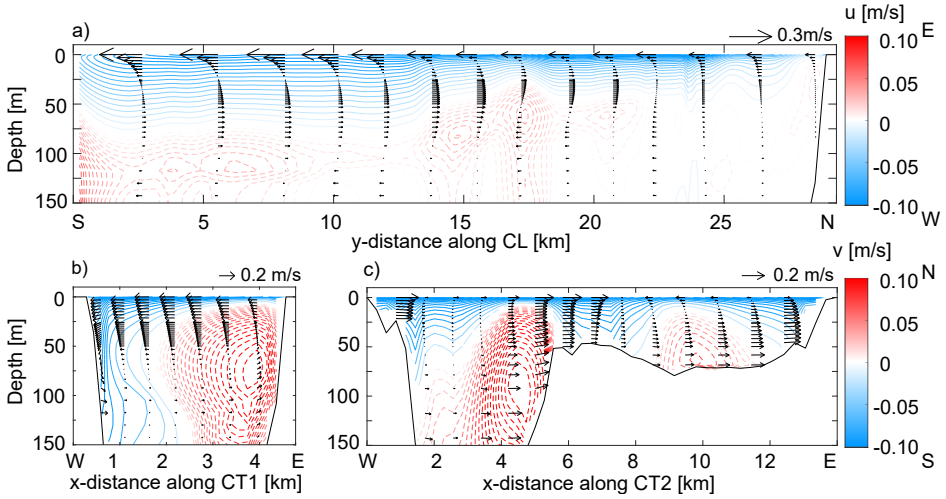

Figure 4.8: Residual cross-section circulation from winter simulation F2, obtained by a time average over day 3: (a) longitudinal section CL, (b) northern transverse section CT1 and (c) southern transverse section CT2.

and time, in both intensity and direction, with cold and dense air descending towards the lake during night and in the morning, and warmer lake breezes blowing from the lake to the northern shores in the afternoon. Surface water velocities are one order of magnitude smaller ($\sim$ 1 cm s^{-1}) than in the previous case due to the lower intensity of breezes (1-5 m s^{-1}). Residual circulations (Fig. 4.9a-c) appear much more complex than those observed in presence of Föhn wind conditions. A counterclockwise gyre develops close to the northern border of the lake, where the wind regime is dominated by alternating northerly and southerly weak thermally-driven winds. The resulting dynamics are similar to those developing in summer conditions and described in the following section. More heterogeneous dynamics develop in the central and southern parts of the lake, where breezes are not as regular and uniform as those in the northern part, and topographic effects are more significant due to the complex and shallower bathymetry.

Particle tracks reveal that Lagrangian transport is very small during simulation W2 (Fig. 4.9e), because the local breezes change direction and intensity during the day, then daily-averaged displacements are shorter. All over the lake, particles drift around the release points during the two-days Lagrangian simulation, along curved trajectories resulting from the combined effect of alternating wind direction and Earth rotation ($R \sim 100$ m in this case). In the other two scenarios (Fig. 4.9d,f), the Lagrangian paths resemble the residual circulations both in the northern trunk and in the southern basin, with a gyre-like structure clearly visible at the eastern junction between the two sub-basins.

4.1.2.3 Summer breezes

Residual circulations in summer cases are dominated by the diurnal variability of the wind field, similar to winter breezes, but with more intense winds and clear alternating directions. Water motion is complicated by the effects of strong thermal stratification. Fig. 4.10a-c shows the residual circulation for the three simulated summer scenarios.

The time and spatial average of wind speed for the three summer simulations is $|\boldsymbol{U_w}| \sim$ 2 m s^{-1} (Tab. 4.1), although large peaks up to 10 m s^{-1} can be reached during the afternoon development of the 'Ora del Garda' wind. Wind-induced average surface velocities are $\sim$ 5 cm s^{-1}, in agreement with summertime observations in other perialpine lakes (e.g., in Lake

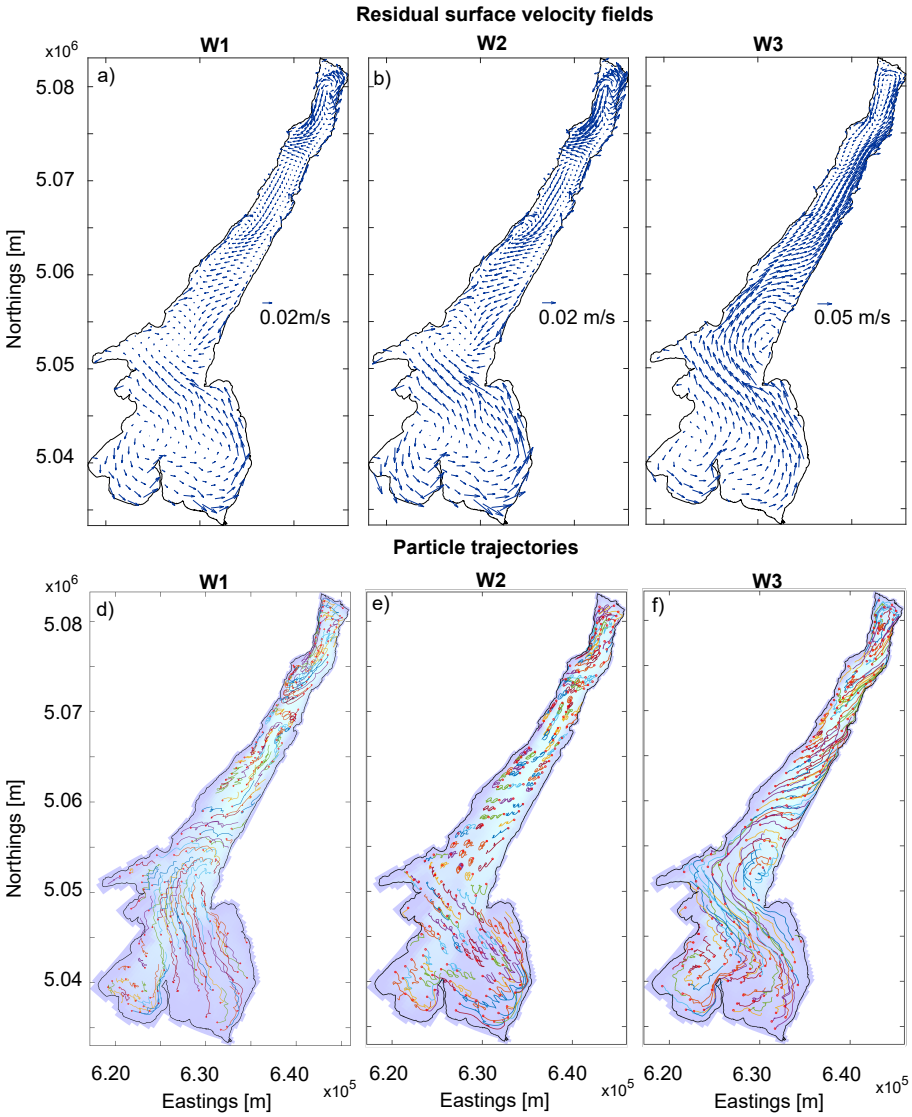

Figure 4.9: Horizontal transport in all winter typical breeze simulations. Top plots: residual surface currents from simulations W1 (a), W2 (b), W3 (c), obtained by an average over day 3. Bottom plots: particles trajectories after two-days Lagrangian tracking in simulations W1 (d), W2 (e), W3 (f).

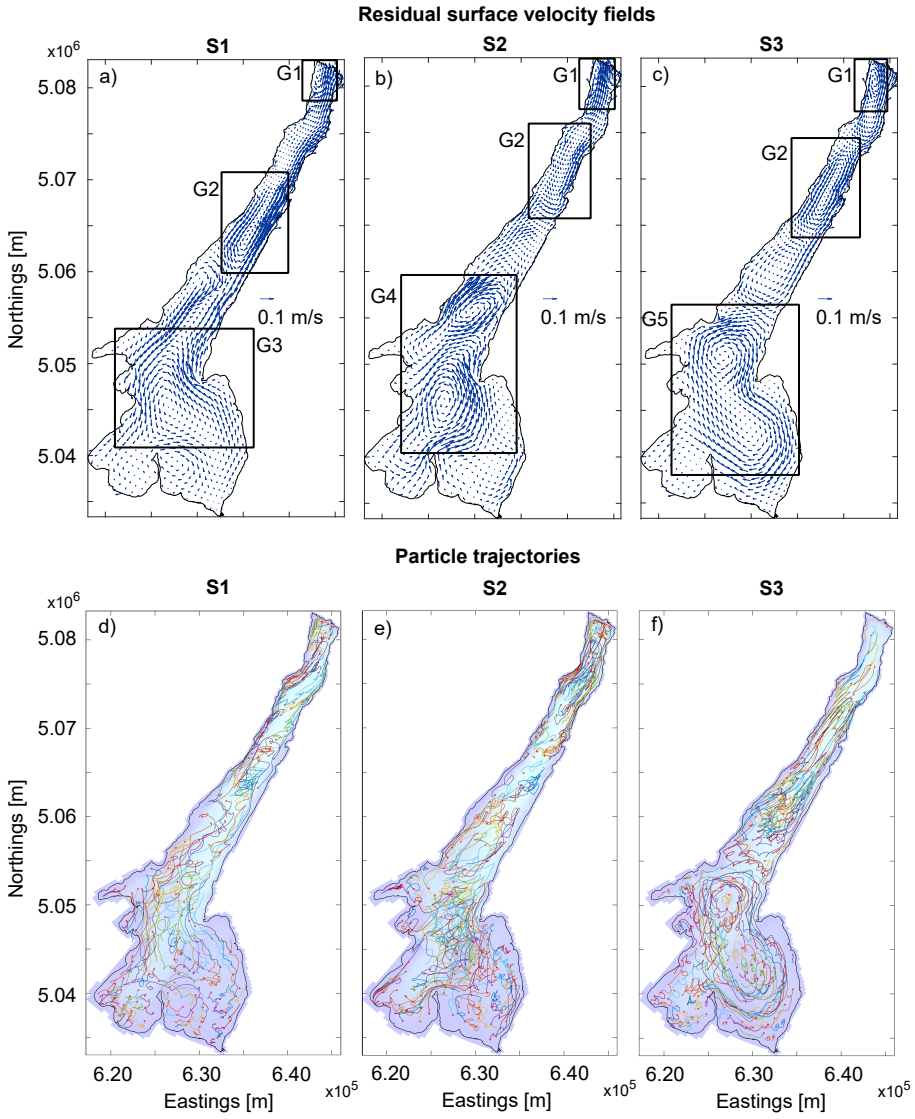

Figure 4.10: Horizontal transport in summer simulations. Top plots: residual surface currents from simulations S1 (a), S2 (b), S3 (c), obtained by a time average over day 3. Relevant gyre patterns are framed in boxes G1 - G5. Bottom plots: particle trajectories after two-day Lagrangian tracking in simulations S1 (d), S2 (e), S3 (f). Particle positions are computed through an average over 100 particles in release points and plotted at 15 minute intervals from the release time (00:00 of hydrodynamic simulation day 3) to the end of Lagrangian simulation (24:00 of hydrodynamic simulation day 4). Note: to ease the comprehension of the figure, 40% of the total number of trajectories are plotted after a random sampling.

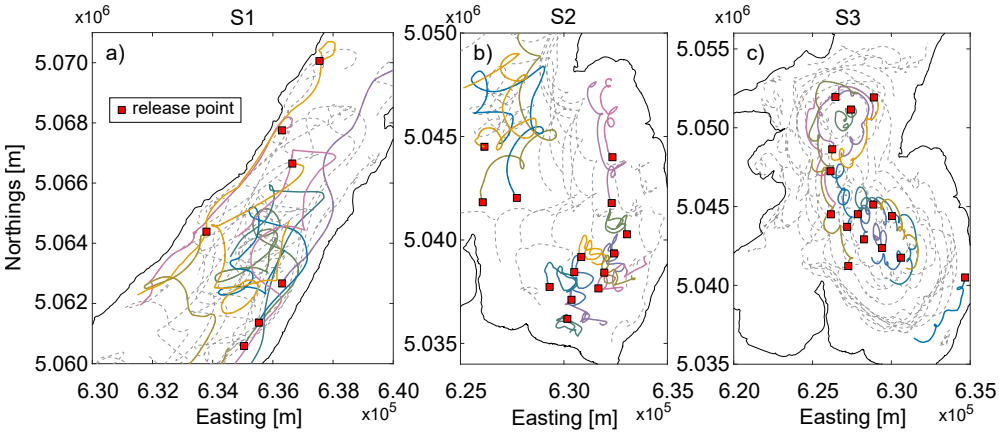

Figure 4.11: Details from Fig. 4.10 of Lagrangian trajectories in simulations S1 (a), S2 (b) and S3 (c). Continuous lines are drawn for the mean paths of selected releases and dotted lines for mean trajectories from neighbor releases. Red squares represent the starting points.

Geneva, Lemmin and D'Adamo 1997; Razmi et al. 2013).

In the narrow and elongated part of the lake, counterclockwise gyres develop: a small one close to the northern shore (G1) and a larger one in the central part of the lake (G2), with slightly different characteristics from one simulation to another. In scenarios S2 and S3 (Fig. 4.10b,c), G2 counterclockwise gyre looks longitudinally oriented and 10-km long, moving water northwards along the eastern shore close to Malcesine and southwards along the western shore near Limone. In S1 (Fig. 4.10a) the same circulation is detected, but its center is slightly shifted to the south. The Lagrangian trajectories (Fig. 4.10d-f) confirm a general gyre-like transport. A zoom from the S1 simulation (Fig. 4.11a) shows that particles released close to the shores are dragged by the surface flow and walk long distances (∼10 km) along the shore, whereas off-shore trajectories follow the residual counter-clockwise gyre, also oscillating at the inertial period (T_i = 16 h 45 min, with a Rossby radius R ranging between 200 m and 1 km, depending on the local velocity). This is consistent with typical near-/off-shore dynamics observed from drifters experiments during summer stratification [e.g., Rao and Murthy, 2001].

In the southern wider part of the lake, the residual surface circulation displays a strong variability. A single counterclockwise gyre develops in simulation S1 (Fig. 4.10a,c G3). A two-gyre circulation develops in simulation S2 (G4 in Fig. 4.10b,e), composed by a clockwise gyre in the central part and by a southern larger counterclockwise gyre, without involving particles released 3 km east of Sirmione (Fig. 4.11b). Finally, two clockwise gyres ensue in simulation S3

(G5 in Fig. 4.10c,f), connected through an eternal lemniscate-shaped circulation. No exchange occurs with the Desenzano Bay, where an additional small counterclockwise circulation develops. A more detailed analysis on Lagrangian tracks for the S3 simulation is proposed in Fig. 4.11c for a few particles involved in the two-gyre circulation. For these particles the alternate pattern of the wind (period of approximately 24 hours) interacts with inertial trajectories, making the interpretation of the whole dynamics more complex.

The greatest differences among summer simulations are detected in the southernmost part of the lake, where bathymetry likely dominates the response of the basin to an extremely variable wind forcing. In addition, inertial currents can develop in this part of the lake where low velocities occur ($U \sim 5$ cm s^{-1}) and consequently the Rossby radius is small ($R \sim 500$ m). Particles following inertial trajectories are those that are not involved in strong surface currents and those released where space is enough for such trajectories to develop. Similar patterns are not detected in the northern part of the lake, because of its narrow shape and the higher velocities (R up to ~ 1 km with an average surface velocity $U \sim 10$ cm s^{-1}). Instead, all summer simulations show a counterclockwise gyre (G2) under similar wind forcing in the northern part of the lake, consistently with its regular shape.

4.1.3 Discussion

4.1.3.1 Wind variability

The results of numerical simulations highlight that circulation patterns in Lake Garda can highly vary according to the spatial distribution and time variation of the wind forcing. It has been shown that the alternating direction of the breezes in summer (Fig. 4.10a-c) and winter days (Fig. 4.9a-c) produces gyre-like structures that cannot be captured using a uniform forcing, which in turns triggers unidirectional currents (Fig. 4.5a-c for winter Föhn simulations). An additional proof that the inhomogeneity of the wind field critically influences transport processes in Lake Garda comes from a summer simulation which was performed with the same setting as for scenario S3, but with a spatially uniform wind field. The results of this test are shown in Fig. 4.12: as it is clear from the residual flow field, in the case of a spatially uniform wind forcing the gyre structures are completely lost in residual surface circulations and Lagrangian tracks.

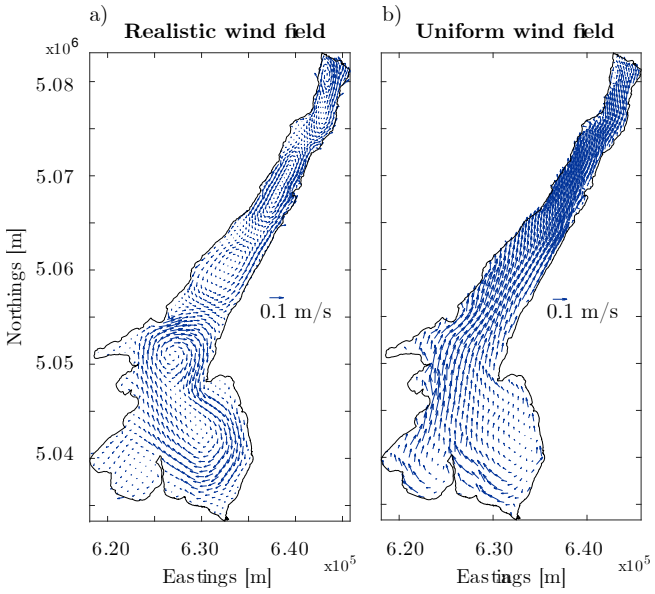

Figure 4.12: Residual surface currents from simulations S3 performed under a) realistic wind field (same as Fig. 4.10c) and b) uniform wind field. Wind forcing in b) is obtained from measured data at Torbole weather station on 18th of August 2012.

Even in the northern region where 'Peler' and 'Ora del Garda' breezes blow almost uniformly for some hours (see Fig. 4.3b,c for the spatial distribution of the mentioned breezes), gyres do not occur under the uniform wind forcing. This suggests that the transition from the northerly to the southerly breezes plays a key role in the development of complex residual patterns. Despite a uniform wind forcing has been widely found to be suitable for predicting some phenomena, internal wave motions amongst all [e.g., Laval et al., 2003], the spatial variability of the wind stress turns out to be fundamental in reproducing basin-scale cyclonic gyres in Lake Garda, which is consistent with what has been already observed by Strub and Powell [1986]; Lemmin and D'Adamo [1997]; Laval et al. [2005]. Such an external forcing was computed through an atmospheric model that was specifically set up for the study region [Giovannini et al., 2014b], in accordance with similar experiences in other lakes [e.g., Pan et al., 2002; Leon et al., 2007]. This approach is preferable in lakes located in perialpine regions where the spatial variability of the wind field is due to terrain complexities [Laiti et al., 2013a, 2014; Giovannini et al., 2015a, 2017], as Valerio et al. [2017] observed in Lake Iseo. The results presented here suggest that the interplay between lake and atmosphere dynamics should be taken into account also in the case of Lake Garda. In this regard, the improvement of more sophisticated, fully coupled simulations of lake processes by means of hydrodynamic and atmospheric models is a challenge for future

research work [e.g., Serafin et al., 2018].

4.1.3.2 Spin up time and scales of vertical diffusion of momentum

The order of magnitude of the outcoming residual velocity fields theoretically supports the definition of a spin up time of two days in the simulations. In Fig. 4.13, 4.14 and 4.15 the mean wind and surface current intensities are plotted from all simulated scenarios.

Describing the vertical momentum transport as a diffusive process in a shear flow, the shear stress τ_{xz} produced by the gradient of the horizontal x-velocity u along the vertical z-direction is evaluated assuming the usual Boussinesq closure:

$$\tau_{xz} = \rho \, \nu_z \frac{\partial u}{\partial z} \, . \tag{4.8}$$

An equivalent relationship holds for τ_{yz} in the other horizontal direction, y. Assuming that the wind shear is transmitted to the lower layers by means of turbulent viscosity, the vertical scale H_m of the turbulent momentum transport can be obtained from eq. (4.8):

$$H_m \simeq \frac{\rho \, \nu_z}{\tau} \, U \, , \tag{4.9}$$

where all variables are averaged over characteristic time and spatial scales, and U is a reference value of the surface velocity magnitude. The time scale of the diffusion process can be defined as:

$$T \simeq \frac{H_m^2}{\nu_{z0}} \, . \tag{4.10}$$

In winter simulations characterized by Föhn winds, the mean wind speed ~ 15 m s^{-1} produces a shear stress $\tau \sim 4 \times 10^{-1}$ Pa and induces velocities $U \sim 30$ cm s^{-1} at lake surface. Hence, the vertical scale of turbulent momentum transport is $H_m \sim 100$ m, due to the high vertical eddy viscosity ($\nu_z \sim 5 \times 10^{-2}$ m^2 s^{-1}) produced by the strong wind intensity. In summer simulations, the shear stress is smaller ($\tau \sim 1 \times 10^{-3}$ Pa) due to the lower wind intensity ($|\boldsymbol{U_w}| \sim 5$ m s^{-1}). Additionally, the vertical eddy viscosity is negatively influenced by thermal stratification ($\nu_z \sim 5\times 10^{-4}$ m^2 s^{-1}). Taking as a reference thickness of the surface layer H_m

the values of 10 m and 100 m for summer and winter simulations, respectively, and ν_z as the values of the vertical eddy viscosities ($\sim 5 \times 10^{-4}$ m^{2}s^{-1} and 5×10^{-2} m^{2}s^{-1}, respectively), the resulting time scale is of the order of two days in both cases.

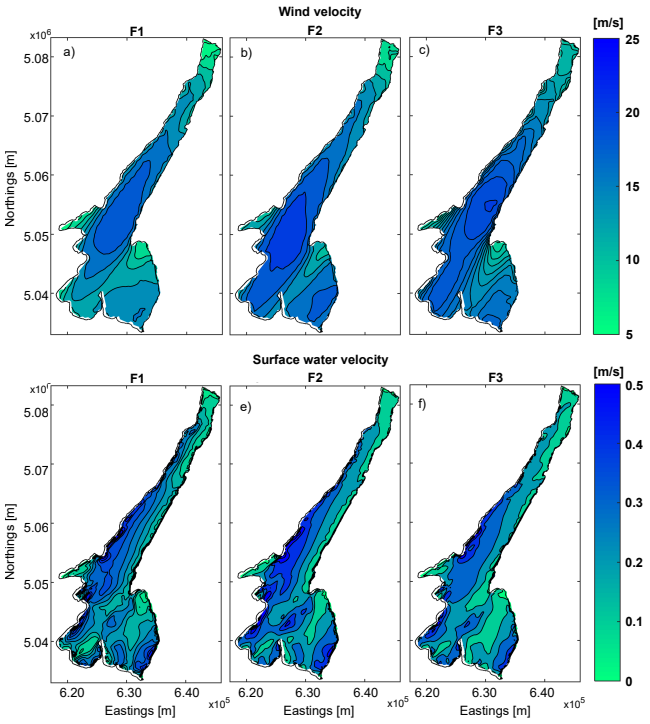

Figure 4.13: Mean wind (top plots) and surface current intensities (bottom plots) in winter Föhn simulations.

4.1.3.3 Lagrangian transport

The particle tracking simulations provide interesting elements to understand the transport processes in the lake, which could not be obtained by the residual circulations alone, especially in the case of alternate wind patterns. Additional tests of the summer scenario S3 were performed to exclude the influence of the starting time in the Lagrangian simulations (Fig. 4.16). If the release starts at a different time (i.e., 6 (b), 12 (c), or 18 (d) hours later than the original simulation (a)), the wind forcing can initially move the Lagrangian drifters in a opposite direction. Nevertheless, the final pattern of the released particles does not significantly differ from the results obtained in Fig. 4.10f (which is the same as in Fig. 4.16a), especially inside the largest gyres.

In other words, even though diurnal fluctuation of wind direction influence the instantaneous water transport, particles tracks reflect the mean flow field: inside the gyre structures, daily

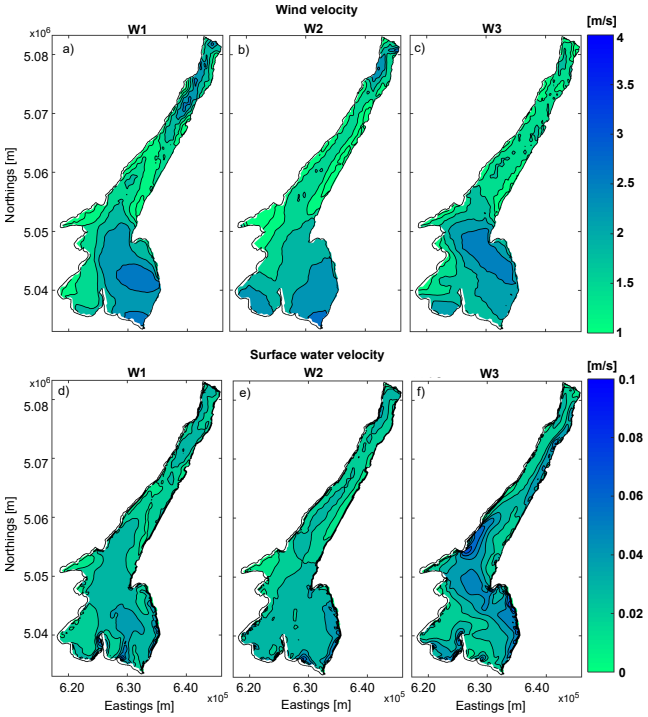

Figure 4.14: Mean wind (top plots) and surface current intensities (bottom plots) in winter ordinary breeze simulations.

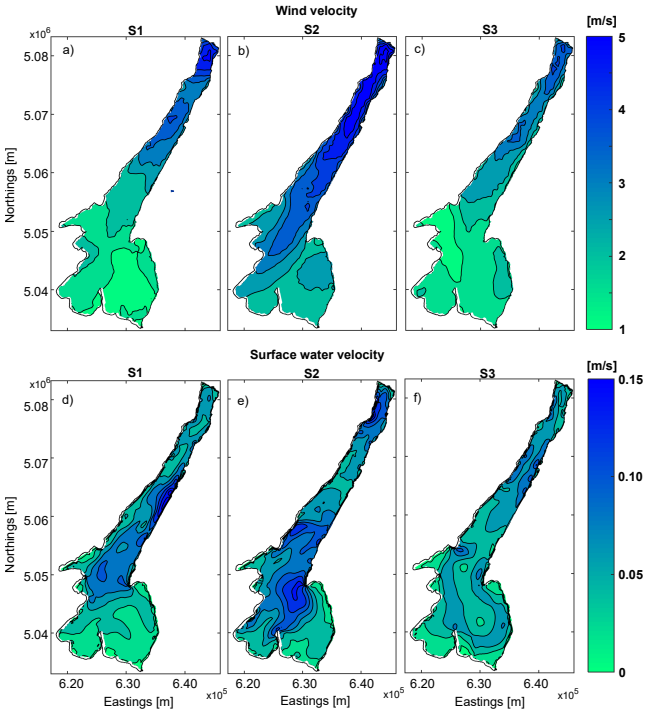

Figure 4.15: Mean wind (top plots) and surface current intensities (bottom plots) in summer simulations.

periodical trajectories develop, suggesting that instantaneous velocities are essentially driven by the alternating wind direction. Inertial trajectories are drawn in the southern part, where

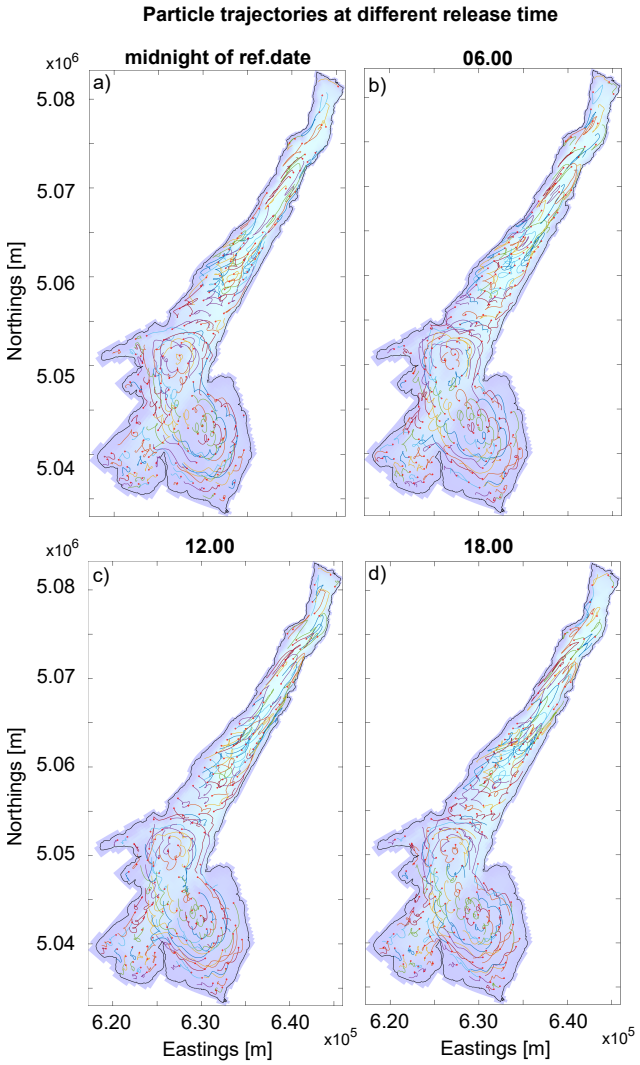

Figure 4.16: Particles trajectories after one-day Lagrangian tracking in simulation S3 at different release time: a) at 00:00 of hydrodynamic simulation day 3; b) at 06:00 of day 3; c) at 12:00 of day 3; d) at 18:00 of day 3; at 00:00 of day 4.

residual velocities are lower, but only where Rossby radii are smaller than the dimensions of the lake. Hence, Lagrangian trajectories confirm that the residual gyres shown in Figures 4.9 and 4.10 are not artifacts of the averaging procedure or sensitive to the timing of the Lagrangian simulations, but they are representative of the mean flow field, actually dragging the released particles in a swirling motion. In this regard, it is interesting to note that similar daily-averaged cyclonic circulations were also simulated by Pan et al. [2002] in Lake Kinneret and successively observed by Stocker and Imberger [2003] after the deployment of Lagrangian drifters.

Fig. 4.17 shows the statistical distribution (box plots) of horizontal and vertical distances

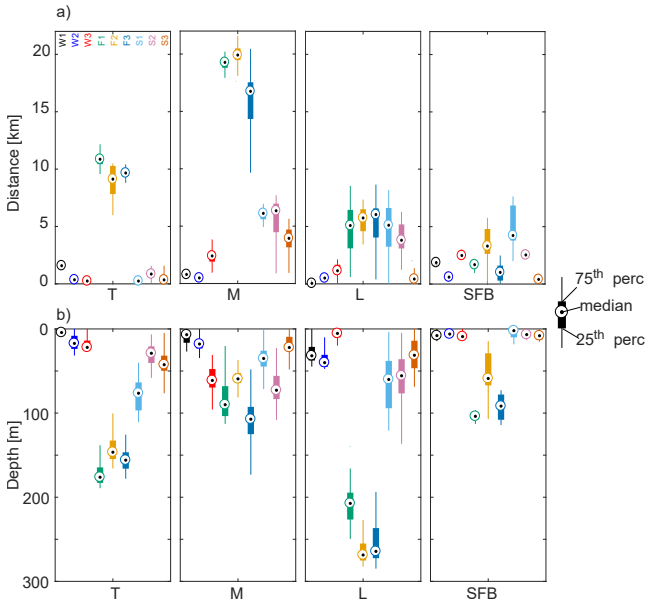

Figure 4.17: Statistics of (a) distances traveled after two days and (b) of time-averaged depths reached by particles in Lagrangian winter and summer simulations. Northern releases: Torbole (T), Malcesine (M), Limone (L); southern release: San Felice del Benaco (SFB).

spanned by the Lagrangian particles at the end of the two-day simulations.

Horizontal transport (Fig. 4.17a) is greater in winter Föhn scenarios due to the strength and persistence of the wind, as expected. North-eastern releases (i.e., Torbole and Malcesine) are transported ∼10-25 km, so that they can almost reach the lower end of the trunk region in two days. Conversely, a distance of less than 5 km is covered after two days for summer and winter typical breeze scenarios. As a general trend, the horizontal displacements in the northern trunk, where strong long-shore currents develop (under both the Föhn wind and the summer breezes 'Ora del Garda' and 'Peler'), are larger than those in the southern basin (San Felice sul Benaco), where gyres develop. This is consistent with the observations of Razmi et al. [2014] in Lake Geneva, who found that the residence time of simulated Lagrangian tracers are shorter for wind forcing aligned with the shoreline, eventually producing long-shore currents, and longer when wind is diverted from the longitudinal axis of the lake, with consequent gyre formation. Vertical displacements (Fig. 4.17b) in winter Föhn scenarios are related to downwelling phenomena produced by the Coriolis force along the western shore. In the northern trunk, particles released in Limone (to the right with respect to the wind direction) reach the largest depths, as horizontal movements are constrained within the bay, and downwelling processes are facilitated by the

steep shores and by the absence of thermal stratification. This is consistent with what Rao and Schwab [2007] summarized for Great Lakes, where the high wind speeds during winter-spring storms work together with nearly homogeneous temperature profile and topographic variability allowing for a deeper penetration of momentum into the water column and vertical transport, and eventually leading to resuspension events in the near-shore areas.

Under weak winter breezes a lower energy input comes from the wind, which is not unidirectional and does not drive a steady (longitudinal and transversal) circulation like in the previous case. As a result, vertical transport is significantly smaller, even though opposite trends found in eastern (Malcesine) and western (Limone) releases suggest the occurring of downwelling - upwelling processes. In the southern basin, particles released close to San Felice del Benaco are pulled down by the large-scale circulation moving surface water downwind (southwards), and deep water upwind (northwards).

In summer, vertical transport is smaller than that in winter because it is inhibited by the thermal stratification. In the northern part of the lake, where wind blows persistently for some hours, vertical displacements can be related to the combined effect of the coastal upwelling zone balancing along-shore wind stress, Coriolis force, and internal pressure gradients [Rao and Murthy, 2001]. In the southern part of the lake, where wind is less intense and with more variable direction, downwelling processes are prevented, and particles tend to stay in the surface layer (final depths less than 10 m).

4.1.3.4 Effects of Earth rotation

The effect of Earth rotation is clearly visible in winter conditions under a synoptic uniform wind, when a closed secondary circulation orthogonal to the wind direction develops in the northern trunk region of the lake. There, the response is as expected in an elongated, laterally confined lake: the strong wind blows southwards and produces downwelling along the western shore and upwelling along the eastern shore.

The effect of Coriolis force can also explain the development of the counterclockwise circulation pattern observed in the summer simulations. In fact, instantaneous surface currents follow the alternating direction induced by the ‘Peler’ and ‘Ora del Garda’ winds, but the Coriolis

force tends to accelerate the right (with respect to the wind direction) part of the flow field. This phenomenon is due to a rightward transfer of high-momentum surface water produced by the secondary Ekman-type circulation, while the upwelling of low-momentum water from deeper regions tends to decelerate the leftward part [Toffolon, 2013]. Hence, the counterclockwise gyre turns out as a residual outcome of the higher velocities close to the western shore during the northerly 'Peler' wind and the higher velocities at the eastern shore during the southerly 'Ora del Garda' wind. A similar phenomenon can be observed also in the winter breeze cases.

In order to verify that the two mentioned processes can be ascribed to the rotation of the Earth, additional tests have been performed running the simulations with opposite latitude (i.e. placing Lake Garda in the southern hemisphere). In winter Föhn test simulations the secondary circulation in the transversal cross section CT1 (Fig. 4.18a) moves water in the opposite direction, with downwelling occurring along the eastern shore and upwelling along the western one, since Coriolis force deviates the flow to the left in the southern hemisphere.

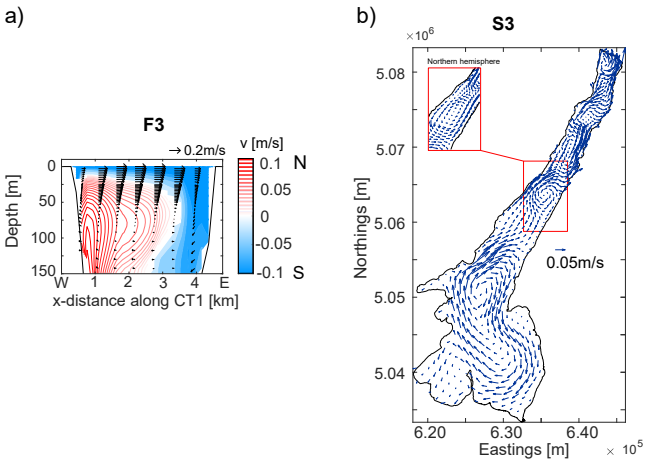

Figure 4.18: a) Residual cross-section circulation in the northern transverse section CT1 from winter F3 simulation and b) surface circulation in summer S3 simulation performed at the opposite latitude.

In summer test simulations the surface gyres developing in the central part of the northern trunk are now clockwise (Fig. 4.18b), as the Earth rotation now accelerates the left part of the flow field. Interestingly, both secondary circulations and surface gyre in the southern part of the lake seem not to be affected by the change in latitude, suggesting that the complex topography and the shallower bathymetry have much more effect than Earth rotation on the flow field.

4.1.3.5 Ekman transport

The amount of water transported in the northern part of the lake by the Ekman transport can be quantified both in winter and summer. For winter Föhn simulations, the volume of water pulled down close to the shore (i.e., the downwelling) is reasonably the same as the volume moved westward on the surface (i.e., the Ekman-type transport, here computed according to eq. (4.7)), because the secondary circulation is approximately closed in a transverse cross-section of the trunk region. In this case the lateral transport Q_x (assumed positive in the westward direction) is computed from the surface to a depth of 70 m, where the sign of the transversal velocity changes, identifying the center of the secondary circulation.

On the other hand, when the wind forcing is spatially and temporally varying (breeze scenarios in winter and summer conditions), the computation of the Ekman transport is more challenging because the secondary circulation is not uniformly developed along the northern part of the lake. Based on the results of the hydrodynamic simulations, the lateral transport Q_x is computed numerically according to eq. (4.7) across the longitudinal section CL over the first 20-30 m (corresponding to the thickness of the surface layer where velocities are significant).

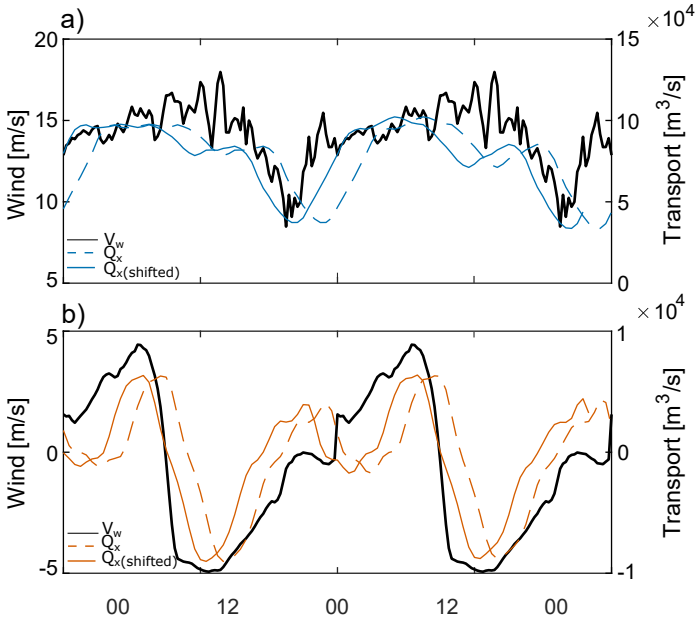

Figure 4.19: Time series of longitudinal wind component V_w (black line), averaged along CL, and total lateral transport Q_x (colored lines: dotted for the actual transport, continuous for delayed) for simulation F3 (a, z_x=70 m, delay = 3 hours) and S3 (b, z_x=20 m, delay = 1.5 hours). Positive sign stands for southward wind intensity and westward transport.

In Fig. 4.19, the temporal variability of Q_x is compared with the wind velocity V_w for the third and the fourth day of simulations F3 (a), and S3(b). The wind velocity V_w is computed as an average of the along-axis component of the wind blowing above the CL section. The longitudinal component of the wind is well correlated with the lateral transport across the cross-section CL, which is orthogonal to the wind forcing and assumed to be produced by the Coriolis force. The positive sign stands for southward direction of wind speed and for westward transport of water mass. In the case of strong Föhn wind (Fig. 4.19a), V_y and Q_x keep the same direction, with a temporal shift due to the delay in the response of the lake to a sudden change of the forcing (dotted blue line). By maximizing the cross-correlation, a delay of ~ 3 hours has been quantified in simulation F3 (continuous blue line). In the summer case (Fig. 4.19b), the changes in wind direction (southward in the morning, northward in the afternoon, i.e. positive and negative respectively) are reflected in the sign variation of lateral transport (westward in the morning and eastward in the afternoon). Maximum cross-correlation between the two trends suggests a delay ~ 1.5 hour in simulation S3 (continuous and dotted orange lines).

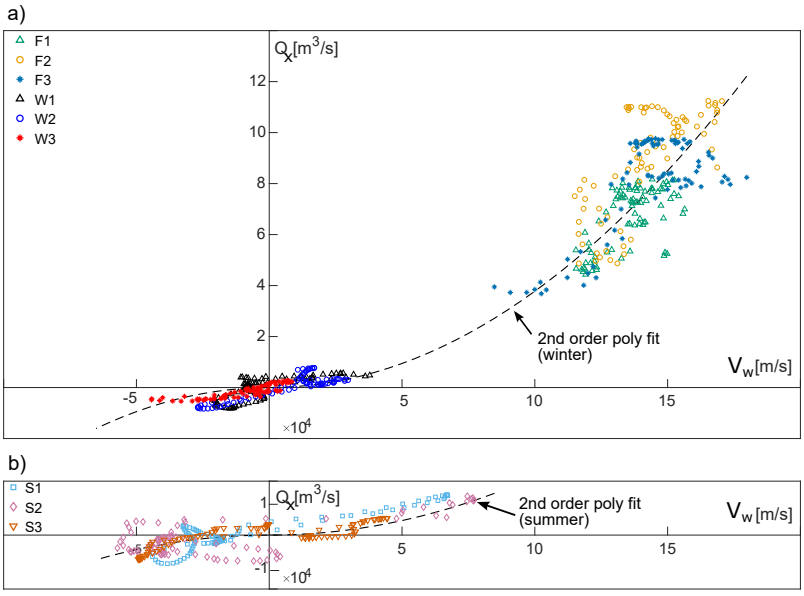

Figure 4.20: Lateral transport versus wind speed in all simulations: (a) winter Föhn (F1, F2, F3; z_x=70 m) and typical breezes (W1, W2, W3; z_x=20 m, delay = 3 hours); (b) summer breezes (S1, S2, S3; z_x=20 m, delay = 1.5 hours). Dotted lines represent quadratic fitting between wind and transport. Positive sign stands for southward wind intensity and westward transport.

The lateral transport is plotted as a function of wind speed (accounting for the estimated time lag) in Fig. 4.20. Despite some scatter, the quadratic dependence suggested by eq. (4.6)

is approximately found both in winter (Fig. 4.20a) and in summer simulations (Fig. 4.20b). The proportionality coefficient is different in the two cases, as it is reasonable because of the different conditions (stratification, vertical eddy viscosity, etc.). Thus, Q_x turns out to lag behind the theoretical dependence (Eq. (4.6)), which is based on the assumption of instantaneous adaptation to the wind forcing and does not account for the water mass inertia. Scatter and hysteretic paths are still visible in summer simulations, which can be easily ascribed to the alternating wind direction. Numerical results show that the amount of water transported in the direction orthogonal to the wind is huge in winter Föhn days ($Q_x \sim 8 \times 10^4$ m^{3}s^{-1}, eventually producing a significant downwelling along the western shore), and smaller in winter and summer typical breeze days ($Q_x \sim 1 \times 10^4$ m^{3}s^{-1}).

4.1.4 Conclusions

In this section we used a three-dimensional hydrodynamic model (Delft3D) to simulate the typical seasonal circulation associated with realistic wind fields provided by an atmospheric model (WRF). To characterize the lake response to the external forcing, different thermal stratification conditions (from *in-situ* measurements) and typical space- and time-varying wind patterns (from WRF simulations) were considered to obtain the Eulerian residual (i.e., time-averaged) circulations and the Lagrangian tracks. The analysis highlighted novel aspects of lake hydrodynamics that can likely be generalized also to other similar contexts. In particular two main aspects were highlighted.

First, under almost uniform and long-lasting synoptic Föhn winds, winter thermal conditions appear to ease upwelling and downwelling phenomena along the lateral shores of the deep and elongated northern region. The phenomenon can be interpreted as an Ekman-type transport controlled by the effect of Earth rotation, and the lateral transport can be correlated to the square of the wind speed after accounting for a delay due to the water mass inertia. Similar relationships are expected to be found also in other elongated perialpine and fjord-like lakes, although further analyses are required to get evidence for generally valid conclusions.

Second, the alternating direction of the typical diurnal summer breezes, interacting with the Coriolis force, drives the development of more complex circulation throughout the lake. In

particular, the observed counterclockwise gyre in the northern trunk region can be explained as an effect of the Coriolis force tending to accelerate the right part of the flow field. In terms of the residual circulation, this mechanism produces a northward prevalence along the eastern shore, and a southward prevalence along the western shore. Analogous counterclockwise patterns are found also in the winter breeze scenarios, suggesting that the mountain-valley dynamics, dominating the wind diurnal cycle, might be responsible of persistent residual surface currents.

We stress that in this section we gave a preliminary description the hydrodynamics of Lake Garda. While the unavailability of hydrodynamic measurements in the case study did not allow for designing a sophisticated predictive modelling tool, here we provide a first-order characterization of the physical processes occurring in the lake. Additionally, the modeling exercise presented here resulted to be an effective preparatory step, providing useful insights and directions to plan field activities. We suggest that this kind of modeling exercise could be performed also in other lakes where nothing is known about hydrodynamics-In fact, it can provide useful background information for the optimal planning of field campaigns, but also insights for local agencies in charge of lake monitoring.

4.2 Characterization of surface transport patterns by integrating local knowledge and numerical modeling

The efforts of the scientific community towards promoting public participation is increasing in all research fields. The potential of involving citizens in research projects is in fact evident. Experiences of this kind range from data collection to the dissemination of scientific knowledge and good practices, which are then translated into changes in attitudes from both scientists and people [Hecker et al., 2018]. As this becomes clearer, initiatives oriented towards public engagement flourish under the wide hat of 'Citizen Science' projects. In the research field of fresh water resources, important work has been done under such a perspective, with many virtuous examples of citizen science data collection and public engagement [we refer to Conrad and Hilchey, 2011; Buytaert et al., 2014; Paul et al., 2018, as extensive reviews on the topic].

Most frequently, the community is involved in collecting information for scientists in a one-way (and top-down) direction, under a 'crowdsourcing' [Paul et al., 2018] or 'collaborative' [Follett and Strezov, 2015; Hecker et al., 2018] approach. In these experiments, citizens are trained on the protocols and are provided with the proper instruments, such as sensors [e.g. Canfield et al., 2002; Lottig et al., 2014; Pohle et al., 2019; Weyhenmeyer et al., 2017] or smartphone applications [e.g. L. S. and Fienen, 2013; Kampf et al., 2018]. The result is a huge amount of data for scientists, who investigate their own research interests and sometimes give back useful guidelines to the community.

Less frequently, the community is called to share its own knowledge with scientists and define what deserves to be investigated. This 'participatory' method engages the citizens at all the scientific investigation stages [Follett and Strezov, 2015]: first, in defining the research questions according to their needs and, second, in providing the answers and the solutions. In this way, citizens bring different points of view and incorporate their everyday life experience in the research process [Hecker et al., 2018]. In this regard, local knowledge can be a source of rich and diverse information and an effective way for involving local communities and establishing a two-way communication on research topics.

According to the traditional definition by Warburton and Martin [1999], the term 'Local

Knowledge' defines the 'system of concepts, beliefs and perceptions that people hold about the world around them'. Due to its dynamic and subjective nature, the consistency and reliability of data collected via local knowledge harvesting can be difficult to achieve and represents one of the major challenges of its usage [Huntington, 2000; Davis and Wagner, 2003; Danielsen et al., 2018]. Nevertheless, some experiences in lake [e.g., Calheiros et al., 2000; Schlacher et al., 2010; Laborde et al., 2012], river [e.g., Hallwass et al., 2013; Scapini Sobczak et al., 2013] and climate [e.g., Klein et al., 2014] applications showed the potential of incorporating local knowledge from citizens when investigating physical and ecological processes. This approach can provide a valuable source of qualitative data, especially in those cases where a lack of scientific knowledge is counterbalanced by an active presence of the local community [Schlacher et al., 2010].

This is the context of Lake Garda, as a worldwide popular destination for wind and water sports (e.g., sailing, wind and kite surfing, scuba diving etc.). Here, sportsmen and local users own a deep, although anecdotal, knowledge of the natural phenomena. In this section, we propose a first attempt towards a virtuous cycle between the involvement of local communities and scientific research in Lake Garda. The qualitative description of winds, currents and transport dynamics provided by lake users are here combined with the results of hydrodynamic simulations and explained. In consistency with the dual nature of our methodology, the expected output of our investigation is twofold: on the one hand we aim at improving our understanding of the lake hydrodynamics and gathering new ideas of exploration; on the other, we aim at building a bridge between the local community and the academia by interpreting the local knowledge through the lens of the scientific method.

4.2.1 Methods

To the aims of this study, we report in Fig. 4.21 the map of Lake Garda with some specific points that resulted to be key location during the interviews. The points are named as increasing numbers in counter-clockwise order starting from the north-western border with the execption of the inflows (SR for Sarca River, AG for Adige Garda gallery) and outflows (MR Mincio River).

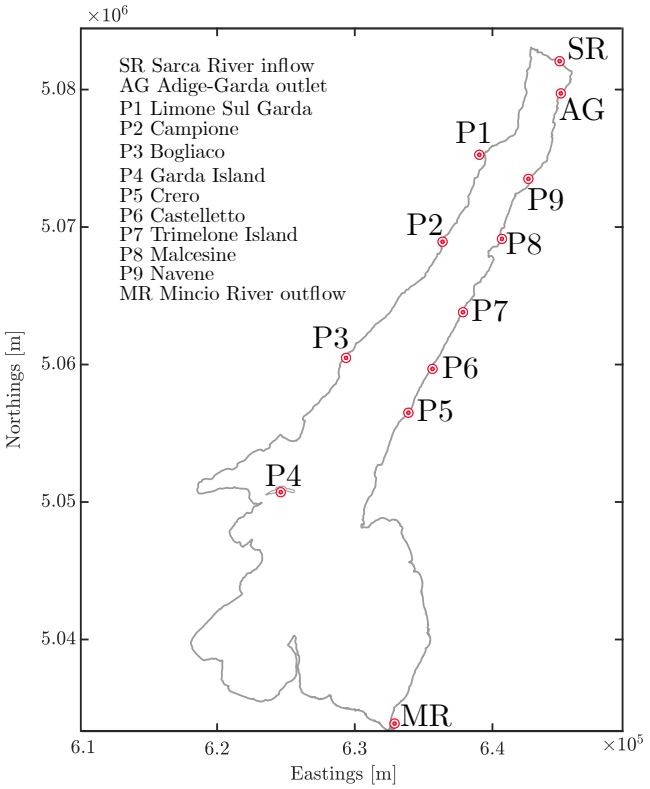

Figure 4.21: Map of Lake Garda with the relevant locations for Local Knowledge experiment.

4.2.1.1 Local knowledge collection

Evaluating the contribution of local knowledge in a scientific research is not that different from the collection, analysis and interpretation of quantitative data. In Fig. 4.22 the workflow for data collection and analysis is presented.

As a first step, we selected the potential owners of local knowledge and we listed the possible physical processes they might be aware of/expert of. We identified several people living or working in the lake region as potential knowledge bearers: fishermen, ferry boat drivers, officers of the environmental protection agency of the Autonomous Province of Trento, the firefighters nautical rescue team of Trento, sporting clubs instructors, employees and volunteers. Moreover, we included also sportsmen (e.g. sailors, surfers, scuba-divers) who choose the lake every year for practising, competing, or just as holiday destination. Hence, in this case study, local knowledge is not owned exclusively by the local community (in the sense of 'Traditional Knowledge' [Schlacher et al., 2010]), but it is embedded in practices and experience held by all those who interact with

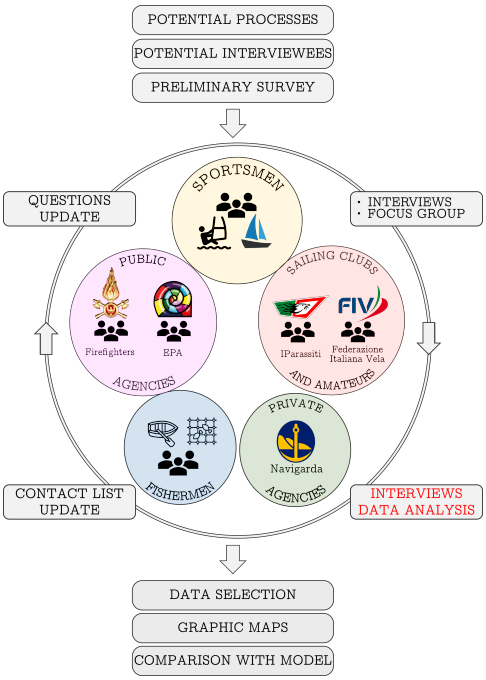

Figure 4.22: Methodology of local knowledge collection.

the lake with any objective and interest. Since most of the people of this community approach the lake on its surface (except for scuba divers), three main categories of surface processes were investigated: winds, currents and transport dynamics, including extreme events such as floods, storms and nautical accidents.

As a second step, a preliminary set of questions was prepared according to the expected knowledge of the interviewees. The was to first testing the reliability of the witnesses on well-known processes and then identifying recurrent surface patterns. The survey took place between October 2017 and December 2017 and was organized in individual interviews and in focus groups[2].

In Tab. 4.3 the number of participants in our survey is reported for each category, together with the interview method adopted and the main interests of the interviewees. A total number of 19 people were interviewed. Fishermen, wind-surfers, ferry boat drivers, and sailors were target of individual interviews. Differently, the firefighters nautical rescue team and the EPA officers

[2]The *focus group* is a group interview method for gathering qualitative information from an ensemble of people which is considered representative of a certain category (e.g., demographic, market preferences). It was initially proposed by Merton et al. [1957] for testing the response of the audience to war propaganda radio programs in USA during World War II [Kitzinger, 1995].

Category	Interview method	Main interests	Number of participants
Windsurfers	individual	wind and flow field	5
Sailors	individual	wind and flow field	4
Fishermen	individual	surface transport, exceptional events	3
Ferry boat driver	individual	surface transport, exceptional events	1
Firefighters	focus group	surface transport, exceptional events, vertical currents	3
EPA officers	focus group	surface transport, exceptional events, water quality	3

Table 4.3: Categories of interviewees, interview method, main interests and number of participants in the survey.

were asked to participate to focus groups. During the individual interviews, interviewees were asked to answer to a codified number of questions. We started from the general perception and belief of the lake environment, and then we went deeper into specific topics, according to the personal experience of the interviewees. Differently, in focus groups, the interviewer acted like a moderator in the discussion between the members of the group. They were encouraged to talk to one another on specific topics, both influencing each other during the discussion and exchanging ideas and anecdotes. As an example, firefighters were asked to tell about some rescue operations (e.g., the search for missing divers, a boat capsizing and the subsequent recovery), comment on each others version of these events and finally agree on what was their common experience.

The data gathered during the preliminary survey were analyzed for internal consistency. Once unreliable witnesses and contradictory information were excluded, we added new questions and we updated the contact lists. In fact, during the interviews interesting and unexpected information arose, as well as suggestions for additional people to get in touch with. Finally, data were translated into qualitative maps summarizing the most relevant processes in terms of winds, surface currents and event-based transport dynamics. Here we will present only the results on hydrodynamic processes taking place at the lake surface, for which little knowledge is available compared to wind patterns [Giovannini et al., 2017].

4.2.1.2 Models setup

Atmospheric-hydrodynamic model The results of the local knowledge survey were used for new exploration with our one-way coupled atmospheric-hydrodynamic model of Lake Garda. Most of the episodes reported by the interviewees were related to the summer season of the year 2017. For this reason, the period of August 2017 was chosen for numerical simulations.

For an exhaustive description of the models settings we refer to the previous Chapter 3 and to Piccolroaz et al. [2019] (see also Chapter 5), where the dynamics of three periods, including August 2017, were analyzed and compared to in-situ temperature measurements.

Simplified Lagrangian model A simple Lagrangian model was developed to reconstruct the trajectory of semi-submerged floating objects in the lake surface (chunks of wood, boats, floating debris etc.). The model is based on the integration of the differential system

$$\frac{d\boldsymbol{x}_p}{dt} = \boldsymbol{v}_p \,, \tag{4.11}$$

$$m_p \frac{d\boldsymbol{v_p}}{dt} = \sum \boldsymbol{F}_{ext} \,, \tag{4.12}$$

where t is time, m_p is the mass of the object, $\mathbf{x}_p$ is the vector denoting its position on the lake surface, $\mathbf{v}_p$ its horizontal velocity, $\sum \mathbf{F}_{ext}$ is the sum of the external horizontal forces acting on the object.

Classical formulations exist for the motion of inertial objects immersed in a homogeneous viscous fluid in unsteady and non-uniform flow conditions [Kundu and Cohen, 2002; Loth and Dorgan, 2009; Beron-Vera et al., 2019]. Such formulations typically take into account several contributions to the external forces:

1. the drag force, caused by the pressure forces and the viscous forces due to velocity gradients between the fluid and the object;
2. the 'added mass' force, which takes into account the inertia of the fluid surrounding the object;
3. the lift force, generated by the object rotation in a fluid shear;
4. the force exterted by waves.

Oceanic applications on drifting particles commonly simplify the system of forces to the drag force only [Daniel et al., 2002; Breivik and Allen, 2008; Röhrs et al., 2012; Nesterov, 2018]. Such an assumption is normally justified by assuming locally uniform and steady state flow field, and by considering the particle size much smaller than both flow field and wavelength scales. In our

case, the characteristic dimensions of chunks of wood, boats and fishing nets are smaller than the hydrodynamic model grid size ($\sim$ 100 m). This suggests that we can assume the flow field as uniform for the duration of a model timestep in the grid cell where the object is locally found.

We distinguish the quasi-steady drag force into two contributions: F_s, acting on the submerged part of the particle due to the surface flow velocity, and F_e, which acts on the emerged part of the particle, i.e., the wind drag. According to these assumptions, Eq. 4.12 can be written as follows:

$$m_p \frac{d\boldsymbol{v_p}}{dt} = \boldsymbol{F}_s + \boldsymbol{F}_e \,, \tag{4.13}$$

In the absence of detailed information on the shape of the body, the object is idealized as a sphere. Hence we defined a radius of the sphere r_p and the submerged volume fraction $f_s = V_s/V_{tot}$, where V_{tot} is the total volume. For the analysis of small objects (e.g., chunks and flood debris) we chose $r_p = 1$ m and $f_s = 1$ (i.e., fully submerged object). These simulations aimed at following the surface flow field and gathering information of the general transport pattern, rather than simulating the small-scale drifting dynamics of specific objects. For the second test-case, where the timing and the development of the boat's trajectory was under investigation, the representation of the boat as a sphere was clearly simplistic. However, given the complexity of defining a simple shape for the boat, especially in its capsized condition, we decided to keep the spheric version of the drifter and to test different values of r_p and of f_s. We eventually chose $r_p = 2$ m and $f_s = 0.6$. The results of this Lagrangian simulation will be interpreted being aware of the limitations of the model.

In both configurations, the mass of the floating object is computed as:

$$m_p = \rho_w V_s \,, \tag{4.14}$$

as a result of the vertical balance between the buoyant force applied to the submerged object and its weight, where ρ_w is the water density. The drag force in turbulent flows depends on the square of the relative velocity of the fluid (i.e., the difference between water/air velocity and the

particle velocity) and on two drag coefficients $C_{d,s}$ and $C_{d,e}$:

$$\mathbf{F}_s = \frac{1}{2}\rho_w \, A_s \, C_{d,s} \, (\mathbf{v}_w - \mathbf{v}_p) \, |\mathbf{v}_w - \mathbf{v}_p| \; , \tag{4.15}$$

$$\mathbf{F}_e = \frac{1}{2}\rho_a \, A_e \, C_{d,e} \, (\mathbf{v}_a - \mathbf{v}_p) \, |\mathbf{v}_a - \mathbf{v}_p| \; , \tag{4.16}$$

where ρ_a is the air density, $\mathbf{v}_w$ and $\mathbf{v}_a$ the water and air velocity vectors, respectively, A_s and A_e the frontal areas of the submerged and emerged parts of the object. Air velocity $\mathbf{v}_a$ at the water surface is computed from wind speed at 10 m a.s.l. by assuming a logarithmic law (we assumed a roughness length of 1 cm). The actual value of the drag coefficients depends the Reynolds number of the object subject to the fluid f_s, either being water (w) for the submerged part or air (a) for the emerged part:

$$Re_{p,f} = \frac{2 \; r_p \, |\mathbf{v}_p - \mathbf{v}_f|}{\nu_f} \, , \tag{4.17}$$

where ν_f is the fluid cinematic viscosity ($\nu_a \sim 10^{-5}$ m^2 s^{-1}, $\nu_w \sim 10^{-6}$ m^2 s^{-1}). In the simulated scenarios, the value of $Re_{p,f}$ is $\sim 10^4 - 10^6$ for both fluids, as the different order of magnitude of the relative velocities ($\sim$ 1 - 10 m s^{-1} for air, $\sim 10^{-2}$ - 10^{-1} m s^{-1} for water) counterbalances the differences in kinematic viscosity. With the value of the drag coefficient varying from 0.1 to 0.5 in this range [Kundu and Cohen, 2002], and considering the uncertainties in the geometrical description of the object, we assumed a uniform value $C_{d,s} = C_{d,e} \simeq 0.2$.

The system (4.11)-(4.13) has been integrated using an implicit Euler numerical scheme, implemented by linearizing the velocity difference in the computation of the drag forces.

Two setups of the particle tracking model were used, according to the aim of the analysis:

1. Assuming water particles as floating but fully submerged, not subject to wind drag but only to surface water flow. Idealized spherical particles of 1 m radius were released at different times of the day and their trajectories were traced by taking into account the effect of the surface water velocity only.

2. Assuming particles as floating and partially submerged, thus being subject to both water flow and wind drag, in order to reproduce the trajectory of a boat after capsizing. In this

case, particles were represented as partially submerged spheres of 2 m radius.

4.2.2 Results

4.2.2.1 Qualitative patterns derived from interviews

The local knowledge survey provided a wide range of data, from wind to lake thermal dynamics (spatial gradients, vertical stratification), including surface flow field and transport processes during exceptional events. In the following sections we will focus on surface currents and transport dynamics.

Fig. 4.23presents the qualitative maps extracted from the interviews in three categories: surface currents (Fig. 4.23a), recurring transport patterns (Fig. 4.23b,c) and a boat capsizing accident (Fig. 4.23d).

Surface flow field The overview of recurring flow patterns was provided by surfers and sailors limited to the summer period, when water sports are mostly played. Fig. 4.23a summarizes the surface currents indicated by most of interviewees (continuous line arrows) or by just some of them (dashed line arrow).

A strong flow in the central part of the high lake, from north to south, was described by all interviewees in the morning, when northerly wind blow. The extension of such a current was not coherent amongst all interviewees: in fact, while most of the sportsmen detected the beginning of the central current close to Limone (P1 in Fig. 4.23a, black continuous arrow), some others suggested that the flow is accelerated further south, near Castelletto (P6, light blue dashed arrow), and only one interviewee indicated that it starts from the northern shore, near the Sarca river mouth (SR, green dashed arrow), with a serpentine trajectory.

All interviewees confirmed the presence of a strong current moving water from south to north (continuous red arrow) along the eastern shore of the lake and named 'Corif'[3]. According to the interviewees, such current usually develops from late morning until the afternoon and often after storm wind events, when they last more than one day. Such intense flow is described as starting

[3]The name 'Corif' comes from a local dialect version of the old italian adjective "corrivo", once used to describe running waters

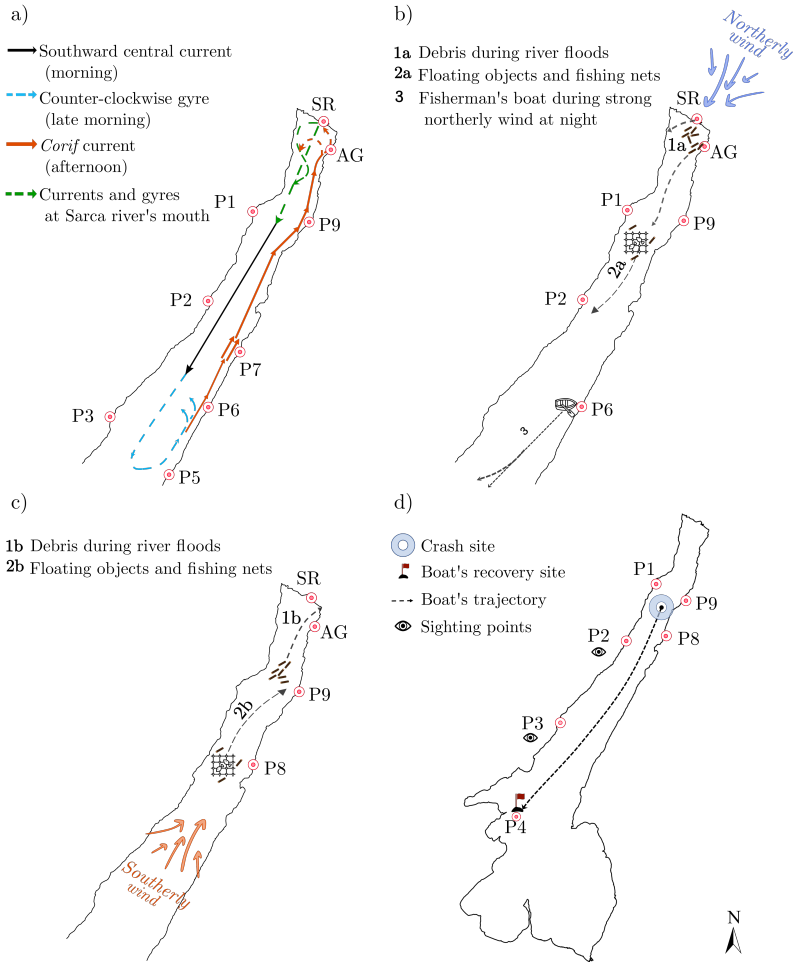

Figure 4.23: Qualitative maps summarizing data from interviews. (a) surface currents , (b) transport patterns under northerly wind and (c) southerly wind, (d) firefighters reconstruction of boat overturn on 6-8 August 2017.

near Crero (P5), accelerating northerly along the shoreline and reaching its maximum velocity between the coast and the Trimelone island (P7). In addition, some interviewees detected a counterclockwise gyre in the central part of the lake (north of P5, light blue dashed arrows), where the 'Corif' begins. One more whirling current was reported at the northern border of the lake, at the end of 'Corif' (from AG to SR, red dashed arrow), reconnecting with the presumed current induced by Sarca river inflow (green dashed arrow).

Surface transport The most relevant evidence on objects transportation on the lake surface were provided by fishermen, EPA officers, ferry boat drivers and by a wood carrier. All of them agreed on the typical trajectories of fishing nets, boats and chunks of wood. In Fig. 4.23b and c, the typical trajectories of such floating objects are summarized in two typical wind configuration in a summer day: under northerly wind (night and morning) and southerly wind (late morning and afternoon).

The EPA officers described the typical transport patterns of the woody and plant debris from river Sarca floods and the path of the turbid water flushed by the Adige-Garda gallery openings. According to them, in presence of northerly winds such materials flowed from the mouths of the river (SR) and of the tunnel (AG), and moved south-west towards the western shore of the lake (trajectory 1a). Then, in the afternoon, when the wind reverses its direction and the 'Ora del Garda' breeze rises, the same objects were dragged back to the starting point, or accumulated in small bays along the eastern shore (trajectory 1b Fig. 4.23c). Similarily, according to other interviewees, fishing nets and chunks of wood in the central part of the high lake, south of Malcesine (P8), tend to be deviated towards the west when wind blows from the north (during the night and in the morning, trajectory 2a in Fig. 4.23b), and to the east when wind blows from the south (in the afternoon, trajectory 2b in Fig. 4.23c). Specifically, a fisherman living near Castelletto, along the eastern coast (P6), told that during stormy nights his boat used to break loose from its mooring and to be transported out into the lake by northerly winds (trajectory 3). Then, according to his witness, he usually recovered the boat after some hours along the western coast.

Boat capsizing accident The focus group with the firefighters nautical rescue team provided a detailed description of one rescue operation involving a boat (with two people on board) on 6 August 2017, when a violent storm battered the lake. According to local newspapers[4] and the firefighters rescue team, the boat was sailing offshore and was capsized in early afternoon somewhere off the coast between Navene (P9), Limone (P1) and Malcesine (P8). The firefighters reached the crashsite around 14:15 and saw the boat capsized, they moored it to two racing buoys (to prevent it from sinking) and searched one of the two people who was still missing. Other witnesses added that the keel of the boat was successively seen off the coast of Campione (P2), lately at Bogliaco (P3), and after two days it was recovered near the Garda Island. The presumed trajectory of the boat is described in Fig. 4.23d.

4.2.2.2 Comparison with simulations

The numerical simulation of the whole month of August 2017 provided a reasonable time window where all the processes described by the interviewees could be investigated. In this section, the results of the numerical simulations are presented and qualitatively compared with the information gathered via local knowledge harvesting.

Surface flow field The most reliable information gathered about the surface flow field in summer season (Fig. 4.23a) are:

1. the development of a central current in the early morning from north (off of P1) to south;
2. the existence of the 'Corif' current towards north along the eastern shore (P6-P7), mostly developing in late morning and in the afternoon after storms;
3. the development of a counterclockwise gyre in the central part of the northern trunk in late morning/afternoon, after the onset of southerly winds, near P5;
4. the development of a counterclockwise gyre at the northern border of the high lake (AG to SR) as the final part of the 'Corif', in the afternoon.

[4]https://www.larena.it/territori/garda-baldo/recuperata-la-barca-del-bolzaninoannegato-domenica-al-largo-di-navene-1.5889961; http://www.altoadige.it/cronaca/bolzano/si-rovescia-con-la-barca-altoatesino-disperso-nel-lago-di-garda-1.1313167; http://www.veronasera.it/cronaca/barca-rovescia-salvataggio-pompieri-disperso-ricerca-navene-lago-6-agosto-2017-.html

5. a serpentine flow near the Sarca river mouth due to the river inflow. No details on the time of such current onset were provided.

The summertime surface circulation reconstructed through the numerical simulations was compared with the experience of local people at different times of the day. In Fig. 4.24, three snapshots of the early morning (a-b), late morning (c-d) and afternoon (e-f) are presented in order to compare the wind (left plots) and the water flow (right plots) modelled fields.

Fig. 4.24b shows that during the night and early morning, the flow is stronger in the central part of the northern trunk close to P1, as reported by the interviewees. The development of such a current, moving a large amount of water from northeast to southwest, is strictly correlated with the northerly 'Peler' breeze (Fig. 4.24a). This breeze starts blowing during the night until late morning and is channeled by the steep orography around the lake, with an acceleration in the central part.

A few hours later, at 10:00, both wind and flow direction starts being reverted, with a front coming from south, likely coherent with the onset of the 'Corif' current (Fig. 4.24d). The flow direction overturn is consistent with the counterclockwise gyre observed by some interviewees near P5, and clearly mirrors the picking up of the southerly 'Ora del Garda' breeze (Fig. 4.24c), which replaces the 'Peler' late in the morning on sunny summer days [Giovannini et al., 2015a], and keeps blowing until the evening.

In Fig. 4.24e, the 'Ora del Garda' breeze is fully developed at 17:00, with an acceleration on the northern bound of the lake. At the same time, a strong current towards north (Fig. 4.24f) runs along the eastern shore and confirms the 'Corif' current. In consistency with the interviews of the sailors, the highest acceleration starts near Trimelone island (P7). From the snapshots in Fig. 4.24, we cannot detect either the countercloclwise gyre in the northern part of the high lake, or the serpentine current south of SR.

Surface transport Summing up the information gathered about surface particle transport in the high lake (Fig. 4.23b,c), the interviewees agreed that:

1. in presence of northerly winds aligned with the longitudinal axis of the lake (night, morning, or Föhn events), floating objects are transported towards the western shore;

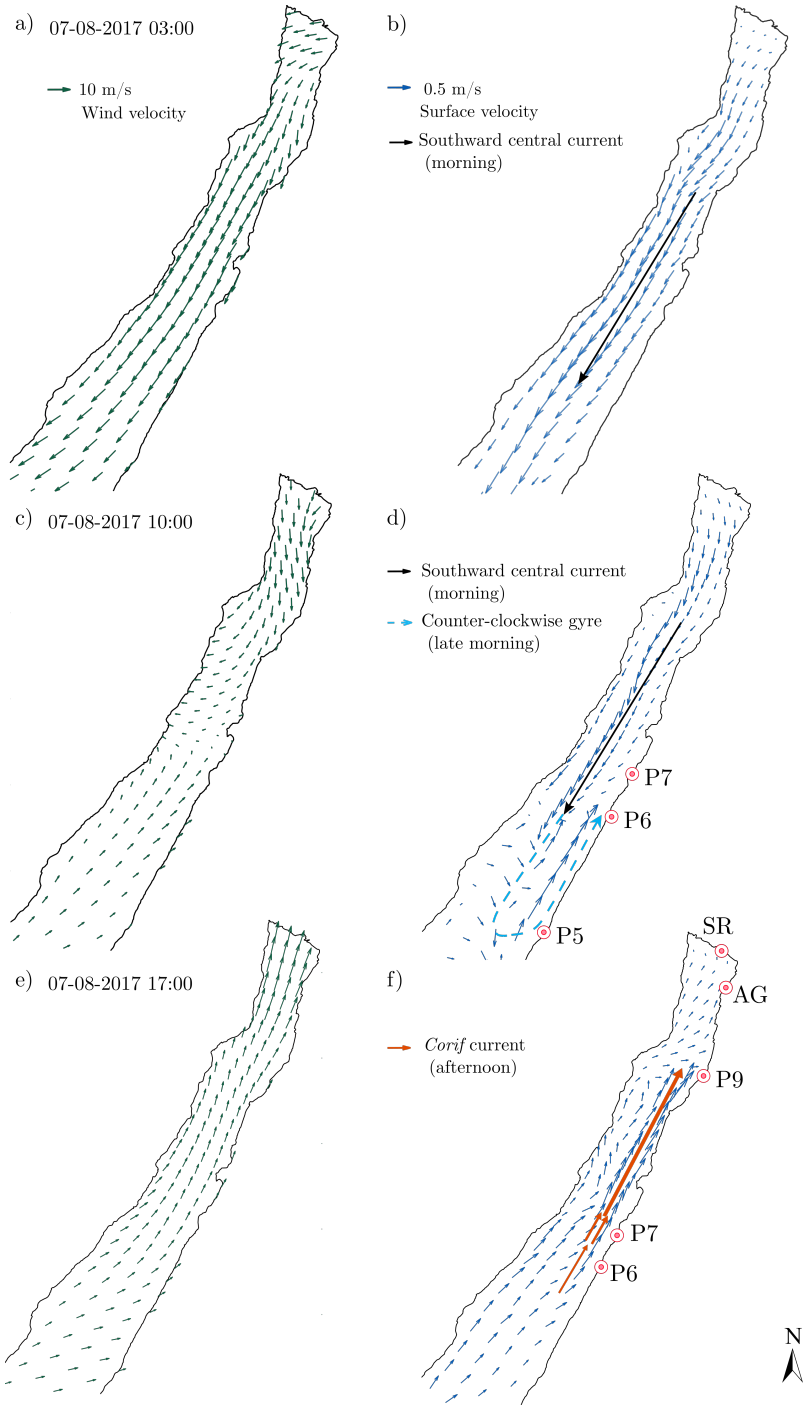

Figure 4.24: Wind (left column) and flow field (right column) on 7 August from numerical simulations at different times: (a,b) 3:00, (c,d) 10:00, and (e,f) 17:00. Note: not all grid points are drawn in the quiver plot.

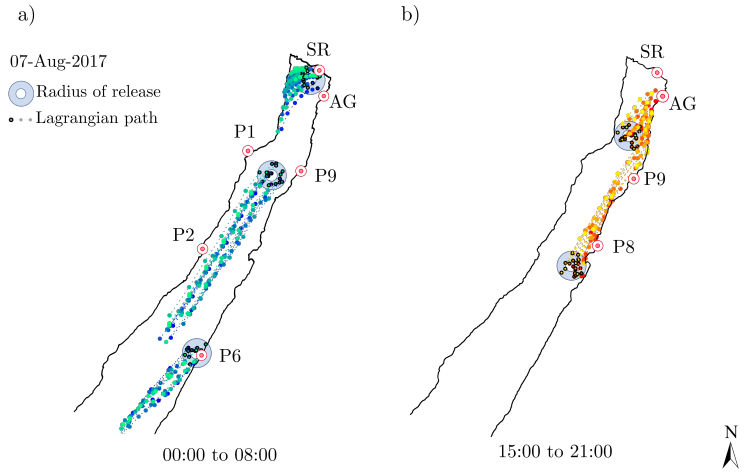

Figure 4.25: Surface transport reconstructed from the Lagrangian model under (a) northerly wind (7 August, from 00:00 to 08:00) and (b) southerly wind (7 August, from 15:00 to 21:00). Note: dots outlined in black are the starting points.

2. in presence of southerly winds aligned with the longitudinal axis of the lake (late morning, afternoon), floating objects accumulate along the eastern shore.

To verify the patterns described by the interviewees, we used the simplified Lagrangian model based on the surface flow field resulting from the hydrodynamic simulations. We released fully-submerged neutral particles within a radius of 1 km around the locations indicated during the interviews. A 24-hour simulation was run for the 7th of August 2017, when strong and long-lasting northerly winds blew in the night and the typical summer breezes developed in the day.

The trajectories of objects during the night and in the morning were investigated by starting the Lagrangian simulation in a period from midnight to 08:00 at three locations (Fig. 4.25a): Sarca river mouth (SR), off of Limone (P1) and Castelletto (P6). An example of the wind field during this simulation is shown in Fig. 4.24a at 03:00, when local northerly winds blow uniformly and aligned with the main axis in the high lake. In Fig. 4.25a, the positions of the particles are plotted every hour during the simulation time. At a first glance, all particles drift south-west throughout the night, In consistency with the direction of the wind. Those released near the northern border (SR) travel a short distance and accumulate close to the western shore. The particles released in P6 cover the longest distances (maximum ∼15 km in 8 hours, with a mean velocity of $\sim$ 0.5 m/s). The path of the boat of the fisherman (see trajectory 3 in Fig. 4.23b),

however, is not fully verified, as the particles do not reach the opposite shore during the night as he told.

We tested the surface transport in the afternoon, when the southerly 'Ora del Garda' blows aligned with the main axis of the lake, from 15:00 to 21:00 (see Fig. 4.24e for an example of the wind field on 7 August at 17:00). The starting points for these simulations were two: north of P9 and south of P8. The trajectories of the particles released in the afternoon show a clear deviation towards the eastern shore for both starting points (Fig. 4.25b), confirming the pattern described by the interviewees. The transport of those released more south is much stronger and brings the particles to cover $\sim$ 12 km in 6 hours ($\sim$ 0.5 m/s on average). Differently, the path of the northern release is shorter, because most of the particles reach the eastern shore and accumulate along the small bays north of P9, very close to the mouth of the Adige-Garda tunnel.

Boat capsizing accident The main temporal steps of the story of the boat accident reported by the firefighters, other witnesses and local newspapers (Fig. 4.23d) are:

1. capsizing occurred on 6 August 2017 in early afternoon between P1,P8 and P9.
2. intervention of the firefighters at 14:15 at the crashsite; the boat was moored with racing buoys;
3. the boat was sighted in the successive hours at P2 and P3;
4. the boat was recovered on 8 August close to the Garda island.

To reconstruct this boat accident we tested our simplified Lagrangian model by assuming an idealized boat shape (i.e., a sphere). Since the exact location and timing of the accident were uncertain, we run an ensemble of simulations to test different starting times and points for the trajectory of the boat.

In Fig. 4.26, we report the results of our sensitivity tests on the starting location (a) and time (b). Fig. 4.26a shows the importance of the starting point for the trajectory of the boat. The exact time of boat capsizing is unknown, but it is sure that the firefighters intervened around 14:15 to search for the missing person and the boat was moored to some racing buoys. From

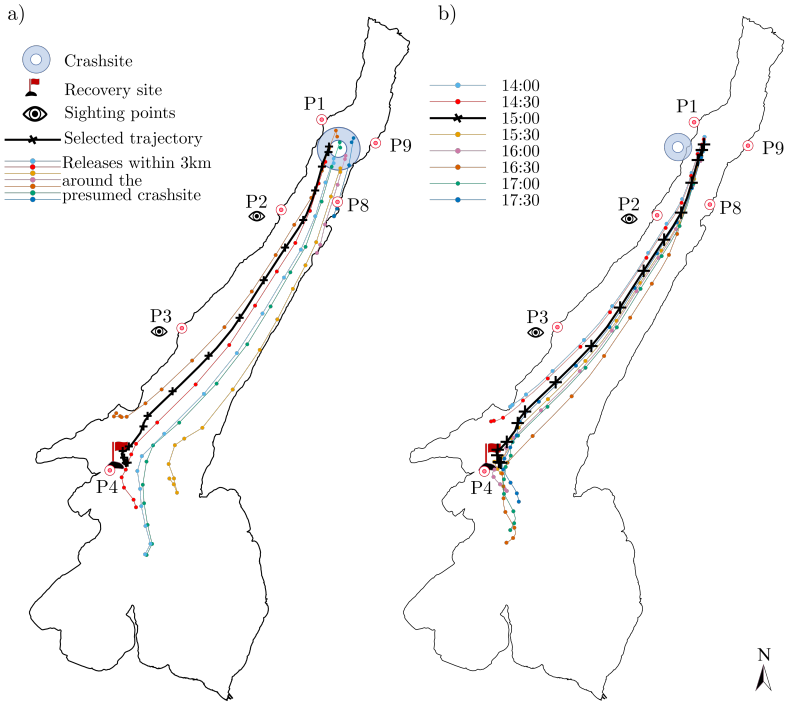

Figure 4.26: Sensitivity analysis on the choice of the starting location (a) and time (b) on the trajectory of the idealized boat in Lagrangian simulations. Coloured dotted lines show the different paths obtained by changing the starting point and time; the black crosses display the optimal trajectory. Note: points are plotted every hour.

that time on, the boat potentially started its path. Some unspecified period of time passed since when the firefighters arrived on the crash-site and moored the boat. Thus, we released semi-submerged numerical particles at 15:00 of 6 August 2017 within a radius of 1.5 km in the area between Navene (P9), Limone (P1) and Malcesine (P8), assuming that it was a reasonable time for the boat to drift as moved by the combined action of water flow and wind. The tests revealed that the trajectories of the particles are highly sensitive to the location of the release, and that only those released close to the western shore effectively reach the recovery site within the simulation time. Instead, those released close to the eastern shore, deviate to the east when they reach the southern low lake. The results shown in the figure are relative to Lagrangian simulation run until 8:00 of 7 August. If the numerical simulation is prolonged to the successive day, when the boat was actually recovered, the latter particles are moved even further due to the onset of the daily alternating breezes (not shown). We test the effect of the starting time in Fig. 4.26b. By observing the drift of the boat within a time window of 3 hours around 15:00, we note that the overall trajectory of the object does not change significantly. In fact, from 15:00 to 17:00 the wind is substantially constant and uniform in the area of the accident, and even if small fluctuations in the flow field can initially move the Lagrangian drifter in an opposite direction, the final path is substantially insensitive of the release time. However, Fig. 4.26b shows that particles released earlier, which are subject to a weak and fluctuating wind forcing, reach the recovery site at the end of the simulation. The particles released afterwards, when the wind field is fully and uniformly developed with high wind speeds, reach the final destination late at night on the release day or at the very early morning hours of the successive day, i.e. some hours before the end of simulations. Hence, the sensitivity tests showed that in the Lagrangian simulations the trajectory of the boat is more influenced by the starting point rather than by the release time. The best match for starting the Lagrangian drift of the idealized floating boat was then found at 15:00, at a distance of 1.5 km south-east of P1.

In order to verify the story told by the witnesses, three significant moments have been identified and plotted in Fig. 4.27: (a-b) the plausible time the boat was moored and let free to drift (around 15:00); (c-d) intermediate time steps in the afternoon until night (from 16:00 to 22:00) when the sight of the boat in several locations was reported; (e-f) the time of the arrival to the recovery site. Fig. 4.27a shows that around 15:30, the wind was blowing from

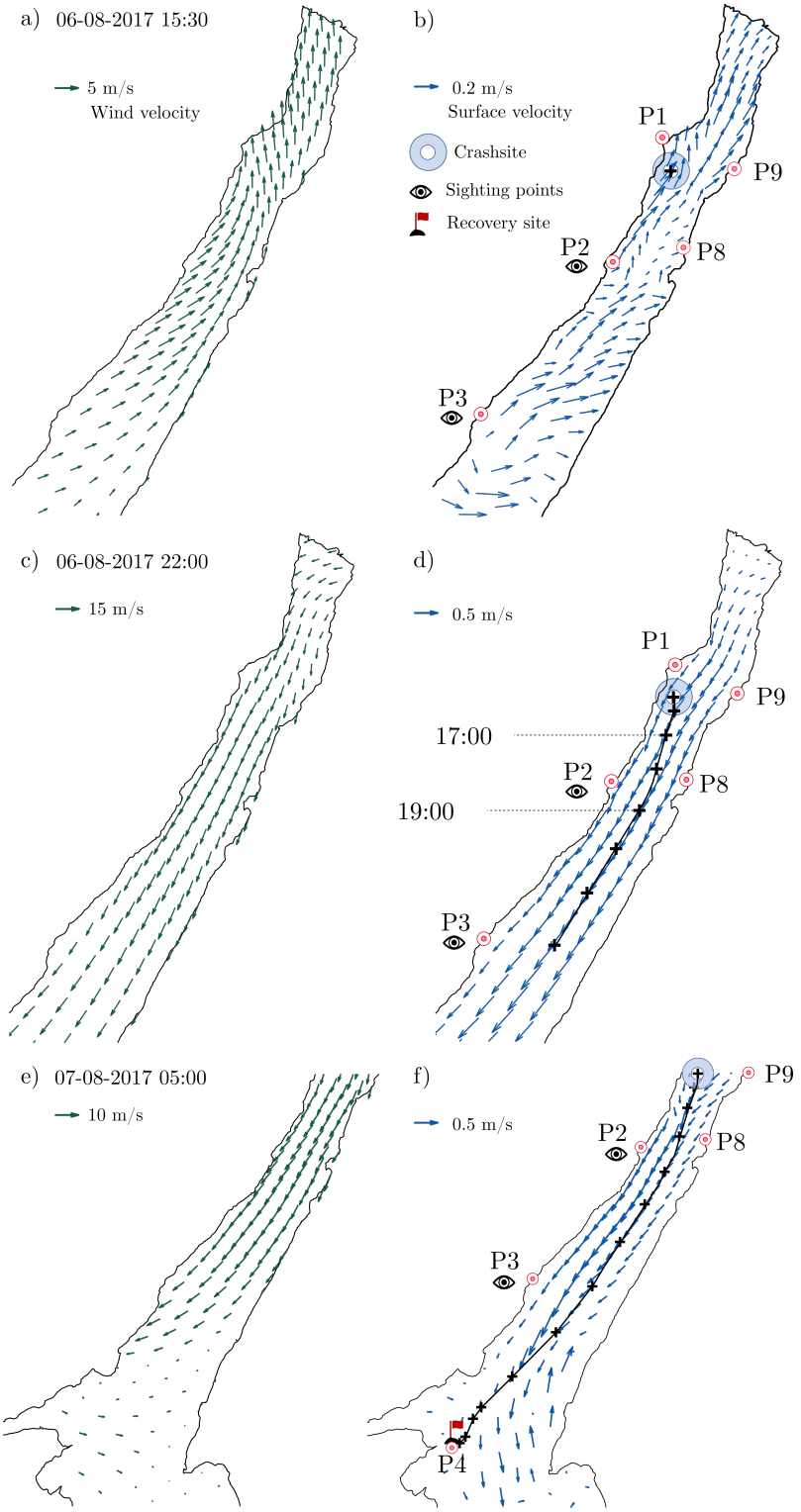

Figure 4.27: Wind (left column) and flow field (right column), together with the numerical reconstruction of the boat drift at different times; (a,b) 15:30, (c,d) 22:00 on 6 August, and (e,f) at 05:00 on 7 August. Note: points are plotted every hour.

south with velocities of the order of 5 m/s (at 10 m above the water surface), while surface currents were on the order of 0.2 m/s (Fig. 4.27b). At 16:00, a northerly wind started blowing intensely: the snapshot of the wind field at this time could be taken at anytime from 16:00 to 22:00 (Fig. 4.27c) because the wind blew uniform and constant with a velocity on the order of 15 m/s. In Fig. 4.27d the position of the boat every hour from 15:30 to 22:00 is superimposed to the flow field at 22:00. From this plot it is clear that during the afternoon the boat was dragged southward reaching the first sight point P2 between 17:00 and 19:00 and the second point P3 after 6 hours (at 22:00). The drifting boat covers 15 km in 6 hours, hence the estimated velocity of the boat is of 0.7 m/s. It worths noting that the Lagrangian drifter used in the simulation is semi-submerged, and thus it is subject to the combined action of wind and flow field. Hence, the resulting Lagrangian velocity of the idealized boat is larger than the flow velocity, thanks to the contribution of the additional wind drag. From 22:00 to the early morning of the successive day, the wind kept blowing in the same direction (Fig. 4.27e), moving the water and the boat towards south-west. Finally, the modelled drifting boat reached the recovery site (Fig. 4.27f) at 5:00 on 7 August.

4.2.3 Discussion

The dynamics simulated using the numerical model show a good agreement with the description of the physical processes gathered from the interviewees. The comparison has confirmed that surface transport is not always perfectly aligned with the wind forcing. This fact, which surprised the interviewees, was not unexpected: in fact, the deviation of objects towards the eastern shore under the 'Ora del Garda' breeze (which blows along the longitudinal axis of the lake) can be easily ascribed to the Coriolis effect, whereby the wind-driven movement of surface water is deflected to the right of the wind in the Northern hemisphere. This effect justifies the westward surface transport observed by some interviewees during northerly winds, and was already described by Amadori et al. [2018] and demonstrated via observational and modeling efforts by Piccolroaz et al. [2019].

By combining the trajectories reconstructed using the Lagrangian model (Fig. 4.25) and the flow field resulting from the hydrodynamic simulations (Fig. 4.24), it is possible to give an

additional explanation of the transport patterns highlighted during the interviews. In fact, the higher velocities (~ 0.5 m/s) of particles released in the central part of the lake during the night-morning period ('Peler' breeze, Fig. 4.25a) are consistent with the development of a southward central current (Fig. 4.24a and b).

Moreover, the relevance of a surface current named 'Corif' is confirmed. Such a current develops in the northern trunk of the lake along the eastern shore and is induced by the 'Ora del Garda' wind. Its effect is consistent also with the afternoon surface transport from the Lagrangian simulations (Fig 4.25b). In fact, particles released near the eastern shore (close to P7, which is the point of maximum acceleration of the 'Corif' according to the interviewees) move much faster than the others, with a mean velocity of 0.5 m/s. Although such a current was not explicitly recognized by Amadori et al. [2018], its existence can be explained theoretically: high-velocity surface waters are pushed to the right by the Coriolis acceleration, according to the phenomenon already discussed above, eventually generating a secondary circulation in the cross-section, see Toffolon [2013]. This same secondary circulation is responsible for the existence of lateral gradients of temperature between the eastern and western shores, which were measured and simulated by Piccolroaz et al. [2019], and also commented by some interviewees. The absence of a strong southward current along the western shore during the 'Peler' winds is likely due to the morphology of the lake, with the presence of the promontory north of Limone gulf (P1) that deviates the current towards the centre of the lake.

The counterclockwise gyre developing in the central part of the lake in late morning was found in the numerical simulations as well. The flow fields in Fig. 4.24d show a transition from the central southward current in the morning (subplot b) to the northward 'Corif' current (subplot f). From this, one can infer that the counterclockwise tendency of surface flow occurs as a result of the wind stress and of the transition between the two currents [Amadori et al., 2018] (as we described in Section 4.1). Conversely, the counterclockwise northern gyre reported by the interviewees (Fig. 4.23c) is not clearly visible in the flow field snapshots in Fig. 4.24, but it can be inferred from the transport patterns occurring at the northern border of the lake out of the Sarca river mouth SR (Fig. 4.25a). Interestingly, such a tendency of the flow was observed in the preliminary investigations on the mean flow in Lake Garda by Amadori et al. [2018], who described it as a direct circulation [Strub and Powell, 1986; Lemmin and D'Adamo,

1997] and demonstrated that it is independent of rotational effects and is more likely driven by the topography of the region and by the spatial distribution of the wind. Such a conclusion is supported by our numerical results, in fact the wind field displayed in Fig. 4.24a is clearly directed towards the west and is more likely to be responsible of the westward surface transport than rotational effects near the northern border of the lake.

Some interviewees suggested that the Sarca river plays a role in causing a serpentine flow heading south and being responsible of westward transport and thermal gradients. We did not find this pattern, but we recall that the river inflow was not included in the numerical model. However, the collected information seems to confirm an analogous pattern that was identified in Lake Iseo Pilotti et al. [2018], which is similar to Lake Garda as for latitude and shape in its northern part.

Finally, the reconstruction of the boat capsizing accident provided new insights to the event. It is important to remind that many assumptions have been made in our analysis and several uncertainties exist, i.e. on the geometry of the boat, on the submerged volume fraction, on the time and the location of the starting point. Moreover, local topographic effects both on air and water side (i.e. local breezes or circulations caused by orographic/bathymetric small-scale variations) might be missing in the model results, due to the coarse horizontal resolution of the atmospheric and, to a lower extension, hydrodynamic grids. Nevertheless, the numerical trajectory of the boat confirms the supposed path and all sighting points are consistent, and only the duration of the journey of the boat is shorter than the one emerging from local newspapers and witnesses. In fact, our numerical results show that the boat covered the distance from the starting point to the recovery site in less than 15 hours, thus reaching the Garda island in the morning of 7 August. However, this result is consistent with the available wind forcing: during the simulated period, a strong northerly wind blew constant and uniform during the night and fell (in the low lake) in the morning, when it gave the way to an easterly breeze first, and to the southerly 'Ora del Garda' later. Thus, given the available wind forcing from WRF simulations, it is reasonable that the boat reached the Garda island in the early morning of 7 August under the drag of the northerly wind and ran aground there until being recovered one day later.

4.2.4 Conclusions

In this work, we presented our experience about the involvement of the local community in limnological investigations of Lake Garda. The knowledge that citizens and lake users developed over time proved to be a source of reliable information on surface circulation and transport processes, mainly during the summer season. In fact, even though the data acquired from the interviews were mainly qualitative, most of the interviewees agreed on the typical surface transport patterns. Some of the emerged processes were already assessed in previous studies of the lake circulation, while some others were not available in the scientific literature. Hence, the interaction with the citizen added new details on surface currents and paved the way to new directions of research in this lake. By this experience, it is clear that many more research questions can be tackled through such a combined approach, and that it is time to let the local knowledge support the traditional scientific methods (and viceversa), as a privileged way to open the scientific community to fruitful opportunities of public engagement.

The strong interest of sportsmen in Lake Garda water and wind dynamics is a distinctive feature of our case study. Despite this, the approach we followed is not case-specific and can be easily extended to other contexts of investigation. In this respect, we stress that the use of local knowledge differs from the traditional citizen-science approach. In the latter case, the objective is usually to collect a large number of data that would be impossible to obtain by means of traditional measuring techniques. Differently, harvesting local knowledge means selecting pieces of information from users that have only a partial expertise, and eventually putting them in a coherent framework. Future steps of this methodology should aim at exploiting social science methods more and more, and connect them to the process-based description of physical phenomena. Such an inter-disciplinary approach could also be easily extended to other fields of environmental investigation, leading in any case to synergistic advances of the scientific research.

Aknowledgments We individually thank all the wind-surfers, sailors, fishermen, ferry boat drivers, firefighters, EPA officers and passionate citizens who shared their knowledge of the lake with the second author of this article. We also acknowledge the firefigthers nautical rescue team of Trento (Corpo Permanente dei Vigili del Fuoco Trento), the EPA of the Autonomous Province

of Trento (APPA), the Italian Sailing Federation (FIV), the amateur wind surfers association 'I Parassiti' and the ferry company Navigarda for facilitating the research. We are also grateful to Lorenzo Giovannini (UniTN) for providing the WRF simulations, and to prof. Henk A. Dijkstra for his constructive comments on a previous version of the manuscript.

Chapter 5

Deep mixing dynamics

Contents

This Chapter is based on:

Piccolroaz, S., Amadori, M., and Dijkstra, M. T. H. A. Importance of planetary rotation for ventilation processes in deep elongated lakes: Evidence from Lake Garda (Italy). *Scientific Reports*, 9, 2019. doi: 10.1038/s41598-019-44730-1

5.1 Importance of planetary rotation for ventilation processes in deep elongated lakes

Deep lakes in the temperate region undergo long periods of thermal stratification. During these periods an upper well-mixed layer forms, exchanging heat and gases with the atmosphere and laying above a poorly mixed and nutrient rich deep waters. If thermal stratification weakens enough, surface and deep water mix, promoting the redistribution of oxygen, nutrients, and energy along the water column, until possible homogenization (e.g. Boehrer and Schultze [2008]; Kirillin and Shatwell [2016]). In this way, surface properties such as temperature and dissolved gas concentrations are imprinted on deep layers, in a process commonly referred to as deep ventilation (e.g. Matsumoto et al. [2015]).

Vertical transport and mixing are therefore key factors affecting the water quality and trophic status of lakes (e.g. Berger et al. [2007]; Boehrer et al. [2008]; Edlund et al. [2017]), including several chemical and biological processes (e.g. Salmaso et al. [2003]; Dokulil [2014]; Leoni et al. [2014]). The occurrence of deep mixing events (DMEs), in particular, is highly relevant in those lakes that undergo irregular ventilation, i.e. less frequently than once a year (oligomixis). In these lakes, deep layers remain isolated from the surface waters for a relatively long time. DMEs are primarily controlled by the thermal stratification of the water column and by the fluxes of heat and momentum at the lake-atmosphere interface (e.g. Imboden and Wüest [1995]; Wüest and Lorke [2003]; Boehrer and Schultze [2008]; Laval et al. [2012]). Consequently, any ongoing and future change in climate forcing potentially alters the stratification and mixing regimes of a lake [Butcher et al., 2015; Kraemer et al., 2015; Piccolroaz et al., 2015], thus seriously threatening the occurrence of DMEs and its ecological status.

Recent studies suggest that thermal stratification is expected to increase in response to a warming climate, with consequent inhibition of extent and frequency of convective DMEs in the future (e.g. Danis et al. [2004]; Sahoo et al. [2013]; Wood et al. [2016]; Piccolroaz et al. [2018]). The effect of an enduring decrease of DMEs is the progressive warming, depletion of oxygen, and increase of nutrient concentrations in deep layers, counterbalanced by a reduced fertilization of surface water. This scenario has already been observed in many temperate lakes

(e.g. Ambrosetti and Barbanti [1999]; Dokulil et al. [2006]; Rempfer et al. [2010]), including several deep perialpine lakes. Examples are Lake Zurich [North et al., 2014], Lake Constance Straile et al. [2003]; Wahl and Peeters [2014], Lake Lugano[Aeschbach-Hertig et al., 2007], Lake Geneva [Schwefel et al., 2016], Lake Maggiore [Fenocchi et al., 2018], and Lake Iseo, where the lack of DMEs over the last decades led to significant deoxygenation of deep layers Ambrosetti and Barbanti [2005]; Pilotti et al. [2013b]; Valerio et al. [2015b].

In deep lakes where water temperature is warmer than the temperature of maximum density, DMEs are typically associated with buoyancy-driven convective processes. This mechanism is caused by the increase of surface water density, e.g. due to cooling of surface water during cold winters or to inflows of denser waters. The effect can be seen in a typical sawtooth structure of deep water temperature [Livingstone, 1997], whereby gradual warming is punctuated by abrupt cooling events. However, convective mixing is not the only mechanism of ventilation in long, narrow, and deep lakes (such as alpine, glacial, and rift valley lakes, fjords, and river valley reservoirs [Rawson, 1942; Salmaso and Mosello, 2010]). Strong and sustained wind events can generate along-lake up-/downwelling episodes due to tilting of the thermocline and internal waves (e.g. [Laval et al., 2008; Becherer and Umlauf, 2011; Bocaniov et al., 2014]), or large scale overturning circulation reaching down to the lake bottom [Ambrosetti et al., 2010].

Theoretical studies for constant density flows in rotating narrow, elongated, and deep basins have also shown that intense closed circulations in cross-sections orthogonal to the wind direction may develop, due to the effect of the Coriolis acceleration [Winant, 2004; Ponte, 2010; Toffolon, 2013] and to the presence of lateral boundaries. Such flows are associtated to up- and downwelling at the shores and were previously observed in numerical experiments in enclosed [Wang et al., 2001; Appt et al., 2004] and semi-enclosed basins [Sanay and Valle-Levinson, 2005; Valle-Levinson et al., 2003; Cheng and Valle-Levinson, 2009]. The latter case is relative to the context of Regions of Freshwater Influence (ROFIs), where density-driven exchanges between estuary and ocean are relevant. However, they have never been explicitly measured in narrow deep lakes, where, in addition, their possible contribution to deep ventilation remains unexplored. In fact, after the pioneering work of Ekman [1905], this flow regime was traditionally observed and analyzed in large domains such as the ocean or large lakes Birchfield [1972], while it was largely overlooked in relatively small enclosed basins Winant [2004]; Valle-Levinson [2008].

In this chapter, we use observations in Lake Garda and numerical simulations to demonstrate that the combined effect of wind-induced circulation and planetary rotation is relevant for the ventilation of deep layers also in elongated lakes having a width on the order of a few km. These results add a new aspect of complexity when assessing the response of deep and narrow lakes to external forcing and climate change.

5.1.1 Methods

5.1.1.1 Field campaign

The data used in this work come from the IMAU-UNITN a two-year monitoring program mentioned in Chapter 2. Here we use high-resolution profiles of temperature and chlorophyll-a measured though a CTD microprofiler (MicroCTD, Rockland Scientific International, RSI, Canada). Three reference stations were selected during the monitoring campaign: Central Station (CS), located in the center of the narrow trunk at about 4 km from the northern edge of the lake, and two additional reference stations on the east (East Station, ES) and west (West Station, WS) sides of the CS. The three stations are aligned along a transect where the lake is ∼2.5 km wide (Fig. 5.1).

Here we analyze the vertical profiles measured at the three monitoring sites after three significant synoptic northerly wind events on 10 March, 21 April, and 7 August 2017. All downcast profiles were taken at the same time of day, between 10:00 and 13:00 CET.

Wind speed and direction data were obtained from the meteorological stations operated by the Regional Meteorological Service of the Environmental Protection Agency (ARPA Lombardia). We analyzed the time series of wind speed measured at Limone del Garda and Toscolano-Maderno, respectively site M1 and M2 in Fig. 5.1. Specifically, Limone del Garda (M1) was chosen as reference station, as it is located ∼6 km south of the reference transect and 200 m from the shore.

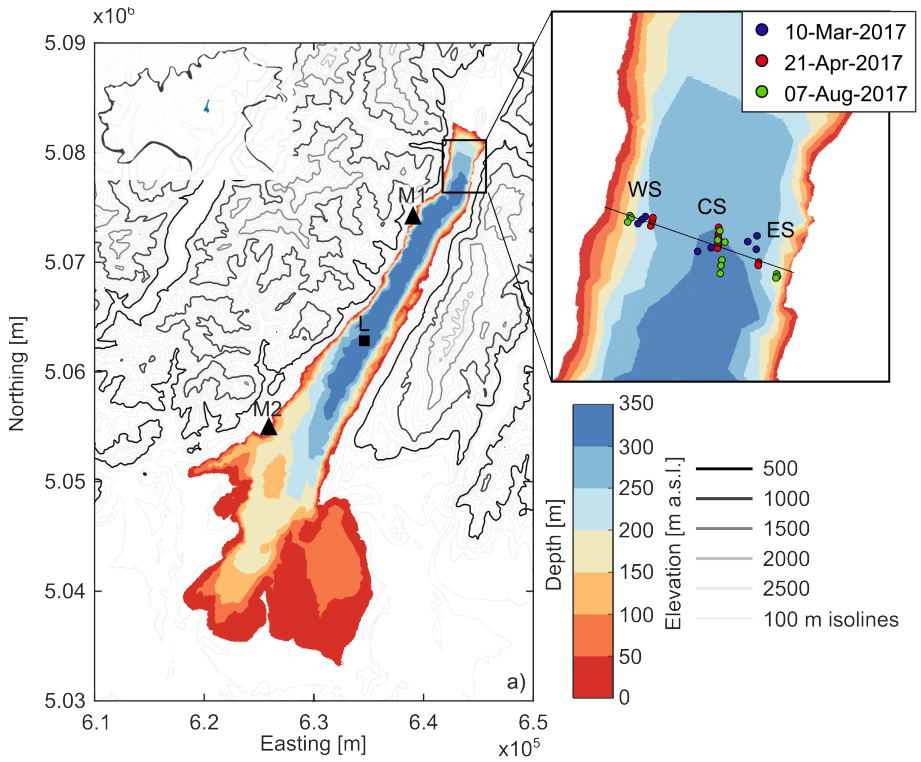

Figure 5.1: Map of Lake Garda with the relevant locations for the field campaign. Reference transect with the monitoring stations (zoom-in view), and the meteorological (M1 and M2) and ARPAV monitoring (L) stations used in the analysis (black triangles and square, respectively).

5.1.1.2 Models setup

Atmospheric-hydrodynamic model As a complement to *in-situ* measurements, numerical simulations of atmospheric and lake conditions were performed with the one-way coupled atmospheric-hydrodynamic model of Lake Garda described in the previous chapters. For an exhaustive description of the two models' settings we refer again to the Chapter 3. The value of the main parameters of the model are summarized in Tab. 5.1. Numerical simulations were run for the 3-11 March, 18-21 April, 1-15 August 2017, according to the field campaign dates (10 March, 21 April, and 7 August 2017).

Tracer experiment The hydrodynamic simulations described above included numerical tracer experiments. We quantified wind-induced ventilationfth by analyzing the evolution of a passive tracer initially distributed with constant concentration C_{surf} in the upper 50 m (based on the profiles in Fig. 5.5), while it was set to 0 mg/l along the remaining of the water column.

Model settings				
Wall b.cs	free slip			
Bottom roughness (Chézy)	65 $m^{1/2}$ s^{-1}	(default)		
Wind drag coefficient C_d	0.0044	0.0010	0.0020	
(for wind velocities U [1])	(1 m s^{-1})	(5 m s^{-1})	(20 m s^{-1})	
Turbulence closure	$k-\varepsilon$	Heat fluxes	*Ocean model*	
Horizontal eddy diffusivity	0.2 m^2 s^{-1}	Stanton number	1.3×10^{-3}	(default)
Horizontal eddy viscosity	0.2 m^2 s^{-1}	Dalton number	1.3×10^{-3}	(default)
Event-based simulations				
Event	Start time		End time	time step
March 2017	3 March 00:00		12 March 00:00	60 s
April 2017	18 April 00:00		22 April 00:00	60 s
August 2017	1 August 00:00		16 August, 00:00	30 s
Numerical tracer simulations				
Event	Instantaneous release time t_1		End time t_2	time step
March 2017	7 March 12:00		10 March 12:00	60 s
April 2017	19 April 00:00		22 April 00:00	60 s

[1] at 10 m above ground level

Table 5.1: Hydrodynamic model set up.

We instantaneously released the tracer at the beginning of the wind event (t_1) and let it be transported by the flow up to time t_2 (see Tab. 5.1).

We estimated the volume $V_{vent}(i,t)$ of surface water ventilated in the deep lake from the beginning of the tracer experiment (time t_1) until time t. The computation based on the mass balance of the tracer at each transverse model cross-section i (similar to Bocaniov et al. [2014])

$$V_{vent}(i,t) = \frac{V_{isopy}(i,t)C_{isopy}(i,t)}{C_{surf}}\,, \tag{5.1}$$

where $V_{isopy}(i,t)$ is the volume of water below a reference isopycnal surface at model cross-section i at time t, and $C_{isopy}(i,t)$ is its average tracer concentration. The above mass balance assumes that the tracer concentration of downwelled water is time-invariant and equal to C_{surf}. The isopycnal surface was chosen such that the overall V_{isopy} was relatively small compared to the lake volume in order to be representative of the deep layer when the lake is calm and the isopycnals are horizontal. We chose the isopycnal such that V_{isopy} was about 18% of the lake volume (corresponding to the lake volume below nearly 200 m depth). V_{isopy} showed limited variability during the tracer experiment ($\pm$1% of lake volume), thus making it well delimited throughout the simulation.

In order to quantify the wind-induced ventilation in the lake, we calculated the ratio η between the ventilation volume and V_{isopy}:

$$\eta(i,t) = \frac{V_{vent}(i,t)}{V_{isopy}(t)}\,. \tag{5.2}$$

The sum of $\eta(i,t)$ over index i at a given time t can be interpreted as the efficiency of wind-driven ventilation of V_{isopy} at that time. The tracer experiment was not performed for the wind event on August 2017 since it was not significant for the analysis of deep ventilation, due to the strong thermal stratification of the lake in that period.

5.1.2 Results

5.1.2.1 Field campaign

In this section, the observations from our field campaign are presented in combination with data collected by the Environmental Protection Agency of the Veneto (ARPAV) and Lombardia Region within the investigated period, in order to provide the most complete description of the processes potentially involved. The time series of the wind speed measured at M1 and M2 stations are plotted in Fig. 5.2. The figure shows the wind speed component along the major axis of the lake, with positive values indicating wind from north-east and negative from south-west. Raw data are available at hourly interval, but for clearer reading the 1-day moving average is also shown.

Strong and persistent wind events occurred during the fieldwork periods (vertical continuous lines), with significant events also in January and February, when the lake is typically weakly stratified [Pareeth et al., 2016], and in early April. Concurrently with the latter strong wind events, the full (i.e., down to the bottom) vertical profiles measured by the ARPAV (Fig. 5.3a-b) between March and April 2017 (these two dates are indicated as vertical dashed lines in Fig. 5.2) show a visible warming of deep water down to 250 m depth accompanied by decrease in conductivity.

Fig. 5.2c-e shows the wind roses relative to the monitoring day and the preceding two-day time window. The wind roses for all analyzed periods confirm that a synoptic wind blew from

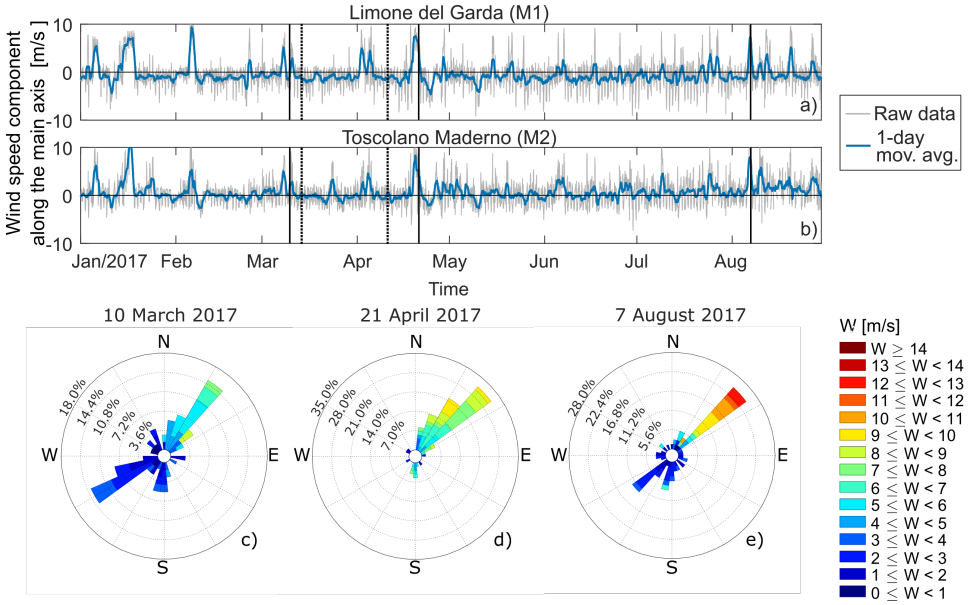

Figure 5.2: (a-b) Time series of wind speed component along the major axis of the lake (oriented about 30°E) measured at the meteorological stations in Limone del Garda-M1 (a) and Toscolano-Maderno-M2 (b, see Fig. 5.1a for M1 ans M2 stations location). Vertical continuous lines indicate fieldwork days, while vertical dashed lines indicate ARPAV monitoring days. (c-e) Wind roses for the three analyzed periods based on measurements collected at station M1 relative to a three-day period, including the fieldwork day and the two preceding days.

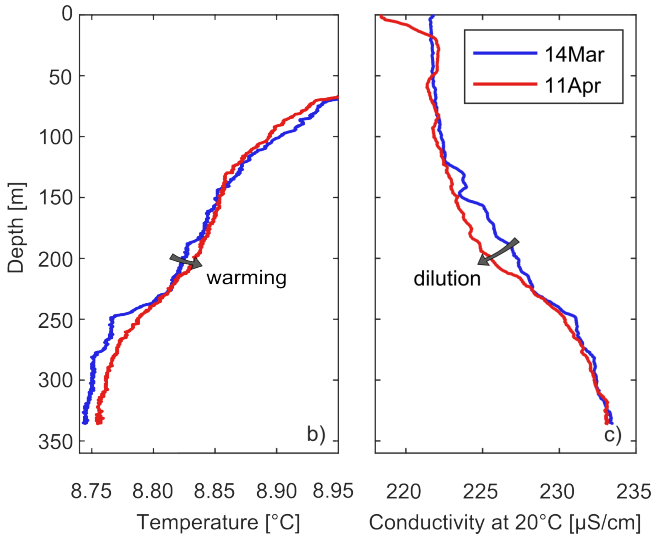

Figure 5.3: Vertical profiles of temperature (a) and conductivity at 20°C (b) measured at the L station by ARPAV between March and April 2017 using a SBE-19plus SEACAT profiler.

North-East with wind speeds of 5.3 ± 1.3 m s^{-1}, 6.7 ± 1.6 m s^{-1} and 6.9 ± 3.8 m s^{-1} (mean $\pm$ standard deviation, computed from the raw hourly data of the three events, respectively).

Fig. 5.5a-f shows the lateral variation of the vertical profiles of temperature and chlorophyll-a measured at the three monitoring sites along the reference transect, down to 100 m depth. A significant lateral gradient is clearly visible, with water temperature and chlorophyll-a concentrations increasing from ES to WS along the upper 100 m of the water column. In March and April, the thermocline depth was deeper moving from east to west and the thermal stratification was stronger, while still being characterized by small vertical temperature gradients (i.e., on the order of 0.1°C) according to the typical seasonal conditions. The temperature profiles at ES were nearly homogeneous (particularly in April), except for the upper ∼10 m. The peak of chlorophyll-a concentration was deeper and more intense at WS, with high chlorophyll-a concentrations being well distributed over a wider range of depths. In particular,the March profile at WS has a ∼40 m-thick layer of nearly homogeneous chlorophyll-a concentrations, accordingly to the thick well-mixed layer (Fig. 5.5d). Similar considerations apply to the profiles measured in August, although the largest lateral differences were bounded within the upper ∼30 m due to much stronger thermal stratification (Fig. 5.5c).

For all monitoring periods, the observations are consistent in showing a significant surface westward transport accumulating chlorophyll-a and warm water at station WS, which was not observed in the profiles measured in absence of persistent wind events in other periods of the year (see Fig. 5.4).

5.1.2.2 Numerical modeling

To validate the interpretation of the processes causing the lateral gradients described above, we performed numerical simulations of the lake thermo-hydrodynamics during the analyzed wind events.

Validation of the models In this section, we present the validation of the atmospheric and hydrodynamic models by comparing observed and simulated wind forcing and lake thermal profiles for the event-based simulations. The validation of the atmospheric model was performed comparing observed wind roses at the Limone del Garda-M1 meteorological station (Fig. 5.6a, b, and c) with simulated wind roses extracted from the WRF lake cell closest to that station (Fig. 5.6g, h, and i).

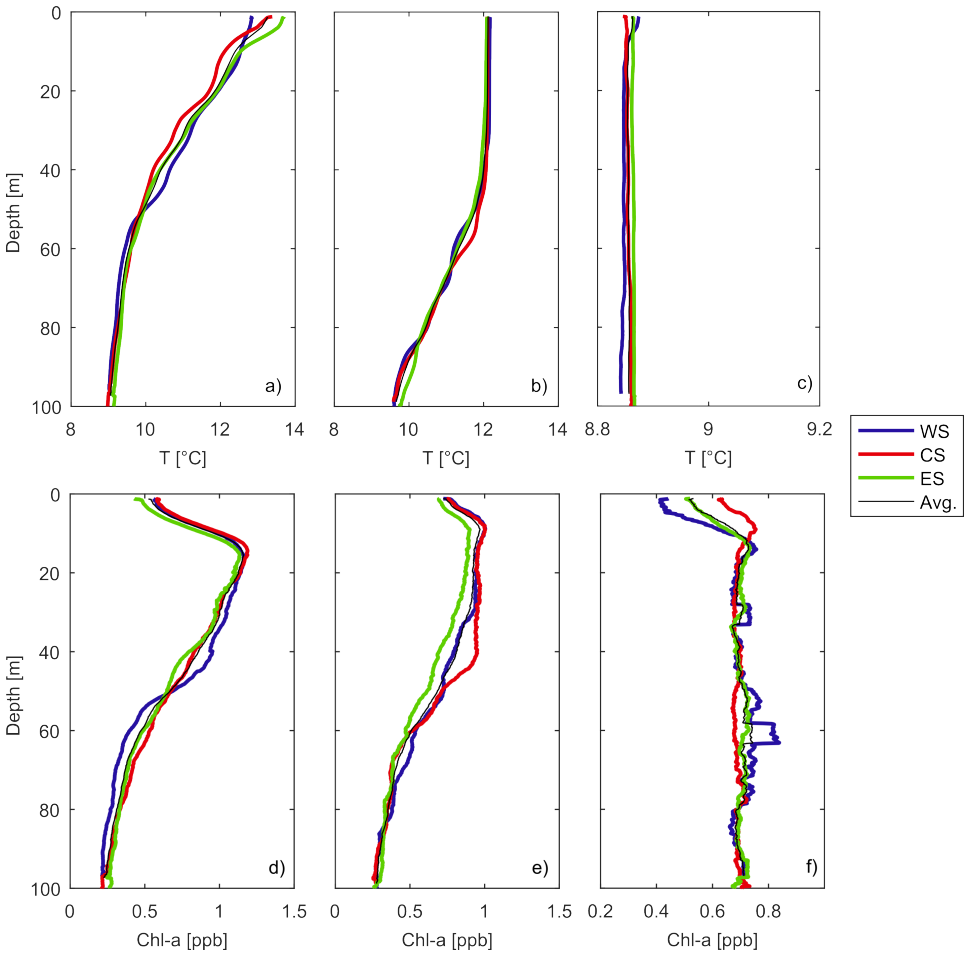

Figure 5.4: (a-c) Vertical profiles of temperature measured at the three sampling stations (ES, CS, and WS), on 22 May 2017, 21 November 2017, and 28 February 2018, respectively. (d-f) As in panels (a-c) but for chlorophyll-a. The profiles, measured in absence of persistent wind events, do not show any systematic lateral variability in temperature or chlorophyll-a.

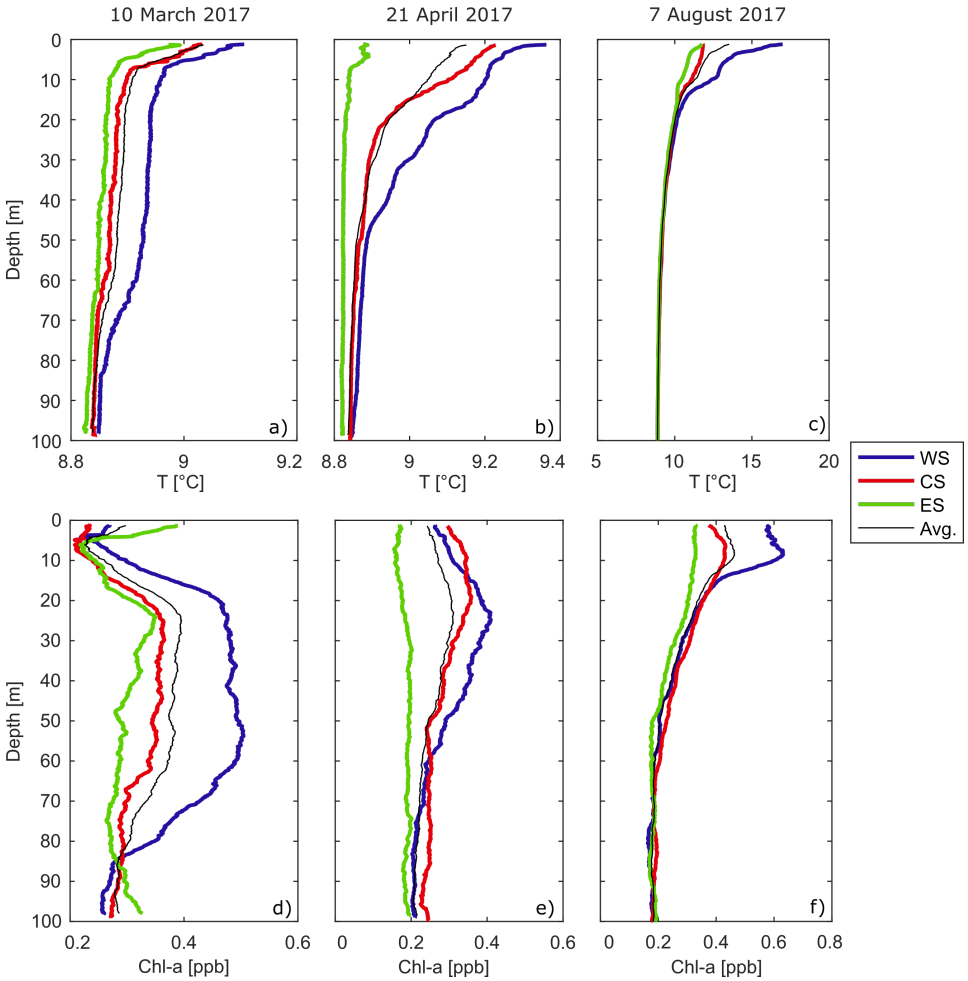

Figure 5.5: (a-c) Vertical profiles of temperature measured at the three sampling stations (ES, CS, and WS) in the three analyzed periods. (d-f) As in panels (a-c) but for chlorophyll-a. We notice that the depth of vertical profiles here and in Fig. 5.1 are different.

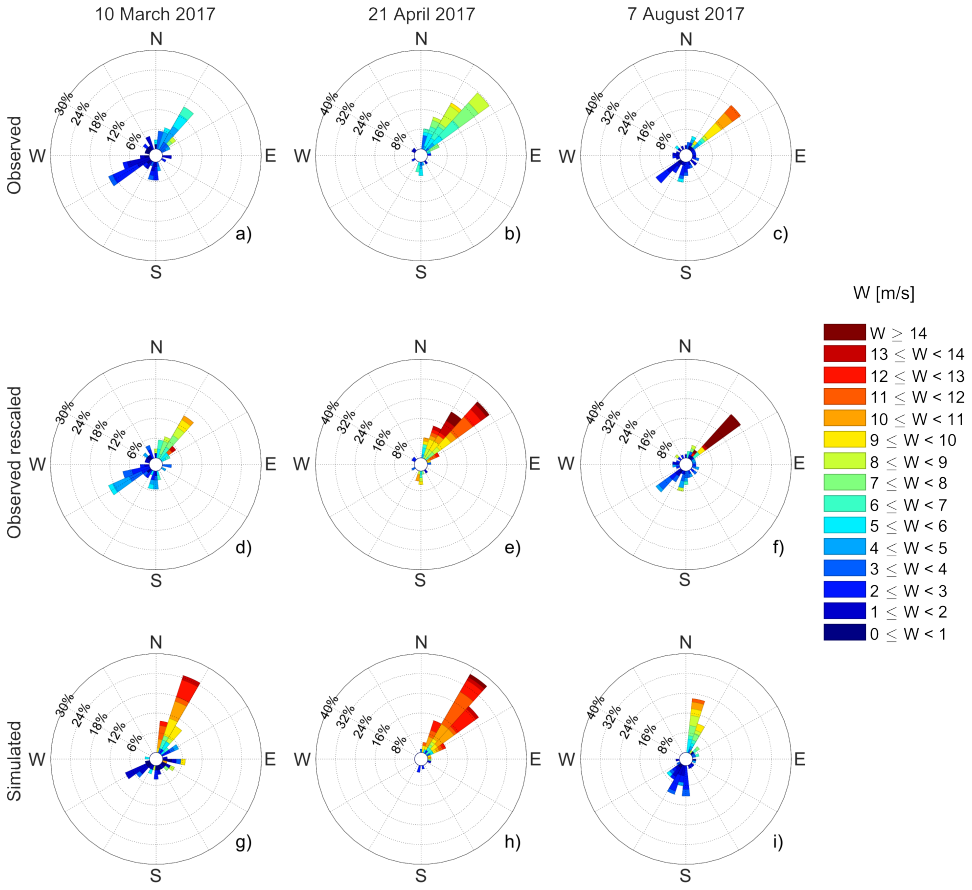

Figure 5.6: Wind roses for the three analyzed periods based on measurements collected at 16 m above ground at station M1 (see Fig. 1 a) (a-c), measurements collected at station M1 referred to 10 m above ground and rescaled according to $WS_{lake} = 1.6\,WS_{land}$ (d-f), and WRF simulations at 10 m above ground (g-i). Wind roses refer to a three-day period, including the fieldwork day and the two preceding days.

The comparison shows a very good match between simulated and observed wind direction, confirming that the model well captures the predominant winds during the three analyzed events. Concerning wind intensity, simulated values (Fig. 5.6g, h, and i) are generally higher than observed (Fig. 5.6a, b, and c). This mismatch is due to the different height at which the wind is referenced and to the small-scale factors affecting ground observations (e.g., trees, buildings, local morphology) that are partially filtered out by the 1 km spatial resolution of the WRF model. Moreover, wind speed measurements collected at ground stations do not necessarily represent over lake conditions. By comparing the wind speed data measured at the Limone meteorological station and by a portable meteorological station installed on the boat during fieldwork, we found that the wind speed above the lake was on average 1.6 times the one

measured by the ground station ($WS_{lake} = 1.6\,WS_{land}$). This proportionality was used to rescale land-based measurements In all cases, wind speed values were converted to the standard height of 10 m for fair comparison (the same height above ground of WRF results). This is just a rescaling of wind intensity and hence cannot obviate the inherent differences between over lake and over ground wind patterns that certainly exist. However, the improved comparison between rescaled observations (Fig. 5.6d, e, and f) and WRF results confirms that WRF results are representative of the lake forcing conditions. Additional and systematic validation of the WRF model is provided in Giovannini et al. [2014a] and Giovannini et al. [2014c], who used the same setup of the WRF model to simulate thermally-driven circulations in the lake area and surrounding territory.

The hydrodynamic model was validated by comparing simulated and observed vertical temperature profiles along the reference transect. A one-to-one comparison for the three analyzed periods is provided in Fig. 5.7. Considering the uncertainties in the meteorological forcing and given the limited data for model calibration, the results show a high degree of coherence with observations in terms of stratification and lateral variability. In general, the RMSD between simulations and measurements in the upper 100 m is small and on the order of 0.01 °C in March, on the order of 0.1 °C in April, and less than 1 °C in August. These values of RMSD are fully compatible with model performances in other studies conducted with the use of Delft3D (e.g. Razmi et al. [2013]; Wahl and Peeters [2014]). The positioning of the deepest thermocline is also well simulated at the western station (WS, 60-70 m in March, 40-50 m in April, 10 m in August), and the more homogeneous conditions at the eastern station (ES) are correctly reproduced. While we acknowledge that the model slightly underestimates temperature and stratification in April, we notice that the lake was very weakly stratified in March and April. This fact certainly hampered the simulation of the temperature profiles. In fact, observed vertical temperature and density gradients were about 0.01 °Cm^{-1} and 5×10^{-3} kg m^{-3} m^{-1}, substantially lower - one to two order of magnitude - than the typical thresholds used to identify the well mixed layer (e.g. Read et al. [2011]).

5.1.2.2.1 Simulation of April event In this paragraph the results from the simulation of the April event is chosen as a typical example of cold weather conditions and weakly stratified

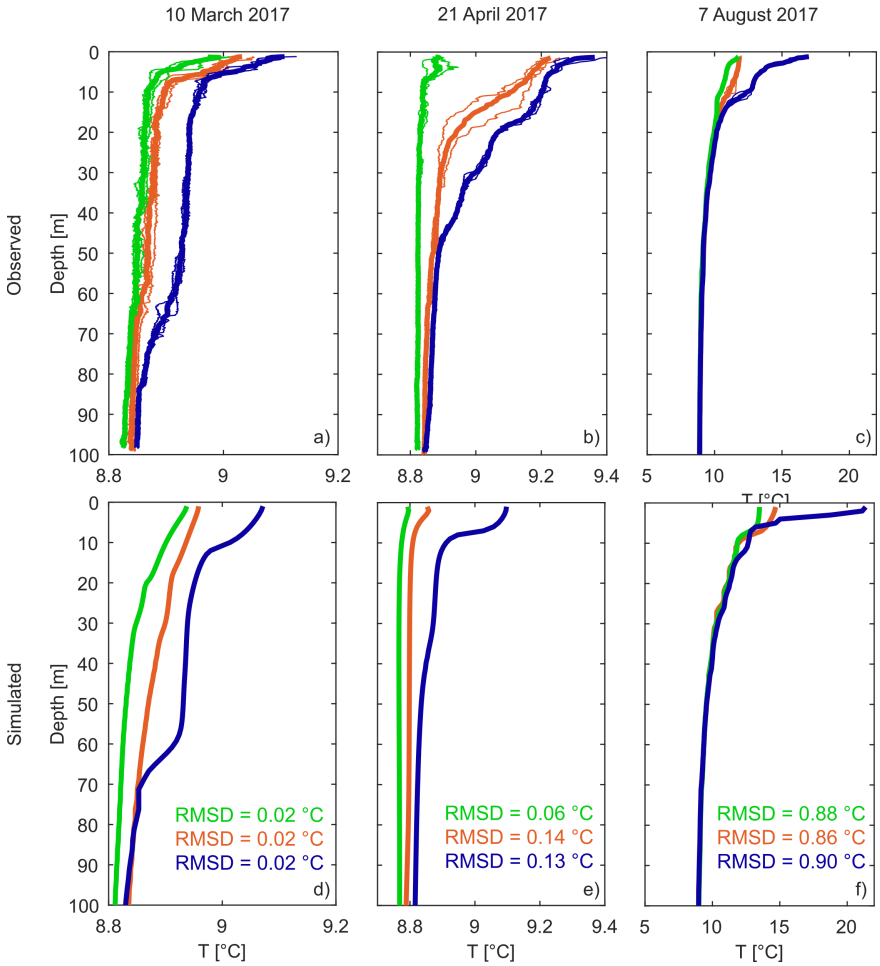

Figure 5.7: Vertical profiles of temperature measured at the three sampling stations (ES, CS, and WS) in the three analyzed periods (a-c) and simulated by the Delft3D model (d-f). The Root Mean Square Error (RMSD) between simulated and observed profiles is also shown.

lake. A similar discussion holds for the March event, which is reported together with August events, but not commented.

Fig. 5.8a shows the simulated water temperature along the model cross-section closest to the reference transect of the monitoring campaign. In addition to temperature, the simulated flow field is also shown. In order to improve representativeness and filter out possible short-time oscillatory effects, numerical results were averaged over a 6-hour period between 00:00 and 06:00 of 21 April, corresponding to the final part of the persistent wind event. Lateral temperature variability is fully consistent with observations in terms of both intensity and vertical extent. The simulated flow field confirms the existence of a significant westward transport within the upper 75 m, associated with a secondary circulation involving almost the whole cross-section.

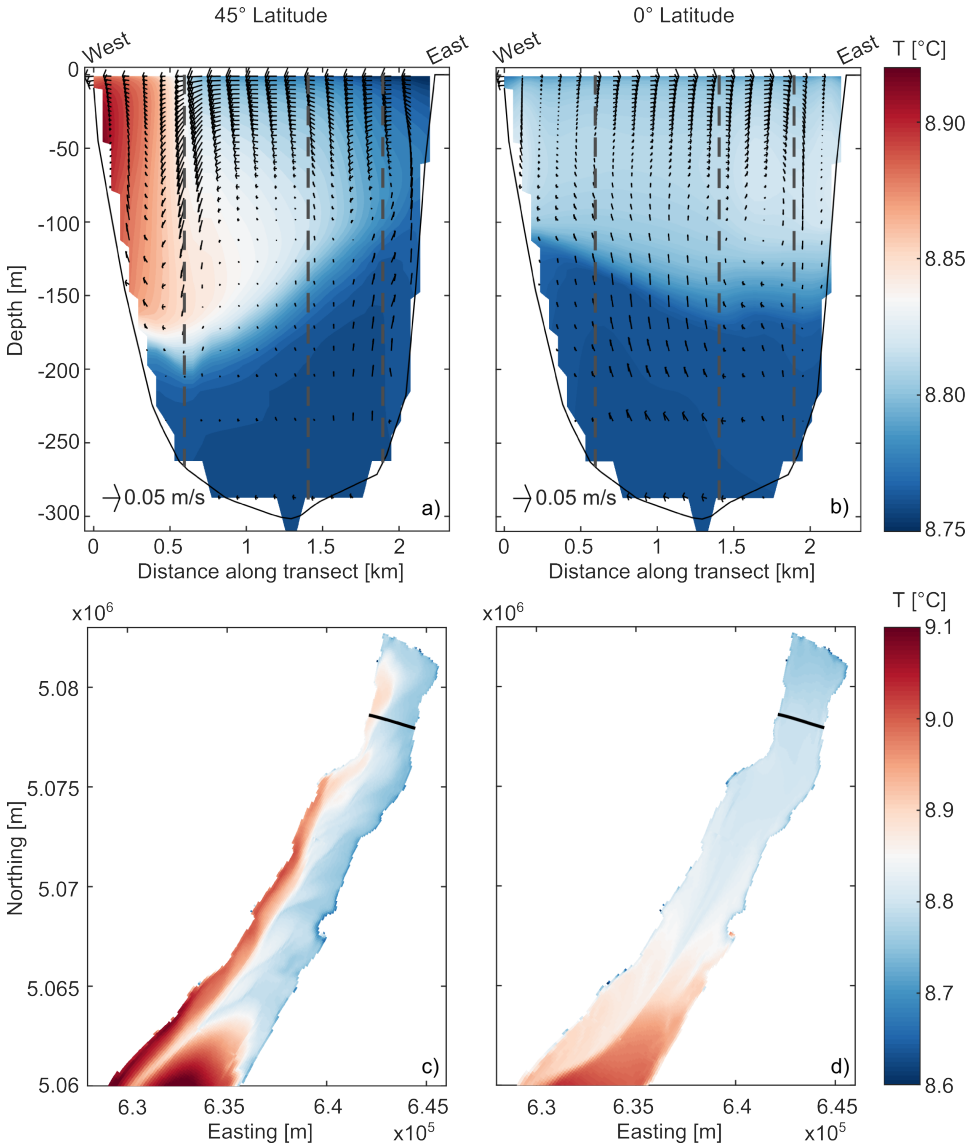

Figure 5.8: Results of thermo-hydrodynamic numerical simulations for the wind event on April 2017. Upper panels: water temperature and flow field (arrows) at the reference transect accounting for (a) and excluding (b) the Coriolis force. Vertical dashed lines indicate the approximate position of the monitoring stations. Lower panels: map of surface water temperature accounting for (c) and excluding (d) the Coriolis force. Black lines indicate the position of the transects shown in subplots a and b.

The general pattern clearly matches that of wind-driven circulation influenced by Earth rotation. In fact, the corresponding averaged wind field over the lake (see Fig. 5.9b for April, a and c for March and August runs) is perfectly aligned with the longitudinal ax of the lake, hence the secondary component of the flow field is not a direct result of the wind forcing.

In order to dispel any doubts in this regard, we performed a twin simulation keeping the same

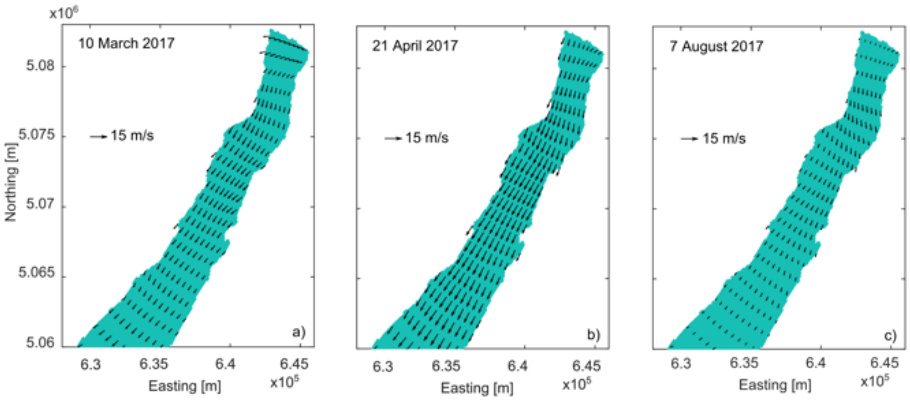

Figure 5.9: Wind fields simulated by the WRF model on 10 March 2017 (a), 21 April 2017 (b), 7 August 2017 (c). Wind fields have been averaged over a 6-hour period coherently with the hydrodynamic results shown in the corresponding Fig. 5.8 and Fig. 5.8

meteorological forcing and model setup, but neglecting the Coriolis acceleration. The numerical results are shown in Fig. 5.8b. The difference is glaring: in the non-rotating case the secondary circulation and the lateral temperature gradient are absent. The same behavior is found in the maps of simulated surface water temperature shown in Fig. 5.8c-d. When the Coriolis effect is included, the entire narrow trunk of the lake is affected by a clear transverse flow that moves warmer surface water westwards. At the eastern shore, surface warm water is replaced by upwelled colder deep water (Fig. 5.8c). In the non-rotating case this effect is absent, and the water circulation is exclusively influenced by spatial heterogeneities of wind field, water temperature, and bathymetry (Fig. 5.8d). Similar results were found in March and April simulations as shown in Fig. 5.10.

In Fig. 5.11 the effect of the secondary flow on deep ventilation is investigated by means of the results of the tracers experiments, for the (actual) rotating case. Results are presented in terms of along-lake distribution of normalized ventilation volume $\eta(i,t)$ (defined as in eq. (5.2), Fig. 5.11a), and maps of mean tracer concentration normalized by C_{surf} relative to V_{isopy} and at time t_2 (Fig. 5.11b).

The ventilation of the water volume below the reference isopycnal surface affects the whole northern trunk of the lake. This phenomenon is the result of lateral flows orthogonal to the wind direction, which are well distributed along the entire region (see Fig. 5.8c). Specifically, significant ventilation of V_{isopy} occurs between 20 km from the southernmost shore and the

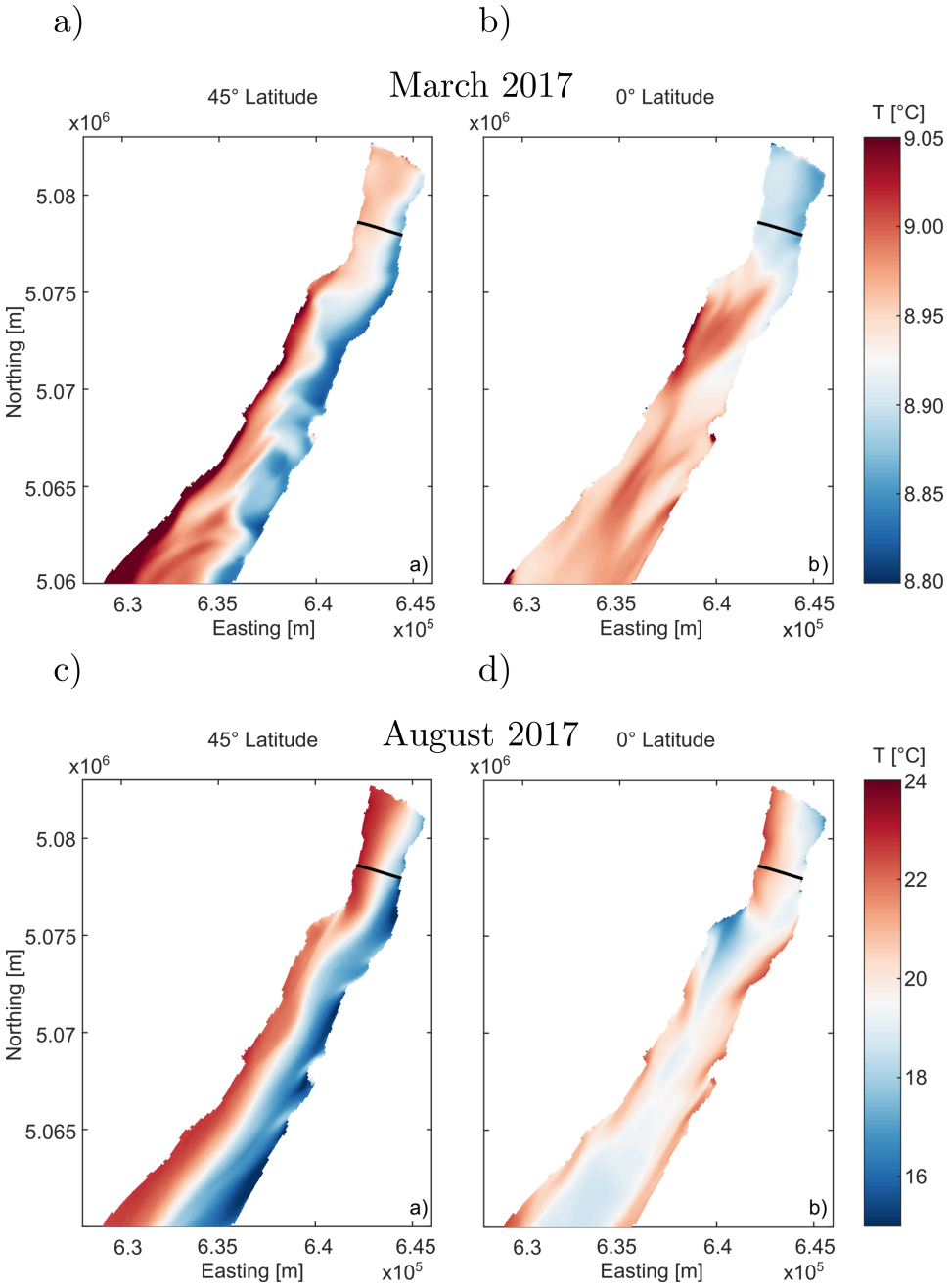

Figure 5.10: Results of thermo-hydrodynamic numerical simulations for the wind event on March 2017 (top plots, averaged over a 6-hour period between 06:00 and 12:00 on 10 March 2017) and August 2017 (bottom plots, averaged between 00:00 and 06:00 on 7 August 2017): map of surface water temperature accounting for (a,c) and excluding (b,d) the Coriolis force.

northern end, corresponding to about the 60% of the lake length. The process shows a progressive intensification in time, according to the initiation and evolution of the wind-driven secondary flows discussed above. In addition, such intensification gradually propagates from the south towards the north end of the lake, consistently with an expected along-lake circulation aligned

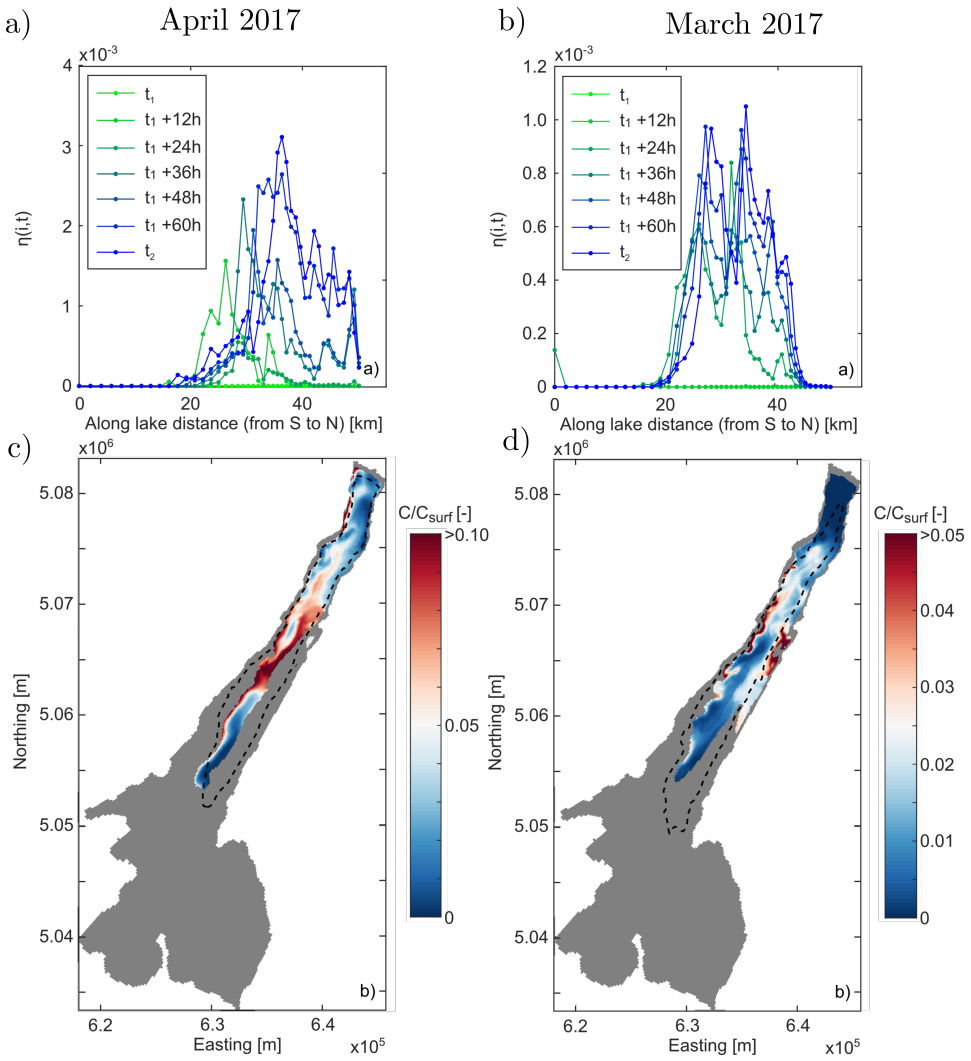

Figure 5.11: Results of the numerical tracer experiment for the wind event on April 2017 (left plots) and March 2017 (right plots). (a,c) Along-lake distribution of the normalized ventilation volume η from the release of the tracer (t_1) to the end of the experiment (t_2). (b,d) map of tracer concentration normalized by C_{surf}, relative to V_{isopy} and at time t_2. The dashed contour in subplot (b) identify the reference isopycnal surface at the initial time t_1.

with the wind forcing. The along lake circulation causes a progressive tilting of the isopycnals, with upwelling at the upwind end of the lake (north) and downwelling at the other end (south). The combined transverse (due to lateral flows, see Fig. 5.8a and c) and longitudinal (due to along-lake circulation) tilting of the isopycnals produces enhanced shear in the thermocline region due to vertical and lateral density gradients. The ispycnal tilt increases after wind relaxes as water masses return to new equilibrium conditions, causing large-scale convective mixing among adjacent water masses. In the southern and wider part of the lake, no deep ventilation is observed, the bathymetry being shallower than the reference isopycnal surface (Fig. 5.11b).

Based on these results, we estimate that after two and four days (i.e., at t_2) of persistent northerly wind (with an average speed of $\sim$ 6.5 m/s), about the 2% and 4% of V_{isopy} are ventilated by wind-driven mixing. Similar results are found for the March simulation, although due to the shorter and weaker wind forcing (see Fig. 5.2) the overall ventilation efficiency η after two and four days was about 1.1% and 1.3%.

The above quantification of deep ventilation efficiency depends on several factors, among which the setup of the tracer exercise (e.g., duration, initial tracer distribution) certainly plays a role. However, this computation gives a rough estimate of the order of magnitude of such deep ventilation.

5.1.3 Discussion

Our results highlight that wind-driven mixing and planetary rotation play a role in the development of along lake and secondary circulations, eventually affecting the deep ventilation in Lake Garda. As anticipated in Chapter 2, long-term analyses suggested that air temperature is the main driver of DMEs in Lake Garda [Salmaso et al., 2017], and observed that such phenomena have become less frequent in the past three decades, with important consequences for water quality in terms of nutrients and oxygen distribution. However, the deep warmth and the dilution (in terms of conductivity) seen in the profiles in Fig. 5.3 suggest that DMEs occurred after March 2017 and were most likely driven by the wind. In fact, the formation of progressively steeper profiles is not compatible with diffusive processes alone, and we have seen that strong wind events occurred between March and April 2017 in Fig. 5.2. The process causing the observed DMEs can be furthermore explored by computing the heat flux to the lake during this period. The net heat flux ϕ_n at the lake-atmosphere interface is here calculated using the meteorological variables from ground stations and by means of the Lake Heat Flux Analyzer code [Woolway et al., 2015].

In Fig. 5.12 we report the time series of the cumulative heat per unit area exchanged between the lake and the atmosphere after 1 January 2017: $E(t) = \int \phi_n dt$, where t is time. Decreasing trends in E mean negative net heat flux to the lake (cooling), while increasing trends mean positive heat flux to the lake (warming). As the figure clearly shows, winter cooling occurred

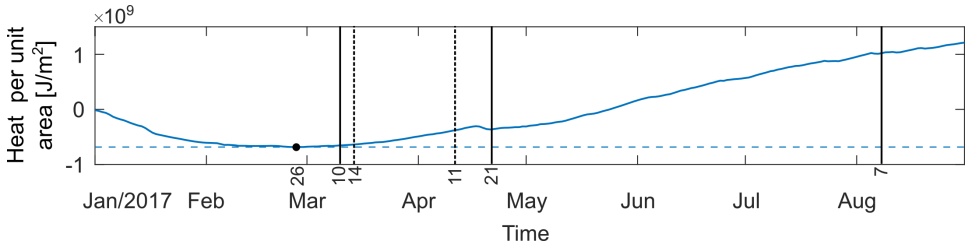

Figure 5.12: Cumulative net heat flux per unit area exchanged between the lake and the atmosphere after 1 January 2017. The black dot represents the end of the cooling period (end of February), while vertical lines indicate the sampling dates from our field campaign (continuous) and from ARPAV (dashed).

until end of February (black dot), thereafter the lake started to warm up, hence the occurrence of buoyancy-driven DMEs can be also excluded and the existence of wind-driven flows can be inferred as an additional, previously not recognized, ventilation mechanism.

Moreover, our results show that planetary rotation is responsible for the existence of lateral temperature and chlorophyll-a gradients in the elongated and deep trunk of Lake Garda. The combined effect of rotation and closed boundaries at the shores generates a secondary circulation which leads to up- and downwelling mechanisms and causes the observed lateral gradients. Such secondary flows were theoretically analyzed for homogeneous density conditions in elongated rotating basins [Winant, 2004; Ponte, 2010; Toffolon, 2013] and were hypothesized as possible deep ventilation mechanism in large lakes such as Lake Baikal [Boehrer and Schultze, 2008; Schmid et al., 2008; Piccolroaz and Toffolon, 2013b, 2018], where the effect of Earth rotation is undoubtedly present. However, their effects had so far never been explicitly observed in relatively small narrow and deep lakes, where their presence was often considered unlikely (e.g. [Tsimitri et al., 2015]).

It is clear that an elongated shape favors the development of persistent one-directional winds, which is a key condition for the existence of such secondary flows. The magnitude of such secondary flows and associated DMEs versus relevant parameters of a lake such as geometry, bathymetry, thermal stratification (e.g., thermobaric effects), latitude, and wind-stress forcing remains to be quantified. For example, by analyzing some deep Norwegian thermobarically stratified fjord lakes, [Boehrer, 2013] found a close relationship between ventilation due to deep water formation and lake length. However, classical analytical solutions for finite or infinite domains exist, and suggest that wind-driven lateral transport due to the Coriolis force depends

on the square of the wind speed [Hutter et al., 2011b], a relationship that was confirmed also in the preliminary numerical study of the transport processes in Lake Garda [Amadori et al., 2018, see also chapter 4] .

In this regard, it should be noted that the ventilation efficiency of buoyancy-driven DMEs is certainly larger than that resulting from wind-driven mixing, which has been estimated here. However, the observed climate-induced decrease in buoyancy-driven DMEs due to global warming [Salmaso et al., 2017] suggests that the relative importance of these two processes causing DME may change in the future. In fact, despite the relatively small ventilation efficiency of an isolate wind-driven DME, intense and long-lasting wind events are abundant in the winter season in the perialpine region [de Franceschi and Zardi, 2009]. In Fig. 5.13 we report the frequency of occurrence (a), the duration (b) and the average wind velocity(c) of significant wind events defined as persistent events with the along-lake component of wind speed larger than 5 m s^{-1} (considering the 1-day moving average) for at least one day. Statistics refer to the meteorological stations in Limone del Garda-M1 during the weak stratification period (February to April).

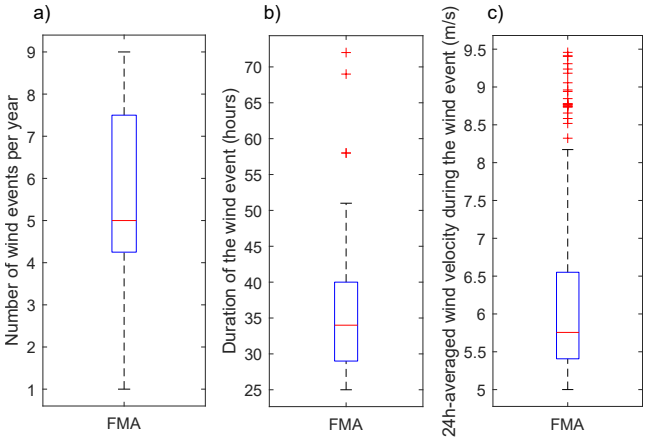

Figure 5.13: Statistics of significant wind events measured at Limone (M1) weather station: a) number of events occurring per year; b) duration of the wind events; c) wind velocity along the longitudinal axis of the lake.

The figure shows that wind events of the kind observed in March and April 2017 are very common during the unstratified period in Lake Garda, as they occur on average 5 times per year, with a mean duration of 34 hours and with an average wind speed (over one day) between 5.5 and 6.5 ms^{-1}. In order to have a rough estimate of the potential contribution of the wind-driven DMEs, we refer to the statistics of the three events investigated here, and define as a significant event the persistence of a wind speed larger than 5 m s^{-1} (considering the 1-day moving average

of the along-lake component of wind speed) for at least one day. The analysis of the historical records for the M1 meteorological station (seven years, from 2012 to 2018) evidenced that the winter period (i.e., February-April) is characterized by the occurrence of 5 significant wind events per year (median value; 25^{th}-75^{th} percentiles: 4–8 events), with a duration of 34 h (median value; 25^{th}-75^{th} percentiles: 29–40 h) and intensity of 5.8 m s^{-1} (median value; 25th-75th percentiles: 5.4–6.6 m s^{-1}). Thus, considering the estimates of η for the single March and April events, and despite the inherent uncertainty associated to them, the exchanges between surface and deep waters may be larger than expected, and in any case should be compared to absence of buoyancy-driven DMEs since 2006.

5.1.4 Conclusions

In this chapter, we provided observational and numerical evidence of the occurrence of secondary circulations induced by Earth rotation and we attempted a first quantification of their effect on mixing efficiency in deep Lake Garda. The existence of such flows has several implications for the hydrodynamics and ecosystem of lakes. In fact, they are associated with lateral but also deep vertical transport of energy and mass along the entire elongated basin, causing basin-wide DMEs that contribute to the exchange of oxygen and nutrients (but also contaminants) between surface and deep water layers. Improving our understanding of these processes is henceforth required, in order to assess to what extent wind-driven ventilation and the more ordinary buoyancy-driven convective mixing combine to prevent deoxygenation and eutrophication. Importantly, secondary flows were observed also in stratified conditions in summer (albeit with a smaller vertical extent), indicating their year-round importance for transport processes in the lake. Finally, our analysis suggests that identifying all the drivers of DMEs is a necessary step towards determining the impact of climate change on the ecosystem functioning of Lake Garda, an issue that should be high on the agenda of regional policy makers, considering the environmental and economic (for tourism in particular) importance of this water resource.

Acknowledgements We thank Circolo Vela Arco for logistic support, and in particular Alessandro Bottazzi and Walter Merighi for their dedication to the fieldwork. We are grateful to Lorenzo Giovannini (UniTN) for providing the WRF simulations, Menno Genseberger (Deltares)

for his initial work on the Delft3D model of Lake Garda, and Michael Kliphuis (IMAU, UU) for his help with the Delft3D simulations. We thank Giorgio Franzini and Giovanna Pellegrini for discussion on the data. Part of the simulations were carried out on the Cartesius supercomputer at SURFsara (www.surfsara.nl) through the project SH284.

Chapter 6

Ekman transport in elongated lakes

Contents

This Chapter is based on:

Amadori, M., Piccolroaz, S., Dijkstra, H. A., and Toffolon, M. What makes an elongated lake 'large'? Scales from wind-driven steady circulation on a rotating Earth. *Journal of Great Lakes Research*, 2019. ISSN 0380-1330. doi: 10.1016/j.jglr.2019.10.013

6.1 Introduction

The results presented in the previous chapters outlined a key contribution of the Earth rotation on basin scale circulation and mixing regime. In this chapter, we go deeper into the theoretical definition of this contribution.

The role of Earth rotation on three-dimensional circulation in an ocean is a rather classical subject after the seminal contribution by Vagn Walfrid Ekman at the beginning of the twentieth century [Ekman, 1905]. Assuming steady and uniform conditions in a horizontally infinite water body, he derived an analytical solution for the vertical distribution of the horizontal velocity induced by the wind stress at the surface. Ekman found that the resulting volume transport is oriented perpendicular to the wind stress, a simple observation with profound consequences. In fact, his solution was further extended to more complex conditions by the oceanographic community, with few contributions focusing on the quantification of the transport in closed water bodies such as lakes.

When investigating the circulation in enclosed or semi-enclosed basins, the inclusion/exclusion of the Earth rotation as a relevant process often produces some ambiguity. It is a common assumption in limnological studies that Earth rotation is relevant only in 'large' water bodies, while it can be neglected in relatively 'small' ones. The origin of this assumption is twofold: first, it comes from the literature on gravity waves and density-driven currents in rotating water bodies, where the horizontal extent of the basin is compared to the Rossby radius. Secondly, it comes from the fact that the Ekman problem was initially designed for the case of infinitely wide ocean, far enough from boundaries.

On the first point, there are a number of situations where the relevance of Earth rotation can be assessed referring to the Rossby number,

$$\mathrm{Ro} = \frac{R}{L}\,, \tag{6.1}$$

with R being the Rossby radius and L the characteristic horizontal size. The Rossby radius is often computed as $R = U/f$, where U is a typical scale of flow velocity and $f = 2\Omega \sin\phi$

the Coriolis parameter, with Ω the angular frequency and ϕ the latitude on Earth. A different definition of Ro is based on the so-called Rossby radius of deformation, $\widetilde{R} = c/f$, where $c = \sqrt{gH}$ is the celerity of the barotropic wave, with g the gravitational acceleration and H the depth [Rossby, 1937]. If baroclinic waves are considered, $c = \sqrt{g' H_1 H_2/H}$, with g' the reduced gravity in stratified conditions and H_1 and H_2 the thicknesses of a two-layer stratification, such that $H = H_1 + H_2$ [Rossby, 1938]. Based on the traditional scaling analysis, water bodies smaller than R (i.e., Ro > 1) are not significantly affected by rotation, and the Coriolis acceleration is considered important only if Ro < 1 [Gill, 1982]. Such a scaling, which was formulated for oscillatory motions induced by the Earth rotation, was next extended to basin-scale circulation and vertical current structure in lakes [Hutter et al., 1991; Rueda and Vidal, 2009]. In this respect, we note that the existence of different definitions of the Rossby number, which depend on the phenomenon under investigation, may generate some confusion.

Concerning the second point, i.e. the legacy of the original formulation of the Ekman problem in an infinite domain [Ekman, 1905], several generalizations of the theory have been proposed to describe the effect of Earth rotation on steady circulation in enclosed or semi-enclosed basins, with relevant contributions in the field of estuarine and coastal oceanography. In several of these contributions, the so-called Ekman depth

$$D_E = \sqrt{\frac{2\nu_z}{f}} \tag{6.2}$$

is introduced as the relevant scale, with ν_z a reference value of the vertical viscosity, and the Ekman number, i.e. the ratio Ek $= H/D_E$, enters into several analytical solutions. It is argued [Kasai et al., 2000] that, when Ek is small (i.e., $H \ll D_E$), the whole water column is inside the Ekman layer and the flow is governed by viscosity; when Ek is large ($H \gg D_E$), the effect of Coriolis force becomes important.

Hence, two different dimensional parameters seem to describe the role of Earth rotation on steady circulation in closed domains. One of them (Ro) depends on the horizontal scales and the other one (Ek) on the vertical scales. The question arises as to what makes a lake 'large', such that we should include the Coriolis acceleration when investigating steady circulation? The answer to this relevant question is not clear-cut.

6.2 Literature review on Ekman transport

A brief review of the state of the art about the effect of Earth rotation on steady circulation in lakes can be useful to frame the analytical problem and to get rid of any prejudice on its application to enclosed real basins. The original work of Ekman [1905] was derived for infinitely deep and wide rotating systems (as the ocean can be approximated) subject to constant and uniform wind. To the other extreme, analytical solutions were proposed for idealized narrow rectangular lakes [e.g. Heaps and Ramsbottom, 1966] or enclosed basins with variable bathymetry [e.g. Csanady, 1982], but neglecting the effect of rotation. The path from the original solution of Ekman to the description of steady currents in real enclosed basins was certainly long, but for the range of intermediate conditions several generalizations of the original Ekman theory have been proposed (see also Simons [1980], Hutter et al. [2011a] and Defant [1962] for a review). Finite-depth and time-dependent solutions followed the initial suggestion by Ekman [Fjeldstad, 1930; Hidaka, 1933; Platzman, 1963; Madsen, 1977], together with the inclusion of horizontal pressure gradients associated to wind set up [Welander, 1957; Birchfield, 1972], which were particularly relevant for the case of enclosed basins and were successfully applied to describe circulation in large lakes [Gedney and Lick, 1972]. Additional complexity was added by taking into account density stratification [Lee and Ligget, 1970], with relevant contributions from estuarine studies [Kasai et al., 2000; Valle-Levinson et al., 2003], and non constant vertical turbulence [Thomas, 1975; Madsen, 1977; Svensson, 1979]. A few analytical studies specifically focused on narrow, elongated and deep basins (such as glacial and rift valley lakes) with homogeneous water, which is a condition that dimictic lakes experience twice a year. For these lakes, some analytical works predict the development of intense closed circulation, orthogonal to the wind direction and forced by the presence of lateral boundaries, with consequent significant coastal up- and down-welling [Simons, 1980; Winant, 2004; Ponte, 2010; Toffolon, 2013].

Analytical, numerical and observational studies followed to define the role of Earth rotation on horizontal and vertical circulation in closed basins, with diverse and sometimes contradictory results which enhanced the confusion on the relevant length scales. In estuarine applications, the lateral distribution of the flow in semi-enclosed basins was well investigated by a wide number of studies. To the purposes of the present work, a milestone is represented by the analytical

study of Kasai et al. [2000], who questioned the conventional assumption of the Rossby radius as a predictive parameter for the development of rotational currents. They demonstrated that Earth rotation can be less important than density gradients also in basins where the width is larger than Rossby radius. In order to quantify the effects of Coriolis acceleration in steady circulation, they used the Ekman number Ek. The main conclusion of their work was that when Ek is small (i.e., $H < D_E$), the whole water column is inside the Ekman layer and the flow is governed by viscosity effects. When Ek is large ($H > D_E$), a part of the water column is not in geostrophic balance and is affected by Coriolis force. Following this result, the numerical work by Sanay and Valle-Levinson [2005] confirmed that in homogeneous, rotating basins the Ekman depth is a predictive scale for the development of transverse circulation, as those predicted by Winant [2004]. This achievement was then extended to the stratified case by Valle-Levinson [2008], where the relative importance of the width and depth of the basin was discussed for density-driven exchanges. Some years later, Ponte et al. [2012] observed a similar transverse circulation in the Gulf of California. In the same context, Cheng and Valle-Levinson [2009] compared the magnitude of lateral advection and Coriolis acceleration by means of numerical experiments in basins of different sizes. By quantifying the terms of the momentum equation as functions of Ekman and Rossby numbers, they observed that lateral advection is relevant in narrow and deep basins (large Ro and Ek) and decreases with mixing (large ν_z), while the relevance of the Coriolis term increases in wider basins (small Ro) and is less sensitive to the depth.

Earth rotation was also taken into account for investigating gravity currents caused by riverine intrusions (we refer to Griffiths [1986] for an extensive review). In particular, interesting studies on relatively narrow lakes in unstratified [Pilotti et al., 2018] and stratified [Laborde et al., 2010] conditions revealed the existence of relevant deflections of the river plume to the right-hand shoreline (in northern hemisphere). The scaling suggested by the authors was based on Rossby radius, computed as U/f where U was taken as the inflow velocity. Despite the limited width of the basins, the Rossby number in the cited works was found to be much smaller than 1, as the inflow velocity was extremely low (generally ~ 1 cm/s), hence Coriolis acceleration acts on the flow path of riverine intrusions in the same way as for inertial currents.

The relative importance of the internal wave field vs geostrophic currents (i.e., density strat-

ification vs steady state currents) was investigated in oceans [Veronis, 1956] and enclosed basins [Stocker and Imberger, 2003] through analytical approaches based on energy partitioning [Antenucci and Imberger, 2001] as a function of the Burger number $S = N\,H/(f\,L)$, with N the buoyancy frequency. By splitting the total energy budget into a geostrophic component and a set of cyclonic and anticyclonic waves, these studies found that low Burger numbers and long lasting winds were the condition for the geostrophic component to dominate on density driven waves, but the effect of Earth rotation on the steady geostrophic current was not taken into account.

Besides the studies based on the size of the basin, some analyses focused on the role of time scales for the rotational response of the basin. Amongst these, Mohammed-Zaki [1980] solved analytically the momentum and continuity equations under the assumptions derived from Ekman theory in the case of deep basins ($\mathrm{Ek} \gg 1$) and observed that the steady state solution is achieved under uniform wind forcing after a diffusive time scale proportional to the Ekman number and independent on the horizontal extent of the lake. An inverse frictional timescale, scaled again with the Ekman number, was then introduced by Dever [1997], controlling the vertical structure of the wind-driven response to the Earth rotation in the cross-shelf circulation of the Northern California Shelf. Differently, Ponte [2010] linked the rotational response of the basin to the frequency of the wind forcing in such a way that the Ekman transport is triggered only in the 'sub-inertial range', when the frequency of the wind forcing is smaller than inertial frequency.

Interestingly, also the contributions described above were made under the assumption that the horizontal dimension of the basin is smaller than the barotropic Rossby radius of deformation. However, we should recall that "it is not just the horizontal extent of a basin, but its depth which dictates whether the Earth rotation affects the circulation of a water body" [Hutter et al., 2011a]. Hence, shall we include the Coriolis acceleration when investigating steady circulation in relatively small lakes? And what does "small" mean? Citing Hutter et al. [2011a] again, few kilometers horizontal extent seem to be enough for rotational effects to be relevant in a basin of at least 50 m depth. Nevertheless, since a horizontal scale other than the Rossby radius (whatever defined) is still missing, the issue on the meaningful scales for wind-driven steady currents in enclosed basins on a rotation Earth is still open and deserves a conclusive answer we tried to give in this chapter.

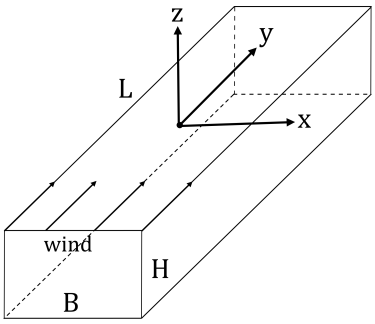

Figure 6.1: Sketch of the simplified domain and wind forcing directed along the longitudinal axis of the lake.

6.3 Modified Ekman solution for idealized basins

In order to interpret lake steady circulation dynamics induced by rotation, we derive a simple analytical solution to be applied to all latitudes and to a wide range of lake sizes. The analytical solution is compared with numerical results to demonstrate its consistency and to investigate the role of some specific aspects such as the horizontal and vertical size of the basin, the bottom boundary condition, the turbulence model and the turbulence anisotropy on the resulting steady circulation.

6.3.1 Mathematical formulation for no-slip bottom boundary condition

In our analytical solution we assume an idealized rectangular domain of elongated shape characterized by length L along the main longitudinal axis (y), width B along the crosswise axis (x), and depth H along the vertical axis (z). The Cartesian reference system is centered in the middle of the lake surface (Fig. 6.1), with the z-axis pointing upward.

We describe the flow with the Reynolds-averaged Navier Stokes equations in hydrostatic approximation (6.3)-(6.6) for a fluid of uniform density,

$$\frac{\partial u}{\partial t} + u\frac{\partial u}{\partial x} + v\frac{\partial u}{\partial y} + w\frac{\partial u}{\partial z} = fv - \frac{1}{\rho}\frac{\partial p}{\partial x} + \frac{\partial}{\partial x}\left(\nu_h \frac{\partial u}{\partial x}\right) + \frac{\partial}{\partial y}\left(\nu_h \frac{\partial u}{\partial y}\right) + \frac{\partial}{\partial z}\left(\nu_z \frac{\partial u}{\partial z}\right), \quad (6.3)$$

$$\frac{\partial v}{\partial t} + u\frac{\partial v}{\partial x} + v\frac{\partial v}{\partial y} + w\frac{\partial v}{\partial z} = -fu - \frac{1}{\rho}\frac{\partial p}{\partial y} + \frac{\partial}{\partial x}\left(\nu_h \frac{\partial v}{\partial x}\right) + \frac{\partial}{\partial y}\left(\nu_h \frac{\partial v}{\partial y}\right) + \frac{\partial}{\partial z}\left(\nu_z \frac{\partial v}{\partial z}\right), \quad (6.4)$$

$$\frac{1}{\rho}\frac{\partial p}{\partial z} + g = 0\,, \quad (6.5)$$

$$\frac{\partial u}{\partial x} + \frac{\partial v}{\partial y} + \frac{\partial w}{\partial z} = 0\,, \quad (6.6)$$

where u, v and w are the three components of the velocity vector, t is time, p is pressure, and g is the acceleration due to gravity. The Reynolds stresses were closed using the Boussinesq formulation, where the eddy viscosity tensor is assumed anisotropic, with the vertical ν_z smaller than the horizontal ν_h. Following the standard derivation originally proposed by Ekman [1905], we consider a steady state with constant in time and uniform in space eddy viscosities. While Ekman neglected the pressure gradient, we retain it following more elaborate solutions that take into account the effect of geostrophic gradients [e.g., Welander, 1957]. In the original formulation of the Ekman problem for an unbounded domain, horizontal gradients of velocity were neglected and all the non-linear advection terms, as well as horizontal diffusion terms, vanished giving a linearized version of the RANS. Following this simplification, standard solutions extended the linearized equations of motion also to the case of closed domains [Hutter et al., 2011a; Simons, 1980]. However, we note that in presence of lateral boundaries, the assumption of horizontal uniformity is not necessarily valid and must be verified. Toffolon and Rizzi [2009] demonstrated via a dimensional scaling that longitudinal gradients can be neglected in the central trunk of non-rotating elongated lakes, while Toffolon [2013] showed that in the rotating case also the crosswise gradients are negligible as a first approximation on condition that we focus on the central part of the cross section. Under such an approximation we simplify Eq. (6.3), (6.4) and (6.6) removing the non-linear advective and diffusive terms depending on horizontal gradients of velocity. As a consequence, in the central part of the domain the continuity equation reduces to $\frac{\partial w}{\partial z} = 0$, which gives $w = 0$ under a rigid lid approximation. As a result of these assumptions, also the non-linear advective terms and $w\frac{\partial u}{\partial z}$ disappear and the problem to be solved reduces to a system of two linear equations depending only on the vertical direction and on the two components of the slope of the free surface z_t:

$$\nu_z \frac{\partial^2 u}{\partial z^2} + fv = g\frac{\partial z_t}{\partial x}\,, \quad (6.7)$$

$$\nu_z \frac{\partial^2 v}{\partial z^2} - fu = g \frac{\partial z_t}{\partial y}\,, \tag{6.8}$$

The originally three-dimensional problem is simplified into a one-dimensional (1D) problem of momentum transfer along the vertical direction z from the surface to the bottom (left-hand side of the equations), with the barotropic pressure gradients on the right-hand side to be determined. The first problem alone is nothing but the traditional vertical Ekman problem, where friction determines the vertical distribution of momentum to balance the Coriolis acceleration and is independent of the lateral walls. The second problem interacts with the horizontal boundaries of the domain, whose presence provides the relations needed to determine the value of barotropic pressure gradients.

The two second-order differential equations are complemented with suitable boundary conditions. Referring again to standard solutions, here we assume uniform wind stress at the surface ($z = z_t$),

$$\left.\frac{\partial u}{\partial z}\right|_{z=z_t} = \frac{\tau_x}{\rho \nu_z}\,, \qquad \left.\frac{\partial v}{\partial z}\right|_{z=z_t} = \frac{\tau_y}{\rho \nu_z}\,, \tag{6.9}$$

and no-slip condition at the bottom ($z = z_b$),

$$u|_{z=z_b} = 0\,, \qquad v|_{z=z_b} = 0\,. \tag{6.10}$$

In Eq. (6.9), τ_x and τ_y are the two components of wind tangential stress $\boldsymbol{\tau} = (\tau_x, \tau_y)$, where $\boldsymbol{\tau}{=}\rho_a C_d |\mathbf{U_w}| \mathbf{U_w}$, ρ_a is the air density, C_d the drag coefficient, and $\mathbf{U_w}$ is the wind velocity vector at 10 m above the water surface.

The differential problem composed by (6.7)-(6.8) with boundary conditions (6.9) and (6.10) is mathematically closed if the surface slope $(\partial z_t/\partial x, \partial z_t/\partial y)$ is provided. The original solution neglected it due to the assumption of infinite domain [Ekman, 1905], while following contributions imposed it in the form of external geostrophic pressure gradients [Welander, 1957].

In our approach, we do not assume any external value of the surface slope, but we compute the value that satisfies the condition of vanishing volume transport across any surface separating the closed domain in two parts in the steady state. A similar condition was applied by Simons [1980] solely along the crosswise direction for the case of narrow and elongated basins, by Heaps [1984]

along the longitudinal in the non-rotating case. Kasai et al. [2000] assumed the same condition in both directions to estimate surface slope in regions of freshwater influence (ROFI). In his solution he derived the horizontal velocity by decomposing it into two terms: the unidirectional barotropic component, driven by surface slope, and the bidirectional baroclinic motion due to the density gradient between the sea and the river inflow. For estimating slope, he attributed null volume transport ($m^3 s^{-1}$) along or across a cross section by assuming that river discharge is negligible compared to the flow induced by wind and Coriolis force. Such an assumption was then defined as a limit case by Valle-Levinson et al. [2003], who extended the solution by Kasai et al. [2000] to more complex cases of estuary–ocean exchange areas. As in Kasai et al. [2000], here we assume that the vertical integral of horizontal velocity is zero, as a direct consequence of the presence of closed boundaries when the free surface does not change in time: the volume of any region of the domain cannot change and the incoming transport must be balanced by the outgoing one [Toffolon and Rizzi, 2009]. The physical consistency of such assumption is also supported by Mohammed-Zaki [1980]. In fact, by solving analytically the case of uniform wind stress applied to a closed domain (in his case limited to $E_k << 1$), he demonstrated that the resulting steady current is horizontal far enough from the boundaries and has null vertically integrated transport. Hence, focusing again on the central part of the domain, we simplify this condition by assuming a local integral condition:

$$\int_{z_b}^{z_t} u\, dz = 0\,, \qquad \int_{z_b}^{z_t} v\, dz = 0\,. \tag{6.11}$$

6.3.1.1 Derivation of the solution

Introducing the complex variable $W = u + i\, v$, the problem composed by equations (6.7)-(6.11) can be cast in a more compact form:

$$\nu_z \frac{\partial^2 W}{\partial z^2} - i\, f\, W = g\, S\,, \tag{6.12}$$

$$\left.\frac{\partial W}{\partial z}\right|_{z=z_t} = \frac{T}{\rho \nu_z}\,, \qquad W|_{z=z_b} = 0\,, \tag{6.13}$$

$$\int_{z_b}^{z_t} W\, dz = 0\,, \tag{6.14}$$

where $T = \tau_x + i\,\tau_y$ and $S = \partial z_t/\partial x + i\,\partial z_t/\partial y$.

To formulate the problem (6.12-6.14) in dimensionless form, we introduce:

$$\mathcal{T} = \frac{T}{T_0}\,, \qquad \omega = \frac{W}{U_0}\,, \qquad \sigma = \frac{S}{S_0}\,, \tag{6.15}$$

with the scales

$$T_0 = \sqrt{\tau_x^2 + \tau_y^2}\,, \qquad U_0 = \frac{T_0 H}{\rho \nu_z}\,, \qquad S_0 = \frac{T_0}{\rho g H}\,. \tag{6.16}$$

Finally, we introduce a boundary-fitted vertical coordinate

$$\zeta = \frac{z_t - z}{H}\,, \tag{6.17}$$

where $H = z_t - z_b$. We note that the axis ζ is directed downward (while z is pointing upwards), with $\zeta = 0$ at the surface and $\zeta = 1$ at the bottom, following a common notation [e.g., Hutter et al., 2011a].

As a result, the dimensionless form of the problem (6.12-6.14) becomes

$$\frac{\partial^2 \omega}{\partial \zeta^2} - i\,\varepsilon^2\,\omega = \sigma\,, \tag{6.18}$$

$$\left.\frac{\partial \omega}{\partial \zeta}\right|_{\zeta=0} = -\mathcal{T}\,, \qquad \omega|_{\zeta=1} = 0\,, \tag{6.19}$$

$$\int_0^1 \omega\, d\zeta = 0\,, \tag{6.20}$$

where the single dimensionless parameter

$$\varepsilon = \sqrt{\frac{f H^2}{\nu_z}} = \sqrt{2}\,\mathrm{Ek} \tag{6.21}$$

governs the problem ($\mathcal{T}$ indicates the wind direction only, so that $|\mathcal{T}| = 1$).

The two complex numbers obtained as integration constants from the integration of (6.18) can be determined using the two boundary conditions (6.19) if the value of σ is prescribed. This is the case of the traditional Ekman solution, whereby $\sigma = 0$, or when the surface slope is determined from a geostrophic balance [Simons, 1980]. For a flow determined solely by wind

set up of the water level (excluding any rotational effect) and no-slip conditions at the bottom, $\sigma = 3/2\,\mathcal{T}$ and the free surface is tilted in the direction of the wind [e.g., Heaps, 1984; Toffolon, 2013].

The general solution to the dimensionless problem (6.18-6.19) can be written as a function of σ (whatever prescribed or solved) and ε as follows:

$$\omega(\zeta) = \frac{\sin\left[\Theta\,(\zeta-1)\right]}{\Theta\,\cos\Theta}\,\mathcal{T} + \left[\frac{1-\cos\left(\Theta\,\zeta\right)}{\cos\Theta}\right]\,\frac{\sigma}{\Theta^2}\,, \tag{6.22}$$

where $\Theta = \frac{\sqrt{2}}{2}\varepsilon\,(1-i)$ and, hence, $\varepsilon^2 = i\,\Theta^2$. As it is clear from Eq. (6.22), the solution is explicitly dependent on the free surface inclination expressed by the parameter σ.

In the case of closed lakes in steady conditions, Eq. (6.20) applies and forces the value of σ to respect the requirement of vanishing volume transport as

$$\sigma = \mathcal{T}\,\Theta\,\frac{1-\cos\Theta}{\sin\Theta - \Theta\,\cos\Theta}\,. \tag{6.23}$$

From now on, the proposed solution, characterized by the integral condition valid for a closed boundary case, will be referred to as A2019. Hereafter, we refer to a wind aligned with the main axis of the lake ($\mathcal{T} = i$), such that the longitudinal y direction is also the along-wind direction and the imaginary part of the complex variables, while the crosswise x is the across-wind direction and the real part of the complex variables.

The behavior of the real (σ_x) and imaginary (σ_y) part of σ is represented in Fig. 6.2 as a function of ε. It immediately appears that the longitudinal components σ_y (Fig. 6.2a) ranges from 1 to 3/2 with a trend that is consistent with Simons [1980] in the case of narrow and elongated basins. In the crosswise direction, the surface slope σ_x (Fig. 6.2b) vanishes at the extremes of the ε range and has a bell shape suggesting that rotation plays a role on the crosswise component only in an intermediate range of H, f and ν_z.

The behavior of the surface velocity obtained from Eq. (6.22) by imposing $\zeta = 0$ is plotted in Fig. 6.3 and compared with the Ekman solution (E1905) in the finite-depth version.

The longitudinal velocity ω_y (i.e. the imaginary part of the complex dimensionless velocity

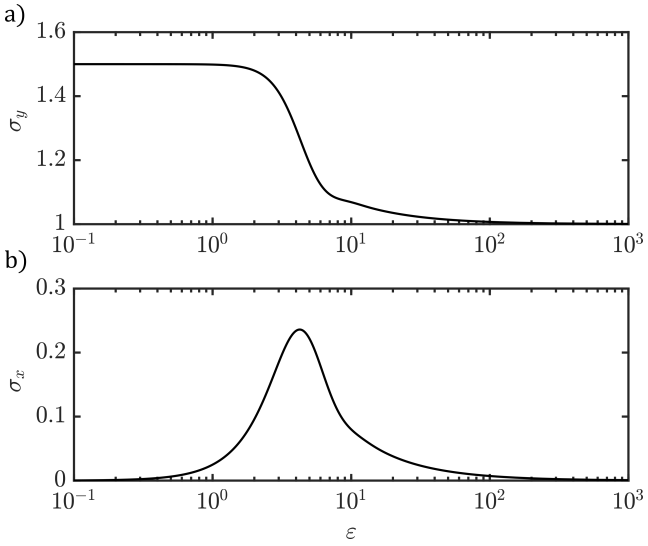

Figure 6.2: Surface slope rescaled with the reference values S_0 from A2019 analytical solution: (a) longitudinal component σ_y, and (b) crosswise component σ_x. Wind aligned with the y axis, no-slip bottom boundary condition.

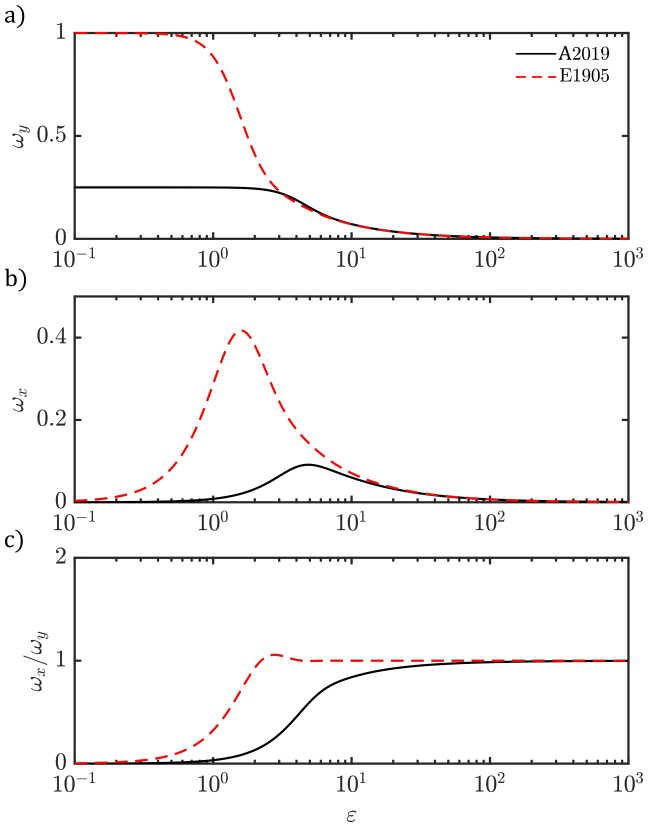

Figure 6.3: Dimensionless surface velocity obtained from the analytical solutions A2019 and E1905: (a) longitudinal component ω_y , (b) crosswise component ω_x, and (c) direction. Wind aligned with the y axis, no-slip bottom boundary condition.

ω) is not affected by the Coriolis force for $\varepsilon < 1$ (Fig. 6.3a), while it starts being decelerated in favor of the crosswise flow ω_x for higher values of ε (Fig. 6.3b). In the range of ε where ω_x increases, ω_y decreases until the same magnitude is reached and the surface water moves at 45° to the right of the wind (Fig. 6.3c) as in the Ekman spiral theory. It is easily understood that the classical Ekman approach correctly describes the motion for large values of ε (deep lakes, high latitudes and/or weak mixing regimes), but it overestimates the velocity in both directions within the range of lower ε.

6.3.1.2 Limiting cases

Two limiting cases can be conveniently analyzed depending on the value of ε. First, we consider the case of very shallow lakes, where the shallowness is defined with respect to the Ekman depth ($H \ll D_E$). Note that D_E can become very large for vanishing values of f, for instance close to the equator where the influence of Coriolis acceleration disappears. For $\varepsilon \to 0$ (hence, $\Theta \to 0$), the solution (6.22) tends to

$$\omega(\zeta) = \mathcal{T}(1-\zeta) + \frac{\sigma}{2}\left(\zeta^2 - 1\right) , \tag{6.24}$$

and the slope $\sigma = 3/2\mathcal{T}$ can be obtained from Eq. (6.23), revealing that the tilt of the free surface is exactly oriented as the wind forcing (see also Fig. 6.2 for low ε). Combining the two results, it is straightforward to obtain the well-known velocity profile induced by wind stress in a non-rotating system [e.g., Heaps, 1984]:

$$\frac{\omega}{\mathcal{T}} = \frac{1}{4} - \zeta + \frac{3}{4}\zeta^2 . \tag{6.25}$$

It is interesting to analyze how the solution in the shallow case is modified by the Coriolis acceleration and how the correction depends on ε. By developing the solution (6.22)-(6.23) in Taylor series for $\varepsilon \ll 1$, we obtain that

$$\frac{\sigma}{\mathcal{T}} = \frac{3}{2} - \frac{i}{40}\varepsilon^2 + O\left(\varepsilon^4\right) , \tag{6.26}$$

$$\frac{\omega}{\mathcal{T}} = \frac{1}{4} - \zeta + \frac{3}{4}\zeta^2 - \frac{i}{240}\left(1-\zeta\right)\left(2+2\zeta-25\zeta^2+15\zeta^3\right)\,\varepsilon^2 + O\left(\varepsilon^4\right)\,. \tag{6.27}$$

eq. (6.26) shows that the longitudinal slope is not modified up to $O\left(\varepsilon^4\right)$, and that Coriolis acceleration produces a crosswise tilt at $O\left(\varepsilon^2\right)$. This is reflected in the velocity distribution of Eq. (6.27), where a secondary circulation develops without interfering with the primary flow, as already proposed by Toffolon [2013].

The second case is that of infinite depth ($\varepsilon \to \infty$). In this case, it is possible to demonstrate that $\sigma \to \mathcal{T}$ (see Fig. 6.2 for high ε). From a physical point of view, the consequence is that the actual slope, $S = S_0\,\sigma$, vanishes because $S_0 \to 0$ for $H \to \infty$ (see equations (6.15) and (6.16)). Such a consideration suggests that the infinite-depth case tends to the traditional Ekman solution. In fact, the difference between the solution (6.22)-(6.23) and that obtained for $\sigma = 0$ becomes negligible for large values of ε.

6.3.1.3 Crosswise transport

We have seen that the A2019 solution (6.22-6.23) describes a flow field that is affected by the action of Coriolis acceleration (Fig. 6.3). For small values of ε, a secondary motion is established without significantly altering the main flow [Toffolon, 2013]. When ε grows, the longitudinal primary circulation is progressively modified and the crosswise velocity is enhanced until a state is reached where ω_x and ω_y are of the same magnitude (Ekman spiral).

In a closed water body, the crosswise transport produces a downwelling at the coast on the right of the wind (in the northern hemisphere) and upwelling at the leftward coast. It is therefore important to compute the crosswise flux by integrating the crosswise velocity profile from the surface to the depth where the velocity changes sign. Defining this point as z_x for the velocity u, and z_y for v (the two values are different, in general), we introduce the fluxes per unit length

$$q_x = \int_{z_x}^{z_t} u\,dz, \qquad q_y = \int_{z_y}^{z_t} v\,dz\,, \tag{6.28}$$

Given the integral condition (6.11), it is also valid that $q_x = -\int_{z_b}^{z_x} u\,dz$ and $q_y = -\int_{z_b}^{z_y} v\,dz$, as the circulation is closed in both directions. In dimensionless terms and using the complex

notation, we can rewrite the Eq. (6.28) as

$$\Phi_x = \frac{q_x}{U_0\, H} = \int_0^{\zeta_x} \omega_x \, d\zeta, \qquad \Phi_y = \frac{q_y}{U_0\, H} = \int_0^{\zeta_y} \omega_y \, d\zeta \, . \tag{6.29}$$

Unfortunately, it is not possible to derive a solution for ζ_j (with $j = x, y$) in closed form satisfying the condition $\omega_j = 0$ for the solution (6.22-6.23). However, a numerical algorithm can be easily implemented to perform this computation and obtain the corresponding fluxes. With the same algorithm, we can also compute the crosswise transport predicted by all the classical solutions.

In order to quantify the relevance of Earth rotation on the development of the secondary circulation, we introduce the ratio

$$r = \frac{\Phi_x}{\Phi_y} \tag{6.30}$$

between the cross-wind and the longitudinal surface transport. In Fig. 6.4 the transport in the longitudinal and crosswise directions is shown as a function of ε.

As previously seen in the surface velocity plots (Fig. 6.3), the longitudinal transport Φ_y (Fig. 6.4a) is not sensitive to rotational effects for $\varepsilon < 1$ and decreases for higher values of ε as the crosswise transport Φ_x grows (Fig. 6.4b). The classical Ekman approach greatly overestimates the transport along both the x and y direction because it does not take into account the counterbalancing effect of the surface tilt between the lateral boundaries. As for the ratio r computed from (6.30), Fig. 6.4c shows that the threshold value of 1 ($\Phi_x = \Phi_y$) is exceeded when the crosswise transport Φ_x reaches its maximum: for increasing values of ε, the crosswise transport induced by rotation is larger than the longitudinal one, and approaches the asymptotic ratio coincident with the classical Ekman solution for $\varepsilon > 10^2$. Both Φ_x and Φ_y tend to zero for large ε, while the ratio r does not. In fact, at an intermediate latitude (with f fixed, i.e. $\sim 10^{-4}$ at 45°), values of $\varepsilon > 10^2$ are achieved either for low turbulent regimes or very deep lakes. In both cases the dimensionless transport goes to zero because transport is scaled by the term $U_0 H = \frac{T_0 H^2}{\rho \nu_z}$ (see equations (6.16) and (6.29)), which goes to infinity if $H \to \infty$ or $\nu_z \to 0$. Conversely, the ratio r is not affected by the scaling term, thus providing a good estimation of the relative importance of Earth rotation. High values of r correspond to cases where the Coriolis force is relevant, while $r = 0$ is obtained for the non-rotating case.

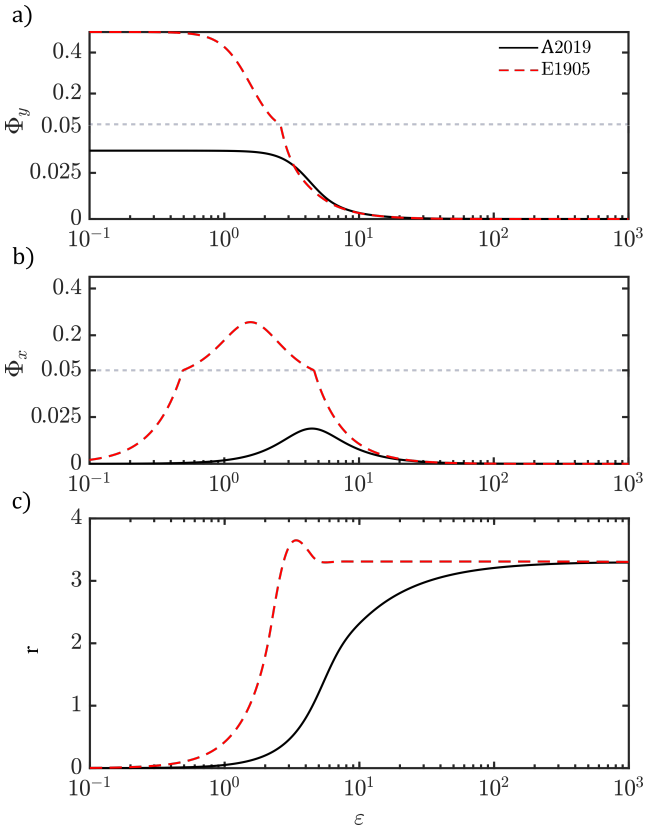

Figure 6.4: Dimensionless transport obtained from the analytical solutions A2019 and E1905: (a) longitudinal component Φ_y, (b) crosswise component Φ_x, and (c) ratio r between crosswise and longitudinal transport. Wind aligned with the y axis, no-slip bottom boundary condition. Note: for a better visualization, y axis is plotted with two different scales, separated by the gray dotted line.

6.3.2 Mathematical formulation for free slip bottom boundary condition

In this section the A2019 solution is derived for the case of free-slip bottom boundary condition. For consistency with the derivation in the no-slip case, the free-slip version of the equations provided here are numbered as the corresponding no-slip equations in the no-slip case, after the coding 'FS.'.

6.3.2.1 Derivation of the solution

In the case of free-slip boundary condition, zero tangential stresses are applied to the bottom ($z = z_b$) and equations (FS.10) are combined to the differential problem composed by (6.7)-(6.8), with (6.9) as surface boundary condition.

$$\left.\frac{\partial u}{\partial z}\right|_{z=z_b} = 0\,, \qquad \left.\frac{\partial v}{\partial z}\right|_{z=z_b} = 0\,. \tag{FS.10}$$

The complex formulation of the problem (6.12) is then complemented with the bottom boundary condition (FS.13), the surface boundary condition ($z = z_t$) in (6.13) and the integral condition (6.14).

$$\left.\frac{\partial W}{\partial z}\right|_{z=z_b} = 0\,. \tag{FS.13}$$

By applying the scales (6.16) and according to the dimenionless problem (6.15), we formulate the corresponding dimensionless free-slip boundary condition

$$\left.\frac{\partial \omega}{\partial \zeta}\right|_{\zeta=1} = 0\,. \tag{FS.19}$$

The differential problem we need to solve is therefore composed by the differential eq. (6.18) and by the surface (6.19), bottom (FS.19) and integral (6.20) boundary conditions. The general solution to the dimensionless problem can be written as a function of σ and ε as follows:

$$\omega(\zeta) = \frac{\cos\left[\Theta\left(\zeta - 1\right)\right]}{\Theta\,\sin\Theta}\,\mathcal{T} + \frac{\sigma}{\Theta^2}\,. \tag{FS.22}$$

By forcing the solution (FS.22) to satisfy the integral condition (6.20) we obtain the free-slip

case σ:

$$\sigma = \mathcal{T}, \tag{FS.23}$$

which results to be independent on ε and therefore on Earth rotation. Here the surface slope is indeed counterbalanced by the tangential wind stress only, as zero tangential stresses are considered at the bottom. Thus, the solution for the surface slope obtained by applying the integral condition (6.20) and free-slip bottom boundary condition (FS.19) is the same as in [Heaps, 1984], which is computed by assuming a closed integral in the direction of wind only (in our case $\int_0^1 \frac{v}{U_0} d\zeta = 0$).

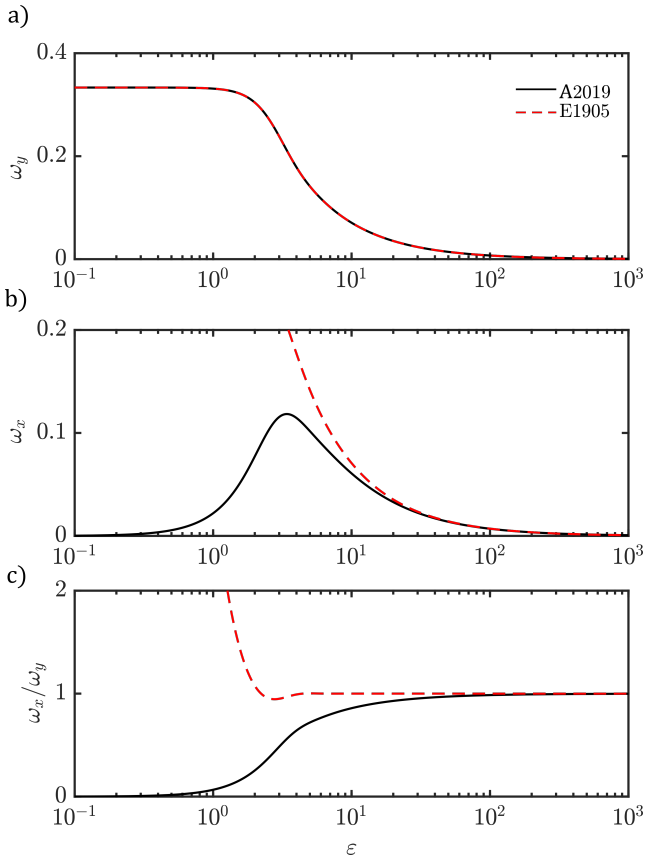

Figure 6.5: Dimensionless surface velocity obtained from the analytical solutions A2019 and E1905: (a) longitudinal component ω_y, (b) crosswise component ω_x, and (c) direction. Wind aligned with the y axis, free-slip bottom boundary condition.

For consistency with the derivation in the no-slip case, the solution is discussed assuming a wind aligned with the y axis of the domain, such that $\mathcal{T} = i$. The behaviour of surface velocity obtained from Eq. (FS.22) by imposing $\zeta = 0$ is plotted in Fig. 6.5 and compared with the Ekman solution in the finite depth version. The along-wind motion ω_y coincides for both

solutions, being larger for low values of ε and decreasing for increasing ε. The crosswise flow ω_x follows divergent paths: the E1908 solution goes to infinity for small values of ε, while the A2019 solution follows a bell-like curve similar to the no-slip case (see Fig. 6.3 in the no-slip case), but with a lower minimum. In the range of ε where ω_x increases, ω_y decreases until the same magnitude is reached and the surface water moves at 45° to the right of the wind as in the Ekman spiral theory. As previously seen in the no-slip case, the classical Ekman approach correctly describes the motion for large values of ε (deep lakes, high latitudes and/or weak mixing regimes), but it overestimates the velocity in both directions within the range of lower ε.

6.3.2.2 Limiting cases

In the limit case of low ε, we consider the case of very shallow lakes, where the shallowness is defined with respect to the Ekman depth ($H \ll D_E$). By substituting the expression of σ (FS.23) in Eq. (FS.22), the solution for very small values of ε and therefore of Θ is given by Eq. (FS.25):

$$\frac{\omega}{\mathcal{T}} = -\frac{1}{2}\zeta^2 - \zeta + \frac{1}{3}\,. \tag{FS.25}$$

which is the usual velocity profile induced by wind stress in a non-rotating system [e.g., Heaps, 1984].

If transport is numerically computed as in Eq. (6.29), the behaviour of longitudinal and crosswise transport from the supported solution can be studied also in the free-slip case. In Fig. 6.6 Φ_y in the along-wind and Φ_x in the crosswise direction is shown as a function of ε. As for surface velocities plots (Fig. 6.5), the along-wind transport Φ_y is not sensitive to rotational effects for $\varepsilon < 1$ and decreases for higher values of ε as the crosswise transport Φ_x grows. If the ratio Φ_x/Φ_y is computed, the threshold value of 1 is exceeded when the crosswise transport Φ_x reaches its maximum: for increasing values of ε, the crosswise transport induced by rotation is larger than the longitudinal one and approaches the asymptotic ratio, which coincides with the traditional Ekman solution.

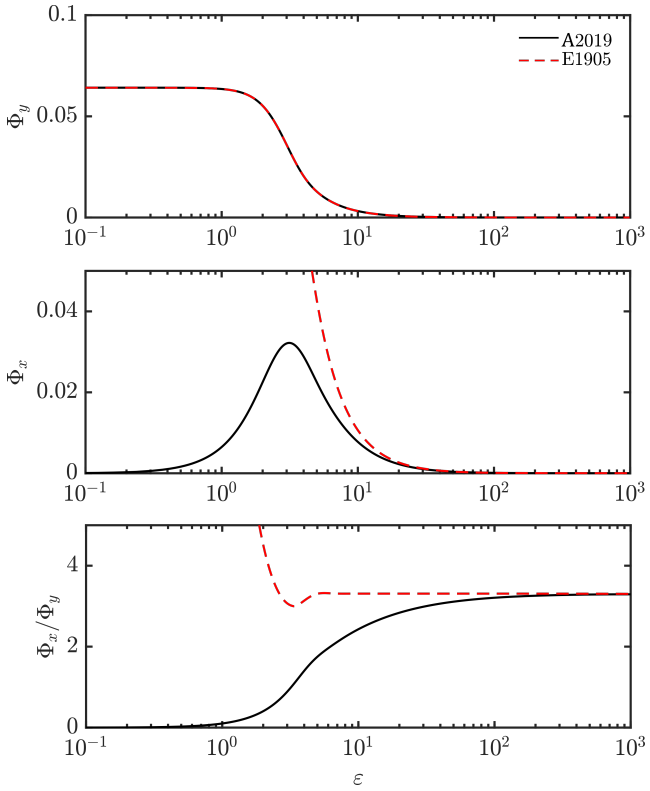

Figure 6.6: Dimensionless transport obtained from the analytical solutions A2019 and E1905: (a) longitudinal component Φ_y, (b) crosswise component Φ_x, and (c) ratio r between lateral and longitudinal transport. Wind aligned with the y axis, free-slip bottom boundary condition.

6.3.3 Numerical simulations

Analytical solutions provide an exceptional way to understand the fundamental mechanisms governing the phenomena under investigation. However, they are typically based on assumptions that can restrict their application, so their validity has to be demonstrated by comparing them with observations and/or numerical simulations. Here, we used a well-known three-dimensional numerical model to test our one-dimensional analytic solution. The hydrodynamic model Delft3D-FLOW [Lesser et al., 2004] was used for numerical experiments in the idealized domain. We defined a reference test case and a number of variations which were setup by changing the main parameters of the model (Tab. 6.1).

Four groups of simulations were designed, exploring the influence of depth (D1 to D5), width (B1 to B8), vertical turbulence model (v1 to v4 with constant values of ν_z), and horizontal turbulence model (h1 to h7 with constant values of ν_h; h8 with ν_h computed via the default

Depth	H [m]	**Vert. turb.**	ν_z [m^2/s]
D0	50	**v0**	0.0373
D1	10	v1	0.01
D2	30	v2	0.05
D3*	100	v3	0.1
D4*	300	v4	0.5
D5 *	500		
Width	B [m]	**Hor. turb.**	ν_h [m^2/s]
B0	5000	**h0**	1
B1**	50	h1	0
B2 **	100	h2	0.01
B3 **	200	h3	0.1
B4 **	500	h4	2
B5	1000	h5	5
B6	2000	h6	10
B7	10000	h7	20
B8	25000	h8	HLES
Reference simulation		**R0 = B0 + D0 + v0 +h0**	
ϕ [°] =0, 0.05, 0.5, 1, 2, 3, 5, 10, 15 , 30, 45, 60, 75, 90			

*coarser vertical discretization.

** finer horizontal discretization.

Table 6.1: Setup of Delft3D numerical experiments of the idealized domain

parametrization of Delft3D Horizontal Large Eddy Simulation - HLES). For each case, 14 simulations were run with different values of background latitude, from 0° to 90°N with uneven spacing to effectively capture the variability of the results over the full range of latitudes. From now on, all latitudes will be refereed to the northern emisphere N. Adiabatic (no thermal fluxes considered) simulations were performed with constant water density. The external forcing was prescribed as a constant wind blowing along the main axis of the box, with speed $U_w = 10$ m/s, using a drag coefficient $C_d = 1.7 \times 10^{-3}$ [Wüest and Lorke, 2003].

6.3.3.1 Spatial resolution of numerical domains

For the reference simulation R0, we assumed a domain of width B= 5 km (along x), length L= 50 km along y, and depth H= 50 m (along z), with a total number of 50×500 horizontal cells (resolution of 100 m) and 50 vertical layers of 1 m each. The resolution of the horizontal grid was set to 100 m along both directions x and y for the reference simulation R0 and for the groups exploring the influence of depth (Dx), vertical turbulence (vx) and width for the large domains (from B5 to B8). For the narrowest domains B1 and B2 (B = 50 and 100 m

respectively) $\Delta x = 5$ m and $\Delta y = 10$ m was used, while for B3 and B4 simulations ($B = 200$ and 500 m respectively) Δxy was set to 10 m. Finally, the setup from B4 simulations was used for the hx group investigating the effect of horizontal turbulence, hence the resolution was 10 m also in this case. Sensitivity tests with the higher resolution of 10 m showed no relevant differences on the numerical outputs from larger horizontal domain simulations.

The reference vertical resolution was set to 1 m per layer up to 50 m depth (D0) in the vx, hx and Bx simulations, and in D1 and D2 simulations ($H = 10$ and 30 m respectively). For deeper domains a larger number of layers was used with a resolution of 2 m each starting from 50 m depth, in such a way that D3 ($H = 100$) simulation had 75 layers (50 of 1 m and 25 of 2 m), D4 ($H = 300$) had 175 layers (50 of 1 m and 125 of 2 m) and D5 ($H = 300$) had 275 layers (50 of 1 m and 225 of 2 m). Sensitivity tests with the resolution of 1 m per each layer showed no relevant differences on the numerical outputs from deeper horizontal domain simulations.

6.3.3.2 Estimation of reference vertical eddy viscosity

A preliminary set of simulation was performed with $k-\varepsilon$ turbulence closure with a free-slip bottom boundary condition. The vertical profiles of ν_z obtained by computing the mean along a central longitudinal cross section at the end of the simulation are plotted in Fig. 6.7 for each numerical simulation. As it is clear from the figure, the vertical eddy viscosity computed by the $k-\varepsilon$ model has a parabolic profile along the water column and varies according to the latitude. Consistently with the classical analytical formulations which will be discussed later (Eq. (6.32)), the magnitude of vertical eddy viscosity decreases with latitude. For the reference simulation R0 the value of the vertical viscosity (v0) was estimated from the above numerical results at the intermediate latitude of 45°. The mean value $\nu_z = 3.73 \times 10^{-2}\ \ m^2/s$ was computed from a vertical average over the water column. Differently, the reference horizontal eddy viscosity (h0), $\nu_h = 1$ m^2/s, was chosen on the basis of the horizontal resolution of the grid, as suggested by the growth of the oceanic horizontal diffusion with cloud size observed by Okubo [1971].

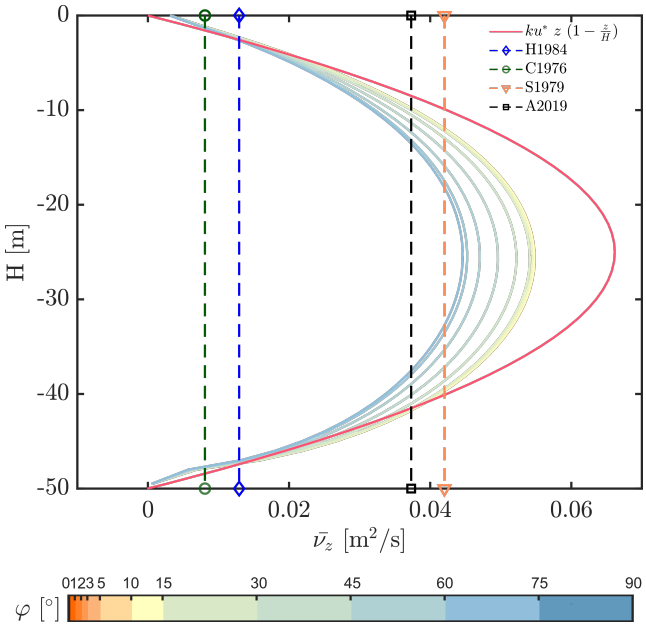

Figure 6.7: Constant vertical eddy viscosity computed with the analytical formulations (dashed marked lines) by Heaps [1984] (H1984), Csanady [1976] (C1976), Svensson [1979] (S1979) at the reference latitude of 45°N; classical parabolic profile (red continuous line); profiles of vertical eddy viscosity obtained as an average along the central longitudinal cross section from $k-\varepsilon$ numerical simulations with free-slip boundary condition (colored continuous lines for each latitude).

6.3.3.3 Spin up time

A spin up time was required to reach the steady state in the numerical model. This was estimated as a first try by taking into account the time scale $T_{\text{diff}} \sim H^2/\nu_z$ for the vertical diffusion of momentum from the surface to the entire water column. As the most critical case, we considered the largest depth (D5, $H = 500$ m) and the reference viscosity $\overline{\nu_z} = 3.73\times10^{-2}$ m^2/s. The diffusion time scale for such case would be $T_{\text{diff}} \sim 77$ days, but it substantially overestimates the spin up time actually needed. As an illustration, the approach to the steady state is reported for the reference simulation R0 and the deepest case D5, both at 45°N latitude (Fig. 6.8), showing the evolution in time of

$$\Delta\Phi_x^* = \frac{\Phi_{x,n+1} - \Phi_{x,n}}{\Phi_{x,n}}\,, \tag{6.31}$$

where n is the time index, which represents the normalized change in time of the dimensionless lateral transport. In both cases, the steady state is reached way before the end of the 10th simulation day (5 hours for R0, and $3-4$ days for D5). In the deep case, the transient response

is more evident, with oscillations of inertial periodicity ($t_i = 2\pi/f$, $\sim$ 17 h at mid-latitudes), which are dampened by viscous forces. This is consistent with Mohammed-Zaki [1980], who observed that for deep lakes (i.e., small Ekman number Ek << 1) and under a uniform wind stress, a quasi-steady spin up time has no significance, as the the basic steady amplitude is achieved in a few inertial periods.

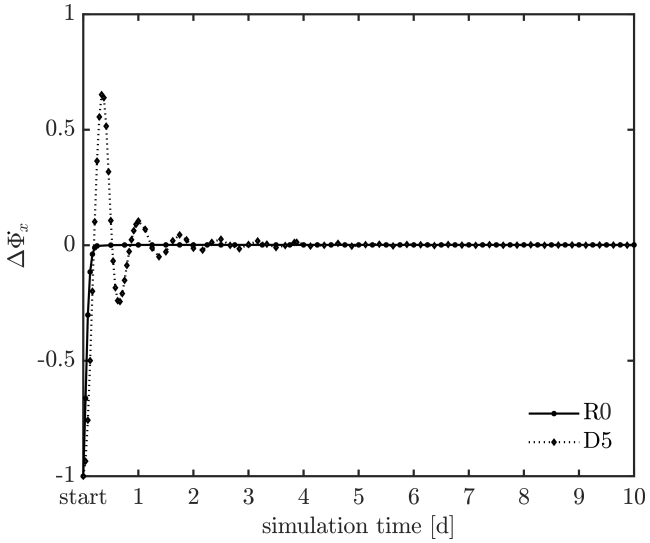

Figure 6.8: Temporal evolution of the normalized dimensionless lateral transport $\Delta\Phi_x^*$ in the reference numerical simulation R0 and in the deepest domain simulation D5.

6.3.4 Results

6.3.4.1 Analytical solutions vs numerical results for no-slip bottom boundary condition

In this section the proposed solution A2019 (6.22)-(6.23) is validated against numerical results and compared with three analytical solutions available in the literature: the classic Ekman spiral with finite depth (E1905), the solution provided by Simons [1980] (S1980) assuming the value $\sigma = 3/2\mathcal{T}$ as in Heaps [1984], and the central profile of the two-dimensional solution derived by Toffolon [2013] (T2013).

As a first analysis, we examine how Earth rotation affects the vertical profiles of the horizontal velocities u and v, considering the reference conditions (R0) and three different latitudes in the numerical simulations (Fig. 6.9): $\phi = 0°$ (at the equator, $\varepsilon = 0$), $\phi = 45°$ ($\varepsilon = 2.63$), $\phi = 90°$

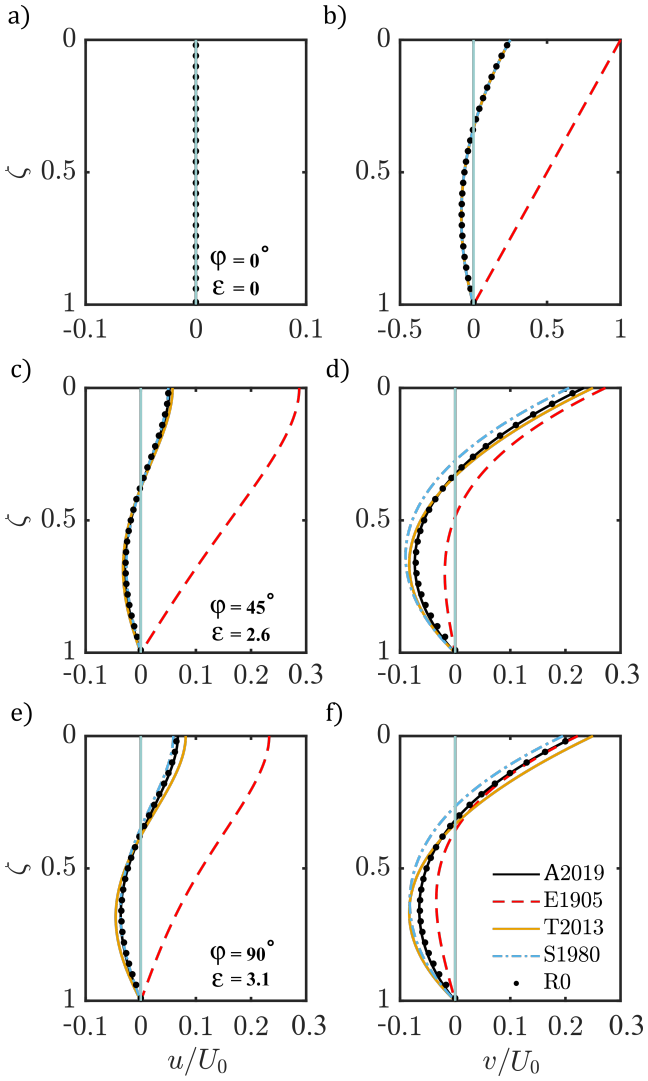

Figure 6.9: Vertical profiles of dimensionless velocities u/U_0, v/U_0 obtained from the analytical solutions (A2019, E1905, S1980, T2013) and from the reference numerical simulation R0 at: a-b) $\phi \simeq 0°$ (equator); c-d) $\phi = 45°$; e-f) $\phi = 90°$ (north pole). Wind aligned with the y axis, no-slip bottom boundary condition.

(north pole, $\varepsilon = 3.13$). The A2019 solution perfectly fits the numerical results for both the crosswise and the longitudinal velocity, and at all latitudes. At the equator (Fig. 6.9a,b), all solutions for u collapse to zero, as the Coriolis acceleration is absent and wind drives the flow along the longitudinal axis. Moreover, all solutions for v, except for the classic finite depth Ekman solution, have the same vertical structure (6.25). The omission of the geostrophic term in the classic formulation of the Ekman solution, with the consequent absence of the surface tilt ($\sigma = 0$), determines a linear profile $v/U_0 = 1 - \zeta$. At mid-latitudes, the S1980 solution is still a reasonable approximation for u (Fig. 6.9c), while it deviates from the numerical result and from

the correct A2019 profile for v, providing smaller velocities. On the contrary, the T2013 solution slightly overestimates the velocities (the reason will be examined in the next paragraph). The mismatch between these solutions (S1980 and T2013) and the numerical results (which coincide with A2019) increases at higher latitudes (Fig. 6.9e,f).

A more general overview of the different solutions is provided in Fig. 6.10, where the dimensionless transport Φ_x calculated from numerical simulations is plotted against the parameter ε, and compared with the continuous curves of the analytical solutions. Markers denote numerical outputs whose ID is summarized in Tab. 6.1. For each case (same marker), the values of Φ_x are computed for 14 different values of latitude, thus each set includes 14 points.

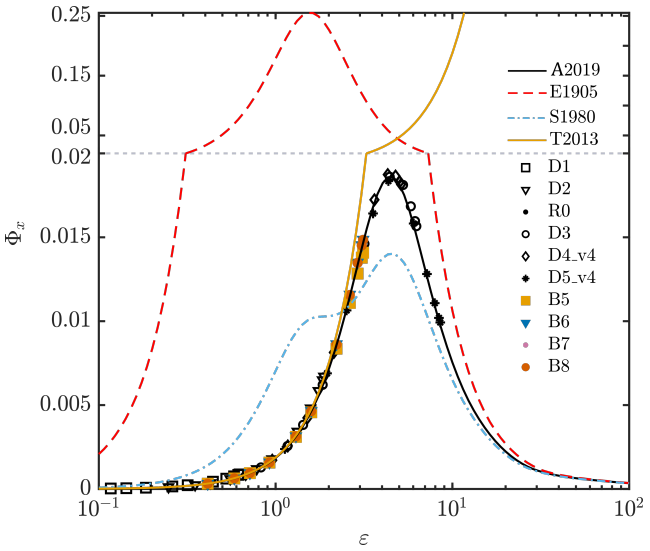

Figure 6.10: Crosswise transport Φ_x computed with analytical solutions (A2019, E1905, S1980 and T2013) and from numerical simulations, wind aligned with the y axis, no-slip bottom boundary condition. Note: for a better visualization, y axis is plotted with two different scales, separated by the gray dotted line.

As a first result, we note that all numerical points lay on the bell-shaped curve provided by the A2019 solution. In the low ε range (< 1, i.e., shallow basins or low latitudes), the A2019 and T2013 solution overlap, while the S1980 and E1905 solutions tend to overestimate the crosswise transport. In fact, both A2019 and T2013 account for the free surface tilt along x, which counterbalances the effect of Coriolis force. Compared to the reference simulation R0, the solution T2013 performs correctly at the lower latitudes, where D_E is large and ε is sufficiently small. Beyond its range of validity (say for $\varepsilon > 1$), the T2013 solution diverges from A2019 and overestimates the transport (as already seen for the velocity profiles, Fig. 6.9c), although

behaving reasonably well up to $\varepsilon \sim 2$. In this range of ε, the largest deviation is found for the E1905 and S1980 solutions, with the latter undergoing a transition from an overestimation to an underestimation of Φ_x. For deeper basins, (from D3 to D5, $H \geq 100$ m) the T2013 solution is not valid anymore and veers away from the correct bell-shaped behavior by following an increasing monotonic trend. On the contrary, the S1980 approach resembles the correct solution along its downslope, for higher latitudes or depths.

For all existing solutions, the error in the crosswise transport becomes large in the intermediate ε range, where only the A2019 solution behaves correctly, as it does in the whole range of ε.

6.3.4.2 Analytical solutions vs numerical results for free slip bottom boundary condition

For a comparison between the analytical solution and the numerical simulations the reference simulation R0 (see Tab. 6.1) is presented. The horizontal dimensionless velocities u/U_0 and v/U_0 obtained from the complex solution (FS.22) are plotted in Fig. 6.11 against the dimensionless depth ζ for the particular cases of latitude $\phi = 0°$ (Equator), $\phi = 45°$, $\phi = 90°$.

As it was clear from the mathematical derivation, the proposed solution we derived is the same we obtain if we assume S1980. Such a solution perfectly fits the simulation outputs along x direction (u/U_0) and is different from the Ekman classic version when $\varepsilon > 0$ (Fig. 6.11c and e). Differently, along the wind direction y the longitudinal velocity v/U_0 from A2019 and S1980 solutions collapses onto the classic E1905 solution at all latitudes. In fact, it can be analytically demonstrated that in the solution proposed here (see Eq. (FS.22)), the imaginary part of ω (i.e. $\omega_y = v/U_0$) is a function of the real value of σ only (σ_x), which is zero according to (FS.23) if $\mathcal{T} = i$. Thus, for the case of free-slip boundary condition the classical solution proposed by Ekman for the along-wind velocity is equivalent to the one that takes into account the effect of pressure gradients. As ε increases, the matching between T2013 solution and the correct solution is lost: this was also found in the case of no-slip bottom boundary condition and can be ascribed to the increasing monotonic trend that the T2013 solution has due to its derivation with a perturbation method assuming small ε. This can be even more easily seen in Fig. 6.12

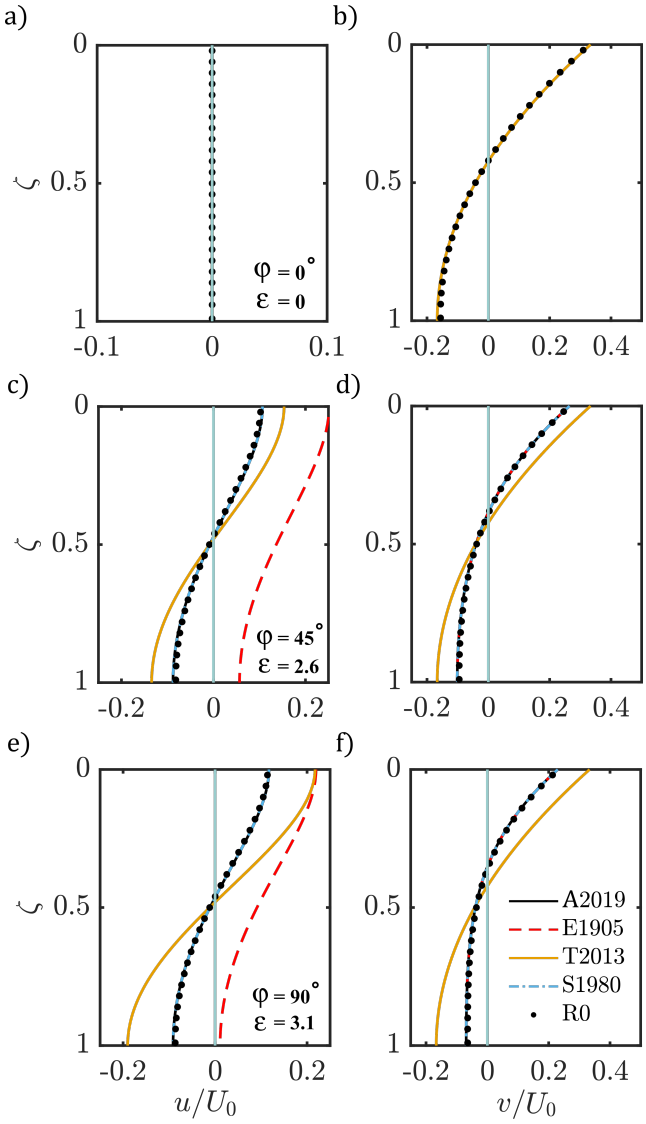

Figure 6.11: Vertical profiles of dimensionless velocities u/U_0, v/U_0 obtained from the analytical solutions (A2019, E1905, S1980, T2013) and from reference numerical simulation R0 at a,b) $\phi \simeq 0°$ (equator), c,d) $\phi = 45°$, e,f) $\phi = 90°$ (north pole). Wind aligned with the y axis, free-slip bottom boundary condition.

where crosswise transport is plotted in the case of free-slip boundary condition from numerical R0 outputs and analytical solutions. For $\varepsilon \leq 1$ the classical E1905 solution goes to infinity, while the proposed solution A2019 (which is equal to S1980) and T2013 provide the correct value for the transport. For $\varepsilon \geq 1$ the T2013 solution detaches from the numerical output and tends to infinity, while the E1905 well reproduces the correct trend in the right part of ε domain, where $\varepsilon \to \infty$.

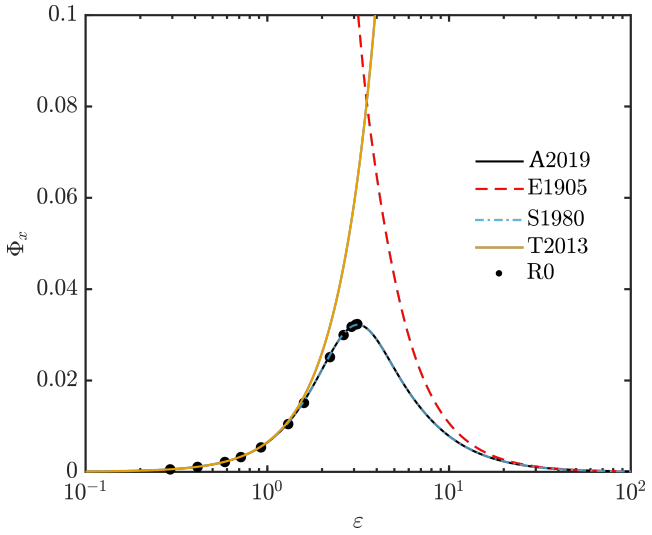

Figure 6.12: Crosswise transport Φ_x computed with analytical solutions (A2019, E1905, S1980 and T2013) and from numerical reference simulation R0. Wind aligned with the y axis, free-slip bottom boundary condition.

6.3.4.3 Effects of the depth

As originally observed by Ekman [1905], the existence of a bottom boundary modifies the shape of the velocity profile and, as a result, the amount of water that is transported orthogonally to the wind forcing. In this section, we analyze the effect of the lake depth on the dimensionless values of velocity and transport.

In Fig. 6.13a, the dimensionless Ekman spiral is plotted from the simulations performed with different lake depths (colored markered lines) and for the corresponding analytical solution (grey dotted lines), at the reference latitude of 45°.

The crosswise velocity u/U_0 is small in shallow basins (D1, D2 and R0 simulations, with H = 10, 30 and 50 m respectively). Its importance relative to the longitudinal component v/U_0 grows with depth until a maximum. The increase of u/U_0 with depth is related to the decreasing effect of bottom friction, which limits the dissipation of the energy coming from the wind to the water column. The maximum extension of the dimensionless Ekman spirals is reached near $H \sim 100$ m (D3 simulation): for larger depths (D4 and D5 simulations, H= 300 and 500 m respectively), the bottom friction becomes negligible and the spiral shrinks because the effect of Earth rotation does not change the dimensional velocity anymore, while the scale U_0 in Eq. (6.16) continuously increases with H.

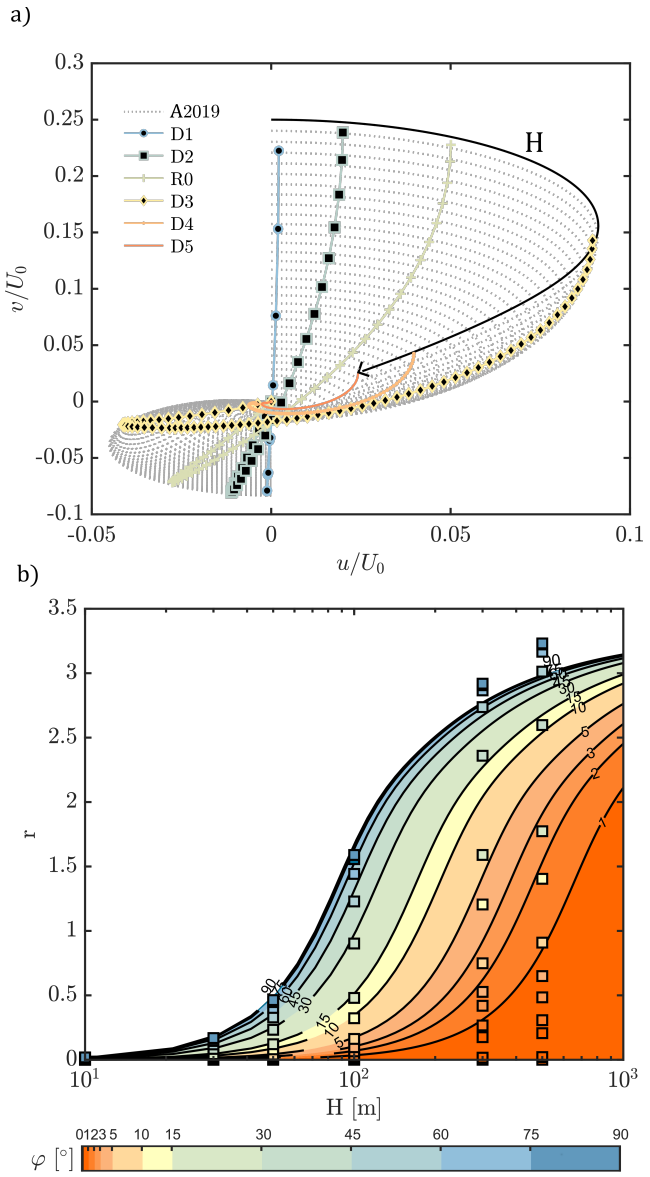

Figure 6.13: Effect of the depth reconstructed from numerical simulations and the analytical A2019 solution: a) dimensionless Ekman spirals for all simulations with varying depths at the reference latitude $\phi = 45°$N (colored marked lines) and analytical solution (dotted grey lines); b) ratio r of dimensionless transport plotted as a function of latitude and depth from numerical simulations (colored squares) and from the analytical solution (contour plot).

The overall trend is illustrated in Fig. 6.13b, where the importance of Earth rotation on the circulation, expressed using the ratio r from Eq. (6.30), is shown as a function of depth at different latitudes for simulations (squares) and the analytical solution A2019 (contour plot). The ratio r grows with both depth and latitude in a continuous way, asymptotically approaching to the infinite depth case (see Fig. 6.3 and 6.4). The A2019 solution provides a good estimation of the crosswise transport, but the perfect matching between the analytical solution and the

numerical results is lost for the two deepest cases (D4, D5), where some of the assumptions of the analytical solution are not satisfied as will be discussed in section 6.3.5.2. However, these results show that for a given value of eddy viscosity, latitude and depth play together a fundamental role: lakes located at low latitudes have to be very deep to experience the maximum effect of Earth rotation, which conversely is more easily achieved in shallower lakes at mid and high latitudes.

6.3.4.4 Effects of the width

The analytical solution A2019 suggests that the width of the basin does not affect the velocity profile. In fact, the A2019 solution relies on the assumption that the crosswise transfer of momentum is unimportant, a condition that is not valid for narrow lakes where the horizontal viscosity is high, as extensively discussed by Toffolon [2013] in the case of small ε. In this section, we examine how the width affects the circulation pattern due to the presence of lateral boundary layers.

Analogous to the previous analysis on the role of the depth (Fig. 6.13a), Fig. 6.14a shows the behaviour of the dimensionless spiral as the width changes, considering the reference latitude (45°) and different widths, from 50 m (B1) to 25 km (B8) and including R0 (5 km). For the range of widths $B > 1$ km (B6, B7, B8 and R0), the crosswise transport is independent of the horizontal extent of the basin, and only increases with latitude. This trend is clear from Fig. 6.14b, where the ratio r is plotted as a function of width at different latitudes. The A2019 solution well captures the magnitude of crosswise transport for these relatively wide cases.

However, simulations with a narrower domain (width < 1 km, B1 to B5) show weaker crosswise transport (Fig. 6.14a). This is illustrated in Fig. 6.14b which shows a mismatch between the numerical and analytical solutions, in the first case the ratio r being smaller than in the latter. In the numerical solution, the crosswise transport decreases for narrower lakes, as a result of the increased internal friction due to the horizontal velocity gradients. In the next section, the reasons behind this mismatch are addressed by taking into account the role of the lateral boundary layers.

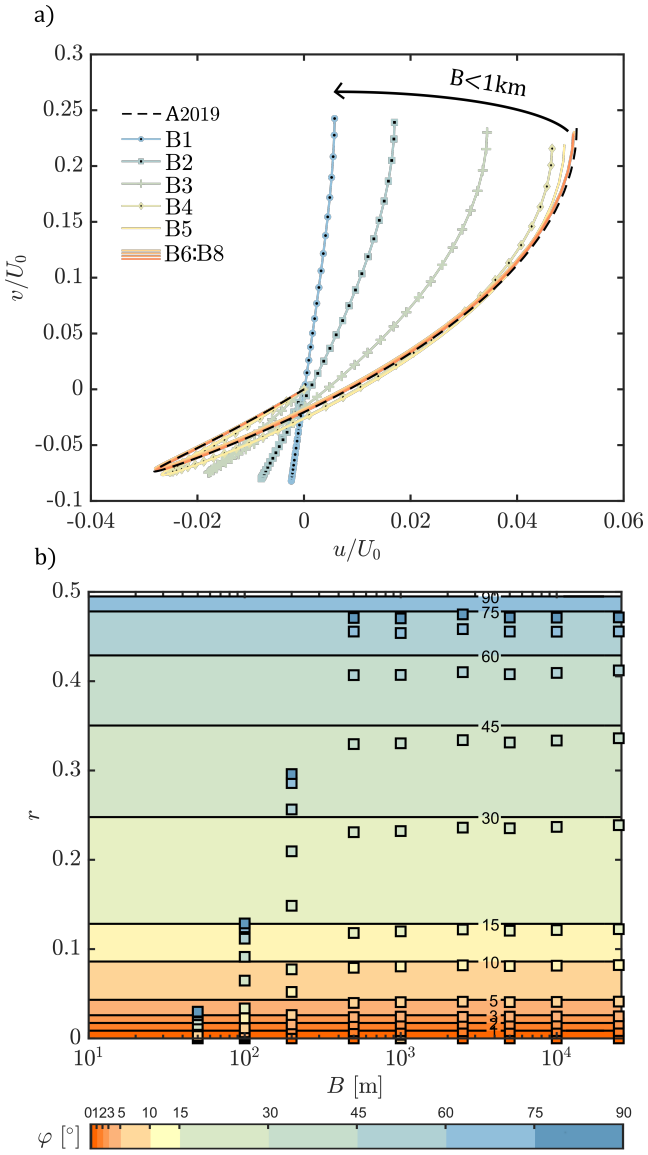

Figure 6.14: Effect of the width reconstructed from numerical simulations and the analytical A2019 solution: a) dimensionless Ekman spirals for all simulations with varying widths at the reference latitude $\phi = 45°$N (colored marked lines) and analytical solution (dashed black line); b) ratio r of dimensionless transport plotted as a function of latitude and width from numerical simulations (colored squares) and from the analytical solution (colored lines).

6.3.4.5 Effect of eddy viscosity and boundary layers

As we have seen before, the results obtained from the numerical model and from the analytical solution A2019 clearly diverge for the case of narrow lakes. Building on previous studies [Toffolon, 2013], we can associate this discrepancy to the aspect ratio of the cross-section and to the turbulence anisotropy. This issue is tightly connected with the estimate of the eddy viscosity

(a parameter of difficult estimation, especially along the horizontal dimension, see e.g. Toffolon and Rizzi [2009]). Here we examine the direct effect of the value of the eddy viscosity (both vertical and horizontal) on velocity and transport.

The traditional approach for estimating the vertical eddy viscosity (ν_z) is through the evaluation of the depth of the wind-induced motion [Madsen, 1977; Csanady, 1982; Heaps, 1984], which is commonly represented by the Ekman depth when rotational effects are taken into account. Therefore ν_z, in unstratified conditions, can vary according to the latitude, depth and wind stress. A reference value can be determined as a function of the Coriolis parameter f and the surface friction velocity $u_* = \sqrt{T_0/\rho}$ as

$$\nu_z = K\frac{u_*^2}{f}\,, \tag{6.32}$$

where the dimensionless coefficient K is 0.008 in Heaps [1984], 0.005 in Csanady [1976] and 0.026 in Svensson [1979]. According to Eq. (6.32), ν_z increases as latitude decreases, leading to $\nu_z \sim 5 \cdot 10^{-1}$ m^2/s at $\phi \simeq 45°$ (assuming $u_* \sim 10^{-2}$ m/s), a large value that is not commonly encountered in real lakes. Hence, we performed a sensitivity analysis to understand the influence of this parameter.

The effect of changing ν_z on the vertical profile of the crosswise velocity is illustrated in Fig. 6.15a for the deep D4 domain at the reference latitude $\phi = 45°$, considering both numerical simulations and the A2019 solution. By increasing ν_z (cases $v3$ and $v4$, 0.1 and 0.5 m^2/s respectively) the dimensionless crosswise velocity increases together with the thickness of the surface layer set in motion by the wind. Conversely, for lower ν_z (cases $v0$ to $v2$, order of magnitude 10^{-2} m^2/s) the circulation is limited to the top layer and the u/U_0 is smaller because the scale U_0 increases with decreasing ν_z. The A2019 solution captures well the shape of the velocity profile, hence the amount of water transported.

Then, we examined the effect of changing the value of the horizontal eddy viscosity. We recall that all simulations presented so far were performed with the same value of $\nu_h = 1$ m^2/s. In Fig. 6.15b, the profiles of crosswise velocity u/U_0 are plotted for simulations h1 to h8, where the value of the horizontal eddy viscosity was changed for the narrow domain B4 (i.e., B=500 m). The crosswise velocity decreases when increasing ν_h, as mixing is enhanced at the expense of

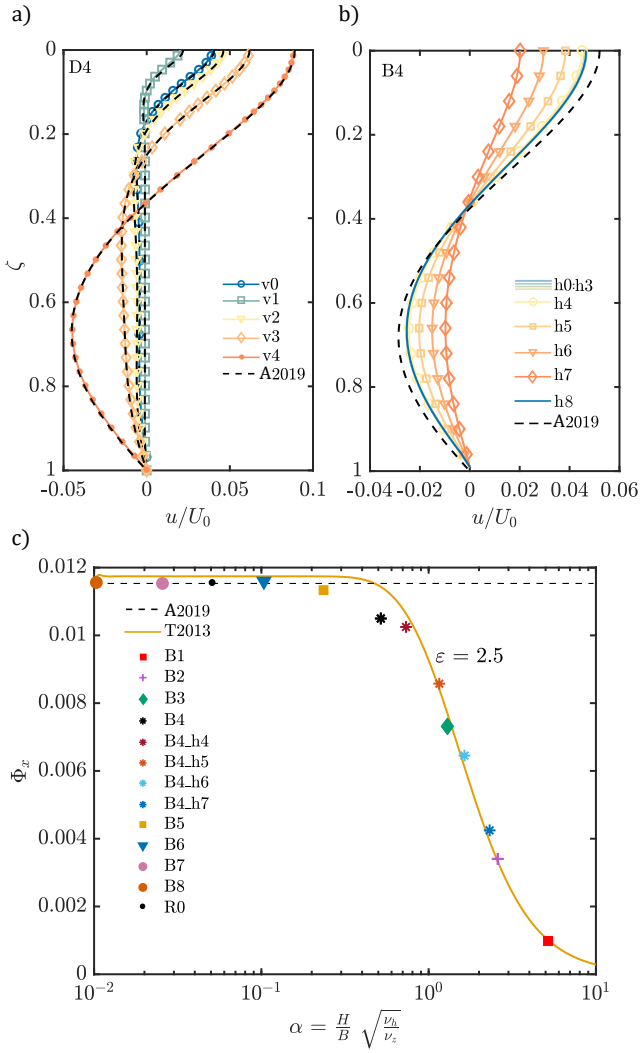

Figure 6.15: Effect of turbulence parameters at the reference latitude $\phi = 45°$N . Top plots: dimensionless crosswise velocity u/U_0 from numerical simulations (colored marked lines) and A2019 analytical solution (black dashed lines), a) deep D4 simulations ($H = 300\ m$) with varying vertical eddy viscosity (v0 to v4), and b) narrow B4 simulations ($B = 500\ m$) with varying horizontal eddy viscosity (h0 to h8). Bottom plot c): dimensionless transport Φ_x against the anisotropy parameter α [Toffolon, 2013], for all B- and h-type simulations (scatter plot), and the A2019 (black dashed line) and T2013 (continuous orange line) analytical solutions for the corresponding ε value.

horizontal gradients. Therefore, the momentum transfer from the lateral boundaries to the center of the lake is more effective and velocity is reduced along the water column due to the decelerating effect of the down-welling and up-welling regions. For small values of ν_h the lateral boundary layers are very thin and the central profile of u/U_0 approaches the one predicted by the A2019 solution.

In order to have a guideline in the interpretation of the results, we refer to the complete

solution proposed by Toffolon [2013], which accounts for the role of ν_h by means of a combined geometry-anisotropy parameter [Toffolon and Rizzi, 2009],

$$\alpha = \frac{H}{B}\sqrt{\frac{\nu_h}{\nu_z}}\,. \tag{6.33}$$

Such a parameter represents the ratio of the vertical (H^2/ν_z) and the horizontal (B^2/ν_h) temporal scales of the diffusion of momentum, and subsumes the effect of the boundary layers at the surface/bottom and at the lateral walls of the domain.

Fig. 6.15c analyzes the variation of the crosswise transport Φ_x versus α, by changing B and ν_h at the reference latitude 45°. The plateau at the left-hand-side part of the graph ($\alpha \leq 10^{-1}$) applies to scenarios B6 to B8, including the reference simulation R0, where the width is larger than 1 km and the numerical transport follows the behavior of the A2019 solution. In this range of widths and for the reference values of ν_h and ν_z, the transport is independent of width and of the effect of the horizontal/vertical boundaries. Differently, the transport decreases exponentially for smaller widths or larger ν_h as the parameter α increases, in good accordance with the complete analytical solution proposed by Toffolon [2013].

6.3.5 Discussion

6.3.5.1 The governing scales

The aim of this work was to analyze the parameters that primarily affect the secondary flow resulting from the interaction of wind forcing and the Coriolis force. As seen in the previous sections, the proposed A2019 solution correctly reproduces the numerical results in most cases, with the exception of narrow lakes with large horizontal viscosity where boundary layer effects become important. Neglecting these particular cases, the general validity of the A2019 solution suggests that for a wide range of depths and widths it is possible to predict how much water is likely to be moved by the Coriolis force, and whether Earth rotation will affect the flow field or not, as a function of the Ekman number $\mathrm{Ek} = H/D_E$, or the equivalent parameter ε, solely.

In Fig. 6.16a, the ratio r is plotted as a function of the actual depth H and the Ekman depth D_E, showing in which range of these two variables the Coriolis acceleration is expected to be

important.

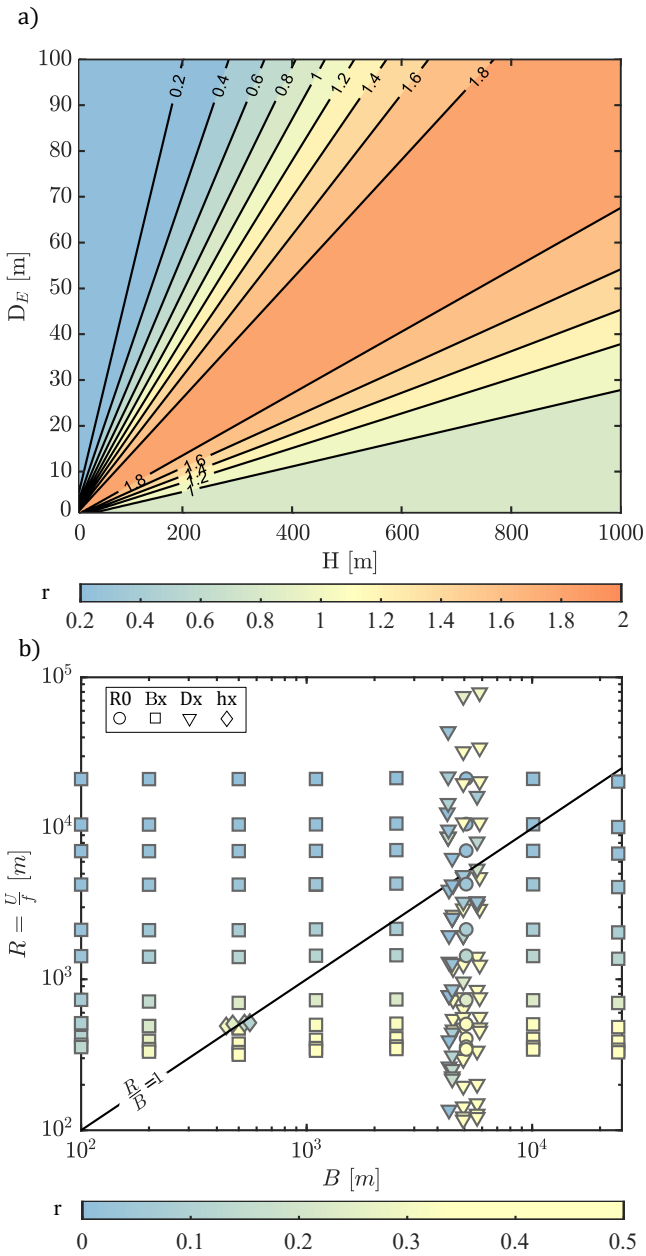

Figure 6.16: Ratio r of the crosswise transport along the two horizontal directions plotted as a function of a) the Ekman depth D_E and depth H; b) the Rossby radius R and width B. Note: in b) diamonds, circles and triangles have been spaced out for a better visualization: R0, Dx and vx sets are associated to B = 5000 m and hx to B = 500 m.

For a lake at a given latitude and specified turbulent regime, the Ekman depth can be computed. Then, the magnitude of the crosswise transport (and consequently of the up-/downwelling) can be determined based on the depth of the lake. The range where the crosswise transport due to Earth rotation is relevant grows with the depth of the basin and with the

Ekman depth. We note that the value assumed for the vertical eddy viscosity is particularly important, as D_E is proportional to $\nu_z^{1/2}$. In this regard, we are aware that the quantification of ν_z is not straightforward in most practical cases. However, the estimation of this coefficient, or at least of its order of magnitude, is possible from temperature microstructure measurements, or through several turbulence models available in literature [e.g., Mellor and Yamada, 1974; Large et al., 1994; Goudsmit et al., 2002, among many others].

When analyzing the effect of the horizontal extent of the basin on the flow regime, the importance of the horizontal eddy viscosity was stressed. In fact, the crosswise transport in narrow lakes decreases due the horizontal friction and the presence of lateral boundaries in the same way as it is limited by the bottom friction in shallow lakes. In this process the lake width affects the horizontal momentum transfer, and should be taken as an important length scale. However, as we demonstrate in Fig. 6.15c, the reason to consider the role of the width B in this phenomenon is not the one usually perceived as important.

Indeed, a criterion often proposed to discriminate if the Earth rotation will affect the flow field (hence, the transport) is when the lake width is larger than the Rossby radius $R = U/f$, that is when the Rossby number Ro is lower than unity. Here we show that this is not correct for the wind-driven steady circulation in lakes. In Fig. 6.16b the ratio r from all simulations is plotted as a function of the Rossby radius R and the width B. We note that at $B = 50$ m and $B = 5000$ m markers have been spaced out for a better visualization. In the case of fixed H and different B (squares, Bx simulations) the increase of crosswise transport with R is only driven by the variation in latitude, as the horizontal extent of the lake does not affect the relative importance of Earth rotation on the secondary circulation. Hence, for a given Rossby number, different values of crosswise transport can be found: as an example, the black line where $R = B$ intersects squares of different colors. As discussed in section 6.3.4.5, in the range of narrow lakes the crosswise transport is smaller due to the effect of the boundary layers and anisotropy, and this effect is not taken into account in the computation of Rossby radius. In fact, if ν_h changes (diamonds), the relevance of Earth rotation r can vary even if Ro is the same. If B is fixed and H changes (triangles), the magnitude of the Coriolis-induced transport can be high (yellow colored markers) or low (blue markers) both for Ro < 1 and Ro > 1. Then, the computation of the Rossby number cannot give any insight on how much Earth rotation affects the Ekman

transport in a closed basin.

6.3.5.2 Limits of the analysis

A one-dimensional steady solution was derived for quantifying the crosswise transport occurring in an elongated basin due to Earth rotation, in unstratified and horizontally homogeneous conditions. The domain was assumed as rectangular with a flat bottom, both choices being an important simplification of a realistic lake, especially when compared to other idealized models available in literature, which consider linear, triangular and even more complex bathymetries [e.g. Simons, 1980; Winant, 2004; Sanay and Valle-Levinson, 2005]. However, on the one hand the simplification of a flat bottom significantly reduces the number of degrees of freedom of the analysis and let us focus purely on the large-scale wind-driven circulation. On the other hand, a rectangular domain is a rather common idealization for elongated enclosed or semi-enclosed basins [e.g. Kasai et al., 2000; Ponte, 2010]. The crucial aspect in our analysis is that the existence of lateral boundaries controls the development of a crosswise transport, overcoming the limits of the traditional Ekman transport solutions derived for 'infinitely large lakes or oceans' [Hutter et al., 2011a]. We refer the reader to more detailed approaches for the accurate representation of topographic effects when irregularities in the horizontal shape of the basin may affect the development of the circulation [e.g. Mohammed-Zaki, 1980].

While presenting the results, we encountered a few cases where the one-dimensional approach embedded in the A2019 solution leads to inaccuracies in the estimation of the crosswise transport, in particular for very deep cases ($H > 300$ m). We observed that these inaccuracies are related to the key assumption that the circulation is closed (i.e., null integral) in the central water column of the lake, which is not satisfied. Such an assumption is a simplified version of the general constraint that a steady flow in a closed domain must have a null exchange across any surface dividing the domain in two parts, and is valid only when the flow field is characterized by some symmetry in the cross-section. For more detailed analyses, two-dimensional [e.g. Dever, 1997; Toffolon, 2013] and three-dimensional solutions [e.g. Winant, 2004; Ponte, 2010] are available for a precise reconstruction of the flow field, but this is not the main scope of this work.

Considering a steady state is the fundamental assumption, because the stationarity is the

prerequisite for the integral condition to be valid and thus for the inclusion of the lateral boundaries. We are not interested in the temporal development of the flow field, which can be studied with time-varying solutions specifically designed for that purpose [e.g. Fjeldstad, 1930; Hidaka, 1933; Platzman, 1963; Madsen, 1977]. The numerical results show that in many cases an equilibrium condition is achieved after a spin-up time that varies from some hours to some days of constant and uniform wind, a condition that many lakes experience from local breezes to large-scale synoptic winds.

We are aware that the assumption of constant eddy viscosity (together with that of constant density) is quite limiting. Some efforts were spent to overcome the gaps related to the definition of ν_h and ν_z in analytical formulations [e.g. Thomas, 1975; Madsen, 1977; Svensson, 1979], but definitive results are not suitable for the derivation of a simple analytical solution in closed form.

Finally, the one-dimensional solution we derived provides an analytical quantification of transport orthogonal to the main flow when wind blows along the main axis of elongated lakes. The numerical results suggest that, despite the simplifications we adopted, such a solution is suitable for simplified three-dimensional domains in unstratified conditions, which typically occurs in many real lakes although with different frequency depending on their mixing regime. Also, long-lasting wind events aligned with the main axis of a lake are common for elongated lakes (e.g. Lake Baikal, Lake Erie, Lake Ontario, Lake Constance, northern Lake Garda), where steady currents of the kind discussed here have been already modeled and observed [Rao and Murty, 1970; Gedney and Lick, 1972; Wang et al., 2001; Amadori et al., 2018; Piccolroaz et al., 2019] and in some cases shown to significantly contribute to deep mixing [Boehrer and Schultze, 2008; Schmid et al., 2008; Tsimitri et al., 2015; Piccolroaz and Toffolon, 2018; Piccolroaz et al., 2019]. Hence, such a simple, even though limited, analytical tool could help in estimating to what extent crosswise up/down-welling ascribed to Earth rotation can be relevant for the transport and mixing processes of a lake.

6.3.6 Conclusions

The analytical solution we derived helps identifying the scales that determine the importance of Coriolis acceleration as a driver of transport in non-stratified lakes. We showed that the

Ekman number (i.e. the ratio of the actual depth of the lake and the Ekman depth) controls whether Earth rotation will affect the steady circulation in a lake of given size at in a given geographical location and therefore should be used as a governing scale instead of the Rossby number. Consistently with some previous findings [Kasai et al., 2000; Sanay and Valle-Levinson, 2005; Valle-Levinson, 2008], we identified the parameter ε, which is directly proportional to the Ekman number, with the novelty of including in the analysis the size of the lake, the turbulent mixing and the effect of a closed domain. The combined analytical and numerical analysis we carried out allows for the following final conclusions:

1. Coriolis force is important also in narrow lakes and produces a crosswise Ekman transport that can be analytically quantified if the effect of lateral boundaries is taken into account through a null flux condition.

2. The steady crosswise transport is scaled by the Ekman number, which is defined once the depth of the lake, the vertical eddy viscosity and the latitude are defined. Such a crosswise transport is responsible for up- and down-welling phenomena at the lake sides.

3. The Rossby number Ro does not provide any useful information about the development of Ekman currents in enclosed basins. The use of a horizontal length scale is appropriate only when the lateral boundary layer is large enough to affect the secondary circulation: in that case, a frictional length scale is needed, bringing into play the horizontal eddy viscosity and requiring the use of an anisotropy parameter like α proposed by Toffolon [2013].

6.4 Application to the real case of Lake Garda

The one-dimensional solution we derived in the previous section for Ekman transport in elongated lakes was validated against synthetic lakes of idealized shape and bathymetry, in simplified thermally homogeneous conditions and assuming constant and uniform wind forcing and turbulence. In this section, we test our analytical solution to the real case of Lake Garda. Since no hydrodynamic measurements are available to test the solution with any observed flow field in the lake, results from model runs, previously validated against temperature observations, are used as representative of the 'real' hydrodynamics.

We are aware of the distance between the simulated scenarios in our case study and the assumptions made to mathematically derive our solution. Nevertheless, our intent is here to verify whether the proposed approach provides an order of magnitude of the amount of laterally-deviated (and eventually downwelled) surface water due to the Earth rotation on a real case, under realistic wind conditions.

6.4.1 Methods

In chapter 5 the role of wind-driven mixing combined with the effect of planetary rotation was investigated. In that specific application, we observed three episodes of strong wind lasting more than one day and uniformly distributed on the lake surface in its northern part. The observations and numerical simulations presented in that case inspired the subsequent theoretical analysis (section 6.3). Hence here we test our analytical solution on those specific events. We refer to section 5.1.1 for the detailed description of the simulated scenarios and we report here the details on how the outputs of those simulations were elaborated, in order to have a consistent comparison with the analytical solution.

6.4.1.1 Sub-domain definition

A sub-domain is extracted from the complete Lake Garda computational grid in order to accomplish to the requirements of the analytical solutions. The approximately narrow rectangular trunk (Fig. 6.17) is identified of length L = 11 km, width B = 1 km.

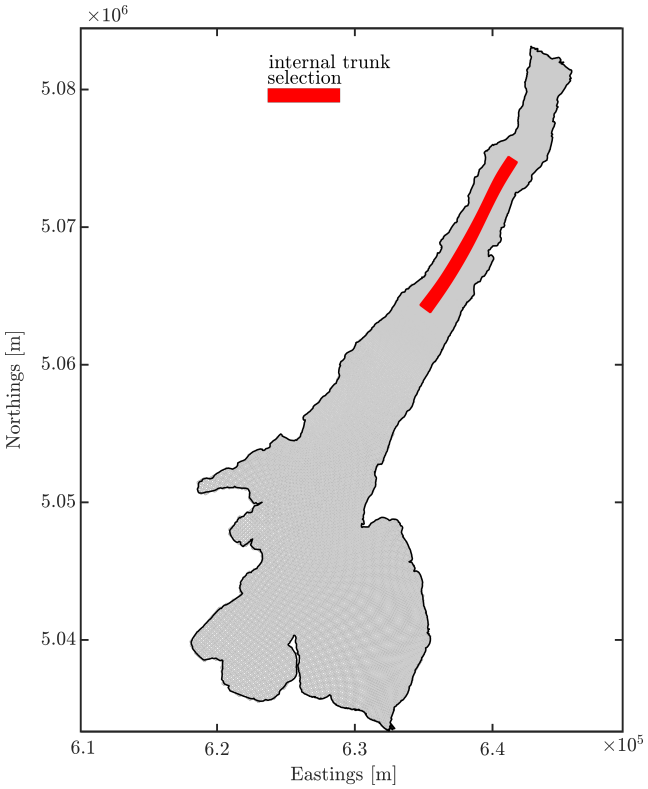

Figure 6.17: Sub-domain of Lake Garda computational grid.

To overcome the issues related to the orientation of the lake of ~ 35 °N and to the irregular original grid spacing, a local coordinate system is adopted. Local Easting (Northing) coordinates of the grid cells are computed by referring each cell to the first cell West (South) of the crosswise (longitudinal) section it belongs to. The 'mean' transects along the two dimensions (Fig. 6.18) are obtained by averaging the local coordinates and the associated bathymetry. These transects being identified, they are assumed to be representative of the general morphology of the northern Lake Garda along its main longitudinal and crosswise axes. Hence, the internal rectangular sub-domain is extracted from these sections. We identify the characteristic depth H, width B and length L, which will be used in the analytical formulations.

All the physical variables from the numerical simulations in Lake Garda are then taken from the portion of computational cells laying within the rectangular domain (red boxes in Fig. 6.18) and successively averaged along the two horizontal directions.

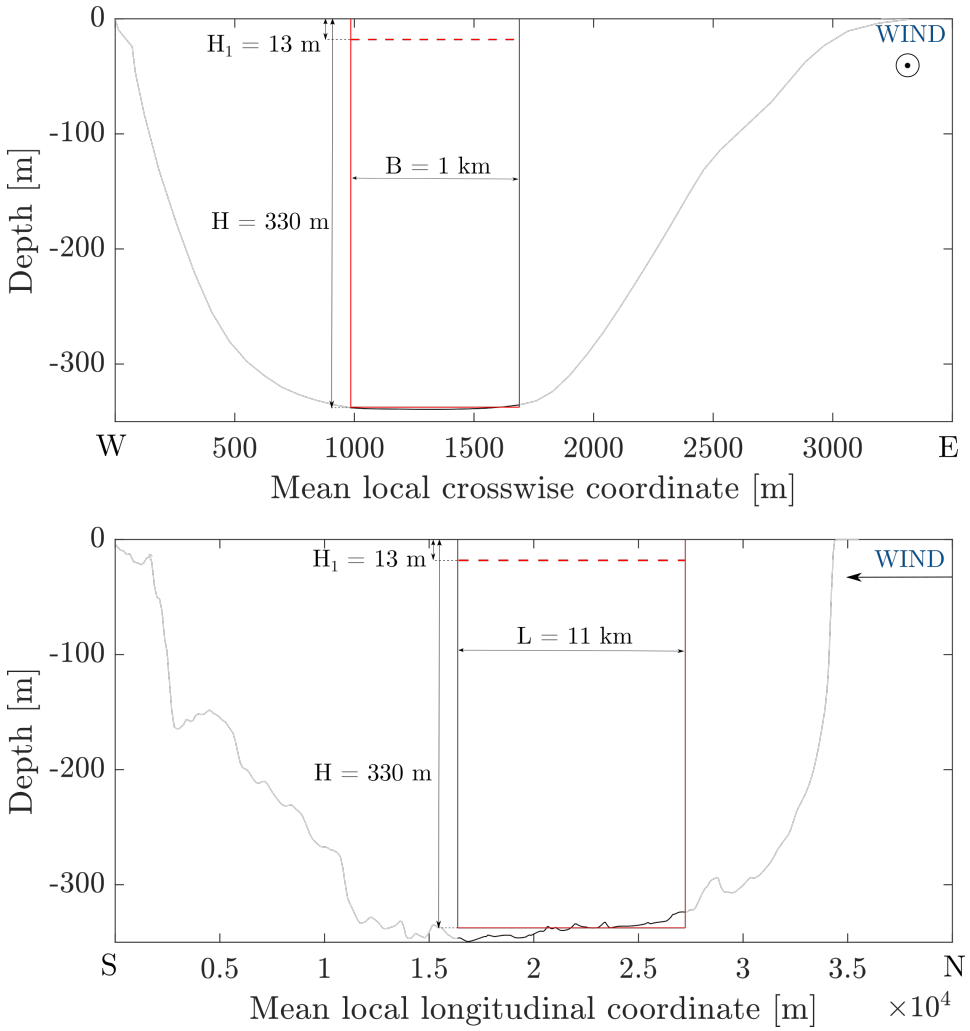

Figure 6.18: Average a) crosswise and b) longitudinal sections in Lake Garda northern basin (gray line). The black line highlights the part of section laying within the internal rectangular trunk (delimited by red continuous lines). The dashed red line depicts the characteristic depth H adopted in the summer case (see next paragraph).

6.4.1.2 Simulated scenarios

In Tab. 6.2 the simulated events are resumed with the key parameters used in this application. The reference days of each scenario are coincident with those chosen in Chapter 5. Differently, the 'Start' and 'End' time refer to the time window in which the results will be evaluated here and which the average wind speed is referred to.

Two simulations are chosen for the nearly unstratified period (March 2017 and April 2017), and one in summer, when the lake is strongly stratified (August 2017). Fig. 6.19 shows the time

Parameter	Symbol	UM	March 2017	April 2017	August 2017
Start time			8 March 05:00	20 April 11:00	6 August 22:00
End time			9 March 02:00	21 April 11:00	7 August 04:00
Average wind velocity[1]	U_w	[m s^{-1}]	7.35	10.71	12.20
Characteristic depth	H	[m]	330	330	13
Uniform temperature	T_w	[°C]	8.86	8.85	17.80
Uniform density	ρ_w	[$kg\ m^{-3}$C]	999.7936	999.7944	998.6724
Uniform vertical eddy viscosity	ν_z	[m^2 s^{-1}]	0.029	0.090	0.0045
Uniform horizontal eddy viscosity	ν_h	[m^2 s^{-1}]	0.2	0.2	0.2
Horizontal velocity scale	U_0	[m s^{-1}]	0.97	0.71	1.16
Wind shear stress scale	T_0	[Pa]	0.085	0.194	0.259
Surface slope scale	S_0	[-]	2.6×10^{-8}	6.0×10^{-8}	1.39×10^{-6}

[1] longitudinal component only

Table 6.2: Details on the simulated events.

evolution of the two wind components and their direction in the three simulated scenarios. In all cases the wind is mainly aligned with the main axis of the northern trunk of the lake for more than 12 hours consecutively. The values of velocity and direction plotted in the figure are obtained from an average of the atmospheric model (WRF) outputs over the rectangular sub-domain, after having verified that the spatial distribution of the wind field in the investigated area and in the simulation period is uniform.

We elaborate the hydrodynamic model outputs during the time window when the wind component along the horizontal direction is nearly null (black vertical lines on Fig. 6.19). In this way, the condition of wind acting only in the longitudinal direction ($\mathcal{T} = i$, see eq. (6.15)) can be safely applied also to the real case.

6.4.1.3 Elaboration of model outputs

In order to compare the hydrodynamic model outputs with the analytical formulation, the following quantities need to be defined, in order to evaluate the scaling factors U_0, S_0 and T_0 described in eq. (6.16):

- Vertical length scale H;
- Uniform density of water ρ;
- Wind mean velocity U_w.

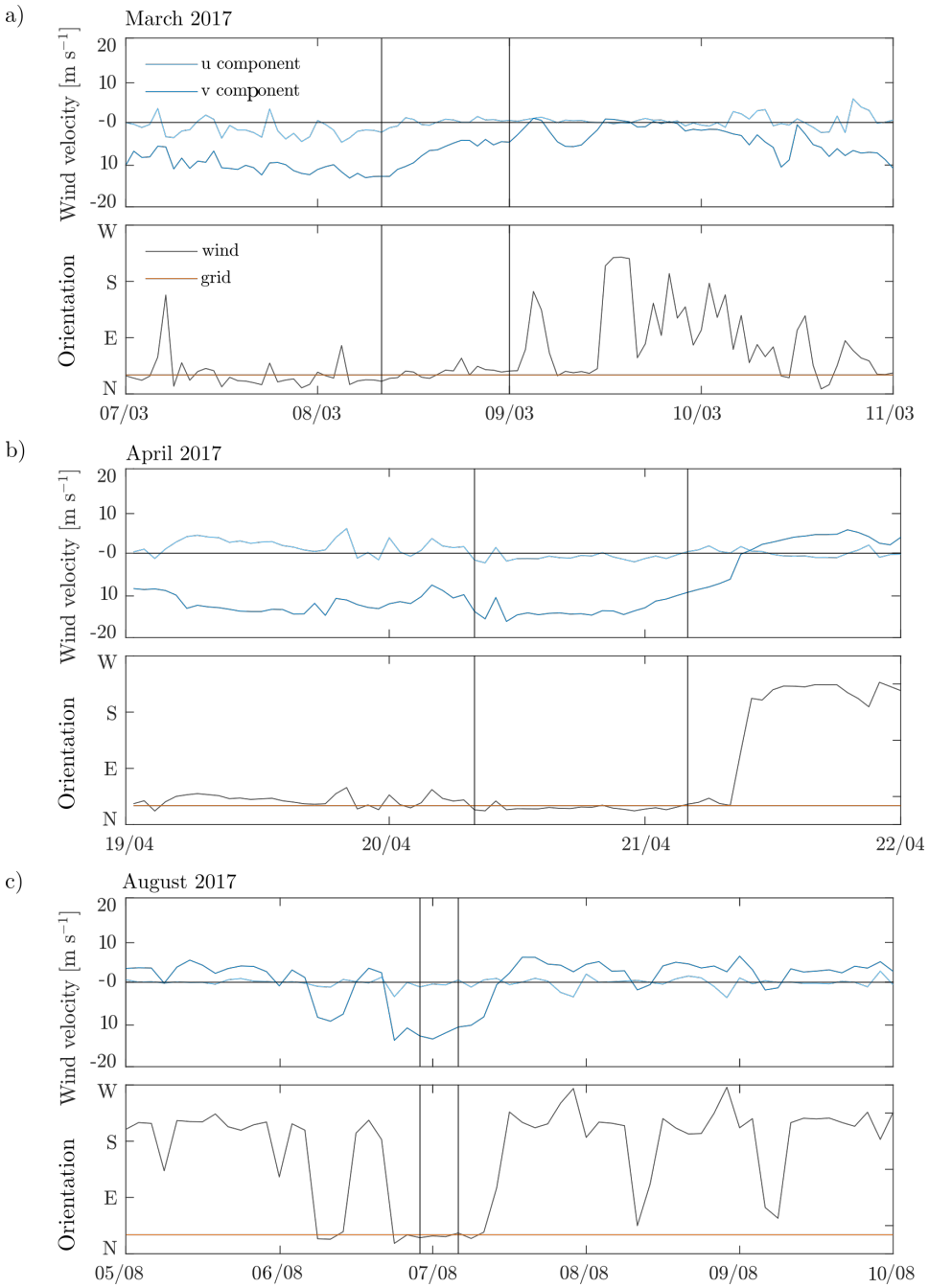

Figure 6.19: Wind forcing in the simulated wind events of a) March 2017, b) April 2017, c) August 2017. Wind components along the crosswise (light blue line) and longitudinal (dark blue) dimensions; main wind (grey) and grid (orange) orientation in the northern Lake Garda. Black lines indicate the time window in which the results of the hydrodynamic simulations are evaluated.

The numerical values of these quantities are reported in Tab. 6.2. For the simulation of idealized box domain in section 6.3, the vertical scale H was equal to the depth of the basin. In the case of a real lake, its definition is more complicated due to the inhomogeneities of the

bathymetry and the vertical density structure. In general, the value H for a real case can be associated to the thickness of the water column directly affected by the action of the wind. In our case, we identify the layer where a closed circulation develops, with the upper layers flowing along-wind and the deeper layers against-wind. The thickness of this layer varies according to the season and to the vertical variations of density. In Fig. 6.20 the average temperature profile from each scenario in the rectangular sub-domain are plotted.

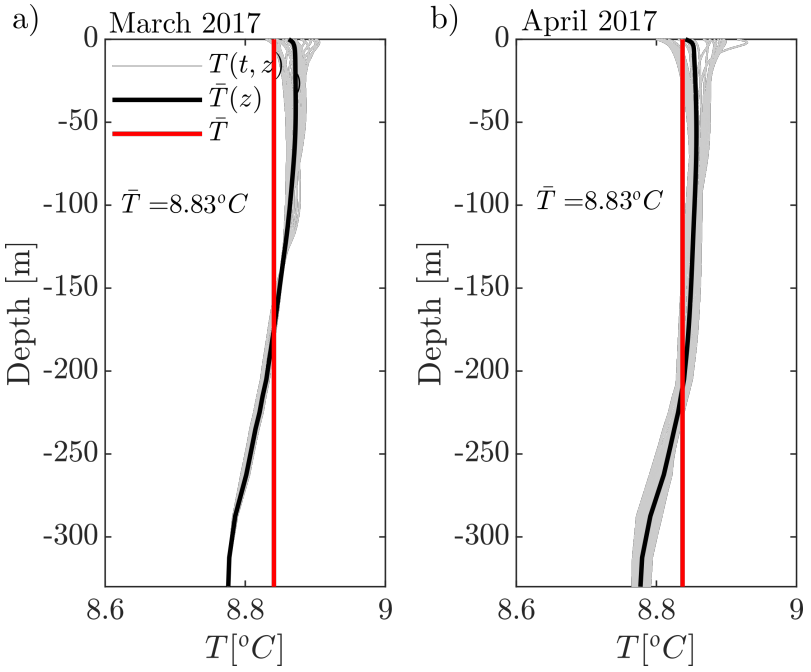

Figure 6.20: Temperature profiles from spring scenarios (a,b) during the investigated hours, obtained by averaging the thermal profiles in the rectangular sub-domain (grey lines), then in time (black line), then along the water column (red line). Note: profiles are plotted every two hours.

As the figure shows, in spring simulations the average temperature oscillates in time around the mean value, with a maximum top-bottom gradient of 0.1 °C (Fig. 6.20). Hence, nearly uniform density conditions can be assumed and H is taken as the mean depth of the rectangular ideal trunk. Differently, during summer (Fig. 6.21), a strong stratification exists, with relevant variations not only along the water column but also in time, as the circulation induced by the wind has a de-stratifying effect. In this latter case, the characteristic depth H_1 is taken as the thickness of the surface mixed layer (13 m).

A uniform temperature value is then computed by averaging temperature from the surface to H depth (H_1 for the summer case). From temperature, a uniform density is evaluated

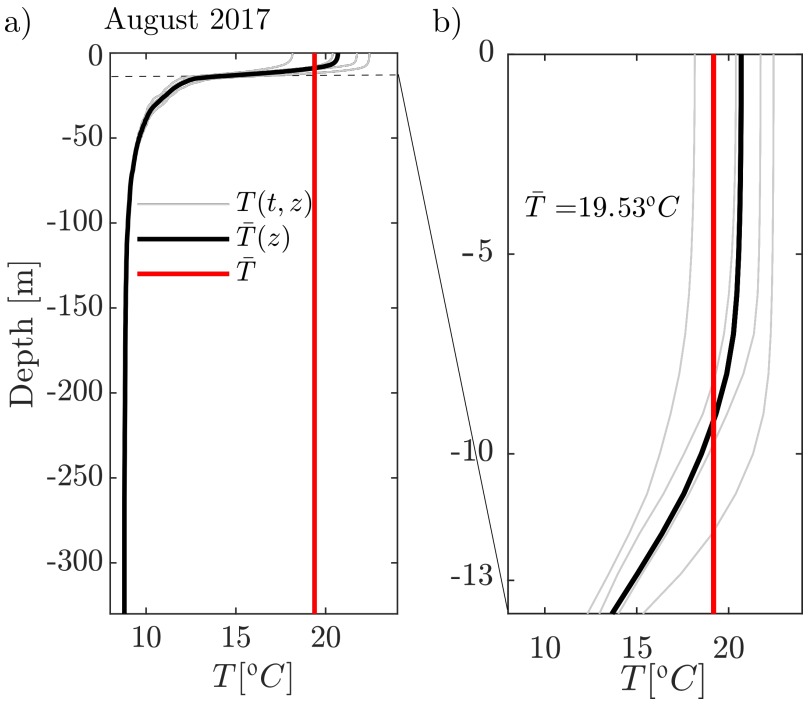

Figure 6.21: Temperature profile from summer scenarios along the whole water column (a) and zoomed on the considered layer (b), during the investigated hours, obtained by averaging the thermal profiles in the rectangular sub-domain (grey lines), then in time (black line), then along the water column (red line). Note: profiles are plotted every two hours.

according to the UNESCO equation of state [UNESCO, 1981], consistent with Delft3D model parametrization [Lesser et al., 2004].

Similarly, the value of uniform vertical eddy viscosity to be used in this application is chosen by taking an average in time and space. In Fig. 6.22 the mean profiles of ν_z are shown for each scenario from the surface to H depth.

Since the hydrodynamic model adopts a k-ε turbulence parametrization, the numerical eddy viscosity obtained from the simulations has a parabolic shape along the vertical. In this application, the uniform value of vertical eddy viscosity computed for each scenario is assumed (red line) and used in the analytical formulations.

Finally, wind tangential stress is computed accounting for the longitudinal wind component only, as crosswise wind stress is minimum in the time window investigated. A uniform and constant value of V_w (wind velocity along y) is obtained by taking an average over the surface of the rectangular sub-domain and over time in the investigated simulation hours. The mean wind shear is then computed as $\tau{=}\rho_a C_d U_w^2$, with the C_d defined based on a piecewise linear function

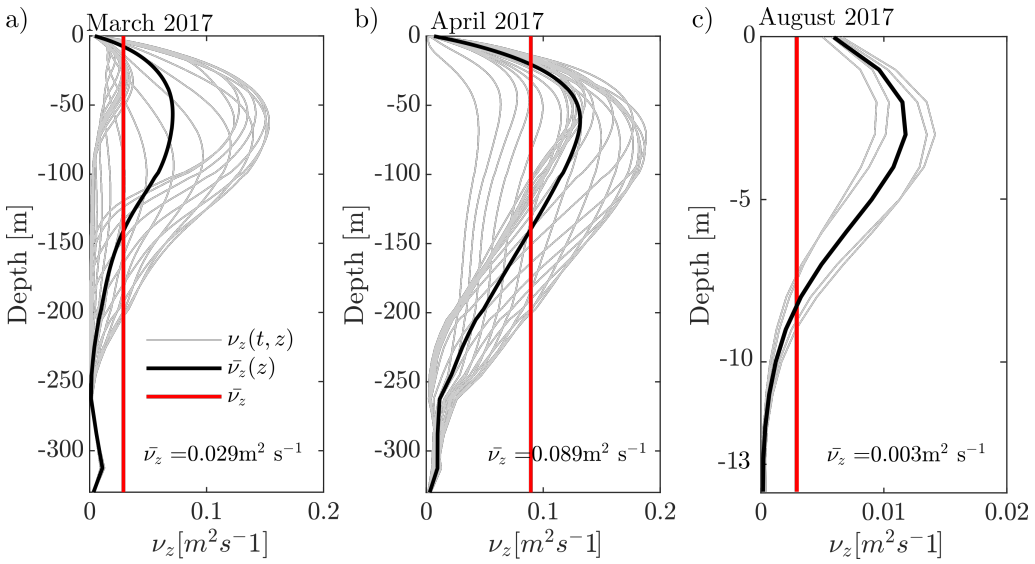

Figure 6.22: Vertical eddy viscosity profiles from each scenario (a,b,c) during the investigated hours, obtained by averaging the profiles in the rectangular sub-domain (grey lines), then in time (black line), then along the water column (red line). Note: profiles are plotted every two hours.

of wind speed derived from [Wüest and Lorke, 2003].

6.4.1.4 Computation of transport

The horizontal components of fluid motion are derived by averaging the profiles in time and along the two horizontal dimensions over the internal domain, while preserving the vertical variation along the water column. The shape and the magnitude of u and v are compared with the analytical formulation in dimensionless terms, by rescaling their value with a factor U_0 (as defined in eq. (6.16)).

Horizontal transport is then computed by integrating the dimensionless profile along the water column until the inversion depth, i.e. the depth where the sign of velocity changes. In this application, only cross-wise transport is computed (Φ_x from eq. (6.29)), as it will be discussed further on.

6.4.2 Results

The analysis conducted in Chapter 5 already demonstrated that the Earth rotation drives transport in Lake Garda by forcing a secondary circulation that involves either the whole water

column, during the nearly unstratified season, or the surface mixed layer, during the warm stratified season. Here, our aim is to verify that the order of magnitude of the crosswise component of motion (induced by planetary rotation and from now on defined as 'Ekman' transport), can be predicted via our analytical solution A2019, despite the strong assumptions we made to derive it. In the following paragraphs, the solution A2019 proposed in section 6.3 is validated against numerical results of Lake Garda simulations and compared with the additional three analytical solutions available in the literature: the classic Ekman spiral with finite depth (E1905), the solution provided by Simons [1980] (S1980), and by Toffolon [2013] (T2013).

6.4.2.1 Profiles of horizontal components of motion

As anticipated in the previous sections, the geometrical (H) and hydrodynamic (ρ_w,ν_z) characteristics of the three investigated scenarios are different. In order to have a fair comparison, we aggregate the spring simulations (March and April 2017 events) as representative of the 'Spring' case and we discuss the results for the 'Summer' case (August 2017) separately.

6.4.2.2 Spring simulations

In this paragraph we investigate the horizontal velocity in the nearly unstratified conditions typical of the early spring season. Fig. 6.23 shows the two components u and v in their dimensionless form by rescaling them of a factor U_0, whose numerical value is reported in Tab. 6.2. The numerical profiles are compared with the analytical ones in their no-slip bottom boundary formulations. A similar analysis was conducted also comparing the results with the free-slip formulation, without any relevant differences.

In the spring events the numerical solution of the crosswise velocity profile (u/U_0, Fig. 6.23a,c) resembles the A2019 solution both in the shape and in the overall order of magnitude. In both cases, the inversion depth of the numerical profile is 10% deeper than the one from A2019 and S1980 solutions. In April case, the surface velocity is underestimated by both A2019 and S1980 solutions, while being well predicted by E1905. At the bottom, A2019 and S1980 have the same shape, which is similar to that of the numerical profile.

A different behaviour is found in the longitudinal component of the flow (v/U_0, Fig. 6.23b,d).

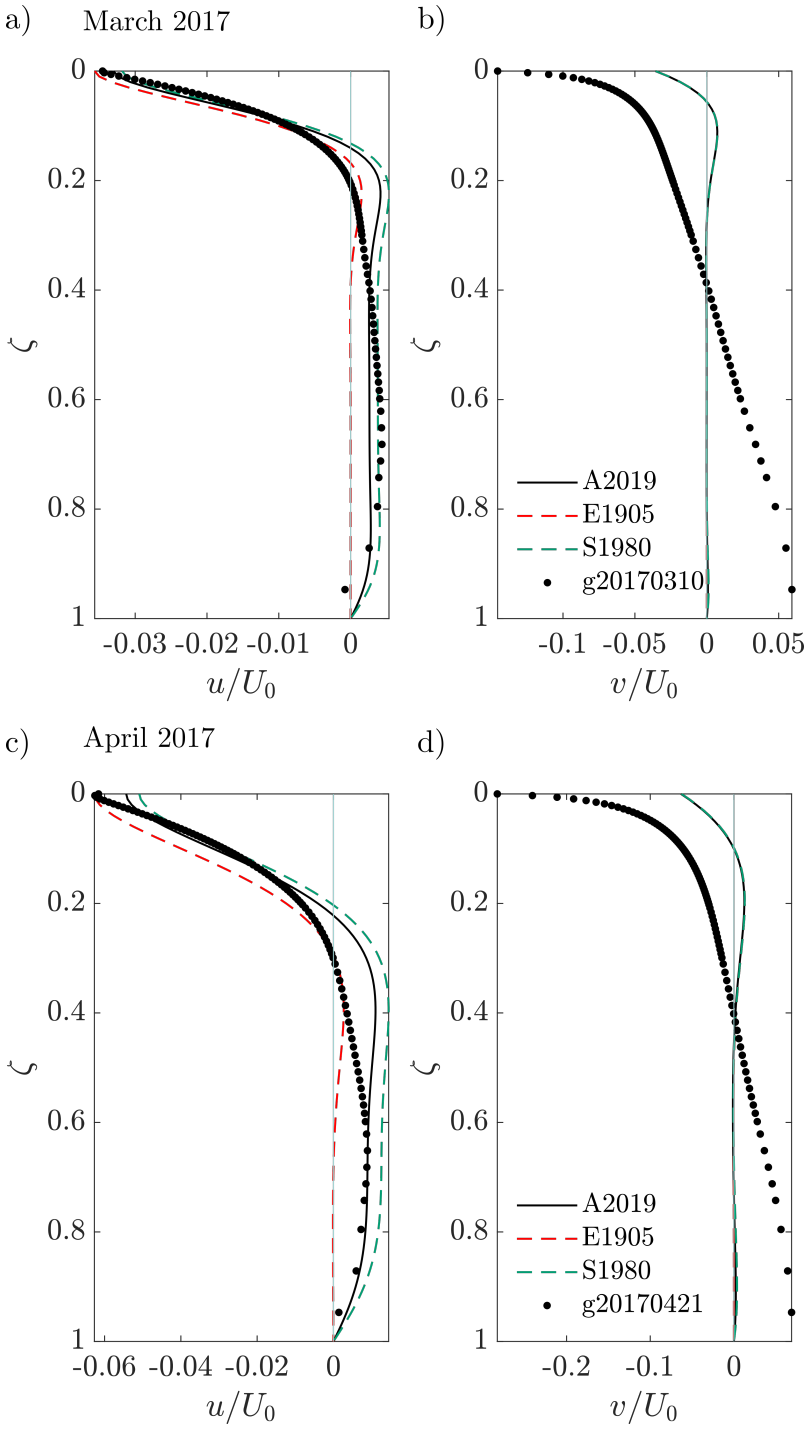

Figure 6.23: Vertical profiles of dimensionless velocities u/U_0 (left column), v/U_0 (right column) obtained from the analytical solutions (A2019, E1905, S1980) and from the numerical simulation of Lake Garda in (a,b) March and (c,d) April 2017. Wind aligned with the y axis, no-slip bottom boundary condition. Note: to ease the visualization of the figure, T2013 profile is not plotted as it is out of range.

The existence of a longitudinal circulation that, as expected, moves the surface water along wind and the bottom layers against wind, is verified. However, the prediction by any of the analytical solution is dramatically wrong in the shape and magnitude. Moreover, the analytical solutions underestimate both surface and bottom transport, and, as previously seen for the u component, they predict a shallower inversion depth: where the numerical inversion occurs ($\sim$ 40% of the total H), the analytical velocity is null already and motion is totally suppressed.

6.4.2.3 Summer case

An comparison is proposed here for the summer case, where the effect of Earth rotation was seen in chapter 5 on lateral density gradients in the upper layer of Lake Garda. In Fig. 6.24 the numerical velocity profiles are compared with the analytical solutions. We recall that in this section the performances of the analytical solutions against the numerical model are tested in a surface layer of the lake, of thickness $H_1 = 13$ m. Since in the summer case the characteristic depth considered does not coincide with the real bottom of the lake, the no-slip condition can not be safely applied in the analytical formulation. In this case, a free-slip condition applies, by assuming zero tangential stress between the upper mixed layer and the water below.

Differently from the previous scenarios, in this case the shape of the crosswise velocity u/U_0 is not exactly captured by any of the analytical solutions (Fig. 6.24a). The wrongest profile is E1905, which does not predict the inversion of sign and greately overestimates the velocity. A2019, S1980 and T2013 profiles catch the order of magnitude of crosswise velocity and the boundary values at the top and at the bottom of the layer, but fail in reproducing the modeled profile. The latter shows a nearly uniform velocity from the surface to the 70 % of the characteristic depth H_1 ($\zeta \sim 0.7$). This shape can be related to the temperature stratification that the model takes into account: in fact, as seen in Fig. 6.21b, temperature is nearly constant from the surface to the depth of 9 m, and then starts to decrease until the thermocline.

While in the spring case the T2013 solution was out of scale, and for this reason we did not even plot it in Fig. 6.23, in this summer case its behaviour is in total agreement with A2019 and S1980, as the smaller depth reduce the value of ε to the range where it behaves correctly. However, all the solutions fail in predicting the inversion depth of the profile ($\sim$ 10 m). Along

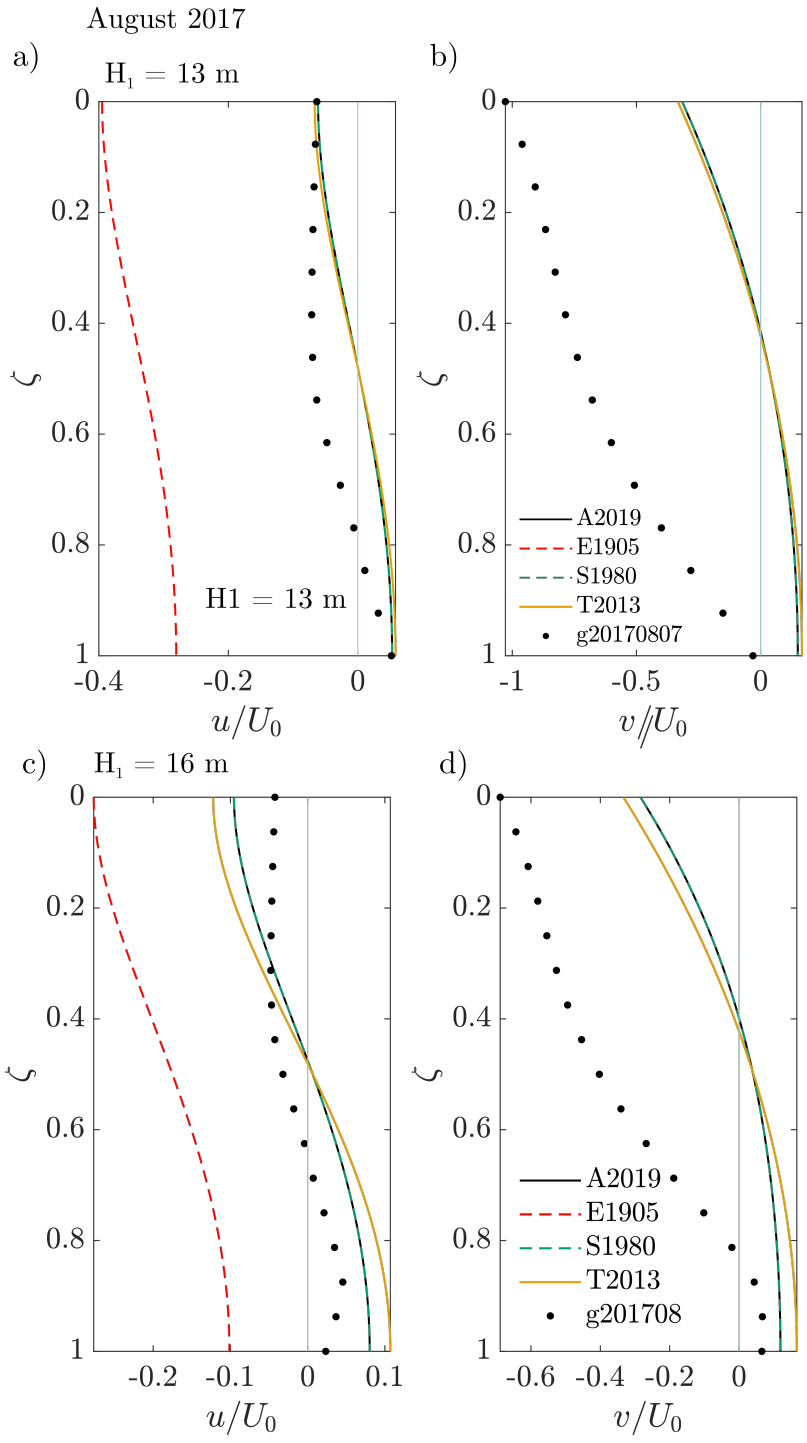

Figure 6.24: Vertical profiles of dimensionless velocities u/U_0, v/U_0 obtained from the analytical solutions (A2019, E1905, S1980, T2013) and from the numerical simulation of Lake Garda in August 2017 assuming (a,b) $H_1 = 13$ m and (c,d) $H_1 = 16$ m. Wind aligned with the y axis, free-slip bottom boundary condition.

the longitudinal direction (Fig. 6.24b), the performance of all analytical solutions are bad, and even worse than in the spring cases. In fact, in this case the numerical solution does not show

any inversion along the water column, which is predicted by all analytical solutions. In both directions (u,v) the integral of the profiles obtained in summer simulations is not null, as most of the water column moves water downwind in the upper layers and the motion in the deeper layer is not fully developed. The reasons of this can be either that the stationary conditions are not achieved yet, or that the surface layer where the secondary circulation should develop is thicker than H_1. In order to verify whether the inconsistent results are related to a incorrect definition of tH_1, we tested the performance of the analytical solution by deepening H_1 down to 16 m (Fig. 6.23b,c). In this case, the obtained profile of u/U_0 reproduce better the simulated results, which in turn are likely to approach a vertically closed shape, even though the match in the order of magnitude at the surface and at the bottom is lost.

6.4.2.4 Ekman transport

A more general overview of the different solutions is provided in Fig. 6.25 and 6.26, where the dimensionless transport Φ_x, calculated from numerical simulations, is plotted against the parameter ε, and compared with the continuous curves of the analytical solutions (markers denote numerical outputs of the simulated scenarios) for the no-slip and free-slip formulations. Due to the evident distance of the simulated longitudinal velocity (v) from the analytical results, transport along y was not computed.

As a first observation, all spring points lay close the bell-shaped curve provided by the A2019 solution for the no-slip formulation (Fig. 6.25). In particular, they fall in the high ε range (> 10) and along the descending part of the A2019 bell. This range is typical of either deep lakes at high latitudes conditions: in the case of spring simulations in Lake Garda, which is located at mid latitude, the condition that is satisfied here is clearly the depth H, assumed as 330 m. However, in this range the difference between A2019, S1980 and E1905 become. In fact, the conditions here approach that of infinite depth, where crosswise surface slope approaches zero (see Fig. 6.2 in section 6.3), such that also S1980 becomes similar to A2019. Interestingly, in this range also the bottom boundary condition becomes irrelevant: in fact, if the same points are plotted in the free slip case (Fig. 6.12), it is clear that they all lay between the analytical curves E1905, S1980 and A2019, in the region where they all provide reliable estimates of small

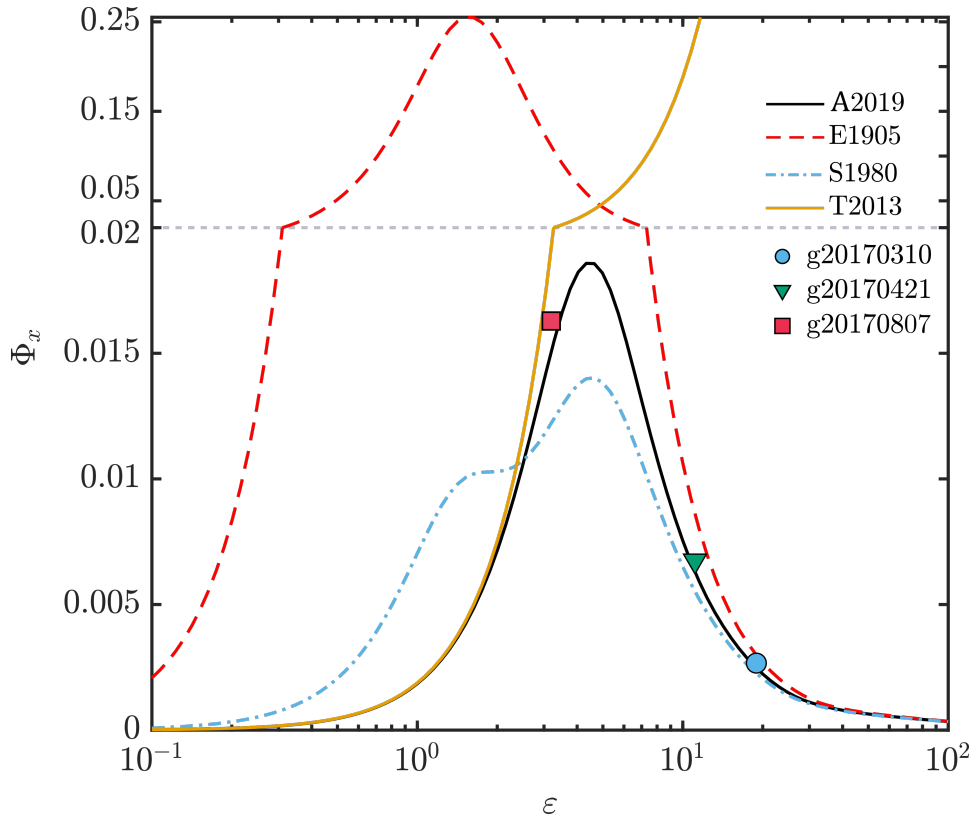

Figure 6.25: Crosswise transport Φ_x computed with analytical solutions (A2019, E1905, S1980 and T2013) and from Lake Garda numerical simulations, wind aligned with the y axis, no-slip bottom boundary condition. Note: for a better visualization, y axis is plotted with two different scales, separated by the gray dotted line.

Ekman transport (Fig. 6.26).

In the same figure, the transport for summer case is plotted as well. As a first consideration, summer case is representative of the intermediate range of ε, where smaller depths affect the development of the Ekman transport. Interestingly, the main point (pink square) lays above A2019 and T2013 solution. In fact, as it was clear from the velocity profiles in Fig. 6.24, by predicting a shallower depth where the velocity profiles changes sign, the analytical solutions A2019, S1980 and T2013 underestimate the thickness of the water column set in motion by Ekman transport, hence underestimating Ekman transport Φ_x itself.

In Fig. 6.26, some additional markers of the same color of the main summer one (red) are plotted in order to show how the quantification of the overall transport changes in summertime if the characteristic depth H_1 is chosen differently. Values from 12 m to 18 m ($\sim$ thermocline depth) are taken. As it is clear from the figure, by changing the characteristic depth H_1 the

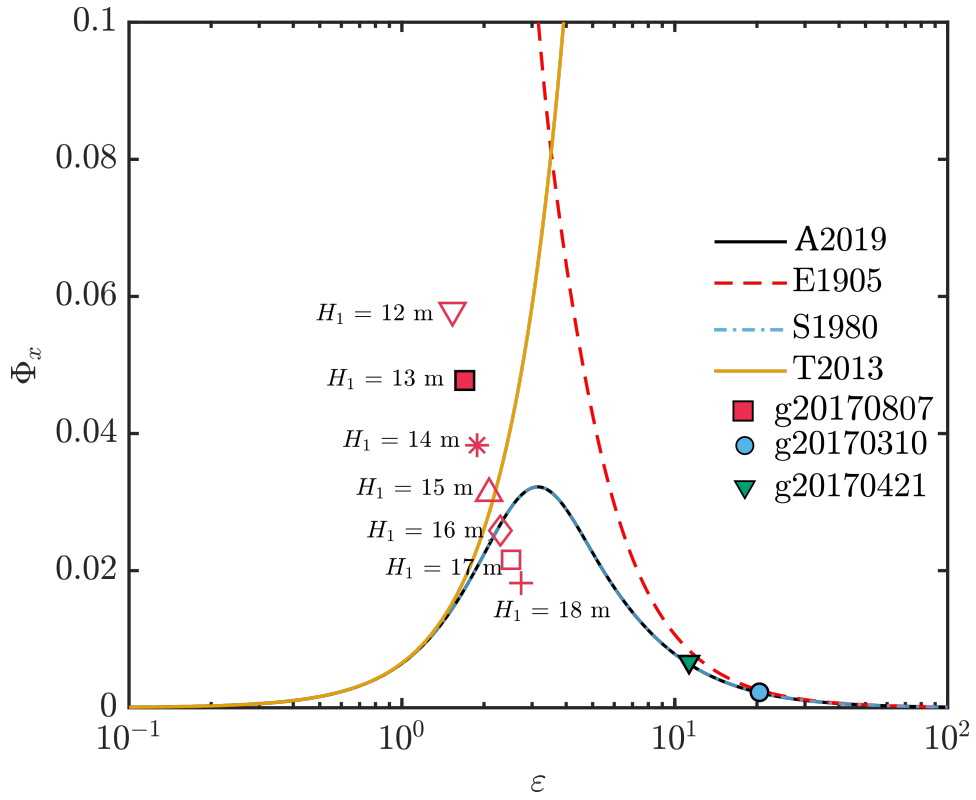

Figure 6.26: Crosswise transport Φ_x computed with analytical solutions (A2019, E1905, S1980 and T2013) and from Lake Garda numerical simulations, wind aligned with the y axis, free-slip bottom boundary condition. Empty red markers are obtained for August 2017 by considering different H_1 characteristic depths.

dimensionless transport Φ_x, associated to the Coriolis force, changes dramatically. In this regard, we stress that it is not the integral of the velocity profile that changes as H_1 changes: in fact, such integration is made from the surface to the depth of sign inversion, which is the same in all the test cases, as we take H_1 always deeper than z_x =10 m (see eq. (6.28)). Hence, the change is given by the scale $U_0 \cdot H$, by which F_x is divided in order to get the dimensionless value Φ_x. The results of changing H_1 in Fig. 6.26 might seem trivial, because increasing H_1 (H in the general formulation), Φ_x inevitably decreases, but in this applied summer case it also has consequences on the corresponding value of ε, which increases. In fact, the uniform values of ρ_w and ν_z are taken according to the mean value in the layer of thinckess H_1. Hence, the shift towards the right of the red empty markers also represents a change in the hydrodynamic characteristics of the fluid, from lighter (warmer) and turbulent water (small H_1, near surface water) to heavier (colder) and more stable water (larger H_1, metalimnetic water).

6.4.3 Discussion and conclusions

The results presented in the previous paragraphs show that the secondary circulation in the deep and narrow trunk of Lake Garda, which was already demonstrated to exist by numerical tests and observations in Chapter 5, is unequivocally caused by Earth rotation. In fact, the analytical solutions adopted take into account the longitudinal component of wind only, and show that the amount of water, driven orthogonally to the wind in Lake Garda simulations, has the same order of magnitude of estimated Ekman transport. However, we also observed that the numerical outputs are not perfectly overlapped to the analytical solutions, and that some differences are evident in all scenarios.

In spring simulations, the largest discrepancy is along the longitudinal direction v, where surface and bottom velocity is largely underestimated by the analytical approaches. This can be related to two main reasons: one is the choice of ν_z, the other is the assumption of steady state conditions and uniform flow field. On the first point, the numerical model uses, in the shallowest and deepest regions, a value of the vertical eddy viscosity that is smaller than the uniform adopted value. The profile out-coming from the numerical model is a direct consequence of the parabolic vertical eddy profile parametrized by the k-ε turbulence model in Delft3D, and can not be reproduced by the analytical solutions assuming ν_z as a constant, whose dependency on ζ is quadratic [see e.g., Heaps, 1984, for the non rotating-case]. As it is clear from Fig 6.22a and b, in the spring cases ν_z approaches zero rapidly below 150 m depth, which is the 45% of the total water depth ($H = 330$ m). The excessive mixing introduced by assuming ν_z uniform along the water column might be the main responsible of the suppression of motion, especially in the deeper layers and along the wind direction, were velocities are 10 times larger than along the cross wind direction. On the second point, it is important to recall that the portion of the lake taken into account for deriving the mean velocity profile is limited to the internal rectangular trunk, which on purpose excludes the lateral boundaries, in order to neglect horizontal variations of the flow field. In our tests on idealized box domains, the steady state conditions were synthetically imposed, and the flow field uniformity was easily achieved. In the real case of Lake Garda, with a realistic wind forcing and an extremely complex morphology, the same assumptions are not that obvious. In fact, by excluding the northern and southern border of the lake, we assure

that topographic variations are limited. Differently, the stationarity, that justifies the integral condition (eq. 6.11), is hardly verified on a lake of a length of 50 km and depth 330 m, after approximately one day of steady wind. In this regard, it is interesting to note that stationary conditions along the longitudinal direction were not satisfied even in the deepest box domains, unless a larger ν_z was imposed (see section 6.3.4.3).

Despite this wrong description of the along wind component of flow, the solution for the crosswise transport is predictive, with with A2019 performing well in all cases. Hence, while along y the integral condition applied to the analytical solution is not reliable, along x nearly stationary conditions are reached and a closed circulation actually establishes. The magnitude and the vertical distribution of such circulation can be precisely predicted by our A2019 approach, if vertical density gradients are weak enough as those in Lake Garda during spring.

The results achieved in the summer conditions question the reliability of the proposed solutions in thermally stratified conditions. In fact, in this case the vertical gradients and the smaller vertical eddy viscosity work against the success of an analytical approach, based on uniform density and steady state conditions. Both issues can be overcome by considering a layer of limited thickness. Hence, we considered a layer of nearly homogeneous density by limiting the analysis to the first H_1 =13 m of water column, where temperature variations exist ($\sim 5°$), but are less critical as if the whole water column is taken into account ($\sim 13°$). The same holds for vertical eddy viscosity, which is higher in the epilimnion than in the rest of the water column during summer (see Fig. 6.22). However, thus showing the existence of a secondary circulation, the velocity profile simulated is not well reproduced by the analytical solutions, and the best match between simulated and analytical transport was found for a different $H_1 = 16$ m.

The computation of Φ_x in Fig. 6.25 and Fig. 6.26 showed that the analytical solution formulated in this chapter is suitable for estimating Ekman transport in a real lake as Lake Garda, if the appropriate combination of duration of the external forcing, thermal stratification and turbulent regime apply. In this regard, it is important to stress that for the summer case the proposed solution provides just as a rough estimate of the overall Ekman transport, which is highly dependent on the depth adopted. In fact, we have seen that summer points in Fig. 6.26 can be very far from the analytical curves or lay on A2019 and T2013 lines according to the

value of H_1. However, the best match obtained with $H_1 = 16$ m does not coincide with a perfect reproduction of the velocity profile (Fig. 6.24c), and the estimated quantity Φ_x comes out as an integral balance between the overestimation of transport at the top layers and the underestimation in the interior.

Conclusively, further research is needed in order to correctly define the significant depth affected by the development of the secondary circulation induced by Earth rotation in stratified conditions. In this regard, a different new solution taking into account density gradients and vertical variations of ν_z would clearly prevent from not rigorous or speculative assumptions. Differently, during spring weakly stratified conditions, the A2019 solution is suitable for quantifying the Ekman transport in a real case under a nearly stationary wind forcing. It is also evident that the cases investigated here lay at specific regions of the Φ_x vs ε diagram, where other analytical approaches would have provided reliable results (i.e. T2013 for the summer case, E1905 and S1980 for spring cases). Hence, additional applications are required in other lakes of different geometries and turbulent regimes in order to verify whether the A2019 is actually the only working solution in the intermediate range of ε, where the tests on idealized boxes demonstrated that all the other approaches failed.

Chapter 7

Conclusions

This doctoral research represents a first step towards the understanding of the hydrodynamics of Lake Garda, as an emblematic case of deep and elongated perialpine lake and a key resource for its country. Each chapter addressed a specific aspect that we considered crucial for a systematic, although exploratory, investigation of the drivers of transport in Lake Garda. In the following list the main research contributions included in this thesis are summarized.

1. *Construction of a comprehensive dataset*

   The construction of a comprehensive set of data from all sources available on Lake Garda region is one of the main achievements of the present doctoral research, as well as a fundamental requisite for the setup of a reliable numerical model. As we mentioned several times throughout this thesis, Lake Garda is within a complex political framework and is subject of heterogeneous fields of investigations. This two factors complicate the quantity, the quality and the type of available data. Thus, not only the understanding of the geographical and political boundaries, but also the interaction and collaboration with several local agencies/institutes, resulted to be fundamental steps that the activity of data collection had to go through. From 2016 to 2019 all existing data on water chemical-physical parameters and meteorological variables were collected. The dataset covers a period going from 1990 to present (up to October 2019) and is composed by in-situ data of the water column in several points, remote sensing maps and data from weather stations all around the lake perimeter.

2. *Set-up of a three-dimensional model*

   At the beginning of this research activity on the case study of Lake Garda, no models were available for any kind of investigation from a hydrodynamic point of view. The second main achievement of this doctoral thesis is the set up of a lake model, consisting of a three-dimensional lake hydrodynamic model (Delft3D-Flow) coupled with an atmospheric model

(WRF, Weather Research and Forecasting). The model chain was tested on either short term simulations (single events) or long term simulations (14 years), and against the dataset commented above. The model results from single events runs were compared with a limited number of vertical temperature profiles, while those from long term simulations were compared with all water temperature data available from our dataset. The comparison with different sources of data allowed us to demonstrate that the lake model correctly describes the interannual, monthly, daily and sub-daily variability, and also the surface spatial gradients of water temperature throughout the year. Our multi-scale approach helped us to highlight the main challenges of handling data from sparse and diverse sources and provided an example for other case studies where the monitoring activities are not systematic yet, but a rigorous validation of a lake model is pursued.

3. *Description of typical basin scale circulation*

   As third main contribution of this work, we provided a first description of typical seasonal circulation of Lake Garda at a basin scale. The effects of wind forcing and Earth rotation on the transport processes were investigated under different thermal stratification conditions and typical diurnal wind cycles. Surface currents and secondary circulations in Lake Garda were found to be very sensitive to the spatial distribution of the wind forcing. Gyre patterns were found to develop in the lake as a residual outcome of varying wind forcing, while uniform and constant wind drives unidirectional currents. Upwelling and downwelling motions resulted to be activated by storm wind events, suggesting a significant contribution of Ekman transport in the northern part of the lake, especially in winter unstratified conditions. Earth rotation was correlated with surface lateral transport also in summer, and a quadratic dependency on the longitudinal component of wind (alinged with the main ax of the lake) was found. The use of our numerical model was linked with a local knowledge survey in order to test the experience held by the community on basin-scale hydrodynamic processes in the lake. Through this combined effort, we were able to recognize and physically understand currents unknown to the scientific community but well-known to sailors and surfers. An example is the 'Corif', which flows along the eastern shore in summertime between late morning and afternoon, when wind blows from the south. The transport patterns were also confirmed: a predominant east-to-west surface transport under northerly storm wind and flood events,

and the west-to-east transport under southerly wind.

4. *Understanding of deep mixing dynamics*

   The description of the basin scale circulation in Lake Garda suggested the occurrence of wind events at a synoptic scale which, combined with nearly unstratified conditions in early spring, are likely to affect deep mixing dynamics. Following this lead, we conducted a field investigation on Lake Garda temperature and chlorophyll-a spatial patterns after persistent and strong we events. As a result, we provided explicit observational evidence for the development of wind-driven secondary flows influenced by the Coriolis force. Such flows were never observed in narrow lakes, and we succeeded in providing a first quantification of their effect on wind-driven mixing efficiency.

5. *Ekman transport in narrow elongated lakes*

   Our findings added a new element, the effect of planetary rotation, to be carefully considered when assessing the response of lakes to external forcing and climate change. These results inspired a more detailed analysis of the Ekman transport in lakes of the shape and size of our case study. In fact, when investigating wind-induced steady circulation, the effect of the acceleration due to Earth rotation was often neglected in narrow lakes of horizontal dimension smaller than the Rossby radius. Based on previous results, we questioned this common assumption by revisiting the classical Ekman transport solution for wind stress acting along the main axis of an elongated lake in steady-state conditions. Our revisited analytical approach demonstrated that a secondary circulation develops, and that the resulting crosswise volume transport, constrained in the closed domain, produces downwelling and upwelling that cannot be predicted by the standard Ekman formulas, and that is consistent with what was observed in Lake Garda. We also proved that the Rossby radius does not play any role in this process, which on the contrary is governed by the ratio between the actual depth and the thickness of the Ekman layer. We supported our theoretical analysis with numerical experiments to show the dependence on latitude, width, depth and turbulence closure. Finally, we applied our solution to the case study of Lake Garda, and we demonstrated that it is suitable for estimating Ekman transport in a real lake.

6. *Joint research efforts on Lake Garda and community engagement*

On completion of this doctoral research, one more conclusion still worths to be addressed. We stressed several times that at the time when this doctoral research started, Lake Garda was one of the most unexplored lakes from the point of view of physical limnology, but several research activities were ongoing on different topics. Nevertheless, all the isolated efforts towards a deeper understanding of the internal dynamics of the lake lacked of a systematic approach and of coordination. During these three years of activity, several opportunities for new interdisciplinary collaborations were created in order to join the effort of both scientific community, local experts and public stakeholders. In 2017, a first workshop named GARDEN (Lake GARDa ENvironmental system) was organized by University of Trento with the aim of building a new international partnership for a synergic effort towards a deeper comprehension of the hydrodynamic behaviour of the lake [Toffolon et al., 2017][1]. This workshop was followed by a second edition hosted by University of Brescia in 2018 [2]. During these occasions, several universities and research institutes were called to share their knowledge on the lake, their expertise on similar case studies (e.g. Lake Iseo, Lake Geneva, Lake Maggiore) and to plan future activities. Amongst the several research questions discussed, the aim of providing practical tools for the management of the lake was highlighted as one of the major challenges for the research community, as well as the cooperation with local environmental protection agencies (EPAs) and stakeholders. In this spirit, a public event was promoted in 2018 Toffolon et al.[3], where the state of the art on Lake Garda was summed up and the urgency of joining the effort between the scientific and local community was pointed out. During this event, in October 28th, 2017, an agreement ("Carta di Verona") was signed on their own behalf by several stakeholders and by researchers from seven universities and three research institutes, who launched the scientific task force named Cluster Garda, and made their competences available to local decision makers. As a proof of this joint monitoring activity, between 2017 and 2019 several instruments were installed under a collaborative perspective: in May 2017 a deep thermistor chain was installed by Nioz (Royal Netherlands Institute for Sea Research) and was operational for one year, thanks to a collaboration with University of Trento, Utrecht

[1] https://webmagazine.unitn.it/en/evento/dicam/14603/garden
[2] http://hydraulics.unibs.it/hydraulics/attivita-scientifica/garden-2018/
[3] https://www.gardapost.it/2017/10/30/cluster-garda-task-force-scientifica-per-salvare-il-lago/

University, and to the technical support of the sailing club of Arco and the nautical rescue team of firefighters of Trento; at the beginning of 2018 a new meteo station was installed on the existing buoy of the EPA in Trento off the coast of Riva del Garda; the deployment of two thermistor chains for high resolution temperature data was scheduled by a joint plan of University of Trento and University of Brescia, the latter having already installed one in the southern part of the lake in October 2019; a 24-hour field investigation was conducted in April 2018 by a team from University of Trento, Utrecht University and CNR-ISMAR with the technical support of the sailing club of Arco. Moreover, this enhanced collaboration was also translated into data sharing and new ideas of joint exploration also with CNR-IREA, FEM, local EPAs, many other signatories of the Carta di Verona, and even private citizens as depositories of knowledge on the lake. Thus, the final contribution of this work is that of having paved the way towards a new direction of research in Lake Garda. This new direction is based on the collaboration among the existing scientific communities and on the promotion of the public participation to the research process from the very beginning, i.e. the definition of the research questions, to its final results, i.e. the answers and the solutions. The final aim is raising public awareness on the efforts of the ongoing scientific research on Lake Garda, and working together for an efficient and sustainable management of the unique water resource that it represents.

List of Symbols and Operators

a	area of single pixel from satellite map
A_s	frontal area of the submerged part of an object floating in the water
A_e	frontal area of the emerged part of an object floating in the water
c	celerity of the barotropic wave
C_d	Drag coefficient
$C_{d,s}$	drag coefficient on the submerged part of an object floating in the water
$C_{d,e}$	drag coefficient on the emerged part of an object floating in the water
C_{isopy}	concentration of a tracer at a reference isopycnal surface
C_{surf}	initial constant concentration at the surface (tracer experiment)
$CORR$	correlation
D_E	Ekman depth
E	cumulative heat exchanged between the lake and the atmosphere (per unit area)
E_k	Ekman number
f	Coriolis frequency
f_s	fraction of submerged volume of an object
F_e	Force acting on the emerged part of an object floating in the water
F_{ext}	sum of external forces on an object floating in the water
F_s	Force acting on the submerged part of an object floating in the water
g	gravitational acceleration
g'	modified gravitational acceleration
H	characteristic vertical length scale
H_1, H_2	thickness of a two-layer stratification
H_m	vertical scale of turbulent momentum transport
L	characteristic horizontal length scale
m_p	mass of an object floating in the water
M	modeled data
MAE	Mean Absolute Error
ME	Mean Error (bias)
$NRMSD$	Normalized Centred Root Mean Square Deviation
NSD	Normalized Standard Deviation
NSE	Nash Sutcliffe Efficiency
O	observed data
p	pressure
q_E	Ekman transport (per unit length)
q_{th}	theoretical lateral transport per unit length
q_T	vertically integrated lateral transport (per unit length) by Toffolon [2013]
q_x, q_y	transport per unit length along x,y direction
Q_x	total transport along the cross-wind x direction
r	ratio between Φ_x and Φ_y
r_p	radius of the spheric particle
R	Rossby radius
R_o	Rossby number
$Re_{p,f}$	Reynolds number of an object subject to a fluid f
$\widetilde{R}$	Rossby radius of deformation
$RMSD$	Root Mean Square Deviation
S	complex water surface slope
S_0	characteristic scale of water surface slope
t	time
T	complex wind stress
T_0	characteristic scale of wind stress
T_i	inertial period

u	component of flow velocity along x direction
U,U_0	scale of horizontal velocity of water
$\boldsymbol{U_w}$	vector of wind velocity
v	component of flow velocity along y direction
$\boldsymbol{v_a}$	velocity vector of air above the lake surface
$\boldsymbol{v_p}$	velocity vector of an object on the lake surface
$\boldsymbol{v_w}$	velocity vector of water surface
V_{isopy}	volume of water below a reference isopycnal surface
V_s	submerged volume of an object
V_{tot}	total volume of an object floating in the water
V_{vent}	ventilated volume
w	component of flow velocity along z direction
W	complex horizontal velocity (dimensionless)
x	first horizontal direction (referred to as transversal, lateral, crosswise)
$\boldsymbol{x_p}$	position vector of an object on the lake surface
y	second horizontal direction (referred to as longitudinal
z	vertical direction
z_b	vertical coordinate of the bottom
z_t	vertical coordinate of the water surface
z_x	depth where u is zero
z_y	depth where v is zero
α	anisotropy parameter by Toffolon [2013]
$\Delta_c T$	unbiased anomaly of temperature
ε	ratio between H and D_E, proportional to E_k
ζ	boundary-fitted vertical coordinate (dimensionless)
ζ_x	depth where ω_x is zero
ζ_y	depth where ω_y is zero
η	ventilation efficiency
Θ	complex function of ε
ν_a	cinematic viscosity of air
ν_h	horizontal eddy viscosity of water
ν_w	cinematic viscosity of water
ν_z	vertical eddy viscosity of water
ρ, ρ_w	density of water
ρ_a	density of air
ρ_1, ρ_2	density of the two layers in a two-layer stratification
σ	complex water surface slope (dimensionless)
σ_x,σ_y	real, imaginary part of σ (dimensionless)
$\boldsymbol{\tau}$	vector of tangential wind stress
τ_x, τ_y	x,y components of tangential wind stress
$\tau_x z$	shear stress produced by the gradient of u along the vertical direction z
$\tau_y z$	shear stress produced by the gradient of v along the vertical direction z
$\mathcal{T}$	complex wind stress (dimensionless)
ϕ	latitude
ϕ_h	net heat flux at the lake-atmosphere interface
Φ_x, Φ_y	flux along x,y direction (dimensionless)
ω	complex horizontal velocity
ω_x,ω_y	real, imaginary part of ω
Ω	angular speed of Earth rotation

List of Research Outputs

Scientific Publications

· Amadori, M., Morini, G., Piccolroaz, S., and Toffolon, M. Involving citizens in hydrodynamic research: A combined local knowledge - numerical experiment on Lake Garda, Italy. *Science of The Total Environment*, 722:137720, 2020b. doi: 10.1016/j.scitotenv.2020.137720;

· Amadori, M., Piccolroaz, S., Dijkstra, H. A., and Toffolon, M. What makes an elongated lake 'large'? Scales from wind-driven steady circulation on a rotating Earth. *Journal of Great Lakes Research*, 2019. ISSN 0380-1330. doi: 10.1016/j.jglr.2019.10.013;

· Piccolroaz, S., Amadori, M., and Dijkstra, M. T. H. A. Importance of planetary rotation for ventilation processes in deep elongated lakes: Evidence from Lake Garda (Italy). *Scientific Reports*, 9, 2019. doi: 10.1038/s41598-019-44730-1;

· Amadori, M., Piccolroaz, S., Giovannini, L., Zardi, D., and Toffolon, M. Wind variability and Earth's rotation as drivers of transport in a deep, elongated subalpine lake: The case of Lake Garda. *Journal of Limnology*, 77(3), 2018. doi: 10.4081/jlimnol.2018.1814.

Unpublished works

· Van Haren, H., Piccolroaz, S., Amadori, M., Toffolon, M., and Dijkstra, H. A. Moored observations of turbulent mixing events in deep Lake Garda (I). *under review for Limnology and Oceanography*, 2020;

· Amadori, M., Giovannini, L., Toffolon, M., Piccolroaz, S., Zardi, D., Bresciani, M., Giardino, C., Luciani, G., Kliphuis, M., van Haren, H., and Dijkstra, H. A. Multi-scale validation of a 3D atmosphere-lake model based on standard monitoring data. *Under review for Environmental Modeling & Software*, 2020a.

Conferences contributions

· Amadori, M., Piccolroaz, S., Toffolon, M., Giovannini, L., Zardi, D., Kliphuis, M., van Haren, H., Bresciani, M., Giardino, C., Luciani, G., Dijkstra, H. A. (2019), Multi-scale validation of a 3D one-way coupled atmospheric and lake hydrodynamic model, LAKE2019, Toulouse, France, 21-24/10/2019.

· Amadori, M. and Toffolon, M. (2019) Modelling the effects of different operational scenarios of hypolimnetic withdrawal on water quality dynamics in a lake, Physical Processes in Natural Waters Workshop (PPNW2019), Yichang, China, 9/09-14/09/2019.

· Amadori, M., Morini, G., Piccolroaz, S. and Toffolon, M. (2019), Catching breezes and currents in Lake Garda: use of Local Knowledge to validate numerical models, International Conference on Alpine Meteorology, (ICAM2019), Riva del Garda, Italy, 2/09-6/09/2019.

· C. Stratmann et al. (2019), SS6 O3 Urban Algae - ecological status of urban ponds and the public perception of their ecosystem services, 11th Symposium for European Freshwater Sciences, Zagreb, Croatia, 30/06-5/07/2019.

· Amadori, M., Morini, G., Pozzi, S. and Toffolon, M. (2019), Long-term ecological modeling of a subalpine lake subject to anthropogenic changes and restoration via hypolimnetic withdrawal, European Geophysical Union (EGU) General Assembly, Vienna, 7–12 April 2019.

· Amadori, M. (2019), Characterisation of transport phenomena in Lake Garda through integrative hydrodynamic and meteorological modelling, Alpine Conference, Innsbruck, 4 April 2019.

· Amadori, M., Morini, G., Piccolroaz, S. and Toffolon, M. (2018), Local knowledge as a validation tool for the hydrodynamic modeling of Lake Garda, Italy, Citizen Obervatories for natural hazards and Water Management (COWM2018), Venice, 27-30 November 2018.

· Amadori, M., Piccolroaz, S., Dijkstra, H. A. and Toffolon, M. (2018), On the significance of lake's size when assessing the effect of Earth's rotation on wind-driven steady state circulations, ELLS-IAGLR 2018, Evian, 23-28 September 2018.

· Piccolroaz, S., Amadori, M., Toffolon, M. and Dijkstra, H. A. (2018), Wind forcing and planetary rotation as key drivers of ventilation in deep elongated lakes: evidence from Lake Garda (Italy), Physical Processes in Natural Waters Workshop (PPNW2018), Solothurn, 20-24 August 2018.

· Amadori, M., Piccolroaz, S., Dijkstra, H. A., Toffolon, M. (2018) Influence of Earth rotation on the transport in narrow lakes, GardEN, 2nd International Scientific Workshop, Manerba del Garda (BS), 10 May 2018.

· Toffolon, M., López Moreira, G. A., Adami, L., Amadori, M., Bresciani, M., Carniel, S., Dijkstra, H. A., Falcieri, F. M., Farinelli, A., Fatone, F., Gerosa, G. and Giardino, C. (2017), A scientific task force to study the largest lake in Italy, GLEON All Hands' Meeting, 27 November – 1 December 2017, Mohonk Lake, NY, USA.

· Amadori, M., Piccolroaz, S., Toffolon, M. (2017), Typical seasonal transport patterns in Lake Garda, Physical Processes in Natural Waters Workshop (PPNW2017), Helsinki, 21-25 August 2017.

· Amadori, M. and Toffolon, M. (2017), Hydrodynamic model of Lake Garda, GardEn, 1st International Scientific Workshop, Trento, 2 February 2017.

· Toffolon, M., Amadori, M., Giovannini, L., Piccolroaz, S., Zardi, D., "Modellazione integrata delle forzanti meteorologiche e delle circolazioni nel lago di Garda" in *XXXV Convegno Nazionale di Idraulica e Costruzioni Idrauliche* ,Bologna, 14-16 Settembre 2016.

List of References

Aeschbach-Hertig, W., Holzner, C. P., Hofer, M., Simona, M., Barbieri, A., and Kipfer, R. A time series of environmental tracer data from deep meromictic Lake Lugano, Switzerland. *Limnology and Oceanography*, 52(1):257–273, 2007. ISSN 1939-5590. doi: 10.4319/lo.2007.52.1.0257.

Amadori, M., Piccolroaz, S., Giovannini, L., Zardi, D., and Toffolon, M. Wind variability and Earth's rotation as drivers of transport in a deep, elongated subalpine lake: The case of Lake Garda. *Journal of Limnology*, 77(3), 2018. doi: 10.4081/jlimnol.2018.1814.

Amadori, M., Giovannini, L., Toffolon, M., Piccolroaz, S., Zardi, D., Bresciani, M., Giardino, C., Luciani, G., Kliphuis, M., van Haren, H., and Dijkstra, H. A. Multi-scale validation of a 3D atmosphere-lake model based on standard monitoring data. *Under review for Environmental Modeling & Software*, 2020a.

Amadori, M., Piccolroaz, S., Dijkstra, H. A., and Toffolon, M. What makes an elongated lake 'large'? Scales from wind-driven steady circulation on a rotating Earth. *Journal of Great Lakes Research*, 2019. ISSN 0380-1330. doi: 10.1016/j.jglr.2019.10.013.

Amadori, M., Morini, G., Piccolroaz, S., and Toffolon, M. Involving citizens in hydrodynamic research: A combined local knowledge - numerical experiment on Lake Garda, Italy. *Science of The Total Environment*, 722:137720, 2020b. doi: 10.1016/j.scitotenv.2020.137720.

Ambrosetti, W. and Barbanti, L. Physical limnology in Italy: An historical review. *Mem. Ist. Ital. Idrobiol.*, 50:37–59, 1992.

Ambrosetti, W. and Barbanti, L. Deep water warming in lakes: an indicator of climatic change. *Journal of Limnology*, 58(1):1–9, 1999. ISSN 1723-8633. doi: 10.4081/jlimnol.1999.1.

Ambrosetti, W. and Barbanti, L. Evolution towards meromixis of Lake Iseo (Northern Italy) as revealed by its stability trend. *Journal of Limnology*, 64(1):1–11, 2005. ISSN 1723-8633. doi: 10.4081/jlimnol.2005.1.

Ambrosetti, W., Barbanti, L., and Carrara, E. Mechanisms of hypolimnion erosion in a deep lake (Lago Maggiore, N. Italy). *Journal of Limnology*, 69(1):3–14, 2010. ISSN 1723-8633. doi: 10.4081/jlimnol.2010.3.

Antenucci, J. P., Imberger, J., and Saggio, A. Seasonal evolution of the basin-scale internal wave field in a large stratified lake. *Limnology and Oceanography*, 45(7):1621–1638, 2000. doi: 10.4319/lo.2000.45.7.1621.

Antenucci, J. P. and Imberger, J. Energetics of long internal gravity waves in large lakes. *Limnology and Oceanography*, 46(7):1760–1773, 2001. doi: 10.4319/lo.2001.46.7.1760.

Appt, J., Imberger, J., and Kobus, H. Basin-scale motion in stratified upper lake constance. *Limnology and Oceanography*, 49(4):919–933, 2004. doi: 10.4319/lo.2004.49.4.0919.

Baracchini, T., Chu, P. Y., Šukys, J., Lieberherr, G., Wunderle, S., Wüest, A., and Bouffard, D. Data assimilation of in situ and satellite remote sensing data to 3d hydrodynamic lake models: a case study using Delft3D-FLOW v4.03 and OpenDA v2.4. *Geoscientific Model Development*, 13(3):1267–1284, 2020a. doi: 10.5194/gmd-13-1267-2020.

Baracchini, T., Wüest, A., and Bouffard, D. Meteolakes: An operational online three-dimensional forecasting platform for lake hydrodynamics. *Water Research*, 172:115529, 2020b. doi: 10.1016/j.watres.2020.115529.

Barbieri, A. and Mosello, R. Chemistry and trophic evolution of Lake Luganoin relation to nutrient budget. *Aquatic Sciences*, 54:219–237, 09 1992. doi: 10.1007/BF00878138.

Barsi, J. A., Schott, J. R., Palluconi, F. D., and Hook, S. J. Validation of a web-based atmospheric correction tool for single thermal band instruments. In Butler, J. J., editor, *Earth Observing Systems X*, volume 5882, pages 136 – 142. International Society for Optics and Photonics, SPIE, 2005. doi: 10.1117/12.619990.

Bauer, S. W. and Graf, W. H. Wind induced water circulation of Lake Geneva. In Nihoul, J. C., editor, *Marine Forecasting*, volume 25 of *Elsevier Oceanography Series*, pages 219 – 233. Elsevier, 1979. doi: 10.1016/S0422-9894(08)71132-2.

Becherer, J. K. and Umlauf, L. Boundary mixing in lakes: 1. Modeling the effect of shear-induced convection. *Journal of Geophysical Research: Oceans*, 116(C10), 2011. doi: 10.1029/2011JC007119.

Beletsky, D., Schwab, D., and McCormick, M. Modeling the 1998–2003 summer circulation and thermal structure in Lake Michigan. *Journal of Geophysical Research: Oceans*, 111(C10), 2006. doi: 10.1029/2005JC003222.

Berger, S. A., Diehl, S., Stibor, H., Trommer, G., Ruhenstroth, M., Wild, A., Weigert, A., Jäger, C. G., and Striebel, M. Water temperature and mixing depth affect timing and magnitude of events during spring succession of the plankton. *Oecologia*, 150(4):643–654, Jan 2007. ISSN 1432-1939. doi: 10.1007/s00442-006-0550-9.

Beron-Vera, F. J., Olascoaga, M. J., and Miron, P. Building a maxey–riley framework for surface ocean inertial particle dynamics. *Physics of Fluids*, 31(9):096602, 2019. doi: 10.1063/1.5110731.

Birchfield, G. E. Theoretical aspects of wind-driven currents in a sea or lake of variable depth with no horizontal mixing. *Journal of Physical Oceanography*, 2(4):355–362, 1972. doi: 10.1175/1520-0485(1972)002<0355:TAOWDC>2.0.CO;2.

Bocaniov, S. A., Ullmann, C., Rinke, K., Lamb, K. G., and Boehrer, B. Internal waves and mixing in a stratified reservoir: Insights from three-dimensional modeling. *Limnologica - Ecology and Management of Inland Waters*, 49:52 – 67, 2014. ISSN 0075-9511. doi: 10.1016/j.limno.2014.08.004.

Boegman, L., Ivey, G. N., and Imberger, J. The energetics of large-scale internal wave degeneration in lakes. *Journal of Fluid Mechanics*, 531:159–180, 2005. doi: 10.1017/S0022112005003915.

Boehrer, B. Thermobaric stratification in very deep Norwegian freshwater lakes. *Journal of Great Lakes Research*, 39(4):690 – 695, 2013. ISSN 0380-1330. doi: 10.1016/j.jglr.2013.08.003.

Boehrer, B. and Schultze, M. Stratification of lakes. *Reviews of Geophysics*, 46(2), 2008. doi: 10.1029/2006RG000210.

Boehrer, B., Imberger, J., and Münnich, K. O. Vertical structure of currents in western lake constance. *Journal of Geophysical Research: Oceans*, 105(C12):28823–28835. doi: 10.1029/2000JC900139.

Boehrer, B., Fukuyama, R., and Chikita, K. Stratification of very deep, thermally stratified lakes. *Geophysical Research Letters*, 35(16), 2008. ISSN 1944-8007. doi: 10.1029/2008GL034519.

Bohle, M. Wind and currents: response patterns of Lake Geneva. *Annales Geophysicae*, 9:82–90, 01 1991.

Bohle-Carbonell, M. Currents in Lake Geneva. *Limnology and Oceanography*, 31(6):1255–1266, 1986. doi: 10.4319/lo.1986.31.6.1255.

Bolpagni, R., Bettoni, E., Bonomi, F., Bresciani, M., Caraffini, K., Costaraoss, S., Giacomazzi, F., Monauni, C., Montanari, P., Mosconi, M., Oggioni, A., Pellegrini, G., and Zampieri, C. Charophytes of Garda lake (Northern Italy): a preliminary assessment of diversity and distribution. *Journal of Limnology*, 72(2):388–393, 2013. doi: 10.4081/jlimnol.2013.e31.

Bouffard, D. and Lemmin, U. Kelvin waves in Lake Geneva. *Journal of Great Lakes Research*, 39(4):637 – 645, 2013. ISSN 0380-1330. doi: 10.1016/j.jglr.2013.09.005.

Bouffard, D., Kiefer, I., Wüest, A., S., W., and D., O. Are surface temperature and chlorophyll in a large deep lake related? an analysis based on satellite observations in synergy with hydrodynamic modelling and in-situ data. *Remote Sensing of Environment*, 209:510 – 523, 2018. ISSN 0034-4257. doi: 10.1016/j.rse.2018.02.056.

Breivik, Ø. and Allen, A. A. An operational search and rescue model for the norwegian sea and the north sea. *Journal of Marine Systems*, 69(1-2):99–113, Jan 2008. ISSN 0924-7963. doi: 10.1016/j.jmarsys.2007.02.010.

Bresciani, M., Giardino, C., and Boschetti, L. Multi-temporal assessment of bio-physical parameters in lakes Garda and Trasimeno from MODIS and MERIS. *Ital. J. Remote Sens.*, 43 (3):49–62, 2011a. doi: 10.5721/ItJRS20114334.

Bresciani, M., Stroppiana, D., Odermatt, D., Morabito, G., and Giardino, C. Assessing remotely sensed chlorophyll-a for the implementation of the Water Framework Directive in European perialpine lakes. *Science of The Total Environment*, 409(17):3083 – 3091, 2011b. ISSN 0048-9697. doi: 10.1016/j.scitotenv.2011.05.001.

Bresciani, M., Bolpagni, R., Braga, F., Oggioni, A., and Giardino, C. Retrospective assessment of macrophytic communities in southern Lake Garda (Italy) from in situ and MIVIS (Multispectral Infrared and Visible Imaging Spectrometer) data. *Journal of limnology*, 71:180–190, 01 2012. doi: 10.4081/JLIMNOL.2012.E19.

Bresciani, M., Cazzaniga, I., Austoni, M., Sforzi, T., Buzzi, F., Morabito, G., and Giardino, C. Mapping phytoplankton blooms in deep subalpine lakes from Sentinel-2A and Landsat-8. *Hydrobiologia*, 824(1):197–214, 2018. doi: 10.1007/s10750-017-3462-2.

Butcher, J. B., Nover, D., Johnson, T. E., and Clark, C. M. Sensitivity of lake thermal and mixing dynamics to climate change. *Climatic Change*, 129(1):295–305, Mar 2015. ISSN 1573-1480. doi: 10.1007/s10584-015-1326-1.

Buytaert, W., Zulkafli, Z., Grainger, S., Acosta, L., Alemie, T. C., Bastiaensen, J., De Bièvre, B., Bhusal, J., Clark, J., Dewulf, A., Foggin, M., Hannah, D. M., Hergarten, C., Isaeva, A., Karpouzoglou, T., Pandeya, B., Paudel, D., Sharma, K., Steenhuis, T., Tilahun, S., Van Hecken, G., and Zhumanova, M. Citizen science in hydrology and water resources: opportunities for knowledge generation, ecosystem service management, and sustainable development. *Frontiers in Earth Science*, 2:26, 2014. doi: 10.3389/feart.2014.00026.

Calheiros, D., Seidl, A., and Ferreira, C. Participatory research methods in environmental science: local and scientific knowledge of a limnological phenomenon in the Pantanal wetland of Brazil. *Journal of Applied Ecology*, 37(4):684–696, 2000. doi: 10.1046/j.1365-2664.2000.00524.x.

Caloi, P. Le sesse del Lago di Garda - parte prima: sesse che interessano l'intero Lago di Garda [Seiches in Lake Garda - Part I: seiches in the whole Lake Garda]. *Annals of Geophysics,*, 1: 24–48, 1948.

Canfield, D. E. J., Brown, C. D., Bachmann, R. W., and Hoyer, M. V. Volunteer lake monitoring: Testing the reliability of data collected by the Florida LAKEWATCH Program. *Lake and Reservoir Management*, 18(1):1–9, 2002. doi: 10.1080/07438140209353924.

Carvalho, D., Rocha, A., Gómez-Gesteira, M., and Santos, C. A sensitivity study of the wrf model in wind simulation for an area of high wind energy. *Environmental Modelling & Software*, 33:23 – 34, 2012. doi: 10.1016/j.envsoft.2012.01.019.

Casulli, V. and Pecenik, G. Modello idrodinamico tridimensionale del lago di Garda [Hydrodynamic model of Lake Garda]. *Cimeca, Ed. Scienza e Supercalcolo al Cimeca*, 67:255–258, 1994.

Cesare, G. D., Boillat, J.-L., and Schleiss, A. J. Circulation in stratified lakes due to flood-induced turbidity currents. *Journal of Environmental Engineering*, 132(11):1508–1517, 2006. doi: 10.1061/(ASCE)0733-9372(2006)132:11(1508).

Chen, C., Huang, J., Chen, Q., Zhang, J., Li, Z., and Lin, Y. Assimilating multi-source data into a three-dimensional hydro-ecological dynamics model using ensemble kalman filter. *Environmental Modelling & Software*, 117:188 – 199, 2019. doi: 10.1016/j.envsoft.2019.03.028.

Chen, F. and Dudhia, J. Coupling an advances land surface-hydrology model with the penn state-ncar mm5 modeling system. Part I: Model implementation and sensitivity. *Monthly Weather Review*, 129:569–585, 2001.

Cheng, P. and Valle-Levinson, A. Influence of lateral advection on residual currents in microtidal estuaries. *Journal of Physical Oceanography*, 39:3177–3190, 12 2009.

Conrad, C.-C. and Hilchey, K. G. A review of citizen science and community-based environmental monitoring: issues and opportunities. *Environmental Monitoring and Assessment*, 176(1): 273–291, May 2011. ISSN 1573-2959. doi: 10.1007/s10661-010-1582-5.

Crosman, E. T. and Horel, J. Sea and lake breezes: A review of numerical studies. *Boundary-layer Meteorology*, 137(1):1–29, 2010. doi: 10.1007/s10546-010-9517-9.

Csanady, G. T. Mean circulation in shallow seas. *Journal of Geophysical Research*, 81(30): 5389–5399, 1976. doi: 10.1029/JC081i030p05389.

Csanady, G. T. *Circulation in the coastal ocean*. D. Reidel Pub, 1982.

Daniel, P., Jan, G., Cabioc'h, F., Landau, Y., and Loiseau, E. Drift modeling of cargo containers. *Spill Science and Technology Bulletin*, 7(5):279 – 288, 2002. ISSN 1353-2561. doi: 10.1016/S1353-2561(02)00075-0.

Danielsen, F., Burgess, N., Coronado, I., Enghoff, M., Holt, S., Jensen, P., Poulsen, M., and Rueda, R. *The value of indigenous and local knowledge as citizen science*, pages 110–123. 10 2018. ISBN ISBN: 978-1-78735-233-9 (PDF). doi: 10.2307/j.ctv550cf2.15.

Danis, P.-A., von Grafenstein, U., Masson-Delmotte, V., Planton, S., Gerdeaux, D., and Moisselin, J.-M. Vulnerability of two European lakes in response to future climatic changes. *Geophysical Research Letters*, 31(21), 2004. ISSN 1944-8007. doi: 10.1029/2004GL020833.

Davis, A. and Wagner, J. R. Who knows? On the importance of identifying "experts" when researching local ecological knowledge. *Human Ecology*, 31(3):463–489, Sep 2003. doi: 10.1023/A:1025075923297.

de Franceschi, M. and Zardi, D. Study of wintertime high pollution episodes during the Brenner-South ALPNAP measurement campaign. *Meteorology and Atmospheric Physics*, 103(1-4): 237–250, 2009. doi: 10.1007/s00703-008-0327-2.

Defant, A. Über die stehenden Seespiegelschwankungen (Seiches) in Riva am Gardasee [about the stationary fluctuations of lake level (seiches) at Riva del Garda]. *S. B. Akad. Wiss. Wien, Math.-Nat. K1.*, 117, 1908.

Defant, A. Berg- und Talwinde in Südtirol [Mountain and valley winds in southern Tyrol]. *S. B. Akad. Wiss. Wien, Abt. IIa.*, 118:553–604, 1909.

Defant, A. Physical Oceanography Pergamon Press, London, 1961. Vol. 1, pp. xvi 729; Vol. 2, pp. viii 598, book review by J.B. Hersey. *Journal of the Marine Biological Association of the United Kingdom*, 42(2):468–468, 1962. doi: 10.1017/S0025315400070089.

Dever, E. P. Wind-forced cross-shelf circulation on the Northern California shelf. *Journal of Physical Oceanography*, 27(8):1566–1580, 1997. doi: 10.1175/1520-0485(1997)027<1566:WFCSCO>2.0.CO;2.

Di Nicolantonio, W., Cazzaniga, I., Cacciari, A., Bresciani, M., and Giardino, C. Synergy of multispectral and multisensors satellite observations to evaluate desert aerosol transport and impact of dust deposition on inland waters: study case of Lake Garda. *Journal of Applied Remote Sensing*, 9(1):1 – 19, 2015. doi: 10.1117/1.JRS.9.095980.

Dissanayake, P., Hofmann, H., and Peeters, F. Comparison of results from two 3D hydrodynamic models with field data: internal seiches and horizontal currents. *Inland Waters*, 9(2):239–260, 2019. doi: 10.1080/20442041.2019.1580079.

Dokulil, M. T. Impact of climate warming on European inland waters. *Inland Waters*, 4(1): 27–40, 2014. doi: 10.5268/IW-4.1.705.

Dokulil, M. T., Jagsch, A., George, G. D., Anneville, O., Jankowski, T., Wahl, B., Lenhart, B., Blenckner, T., and Teubner, K. Twenty years of spatially coherent deepwater warming in lakes across Europe related to the North Atlantic Oscillation. *Limnology and Oceanography*, 51(6):2787–2793, 2006. ISSN 1939-5590. doi: 10.4319/lo.2006.51.6.2787.

Donners, J., Genseberger, M., Jagers, B., Thiange, C., Schaap, M., Boderie, P., Emerson, A., Guarrasi, M., de Kler, T., and van Meersberger, M. Using high performance computing to enable interactive design of measures to improve water quality and ecological state of Lake Marken. Perugia, Italy, 1-5 September 2014. 15th World Lake Conference.

Dudhia, J. Numerical study of convection observed during the winter monsoon experiment using a mesoscale two-dimensional model. *Journal of the Atmospheric Sciences*, 46:3077–3107, 1989.

Edlund, M. B., Almendinger, J. E., Fang, X., Hobbs, J. M. R., VanderMeulen, D. D., Key, R. L., and Engstrom, D. R. Effects of climate change on lake thermal structure and biotic response in Northern Wilderness Lakes. *Water*, 9, 2017. ISSN 2073-4441. doi: 10.3390/w9090678. URL http://www.mdpi.com/2073-4441/9/9/678.

Ekman, V. W. On the influence of the Earth's rotation on the ocean currents. *Ark. Mat. Astr. Fys.*, 2(11):1–52, 1905.

Fang, X. and Stefan, H. G. Simulations of climate effects on water temperature, dissolved oxygen, and ice and snow covers in lakes of the contiguous u.s. under past and future climate scenarios. *Limnology and Oceanography*, 54(6part2):2359–2370, 2009. doi: 10.4319/lo.2009.54.6_part_2.2359.

Fenocchi, A., Rogora, M., Sibilla, S., and Dresti, C. Relevance of inflows on the thermodynamic structure and on the modeling of a deep subalpine lake Lake Maggiore, Northern Italy/Southern Switzerland). *Limnologica*, 63:42 – 56, 2017. ISSN 0075-9511. doi: 10.1016/j.limno.2017.01.006.

Fenocchi, A., Rogora, M., Sibilla, S., Ciampittiello, M., and Dresti, C. Forecasting the evolution in the mixing regime of a deep subalpine lake under climate change scenarios through numerical modelling (Lake Maggiore, Northern Italy/Southern Switzerland). *Climate Dynamics*, Jan 2018. ISSN 1432-0894. doi: 10.1007/s00382-018-4094-6.

Fjeldstad, J. E. Ein problem aus der windstromtheorie. *ZAMM - Journal of Applied Mathematics and Mechanics / Zeitschrift für Angewandte Mathematik und Mechanik*, 10(2):121–137, 1930. doi: 10.1002/zamm.19300100203.

Follett, R. and Strezov, V. An analysis of citizen science based research: Usage and publication patterns. *PLOS ONE*, 10(11):1–14, 11 2015. doi: 10.1371/journal.pone.0143687.

Garibaldi, L., Mezzanotte, V., Brizzio, M., Rogora, M., and Mosello, R. The trophic evolution of Lake Iseo as related to its holomixis. *Journal of Limnology*, 58, 02 1999. doi: 10.4081/jlimnol.1999.10.

Gedney, R. T. and Lick, W. Wind-driven currents in Lake Erie. *Journal of Geophysical Research*, 77(15):2714–2723, 1972. doi: 10.1029/JC077i015p02714.

Giardino, C., Brando, V. E., Dekker, A. G., Strömbeck, N., and Candiani, G. Assessment of water quality in Lake Garda (Italy) using Hyperion. *Remote Sensing of Environment*, 109:183–195, 2007. doi: 10.1016/j.rse.2006.12.017.

Giardino, C., Bresciani, M., Cazzaniga, I., Schenk, K., Rieger, P., Braga, F., Matta, E., and Brando, V. Evaluation of multi-resolution satellite sensors for assessing water quality and bottom depth of Lake Garda. *Sensors*, 14:24116–24131, 12 2014. doi: 10.3390/s141224116.

Gill, A. E. *Atmosphere-ocean dynamics*. Academic Press New York, 1982.

Giovannini, L., Antonacci, G., Zardi, D., Laiti, L., and Panziera, L. Sensitivity of simulated wind speed to spatial resolution over complex terrain. *Energy Procedia*, 59:323–329, 2014a. doi: 10.1016/j.egypro.2014.10.384.

Giovannini, L., Zardi, D., de Franceschi, M., and Chen, F. Numerical simulations of boundary-layer processes and urban-induced alterations in an Alpine valley. *Int.l J. Climatol.*, 34: 1111–1131, 2014b. doi: 10.1002/joc.3750.

Giovannini, L., Laiti, L., Zardi, D., and de Franceschi, M. Climatological characteristics of the ora del garda wind in the alps. *Int.l J. Climatol.*, 35:4103–4115, 2015a. doi: 10.1029/2001JC000954.

Giovannini, L., Laiti, L., Zardi, D., and de Franceschi, M. Climatological characteristics of the Ora del Garda wind in the Alps. *Int.l J. Climatol.*, 35:4103–4115, 2015b. doi: 10.1002/joc.4270.

Giovannini, L., Laiti, L., Serafin, S., and Zardi, D. The thermally driven diurnal wind system of the Adige Valley in the Italian Alps. *Quarterly Journal of the Royal Meteorological Society*, 143(707):2389–2402, 2017. doi: 10.1002/qj.3092.

Giovannini, L., Zardi, D., De Franceschi, M., and Chen, F. Numerical simulations of boundary-layer processes and urban-induced alterations in an alpine valley. *International Journal of Climatology*, 34, 03 2014c. doi: 10.1002/joc.3750.

Goudsmit, G. H., Burchard, H., Peeters, F., and Wüest, A. Application of k-ε turbulence models to enclosed basins: The role of internal seiches. *J. Geophys. Res.*, 107(C12):3230, 2002. doi: 10.1029/2001JC000954.

Goyette, S. and Perroud, M. Interfacing a one-dimensional lake model with a single-column atmospheric model: Application to the deep Lake Geneva, Switzerland. *Water Resources Research*, 48, 2012. doi: 10.1029/2011WR011223.

Griffiths, R. W. Gravity currents in rotating systems. *Annual Review of Fluid Mechanics*, 18 (1):59–89, 1986. doi: 10.1146/annurev.fl.18.010186.000423.

Grossmann, A. and Morlet, J. Decomposition of hardy functions into square integrable wavelets of constant shape. *SIAM Journal on Mathematical Analysis*, 15:723–736, 07 1984. doi: 10.1137/0515056.

Guanter, L., Ruiz-Verdu, A., Odermatt, D., Giardino, C., Simis, S., Estelles, V., Heege, T., Antonio Dominguez-Gomez, J., and Moreno, J. Atmospheric correction of ENVISAT/MERIS

data over inland waters: Validation for European lakes. *Remote sensing of environment*, 114 (3):467–480, 2010.

Guyennon, N., Valerio, G., Salerno, F., Pilotti, M., Tartari, G., and Copetti, D. Internal wave weather heterogeneity in a deep multi-basin subalpine lake resulting from wavelet transform and numerical analysis. *Advances in Water Resources*, 71:149 – 161, 2014. doi: 10.1016/j.advwatres.2014.06.013.

Hallwass, G., Lopes, P., A Juras, A., and Silvano, R. Fishers' knowledge identifies environmental changes and fish abundance trends in impounded tropical rivers. *Ecological applications : a publication of the Ecological Society of America*, 23:392–407, 03 2013. doi: 10.2307/23441004.

Hamblin, P. F. and Hollan, E. On the gravitational seiches of lake constance and their generation. *Schweizerische Zeitschrift für Hydrologie*, 40(1):119–154, Mar 1978. ISSN 1420-9055. doi: 10.1007/BF02502376.

Heaps, N. S. Vertical structure of current in homogeneous and stratified waters. *in: K. Hutter (ed.), Hydrodynamics of lakes: CISM lectures. Springer Verlag*, pages 153–207, 1984.

Heaps, N. S. and Ramsbottom, A. E. Wind effects on the water in a narrow two-layered lake. *Philosophical Transactions of the Royal Society of London A: Mathematical, Physical and Engineering Sciences*, 259(1102):391–430, 1966. ISSN 0080-4614. doi: 10.1098/rsta.1966.0021.

Hecker, S., Haklay, M., Bowser, A., Makuch, Z., Vogel, J., Bonn, A., and Gold, M. *Citizen Science – Innovation in Open Science, Society and Policy.* 10 2018. ISBN 978-1-78735-233-9. doi: 10.14324/111.9781787352339.

Henderson-Sellers, B. The dependence of surface velocity in water bodies on wind velocity and latitude. *Applied Mathematical Modelling*, 12(2):202 – 203, 1988. doi: 10.1016/0307-904X(88)90012-1.

Hidaka, K. Non-stationary Ocean-currents. *Mem. Imp. Mar. Obs.*, 3, 1933.

Hipsey, M. R., Gal, G., Arhonditsis, G. B., Carey, C. C., Elliott, J. A., Frassl, M. A., Janse, J. H., de Mora, L., and Robson, B. J. A system of metrics for the assessment and improvement of aquatic ecosystem models. *Environmental Modelling & Software*, 128:104697, 2020. doi: 10.1016/j.envsoft.2020.104697.

Hodges, B. R., Imberger, J., Saggio, A., and Winters, K. B. Modeling basin-scale internal waves in a stratified lake. *Limnol. Oceanogr.*, 45(7):1603–1620, 2000. doi: 10.4319/lo.2000.45.7.1603.

Hollan, E. *Large Inflow-Driven Vortices in Lake Constance*, chapter 9, pages 123–136. American Geophysical Union (AGU), 2013. ISBN 9781118665381. doi: 10.1029/CE054p0123.

Hollan, T. J., E.and Simons. Wind-induced changes of temperature and currents in lake constance. *Archiv für Meteorologie, Geophysik und Bioklimatologie, Serie A*, 27(3):333–373, Sep 1978. ISSN 1436-5065. doi: 10.1007/BF02247955.

Hong, S. Y., Dudhia, J., and Chen, S. H. A revised approach to ice microphysical processes for the bulk parameterization of clouds and precipitation. *Monthly Weather Review*, 132:103–120, 2004.

Hong, S. Y., Noh, Y., and Dudhia, J. A new vertical diffusion package with an explicit treatment of entrainment processes. *Monthly Weather Review*, 134:2318–2341, 2006.

Horn, W., Mortimer, C., and Schwab, D. Wind-induced internal seiches in Lake Zurich observed and modeled. *Limnology and Oceanography*, 31(6):1232–1254, 1986. doi: 10.4319/lo.1986.31.6.1232.

Horvath, K., Koracin, D., Vellore, R., Jiang, J., and Belu, R. Sub-kilometer dynamical downscaling of near-surface winds in complex terrain using WRF and MM5 mesoscale models. *Journal of Geophysical Research: Atmospheres*, 117, 2012. doi: 10.1029/2012JD017432.

Hostetler, S. W., Bates, G., and Giorgi, F. Interactive coupling of a lake thermal model with a regional climate model. *J. Geophys. Res.*, 98(D3):5045–5057, 1993. doi: 10.1029/92JD02843.

Huntington, P. H. Using traditional ecological knowledge in science: Methods and applications. *Ecological Applications - ECOL APPL*, 10:1270–1274, 10 2000. doi: 10.1890/1051-0761(2000)010[1270:UTEKIS]2.0.CO;2.

Hutchinson, G. E. *A Treatise on Limnology, Vol. I: Geography, Physics and Chemistry.* John Wiley and Sons, New York., 1957.

Hutter, C., Salvadè, G., Spinedi, C., Zamboni, F., and Bäuerle, E. Large scale water movements in lakes. *Aquatic Sciences*, 53:100–135, 06 1991. doi: 10.1007/BF00877057.

Hutter, K., Salvadè, G., and Schwab, D. J. On internal wave dynamics in the northern basin of the lake of Lugano. *Geophysical and Astrophysical Fluid Dynamics*, 27(3):299–336, Jan 1983. doi: 10.1080/03091928308210131.

Hutter, K., Wang, Y., and Chubarenko, I. P. *Physics of Lakes. Volume 1: Foundation of the Mathematical and Physical Background.* Advances in Geophysical and Environmental Mechanics and Mathematics. Springer, 2011a.

Hutter, K., Wang, Y., and Chubarenko, I. *Physics of Lakes, Volume 2: Lakes as Oscillators.* Advances in Geophysical and Environmental Mechanics and Mathematics. Springer Berlin Heidelberg, 2011b. ISBN 9783642191121.

Huziy, O. and Sushama, L. Lake–river and lake–atmosphere interactions in a changing climate over Northeast Canada. *Climate Dynamics*, 48(9):3227–3246, 2017. ISSN 1432-0894. doi: 10.1007/s00382-016-3260-y.

Imboden, D. M. and Wüest, A. *Physics and Chemistry of Lakes*, chapter 4: Mixing Mechanisms in Lakes, pages 83–138. Springer-Verlag, 1995.

Imboden, D., Stotz, B., and Wuest, A. Hypolimnic mixing in a deep alpine lake and the role of a storm event: With 5 figures and 1 table in the text. *SIL Proceedings, 1922-2010*, 23:67–73, 01 1987. doi: 10.1080/03680770.1987.11897904.

IRSA. Research on Lake Garda. *Istituto di Ricerca sulle Acque (IRSA), Quaderni*, 18, 1974.

Jiménez, P. A. and Dudhia, J. Improving the representation of resolved and unresolved topographic effects on surface wind in the WRF model. *Journal of Applied Meteorology and Climatology*, 51:300–316, 2012.

Kain, J. S. and Fritsch, J. M. Convective parameterization for mesoscale models: the kain–fritcsh scheme. *The representation of cumulus convection in numerical models*, 1993.

Kampf, S., Strobl, B., Hammond, J., Anenberg, A., Etter, S., Martin, C., Puntenney-Desmond, K., Seibert, J., and Meerfeld, I. V. Testing the waters: Mobile apps for crowdsourced streamflow data. *EOS Trans Am. Geophys. Union 99*, 99, 2018. doi: 10.1029/2018EO096355.

Kasai, A., Hill, A. E., Fujiwara, T., and Simpson, J. H. Effect of the Earth's rotation on the circulation in regions of freshwater influence. *Journal of Geophysical Research: Oceans*, 105 (C7):16961–16969, 2000. doi: 10.1029/2000JC900058.

Kelley, J. G. W., Hobgood, J. S., Bedford, K. W., and Schwab, D. J. Generation of three-dimensional lake model forecasts for Lake Erie. *Weather and Forescasting*, 13(3):659–687, 1993. doi: 1520-0434(1998)013<0659:GOTDLM>2.0.CO;2.

Kirillin, G. Modeling the impact of global warming on water temperature and seasonal mixing regimes in small temperate lakes. *Boreal Env. Res.*, 15:279–293, 04 2010.

Kirillin, G. and Shatwell, T. Generalized scaling of seasonal thermal stratification in lakes. *Earth-Science Reviews*, 161:179 – 190, 2016. ISSN 0012-8252. doi: 10.1016/j.earscirev.2016.08.008.

Kitzinger, J. Qualitative research: Introducing focus groups. *BMJ (Clinical research ed.)*, 311: 299–302, 08 1995. doi: 10.1136/bmj.311.7000.299.

Klein, A. J., Hopping, L., Yeh, E., Nyima, Y., Boone, R., and Galvin, K. Unexpected climate impacts on the Tibetan Plateau: Local and scientific knowledge in findings of delayed summer. *Global Environmental Change*, 28:141–152, 09 2014. doi: 10.1016/j.gloenvcha.2014.03.007.

Kraemer, B. M., Anneville, O., Chandra, S., Dix, M., Kuusisto, E., Livingstone, D. M., Rimmer, A., Schladow, S. G., Silow, E., Sitoki, L. M., Tamatamah, R., Vadeboncoeur, Y., and McIntyre, P. B. Morphometry and average temperature affect lake stratification responses to climate change. *Geophysical Research Letters*, 42(12):4981–4988, 2015. ISSN 1944-8007. doi: 10.1002/2015GL064097.

Kundu, P. K. and Cohen, I. M. *Fluid Mechanics, Second Edition*. Academic press, Elsevier Science, 2002.

L. S., C. and Fienen, M. N. Crowdhydrology: Crowdsourcing hydrologic data and engaging citizen scientists. *Groundwater*, 51(1):151–156, 2013. doi: 10.1111/j.1745-6584.2012.00956.x.

Laborde, S., Antenucci, J. P., Copetti, D., and Imberger, J. Inflow intrusions at multiple scales in a large temperate lake. *Limnology and Oceanography*, 55(3):1301–1312, 5 2010. ISSN 1939-5590. doi: 10.4319/lo.2010.55.3.1301.

Laborde, S., Imberger, J., and Toussaint, S. Contributions of local knowledge to the physical limnology of Lake Como, Italy. *Proceedings of the National Academy of Sciences*, 109(17): 6441–6445, 2012. doi: 10.1073/pnas.1113740109.

Laiti, L., Zardi, D., de Franceschi, M., and Rampanelli, G. Atmospheric boundary-layer structures associated with the Ora del Garda wind in the Alps as revealed from airborne and surface measurements. *Atmos. Res.*, 132-133:473–489, 2013a. doi: 10.1016/j.atmosres.2013.07.006.

Laiti, L., Zardi, D., de Franceschi, M., and Rampanelli, G. Residual Kriging analysis of airborne measurements: application to the mapping of Atmospheric Boundary-Layer thermal structures in a mountain valley. *Atmos. Sci. Letters*, 14(2):79–85, 2013b. doi: 10.1002/asl2.420.

Laiti, L., Zardi, D., de Franceschi, M., Rampanelli, G., and Giovannini, L. Analysis of the diurnal development of a lake-valley circulation in the Alps based on airborne and surface measurements. *Atmos. Chem. and Phys*, 14:9771–9786, 2014. doi: 10.5194/acp-14-9771-2014.

Large, W. G., McWilliams, J. C., and Doney, S. C. Oceanic vertical mixing: A review and a model with a nonlocal boundary layer parameterization. *Reviews of Geophysics*, 32(4): 363–403, 1994. doi: 10.1029/94RG01872.

Laval, B. E., Imberger, J., and Findikakis, A. N. Dynamics of a large tropical lake: Lake Maracaibo. *Aquat. Sci.*, 67:337–349, 2005. doi: 10.1007/s00027-005-0778-1.

Laval, B., Imberger, J., Hodges, B. R., and Stocker, R. Modeling circulation in lakes: Spatial and temporal variations. *Limnology and Oceanography*, 48(3):983–994, 2003. doi: 10.4319/lo.2003.48.3.0983.

Laval, B. E., Morrison, J., Potts, D. J., Carmack, E. C., Vagle, S., James, C., McLaughlin, F. A., and Foreman, M. Wind-driven summertime upwelling in a fjord-type lake and its impact on downstream river conditions: Quesnel Lake and River, British Columbia, Canada. *J. Great Lakes Res.*, 34(1):189 – 203, 2008. ISSN 0380-1330. doi: 10.3394/0380-1330(2008)34[189:WSUIAF]2.0.CO;2.

Laval, B. E., Vagle, S., Potts, D., Morrison, J., Sentlinger, G., James, C., McLaughlin, F., and Carmack, E. C. The joint effects of riverine, thermal, and wind forcing on a temperate fjord lake: Quesnel Lake, Canada. *J. Great Lakes Res.*, 38(3):540 – 549, 2012. ISSN 0380-1330. doi: 10.1016/j.jglr.2012.06.007.

Le Roux, R., Katurji, M., Zawar-Reza, P., Quénol, H., and Sturman, A. Comparison of statistical and dynamical downscaling results from the wrf model. *Environmental Modelling & Software*, 100:67 – 73, 2018. doi: 10.1016/j.envsoft.2017.11.002.

Lee, K. K. and Ligget, J. A. Computation for circulation in stratified lakes. *Journal of the Hydraulics Division*, 96(10):2089–2115, 1970.

Lemmin, U. The structure and dynamics of internal waves in Baldeggersee. *Limnology and Oceanography*, 32(1):43–61, 1987. doi: 10.4319/lo.1987.32.1.0043.

Lemmin, U. and D'Adamo, N. Summertime winds and direct cyclonic circulation:observations from Lake Geneva. *Ann. Geophysicae*, 14:1207–1220, 1997. doi: 10.1007/s00585-996-1207-z.

Lemmin, U., Mortimer, C. H., and Bäuerle, E. Internal seiche dynamics in Lake Geneva. *Limnology and Oceanography*, 50(1):207–216, 2005. doi: 10.4319/lo.2005.50.1.0207.

Lenstra, W. K., Hahn-Woernle, L., Matta, E., Bresciani, M., Giardino, C., Salmaso, N., Musanti, M., Fila, G., Uittenbogaard, R., Genseberger, M., van der Woerd, H. J., and Dijkstra, H. A. Diurnal variation of turbulence-related quantities in Lake Garda. *Adv. Ocean. Limn.*, 5(2): 184–203, 2014. doi: 10.1080/19475721.2014.971870.

Leon, L. F., Lamb, D. C. L., Schertzer, W. M., Swayne, D. A., and Imberger, J. Towards coupling a 3D hydrodynamic lake model with the Canadian Regional Climate Model: Simulation on Great Slave Lake. *Environmental Modelling & Software*, 22(6):787–796, 2007. doi: 10.1016/j.envsoft.2006.03.005.

Leoni, B., Garibaldi, L., and Gulati, R. How does interannual trophic variability caused by vertical water mixing affect reproduction and population density of the Daphnia longispina group in Lake Iseo, a deep stratified lake in Italy. *Inland Waters*, 4(2):193–203, 2014. doi: 10.5268/IW-4.2.663.

Lesser, G. R., Roelvink, J. A., Keste, T. M. V., and Stelling, G. S. Development and validation of a three-dimensional morphological model. *Coast. Eng.*, 51:883–915, 2004. doi: 10.1016/j.coastaleng.2004.07.014.

Livingstone, D. M. An example of the simultaneous occurrence of climate-driven "sawtooth" deep-water warming/cooling episodes in several Swiss lakes. *Proceedings of the Internat. Assoc. of Theoretical and Applied Limnology*, 26:822–828, 1997. doi: 10.1080/03680770.1995.11900832.

Loth, E. and Dorgan, A. J. An equation of motion for particles of finite Reynolds number and size. *Environmental Fluid Mechanics*, 9(2):187–206, Apr 2009. ISSN 1573-1510. doi: 10.1007/s10652-009-9123-x.

Lottig, N. R., Wagner, T., Norton Henry, E., Spence Cheruvelil, K., Webster, K. E., Downing, J. A., and Stow, C. A. Long-term citizen-collected data reveal geographical patterns and

temporal trends in lake water clarity. *PLOS ONE*, 9(4):1–8, 04 2014. doi: 10.1371/journal.pone.0095769.

Lovato, T. and Pecenik, G. Three-dimensional modeling of pollutant dispersion in Lake Garda (North Italy). *Chapter 19 in:Models of the Ecological Hierarchy: From Molecules to the Ecosphere, Vol. 25, Elsevier, Amsterdam, The Netherlands, 562 pp.*, 2012.

Madsen, O. S. A realistic model of the wind-induced Ekman boundary layer. *Journal of Physical Oceanography*, 7(2):248–255, 1977. doi: 10.1175/1520-0485(1977)007<0248:ARMOTW>2.0.CO;2.

Mari, L., Biotto, C., Decoene, A., and Bonaventura, L. A coupled ecological-hydrodynamic model for the spatial distribution of sessile aquatic species in thermally forced basins. *Ecol. Model.*, 220:2310–2324, 2009. doi: 10.1016/j.ecolmodel.2009.05.012.

Marsili, L. F. *Osservazioni fisiche intorno al lago di Garda [Physicial observations on Lake Garda]*. Scritti inediti di Luigi Ferdinando Marsili [Unpublished writings by L.F. Marsili]. Edited by: Comitato Marsiliano, Accademia delle scienze dell'Istituto di Bologna, 1930.

Matsumoto, K., Tokos, K. S., and Gregory, C. Ventilation and dissolved oxygen cycle in Lake Superior: Insights from a numerical model. *Geochem. Geophys.*, 16(9):3097–3110, 2015. ISSN 1525-2027. doi: 10.1002/2015GC005916.

McDougall, T. J. Thermobaricity, cabbeling, and water-mass conversion. *Journal of Geophysical Research: Oceans*, 92(C5):5448–5464, 1987. doi: 10.1029/JC092iC05p05448.

Mellor, G. L. and Yamada, T. A hierarcy of turbulence closure models for planetary boundary layers. *J. Atmos. Sci.*, 31:1791–1806, 1974.

Merton, R. K., M.Fiske, and P.Kendall. The focused interview, reviewd by Clyde V. Kiser. *The Milbank Memorial Fund Quarterly*, 35(1):85–88, 1957. doi: 10.2307/3348539.

Milan, M., Bigler, C., Salmaso, N., Guella, G., and M.Tolotti. Multiproxy reconstruction of a large and deep subalpine lake's ecological history since the Middle Ages. *Journal of Great Lakes Research*, 41(4):982 – 994, 2015. ISSN 0380-1330. doi: 10.1016/j.jglr.2015.08.008.

Milan, M., Bigler, C., Tolotti, M., and Szeroczynska, K. Effects of long term nutrient and climate variability on subfossil Cladocera in a deep, subalpine lake (Lake Garda, northern Italy). *Journal of Paleolimnology*, 06 2017. doi: 10.1007/s10933-017-9981-z.

Mlawer, E. J., Taubman, S. J., Brown, P. D., Iacono, M. J., and Clough, S. A. Radiative transfer for inhomogeneous atmospheres: Rrtm, a validated correlated-k model for the longwave. *Journal of Geophysical Research*, 102(D14):16663–16682, 1997.

Mohammed-Zaki, M. A. Time scales in wind-driven lake circulations. *Journal of Geophysical Research: Oceans*, 85(C3):1553–1562, 1980. doi: 10.1029/JC085iC03p01553.

Monismith, N. G. and MacIntyre, S. The surface mixed layer in lakes and reservoirs. *in: G. E. Likens (ed.), Biogeochemistry of Inland Waters*, pages 207–221, 2010.

Moriasi, D., Arnold, J., Van Liew, M., Bingner, R., Harmel, R., and Veith, T. Model evaluation guidelines for systematic quantification of accuracy in watershed simulations. *Transactions of the ASABE*, 50, 05 2007. doi: 10.13031/2013.23153.

Mughal, M. O., Lynch, M., Yu, F., McGann, B., Jeanneret, F., and Sutton, J. Wind modelling, validation and sensitivity study using weather research and forecasting model in complex terrain. *Environmental Modelling & Software*, 90:107 – 125, 2017. ISSN 1364-8152. doi: 10.1016/j.envsoft.2017.01.009.

Nesterov, O. Consideration of various aspects in a drift study of MH370 debris. *Ocean Science*, 14 (3):387–402, 2018. doi: 10.5194/os-14-387-2018. URL https://www.ocean-sci.net/14/387/2018/.

North, R. P., North, R. L., Livingstone, D. M., Köster, O., and Kipfer, R. Long-term changes in hypoxia and soluble reactive phosphorus in the hypolimnion of a large temperate lake: consequences of a climate regime shift. *Global Change Biology*, 20(3):811–823, 2014. doi: 10.1111/gcb.12371.

Notaro, M., Holman, K., Zarrin, A., Fluck, E., Vavrus, S., and Bennington, V. Influence of the Laurentian Great Lakes on Regional Climate. *Journal of Climate*, 26(3):789–804, 2013. doi: 10.1175/JCLI-D-12-00140.1.

Odermatt, D., Giardino, C., and Heege, T. Chlorophyll retrieval with MERIS Case-2-Regional in perialpine lakes. *Remote Sensing of Environment*, pages 607–617, 03 2010. doi: 10.1016/j.rse.2009.10.016.

Oke, T. R. *Boundary layer climates*. Routledge London, 1987.

Okubo, A. Oceanic diffusion diagrams. *Deep Sea Research and Oceanographic Abstracts*, 18(8): 789 – 802, 1971. doi: 10.1016/0011-7471(71)90046-5.

Pan, H., Avissar, R., and Haidvoge, D. B. Summer circulation and temperature structure of Lake Kinneret. *J. Phys. Ocean.*, 32(1):295–313, 2002. doi: 1520-0485(2002)032<0295:SCATSO>2.0.CO;2.

Pareeth, S., Salmaso, N., Adrian, R., and Neteler, M. Homogenised daily lake surface water temperature data generated from multiple satellite sensors: A long-term case study of a large sub-Alpine lake. *Scientific Reports*, 6:31251, 2016. doi: 10.1038/srep31251.

Paul, J. D., Buytaert, W., Allen, S., Ballesteros-Cánovas, J. A., Bhusal, J., Cieslik, K., Clark, J., Dugar, S., Hannah, D. M., Stoffel, M., Dewulf, A., Dhital, M. R., Liu, W., Nayaval, J. L., Neupane, B., Schiller, A., Smith, P. J., and Supper, R. Citizen science for hydrological risk reduction and resilience building. *Wiley Interdisciplinary Reviews: Water*, 5(1):e1262, 2018. doi: 10.1002/wat2.1262.

Pecenik, G. and Lovato, T. A combined 1-D turbulence-eutrophication model for Lake Garda. Riva del Garda, Italy, 30 May-2 June 2011. 7th ECEM Congress.

Peeters, F., Livingstone, D. M., Goudsmit, G.-H., Kipfer, R., and Forster, R. Modeling 50 years of historical temperature profiles in a large central European lake. *Limnology and Oceanography*, 47(1):186–197, 2002. doi: 10.4319/lo.2002.47.1.0186.

Perroud, M. and Goyette, S. Impact of warmer climate on Lake Geneva water-temperature profiles. *Boreal Environment Research*, 15, 04 2010.

Perroud, M., Goyette, S., Martynov, A., Beninston, M., and Anneville, O. Simulation of multi-annual thermal profiles in deep Lake Geneva: A comparison of one-dimensional lake models. *Limnol. Oceanogr.*, 54:1574–1594, 2009. doi: 10.4319/lo.2009.54.5.1574.

Piccolroaz, S. and Toffolon, M. Deep water renewal in Lake Baikal: a model for long term analyses. *J. Geophys. Res.*, 118(12):6717–6733, 2013a. doi: 10.1002/2013JC009029.

Piccolroaz, S., Toffolon, M., Sighel, M. C., and Bresciani, M. On the impact of climate change on surface water temperature of Lake Garda. *Geophysical Research Abstracts*, 15(EGU2013-8406), 2013.

Piccolroaz, S., Healey, N. C., Lenters, J. D., Schladow, S. G., Hook, S. J., Sahoo, G. B., and Toffolon, M. On the predictability of lake surface temperature using air temperature in a changing climate: A case study for Lake Tahoe (U.S.A.). *Limnology and Oceanography*, 63 (1):243–261, 2018. ISSN 1939-5590. doi: 10.1002/lno.10626.

Piccolroaz, S., Amadori, M., and Dijkstra, M. T. H. A. Importance of planetary rotation for ventilation processes in deep elongated lakes: Evidence from Lake Garda (Italy). *Scientific Reports*, 9, 2019. doi: 10.1038/s41598-019-44730-1.

Piccolroaz, S. and Toffolon, M. Deep water renewal in Lake Baikal: A model for long-term analyses. *Journal of Geophysical Research: Oceans*, 118(12):6717–6733, 2013b. ISSN 2169-9291. doi: 10.1002/2013JC009029.

Piccolroaz, S. and Toffolon, M. The fate of Lake Baikal: how climate change may alter deep ventilation in the largest lake on Earth. *Climatic Change*, 150(3):181–194, Oct 2018. doi: 10.1007/s10584-018-2275-2.

Piccolroaz, S., Toffolon, M., and Majone, B. The role of stratification on lakes' thermal response: The case of Lake Superior. *Water Resources Research*, 51(10):7878–7894, 2015. ISSN 1944-7973. doi: 10.1002/2014WR016555.

Pilotti, M., Valerio, G., and Leoni, B. Data set for hydrodynamic lake model calibration: A deep prealpine case. *Water Resources Research*, 49(10):7159–7163, 2013a. doi: 10.1002/wrcr.20506.

Pilotti, M., Valerio, G., Gregorini, L., Milanesi, L., and Hogg, C. Study of tributary inflows in Lake Iseo with a rotating physical model. *Journal of Limnology*, 73, 03 2014. doi: 10.4081/jlimnol.2014.772.

Pilotti, M., Valerio, G., Giardino, C., Bresciani, M., and Chapra, S. C. Evidence from field measurements and satellite imaging of impact of Earth rotation on Lake Iseo chemistry. *Journal of Great Lakes Research*, 44(1):14 – 25, 2018. ISSN 0380-1330. doi: 10.1016/j.jglr.2017.10.005.

Pilotti, M., Valerio, G., and Leoni, B. Data set for hydrodynamic lake model calibration: A deep prealpine case. *Water Resources Research*, 49(10):7159–7163, 2013b. ISSN 1944-7973. doi: 10.1002/wrcr.20506.

Platzman, G. W. *The Dynamical Prediction of Wind Tides on Lake Erie*, pages 1–44. American Meteorological Society, Boston, MA, 1963.

Pohle, I., Helliwell, R., Aube, C., Gibbs, S., Spencer, M., and Spezia, L. Citizen science evidence from the past century shows that Scottish rivers are warming. *Science of The Total Environment*, 659:53 – 65, 2019. doi: 10.1016/j.scitotenv.2018.12.325.

Ponte, A. L., Gutiérrez de Velasco, G., Valle-Levinson, A., Winters, K. B., and Winant, C. D. Wind-driven subinertial circulation inside a semienclosed bay in the Gulf of California. *Journal of Physical Oceanography*, 42(6):940–955, 2012. doi: 10.1175/JPO-D-11-0103.1.

Ponte, A. Periodic wind-driven circulation in an elongated and rotating basin. *Journal of Physical Oceanography*, 40(9):2043–2058, 2010. doi: 10.1175/2010JPO4235.1.

Prats, J., Reynaud, N., Rebière, D., Peroux, T., Tormos, T., and Danis, P. A. LakeSST: Lake Skin Surface Temperature in French inland water bodies for 1999-2016 from landsat archives. *Earth System Science Data*, 10(2):727–743, 2018. doi: 10.5194/essd-10-727-2018.

Rao, D. B. and Murty, T. S. Calculation of the steady state wind-driven circulations in Lake Ontario. *Archiv für Meteorologie, Geophysik und Bioklimatologie, Serie A*, 19(2):195–210, Jun 1970. doi: 10.1007/BF02249005.

Rao, Y. R. and Murthy, C. R. Coastal boundary layer characteristics during summer stratification in Lake Ontario. *Journal of Physical Oceanography*, 31(4):1088–1104, 2001. doi: 10.1175/1520-0485(2001)031<1088:CBLCDS>2.0.CO;2.

Rao, Y. R. and Schwab, D. J. Transport and mixing between the coastal and offshore waters in the Great Lakes: a review. *Journal of Great Lakes Research*, 33(1):202 – 218, 2007. ISSN 0380-1330. doi: 10.3394/0380-1330(2007)33[202:TAMBTC]2.0.CO;2.

Rawson, D. S. A comparison of some large alpine lakes in Western Canada. *Ecology*, 23(2):143–161, 1942. ISSN 00129658, 19399170. doi: 10.2307/1931082. URL http://www.jstor.org/stable/1931082.

Razmi, A. M., Barry, D. A., Bakhtyar, R., and Wüest, A. Current variability in a wide and open lacustrine embayment in Lake Geneva (Switzerland). *Journal of Great Lakes Research*, 39(3):455–465, 2013. doi: 10.1016/j.jglr.2013.06.011.

Razmi, A. M., Barry, D. A., Lemmin, U., Bonvin, F., Kohn, T., and Bakhtyar, R. Direct effects of dominant winds on residence and travel times in the wide and open lacustrine embayment: Vidy Bay (Lake Geneva, Switzerland). *Aquat. Sci.*, 76(3):S59–S71, 2014. doi: 10.1007/s00027-013-0321-8.

Razmi, A. M., Lemmin, U., Bouffard, D., Wüest, A., Uittenbogaard, R. E., and Barry, D. A. Gyre formation in open and deep lacustrine embayments: the example of Lake Geneva, Switzerland. *Environ. Fluid Mech.*, 17(3):415–428, 2017. doi: 10.1007/s10652-016-9494-8.

Read, J., Hamilton, D., D. Jones, I., Muraoka, K., Winslow, L., Kroiss, R., Wu, C., and Gaiser, E. Derivation of lake mixing and stratification indices from high-resolution lake buoy data. *Environmental Modelling & Software*, 26:1325 – 1336, 11 2011. doi: 10.1016/j.envsoft.2011.05.006.

Rempfer, J., Livingstone, D. M., Blodau, C., Forster, R., Niederhauser, P., and Kipfer, R. The effect of the exceptionally mild European winter of 2006-2007 on temperature and oxygen profiles in lakes in Switzerland: A foretaste of the future? *Limnology and Oceanography*, 55 (5):2170–2180, 2010. ISSN 1939-5590. doi: 10.4319/lo.2010.55.5.2170.

Riffler, M., Lieberherr, G., and Wunderle, S. Lake surface water temperatures of European Alpine lakes (1989-2013) based on the (AVHRR) 1 km data set, journal = Earth System Science Data, volume = 7, year = 2015, number = 1, pages = 1–17, doi = 10.5194/essd-7-1-2015.

Röhrs, J., Christensen, K. H., Hole, L. R., Broström, G., Drivdal, M., and Sundby, S. Observation-based evaluation of surface wave effects on currents and trajectory forecasts. *Ocean Dynamics*, 62(10):1519–1533, Dec 2012. ISSN 1616-7228. doi: 10.1007/s10236-012-0576-y.

Rossby, C.-G. On the mutual adjustment of pressure and velocity distributions in certain simple current systems I. *Journal of Marine Research*, 1:15–28, 1937.

Rossby, C.-G. On the mutual adjustment of pressure and velocity distributions in certain simple current systems II. *Journal of Marine Research*, 1:239–263, 1938.

Rueda, F. J. and Schladow, S. G. Dynamics of large polymictic lake. ii: Numerical simulations. *Journal of Hydraulic Engineering*, 129(2):92–101, 2003. doi: 10.1061/(ASCE)0733-9429(2003)129:2(92).

Rueda, F. J. and Vidal, J. Currents in the upper mixed layer and in unstratified water bodies. *in: G. E. Likens (ed.), Biogeochemistry of Inland Waters*, pages 286–300, 2009.

Rueda, F. J., Schladow, S. G., Monismith, S. G., and Stacey, M. T. On the effects of topography on wind and the generation of currents in a large multi-basin lake. *Hydrobiologia*, 532:139–151, 2005. doi: 10.1007/s10750-004-9522-4.

Råman Vinnå, L., Wüest, A., and Bouffard, D. Physical effects of thermal pollution in lakes. *Water Resources Research*, 53(5):3968–3987, 2017. doi: 10.1002/2016WR019686.

Sahoo, G. B., Schladow, S. G., Reuter, J. E., Coats, R., Dettinger, M., Riverson, J., Wolfe, B., and Costa-Cabral, M. The response of Lake Tahoe to climate change. *Climatic Change*, 116 (1):71–95, Jan 2013. ISSN 1573-1480. doi: 10.1007/s10584-012-0600-8.

Salmaso, N. Seasonal variation in the composition and rate of change of the phytoplankton community in a deep subalpine lake (lake garda, northern italy). an application of nonmetric multidimensional scaling and cluster analysis. *Hydrobiologia*, 337:49–68, 11 1996. doi: 10.1007/BF00028506.

Salmaso, N. Factors affecting the seasonality and distribution of cyanobacteria and chlorophytes: a case study from the large lakes south of the Alps, with a special reference to Lake Garda. *Hydrobiologia*, 438(1):43–63, 2000. doi: 10.1023/A:1004157828049.

Salmaso, N. Ecological patterns of phytoplankton assemblages in lake garda: Seasonal, spatial and historical features. *J. Limnol*, 61:95–115, 02 2002. doi: 10.4081/jlimnol.2002.95.

Salmaso, N. Effects of climatic fluctuations and vertical mixing on the interannual trophic variability of Lake Garda, Italy. *Limnol. Oceanogr.*, 50(2):553–565, 2005. doi: 10.4319/lo.2005.50.2.0553.

Salmaso, N. and Cerasino, L. Long-term trends and fine year-to-year tuning of phytoplankton in large lakes are ruled by eutrophication and atmospheric modes of variability. *Hydrobiologia*, 698(1):17–28, 2012. doi: 10.1007/s10750-012-1068-2.

Salmaso, N. and Mosello, R. Limnological research in the deep southern subalpine lakes: synthesis, directions and perspectives. *Advances in Oceanography and Limnology*, 1(1):29–66, 2010. doi: 10.1080/19475721003735773.

Salmaso, N., Mosello, R., Garibaldi, L., Decet, F., Brizzio, M. C., and Cordella, P. Vertical mixing as a determinant of trophic status in deep lakes: a case study from two lakes south of the Alps (Lake Garda and Lake Iseo). *Journal of Limnology*, 62(1s):33–41, 2003. ISSN 1723-8633. doi: 10.4081/jlimnol.2003.s1.33.

Salmaso, N., Buzzi, F., Cerasino, L., Garibaldi, L., Leoni, B., Manca, M., Morabito, G., Rogora, M., and Simona, M. Influenza delle fluttuazioni climatiche sui grandi laghi a sud delle Alpi: implicazioni nel contesto del riscaldamento globale [influence of climatic fluctuations on the large lakes south of the Alps: implications in the context of global warming]. *Biologia Ambientale*, 28:17–32, 01 2014.

Salmaso, N., Boscaini, A., Capelli, C., and Cerasino, L. Ongoing ecological shifts in a large lake are driven by climate change and eutrophication: evidences from a three-decade study in lake garda. *Hydrobiologia*, 11 2017. doi: 10.1007/s10750-017-3402-1.

Salmaso, N., Anneville, O., Straile, D., and Viaroli, P. European large perialpine lakes under anthropogenic pressures and climate change: present status, research gaps and future challenges. *Hydrobiologia*, 824:1–32, 09 2018. doi: 10.1007/s10750-018-3758-x.

Sanay, R. and Valle-Levinson, A. Wind-induced circulation in semienclosed homogeneous, rotating basins. *Journal of Physical Oceanography*, 35(12):2520–2531, 2005. doi: 10.1175/JPO2831.1.

Santo, M., Toffolon, M., Zanier, G., Giovannini, L., and Armenio, V. Large Eddy Simulation (LES) of wind-driven circulation in a peri-alpine lake: detection of turbulent structures and implications of a complex surrounding orography. *J. Geophys. Res.*, 2017. doi: 10.1002/2016JC012284.

Scapini Sobczak, J. R., Valduga, A. T., Restello, R. M., Cardoso, R. I., U.Hep, L., and Siqueira, A. B. Local ecological knowledge as a complementary basis for the management of water resources. *Ethnobiology and conservation*, 2:2–10, 12 2013.

Schimmelpfenning, S., Kirillin, G., Engelhardt, C., and Nützmann, G. Effects of wind-driven circulation on river intrusion in Lake Tegel: modeling study with projection on transport of pollutants. *Environ. Fluid Mech.*, 12:321–339, 2012. doi: 10.1007/s10652-012-9236-5.

Schlabing, D., Frassl, M. A., Eder, M. M., Rinke, K., and Bárdossy, A. Use of a weather generator for simulating climate change effects on ecosystems: A case study on lake constance. *Environmental Modelling & Software*, 61:326 – 338, 2014. ISSN 1364-8152. doi: 10.1016/j.envsoft.2014.06.028.

Schlacher, T. A., Lloyd, S., and Wiegand, A. Use of local ecological knowledge in the management of algal blooms. *Environmental Conservation*, 37(2):210–221, 2010. doi: 10.1017/S0376892910000305.

Schmid, M., Budnev, N. M., Granin, N. G., Sturm, M., Schurter, M., and Wüest, A. Lake Baikal deepwater renewal mystery solved. *Geophysical Research Letters*, 35(9), 2008. ISSN 1944-8007. doi: 10.1029/2008GL033223.

Schmidli, J., Böoing, S., and Fuhrer, O. Accuracy of simulated diurnal valley winds in the Swiss Alps: influence of grid resolution, topography filtering, and land surface datasets. *Atmosphere*, 196:9, 2018.

Schwab, D. J., Clites, A. H., Murthy, C. R., Sandall, J. E., Meadows, L. A., and Meadows, G. A. The effect of wind on transport and circulation in Lake St. Clair. *J. Geophys. Res.*, 94(C4):4947–4958, 1989. doi: 10.1029/JC094iC04p04947.

Schwefel, R., Gaudard, A., Wüest, A., and Bouffard, D. Effects of climate change on deepwater oxygen and winter mixing in a deep lake (Lake Geneva): Comparing observational findings and modeling. *Water Resources Research*, 52(11):8811–8826, 2016. ISSN 1944-7973. doi: 10.1002/2016WR019194.

Serafin, S., Adler, B., Cuxart, J., De Wekker, S. F. J., Gohm, A., Grisogono, B., Kalthoff, N., Kirshbaum, D. J., Rotach, M. W., Schmidli, J., Stiperski, I., Večenaj, Ž., and Zardi, D. Exchange processes in the atmospheric boundary layer over mountainous terrain. *Atmosphere*, 9(3), 2018. ISSN 2073-4433. doi: 10.3390/atmos9030102.

Simons, T. J. *Circulation models of lakes and inland seas.* Canadian Bullettin of Fisheries and Aquatic Sciences. Bulletin 203. Department of Fisheries and Oceans, 1980.

Skamarock, W. C., Klemp, J. B., Dudhia, J., Gill, D. O., Barker, D. M., G.Duda, M., Huang, X. Y., Wang, W., and Powers, J. G. A description of the advanced research WRF version 3. *NCAR Technical Note TN-475+STR, 125*, 2008a.

Skamarock, W. C., Klemp, J. B., Dudhia, J., Gill, D. O., Barker, M., Duda, K. G., Huang, X. Y., Wang, W., and Powers, J. G. A description of the Advanced Research WRF Version 3. Technical report, National Center for Atmospheric Research, 2008b.

Song, Y., Semazzi, F. H. M., Xie, L., and Ogallo, L. J. A coupled regional climate model for the Lake Victoria basin of East Africa. *International Journal of Climatology*, 24(1):57–75, 2004. doi: 10.1002/joc.983.

Soulignac, F., Vinçon-Leite, B., Lemaire, B. J., Scarati M., J. R., Bonhomme, C., Dubois, P., Mezemate, Y., Tchiguirinskaia, I., Schertzer, D., and Tassin, B. Performance assessment of a 3D hydrodynamic model using high temporal resolution measurements in a shallow urban lake. *Environmental Modeling & Assessment*, 22(4):309–322, Aug 2017. doi: 10.1007/s10666-017-9548-4.

Steissberg, T. E., Hook, S. J., and Schladow, S. G. Measuring surface currents in lakes with high spatial resolution thermal infrared imagery. *Geophysical Research Letters*, 32(11):1–4, 2005. Cited By :13.

Stocker, R. and Imberger, J. Energy partitioning and horizontal dispersion in a stratified rotating lake. *Journal of Physical Oceanography*, 33(3):512–529, 2003. doi: 10.1175/1520-0485(2003)033<0512:EPAHDI>2.0.CO;2.

Straile, D., Jöhnk, K., and Henno, R. Complex effects of winter warming on the physicochemical characteristics of a deep lake. *Limnology and Oceanography*, 48(4):1432–1438, 2003. ISSN 1939-5590. doi: 10.4319/lo.2003.48.4.1432.

Strub, P. T. and Powell, T. M. Wind-driven surface transport in stratified closed basins: Direct versus residual circulations. *J. Geophys. Res.*, 91(C7):8497–8508, 1986. doi: 10.1029/JC091iC07p08497.

Svensson, U. The structure of the turbulent Ekman layer. *Tellus*, 31(4):340–350, 1979. doi: 10.3402/tellusa.v31i4.10442.

Taylor, K. E. Summarizing multiple aspects of model performance in a single diagram. *Journal of Geophysical Research: Atmospheres*, 106(D7):7183–7192, 2001. doi: 10.1029/2000JD900719.

Thomas, J. H. A theory of steady wind-driven currents in shallow water with variable eddy viscosity. *Journal of Physical Oceanography*, 5(1):136–142, 1975. doi: 10.1175/1520-0485(1975)005<0136:ATOSWD>2.0.CO;2.

Toffolon, M. Ekman circulation and downwelling in narrow lakes. *Adv. Water Resour.*, 53:76–86, 2013. doi: 10.1016/j.advwatres.2012.10.003.

Toffolon, M. and Rizzi, G. Effects of spatial wind inhomogeneity and turbulence anisotropy on circulation in an elongated basin: a simplified analytical solution. *Adv. Water Resour.*, 32:1554–1566, 2009. doi: 10.1016/j.advwatres.2009.08.001.

Toffolon, M., Moreira, G. A. L., Adami, L., Amadori, M., Bresciani, M., Carniel, S., Dijkstra, H. A., Falcieri, F. M., Farinelli, A., Fatone, F., Gerosa, G., Giardino, C., Marzocchi, A., Miglio, E., Piccolroaz, S., Pilotti, M., Salmaso, N., Valerio, G., and Zardi, D. A scientific task force to study the largest lake in Italy, year =.

Toffolon, M., Piccolroaz, S., and Dijkstra, H. A. A plunge into the depths of Italy's Lake Garda. *Eos*, 98, 2017. doi: doi.org/10.1029/2017EO074499.

Tsimitri, C., Rockel, B., Wüest, A., Budnev, N. M., Sturm, M., and Schmid, M. Drivers of deep-water renewal events observed over 13 years in the South Basin of Lake Baikal. *Journal of Geophysical Research: Oceans*, 120(3):1508–1526, 2015. doi: 10.1002/2014JC010449.

Umlauf, L. and Lemmin, U. Interbasin exchange and mixing in the hypolimnion of a large lake: The role of long internal waves. *Limnol. Oceanogr.*, 50(5):1601–1611, 2005. doi: 10.4319/lo.2005.50.5.1601.

UNESCO. *Background papers and supporting data on the international equation of state 1980.* Tech. Rep. UNESCO, 1981.

Valerio, G., Pilotti, M., Marti, C. L., and Imberger, J. The structure of basin-scale internal waves in a stratified lake in response to lake bathymetry and wind spatial and temporal distribution: Lake Iseo, Italy. *Limnology and Oceanography*, 57(3):772–786, 2012. doi: 10.4319/lo.2012.57.3.0772.

Valerio, G., Pilotti, M., Barontini, S., and Leoni, B. Sensitivity of the multiannual thermal dynamics of a deep pre-alpine lake to climatic change. *Hydrological Processes*, 29(5):767–779, 2015a. doi: 10.1002/hyp.10183.

Valerio, G., Cantelli, A., Monti, P., and Leuzzi, G. A modeling approach to identify the effective forcing exerted by wind on a prealpine lake surrounded by a complex topography. *Water Resources Research*, 2017. doi: 10.1002/2016WR020335.

Valerio, G., Pilotti, M., Barontini, S., and Leoni, B. Sensitivity of the multiannual thermal dynamics of a deep pre-alpine lake to climatic change. *Hydrological Processes*, 29(5):767–779, 2015b. ISSN 1099-1085. doi: 10.1002/hyp.10183.

Valle-Levinson, A., C.Reyes, and R.Sanay. Effects of bathymetry, friction, and rotation on estuary–ocean exchange. *Journal of Physical Oceanography*, 33(2):2375–2393, 2003.

Valle-Levinson, A. Density-driven exchange flow in terms of the Kelvin and Ekman numbers. *Journal of Geophysical Research: Oceans*, 113(C4), 2008. doi: 10.1029/2007JC004144.

Van Haren, H. Philosophy and application of high-resolution temperature sensors for stratified waters. *Sensors*, 18(10), 2018. doi: 10.3390/s18103184.

Van Haren, H., Piccolroaz, S., Amadori, M., Toffolon, M., and Dijkstra, H. A. Moored observations of turbulent mixing events in deep Lake Garda (I). *under review for Limnology and Oceanography*, 2020.

Vercelli, F. Le teorie idrodinamiche delle sesse, [Hydrodynamic theories about seiches]. *in: Mem. R. Istituto lombard, volume XXI*, 1909.

Vercelli, F. Risposta alla nota del Dott. A. Defant sulle sesse del lago di Garda, [Reply to the note from Dott. A. Defant on the seiches in Lake Garda.]. *in: Nuovo Cim, volume 20:357*, 1910.

Veronis, G. Partition of energy between geostrophic and non-geostrophic oceanic motions. *Deep Sea Research (1953)*, 3(3):157 – 177, 1956. ISSN 0146-6313. doi: 10.1016/0146-6313(56)90001-6.

Vilhena, L. C., Marti, C. L., and Imberger, J. The importance of nonlinear internal waves in a deep subalpine lake: Lake Iseo, Italy. *Limnology and Oceanography*, 58(5):1871–1891, 2013. doi: 10.4319/lo.2013.58.5.1871.

Wahl, B. and Peeters, F. Effect of climatic changes on stratification and deep-water renewal in lake constance assessed by sensitivity studies with a 3D hydrodynamic model. *Limnology and Oceanography*, 59(3):1035–1052, 2014. ISSN 1939-5590. doi: 10.4319/lo.2014.59.3.1035.

Wang, Y., Hutter, K., and Bäuerle, E. Wind-induced baroclinic response of lake constance. *Ann. Geoph.*, 18(11):1488–14501, 2000. doi: 10.1007/s00585-000-1488-6.

Wang, Y., Hutter, K., and Bäuerle, E. Barotropic response in a lake to wind-forcing. *Annales Geophysicae*, 19(3):367–388, 2001. doi: 10.5194/angeo-19-367-2001.

Warburton, H. and Martin, A. *Local people's knowledge in natural resources research.* Socio-economic methodologies for natural resources research. Best practice guidelines. Natural Resources Institute, Chatham, UK, 1999.

Welander, P. Wind action on a shallow sea: Some generalizations of Ekman's theory. *Tellus*, 9 (1):45–52, 1957. doi: 10.1111/j.2153-3490.1957.tb01852.x.

Weyhenmeyer, G. A., Mackay, M., Stockwell, J. D., Thiery, W., Grossart, H.-P., Augusto-Silva, P. B., Baulch, H. M., de Eyto, E., Hejzlar, J., Kangur, K., Kirillin, G., Pierson, D. C., Rusak, J. A., Sadro, S., and Woolway, R. I. Citizen science shows systematic changes in the temperature difference between air and inland waters with global warming. *Scientific Reports*, 7:2045–2322, 2017.

Wilson, R. C., Hook, S. J., Schneider, P., and Schladow, S. G. Skin and bulk temperature difference at lake tahoe: A case study on lake skin effect. *Journal of Geophysical Research: Atmospheres*, 118(18):10,332–10,346, 2013. doi: 10.1002/jgrd.50786.

Winant, C. Three-dimensional wind-driven flow in an elongated, rotating basin. *Journal of Physical Oceanography*, 34(2):462–476, 2004. doi: 10.1175/1520-0485(2004)034<0462:TWFIAE>2.0.CO;2.

Wood, T. M., Wherry, S. A., Piccolroaz, S., and Girdner, S. F. Simulation of deep ventilation in Crater Lake, Oregon, 1951-2099. Technical report, Reston, VA, 2016.

Woolway, R. I., Jones, I. D., Hamilton, D. P., Maberly, S. C., Muraoka, K., Read, J. S., Smyth, R. L., and Winslow, L. A. Automated calculation of surface energy fluxes with high-frequency lake buoy data. *Environmental Modelling & Software*, 70:191 – 198, 2015. ISSN 1364-8152. doi: 10.1016/j.envsoft.2015.04.013.

Woolway, R. T., Maberly, S. C., Jones, I. D., and Feuchtmayr, H. A novel method for estimating the onset of thermal stratification in lakes from surface water measurements. *Water Resources Research*, 50(6):5131–5140, 2014. doi: 10.1002/2013WR014975.

Wüest, A. and Lorke, A. Small scale hydrodynamics in lakes. *Annu. Rev. Fluid Mech.*, 35: 373–412, 2003. doi: 10.1146/annurev.fluid.35.101101.161220.

Xue, P., Pal, J. S., Ye, X. Y., Lenters, J. D., Huang, C., and Chu, P. Y. Improving the simulation of large lakes in regional climate modeling: Two-way lake-atmosphere coupling with a 3-D hydrodynamic model of the Great Lakes. *Journal of Climate*, 2017. doi: 10.1175/JCLI-D-16-0225.1.

Yamashiki, Y., Kato, M., Takara, K., Nakakita, E., Kumagai, M., and Jiao, C. Sensitivity analysis on Lake Biwa under the A1B SRES climate change scenario using Biwa-3D integrated assessment model:. *Hydrological Research Letters*, 4:45–49, 2010. doi: 10.3178/hrl.4.45.

Zhong, Y., Notaro, M., Vavrus, S. J., and Foster, M. J. Recent accelerated warming of the Laurentian Great Lakes: Physical drivers. *Limnology and Oceanography*, 61(5):1762–1786, 2016. ISSN 1939-5590. doi: 10.1002/lno.10331.

Zilioli, E., Brivio, P., and Gomarasca, M. A correlation between optical properties from satellite data and some indicators of eutrophication in Lake Garda (Italy). *Science of The Total Environment*, 158:127 – 133, 1994. ISSN 0048-9697. doi: 10.1016/0048-9697(94)90052-3.